Investigation of Airfoil Noise Generation Mechanisms at Low-to-Moderate Reynolds Number and Low Angles of Attack

Elias Arcondoulis

A thesis submitted for the degree of

Doctor of Philosophy

School of Mechanical Engineering

The University of Adelaide, Australia

May 10, 2017

ORIGINALITY STATEMENT

I, Elias J. G. Arcondoulis, hereby declare that this thesis, titled "Investigation of Airfoil Noise Generation Mechanisms at Low to Moderate Reynolds Number", submitted for the award of a Doctor of Philosophy in Engineering at The University of Adelaide, is original in every respect. It contains no material that has been accepted for the award of any other degree or diploma in any university. Further to the best of my knowledge and belief, this Ph.D. thesis contains no material previously published or written by another person, except where due reference is made in the thesis.

Elias J. G. Arcondoulis Date

COPYING PERMISSION

In presenting the fulfillment of the requirements for the degree of Doctor of Philosophy in Engineering at The University of Adelaide, I agree that the Library shall make it freely available for inspection and copying under the Copyright Law of Australia. It is understood that any copying or publication of this Ph.D. research for financial gain shall not be allowed without my written permission. I hereby grant permission to the library at The University of Adelaide to photocopy my work for scholarly purposes only.

Elias J. G. Arcondoulis Date

Contents

Contents **3**

List of Abbreviations **9**

List of Tables **10**

List of Figures **14**

Abstract **27**

Acknowledgments **29**

1 Introduction and Motivation **31**

1.1 Research aims 33

1.2 New research and results 34

2 Literature Review **37**

2.1 Historical overview 38

2.2 Characteristics of airfoil self-noise 39

2.3 Low-to-moderate Reynolds number airfoil flow and noise mechanisms 48

2.3.1 Boundary layer development 48

2.3.2 Separation bubbles 50

2.3.3 Flow in the wake region 53

2.3.4 Broadband noise generation 55
2.3.5 Noise source location 57
2.3.6 Acoustic feedback models 58
2.3.7 Non-feedback related models 63
2.4 Research gaps 65
2.5 Hypothesis 66

3 Single Microphone and Flow Measurement Methods 69
3.1 Anechoic Wind Tunnel (AWT) 69
3.1.1 Contraction outlet velocity 71
3.1.2 Boundary layer development and turbulence intensity 72
3.2 Experimental methods and arrangements 75
3.2.1 Reynolds number and angle of attack 78
3.2.2 Angle of attack correction 80
3.2.3 Single microphone tests 81
3.2.3.1 Data acquisition 81
3.2.3.2 Microphone calibration 83
3.2.3.3 Microphone placement 83
3.2.4 Surface flow visualisation 84
3.2.5 Boundary layer trips 86
3.2.6 Hot-wire anemometry 88
3.2.6.1 Apparatus specifications 88
3.2.6.2 Data acquisition 90
3.2.6.3 Probe calibration 90
3.2.6.4 Probe placement 94
3.3 XFOIL method 99
3.4 Summary 102

4 Acoustic Beamforming 105
4.1 Beamforming review 105

4.2 Beamforming theory and algorithms . . . 106
4.2.1 Cross-spectral method . . . 107
4.2.2 DAMAS . . . 109
4.3 Beamformer design . . . 111
4.3.1 DAQ constraints . . . 111
4.3.2 Spatial constraints . . . 112
4.4 Array type comparison . . . 114
4.4.1 Logarithmic spirals . . . 114
4.4.2 Arcondoulis spiral . . . 117
4.4.3 Maximum sidelobe levels . . . 119
4.4.4 Comparison of cross-spectral and DAMAS techniques . . . 122
4.5 Beamformer experiments . . . 124
4.5.1 Data acquisition . . . 129
4.5.2 Shear layer refraction . . . 130
4.5.3 Shear layer refraction approximation method . . . 133
4.6 Error analysis . . . 135
4.6.1 Error calculation method . . . 137
4.6.2 Beamformer error maps . . . 140
4.6.3 AWT standing waves . . . 144
4.7 Summary of beamforming methods . . . 148

5 Experimental Results 149
5.1 Acoustic feedback mechanism parameters . . . 149
5.1.1 Primary and secondary tones . . . 150
5.1.2 Ladder structure . . . 158
5.1.2.1 Tonal noise envelope . . . 163
5.1.3 Maximum acoustic source location . . . 167
5.1.4 Feedback closing point candidates . . . 172
5.1.4.1 Maximum mean velocity location . . . 173

5.1.4.2 Flow separation and reattachment locations 174
5.1.4.3 Locations of change in phase difference and origin of convective disturbances 180
5.1.5 Convective disturbance velocity 192
5.1.6 Summary of feedback mechanism parameters 193
5.2 Investigation of facility effects 194
5.2.1 Effects of contraction walls and airfoil housing 194
5.2.1.1 On the angle of attack 195
5.2.1.2 Effects along the airfoil span 201
5.2.2 Coherence of primary and secondary tones along the airfoil chord 201
5.2.3 Influence of boundary layer trips 213
5.2.3.1 One surface trip 213
5.2.3.2 Both surface trips 219
5.2.4 Discussion of facility effects 221

6 Acoustic Feedback Mechanisms 223
6.1 Acoustic feedback models 223
6.1.1 Leading edge to TE, L_{LE} 225
6.1.2 Point of maximum velocity to TE, L_U 227
6.1.3 Origin of convective disturbances to TE, L_{CD} 231
6.1.4 Point of separated shear layer reattachment to TE, L_R 231
6.1.5 Origin of boundary layer separation to TE, L_S 232
6.2 Discussion of feedback models 233
6.2.1 Dual acoustic feedback mechanisms 235
6.2.2 Magnitudes of tones 237
6.2.3 Influence of boundary layer trips 240
6.2.4 Accuracy of tone prediction 240
6.3 Proposed feedback model 244

6.4 Summary of analysis 247

7 Conclusions **249**

8 Future Work **255**

References **257**

Appendix A **267**

List of Abbreviations

AWT	Anechoic Wind Tunnel
B&K	Brüel & Kjær
BNC	Bayonet Neill-Concelman
CPV	Coherent Particle Velocity
CTA	Constant Temperature Anemometer
DAMAS	Deconvolution Approach for the Mapping of Acoustic Sources
DAQ	Data Acquisition
DNS	Direct Numerical Simulation
FFT	Fast Fourier Transform
LDA	Laser Doppler Anemometry
LES	Large Eddy Simulation
MASL	Maximum Acoustic Source Location
MMVL	Maximum Mean Velocity Location
MSL	Maximum Sidelobe Level
NACA	National Advisory Committee for Aeronautics
NI	National Instruments
PC	Personal Computer
PIV	Particle Image Velocimetry
PSD	Power Spectral Density
SPL	Sound Pressure Level

List of Tables

3.1 Summary of experiments. All non-zero angle of attack tests were performed on both the airfoil pressure and suction surfaces. 103

4.1 Shift of beamformer image (δ) and θ' - θ_0 due to shear layer refraction for each test case. 135

4.2 Beamformer estimation error for a white noise source in the AWT and the anechoic chamber. 148

5.1 Primary tone frequencies for $\alpha = 0°$ and $\pm 1.58°$. 156

5.2 Secondary tone frequencies for $\alpha = 0°$ and $\pm 1.58°$. 156

5.3 Difference between tone frequencies (Hz), for $\alpha = 0°$ and $\pm 1.58°$. The standard deviations between the difference values are presented in brackets. 158

5.4 Maximum mean velocity location (x/C), measured at $z/C = 0.015$. The stated angles are angles of attack, α. 175

5.5 Point of boundary layer separation from the airfoil surface (x/C). Positive and negative angles of attack represent the airfoil pressure and suction surfaces respectively. 180

5.6 Measured start of convective disturbances (x/C) for primary tones at $\alpha = 0°$ and $\pm 1.58°$. Positive and negative α denote the pressure and suction surfaces respectively. 191

5.7 Convective disturbance velocity ratio, C_r/U_∞, for $\alpha = 0°$ and $\pm 1.58°$, calculated using the primary tone frequencies presented in Table 5.1. . . . 193

5.8 Decrease in noise magnitude when a trip line was applied to the airfoil upper surface, compared to the untripped airfoil at $\alpha = 0°$. Entries that have (0) adjacent to them identify values that are within the dB error estimate. 218

6.1 Acoustic feedback analysis using L_{LE} at $\alpha = 0°$ and 1.58°. In each cell, the top number is the predicted tone, f_n (Hz), and the bracketed number adjacent to it is the corresponding value of n. The number in the middle of each cell is the experimentally measured tone frequency (Hz) and the relative error (%) of f_n with respect to the experimentally measured tone is provided at the bottom of each cell. The experimentally measured primary tones are presented in bold case. 226

6.2 Values of L_U for acoustic feedback loop analysis, as obtained via XFOIL (Drela, 1989) and hot-wire anemometry experiments for $\alpha = 0°$ and 1.58°. A positive angle of attack represents the airfoil pressure side, L_{Up} (experimental) and L_{UXp} (XFOIL); a negative angle represents the airfoil suction side, L_{Us} (experimental) and L_{UXs} (XFOIL). 228

6.3 Acoustic feedback analysis using L_U, L_{Up} and L_{Us} at $\alpha = 0°$ and 1.58°. In each cell, the top number is the predicted tone, f_n (Hz), and the bracketed number adjacent to it is the corresponding value of n. The number in the middle of each cell is the experimentally measured tone frequency (Hz) and the relative error (%) of f_n with respect to the experimentally measured tone is provided at the bottom of each cell. The experimentally measured primary tones are presented in bold case. 229

6.4 Acoustic feedback analysis using L_{UX}, L_{UXp} and L_{UXs} at $\alpha = 0°$ and 1.58°. In each cell, the top number is the predicted tone, f_n (Hz), and the bracketed number adjacent to it is the corresponding value of n. The number in the middle of each cell is the experimentally measured tone frequency (Hz) and the relative error (%) of f_n with respect to the experimentally measured tone is provided at the bottom of each cell. The experimentally measured primary tones are presented in bold case. 230

6.5 Values of L_S for $\alpha = 0°$ and values of L_{Sp} and L_{Ss} for $\alpha = \pm 1.58°$ for acoustic feedback loop analysis, as obtained via surface flow visualisation experiments. A positive angle of attack represents the airfoil pressure side, L_{Sp}; a negative angle represents the airfoil suction side, L_{Ss}. 232

6.6 Acoustic feedback analysis using experimentally obtained values of L_S, L_{Sp} and L_{Ss} at $\alpha = 0°$ and 1.58°. In each cell, the top number is the predicted tone, f_n (Hz), and the bracketed number adjacent to it is the corresponding value of n. The number in the middle of each cell is the experimentally measured tone frequency (Hz) and the relative error (%) of f_n with respect to the experimentally measured tone is provided at the bottom of each cell. The experimentally measured primary tones are presented in bold case. 234

6.7 Acoustic feedback analysis using experimentally obtained values of L_S at $\alpha = 0°$ and values of L_{Sp+s} at $\alpha = 1.58°$. In each cell, the top number is the predicted tone, f_n (Hz), and the bracketed number adjacent to it is the corresponding value of n. The number in the middle of each cell is the experimentally measured tone frequency (Hz) and the relative error (%) of f_n with respect to the experimentally measured tone is provided at the bottom of each cell. The experimentally measured primary tones are presented in bold case. 236

6.8 The difference between tone predictions, *df* (Hz), of L_{Sp} and L_{Ss} where applicable and the magnitudes of the tones relative to the broadband noise level (dB). The experimentally measured primary tones are presented in bold case. 239

List of Figures

2.1 Representations of the experimentally obtained acoustic spectra obtained by Arbey and Bataille (1983), using a NACA 0012 airfoil, at $\alpha = 0°$ and at (a) Re = 107,000, chord C = 80 mm, U = 20.2 m/s and (b) Re = 371,000, C = 160 mm, U = 35 m/s. 41

2.2 Representations of the experimentally obtained acoustic spectra obtained by Chong and Joseph (2009), using a NACA 0012 airfoil, C = 150 mm and at (a) $\alpha = 0°$, U = 15 m/s, Re = 149,000 and (b) $\alpha = 4.2°$, U = 54 m/s, Re = 536,500. 42

2.3 Representations of the experimentally obtained acoustic spectra obtained by Nash et al. (1999), using a NACA 0012 airfoil, C = 300 mm and at (a) $\alpha = 3°$, U = 23.4 m/s, Re = 459,000 and (b) $\alpha = 4°$, U = 26.1 m/s, Re = 518,500. 44

2.4 Representations of the acoustic spectra obtained using DNS by Tam and Ju (2011), using a NACA 0012 airfoil, Re = 400,000 and $\alpha = 0°$. 45

2.5 Pattern showing where tonal noise is likely to occur for a NACA 0012 airfoil (adapted from Lowson et al., 1994). Filled markers represent that a tone was present, whilst unfilled markers represent that a tone was not present. Data sources: △ ▲ (Paterson et al., 1973), ▽ (Arbey and Bataille, 1983), ■ □ (Desquesnes et al., 2007), ◆ (Lowson et al., 1994). The tonal envelope and the maximum tonal amplitude lines are from Lowson et al. (1994). 46

2.6 Ladder-type evolution of the primary tone, $f_{n,max}$, for a NACA 0012 airfoil with C = 160 mm. Adapted from Arbey and Bataille (1983). . . . 47

2.7 Schematic diagram of a the typical flow behaviour around an airfoil, at low-to-moderate Reynolds number. 48

2.8 Schematic diagram of a laminar separation bubble and surrounding flow characteristics, adapted from Dovgal et al. (1994). 51

2.9 Streamline plot obtained using PIV of a laminar separation bubble at the trailing edge of a NACA 0018 airfoil placed at Re = 160,000 and α = 6°. Adapted from Nakano et al. (2006). Images (a), (b) and (c) are in order of time, corresponding to 0, 200 and 400 micro-seconds respectively. Note that the pressure side of the airfoil is the lower side and flow is from left to right. Note that x/C = -0.3 and 0.7 denote the airfoil leading and trailing edge respectively, as defined by Nakano et al., (2006). 52

2.10 Cardioid directivity pattern of the noise emitted from eddies in various locations relative to a sharp edge. 56

2.11 Schematic diagram identifying the important features of the proposed acoustic feedback mechanism by Tam (1974). The empty circle represents the proposed acoustic source origin and the arc lines represent acoustic waves travelling upstream. L represents the distance of the acoustic source origin to the feedback loop origin. 58

2.12 Schematic diagram identifying the important features of the acoustic feedback mechanism proposed by Arbey and Bataille (1983). The empty circle represents the proposed acoustic source origin and the arc lines represent acoustic waves travelling upstream. L represents the distance of the acoustic source origin to the feedback loop origin. 59

2.13 Schematic diagram of the tonal noise mechanisms proposed by Desquesnes et al. (2007). 62

2.14 Hypothesised acoustic feedback model, where L represents the distance between the trailing edge (noise source) and point of boundary layer separation. 67

3.1 AWT facility, viewed from above. Note in the coordinate system shown, Z is positive in the downward direction. 70
3.2 AWT contraction outlet. Flow direction is out of the page. 71
3.3 AWT facility, viewed from outside. 72
3.4 Hot-wire probe paths used to measure mean velocity and turbulence intensity at the outlet of the AWT contraction. 73
3.5 Mean velocity profiles across the AWT contraction outlet. Measurements displayed are along the spanwise direction, at $X = 0$. . . . 74
3.6 Mean velocity profiles across the AWT contraction outlet. Measurements displayed are along the vertical direction, at $X = 0$. 74
3.7 Turbulence intensity profiles across the AWT contraction outlet. Measurements displayed are along the spanwise direction. 76
3.8 Turbulence intensity profiles across the AWT contraction outlet. Measurements displayed are along the vertical direction. 76
3.9 Schematic diagram showing the microphone and hot-wire probe locations during airfoil self-noise experiments in the AWT. 77
3.10 NACA 0012 airfoil secured to the AWT contraction. 78
3.11 Photos of fluid patterns showing surface flow behaviour for a NACA 0012 airfoil, at Re = 150,000 and $\alpha = 0°$. LE, TE, S, and R denote Leading Edge, Trailing Edge, Separation and Reattachment, respectively. 85
3.12 Trip line attachment on the upper surface of a NACA 0012 airfoil in the AWT. LE denotes Leading Edge. 87
3.13 TSI 1260A hot-wire probe used for flow measurements. 89
3.14 The TSI probe holder connected to the traverse lever arm and used to secure the probe. 89

3.15 The TSI Model 1127 Air Velocity Calibrator used for calibration of the the hot-wire probes used in the AWT. 92

3.16 An example calibration chart between the hot-wire probe voltage and the measured flow speed through the calibrator. The fitted line represents the calibration curve. 93

3.17 The DANTEC traverse inside the AWT. 95

3.18 A hot-wire probe in a span-wise test configuration in the AWT. 96

3.19 Schematic diagram of the hot-wire path used to measure the coherence between the measured acoustic signal and power spectrum of the velocity fluctuation signal in the wake. 96

3.20 Schematic diagram of the hot-wire path used to measure velocity profiles from the airfoil surface into the free-stream flow region along the airfoil chord. 97

3.21 Schematic diagram of the hot-wire path used to measure near-wake velocity profiles and coherence between the measured acoustic signal and power spectrum of the velocity fluctuation signal in the near-wake. 98

3.22 Schematic diagram of the hot-wire path used to measure the coherence between the measured acoustic signal and power spectrum of the velocity fluctuation signal near the airfoil surface along the length of the airfoil chord. 98

3.23 XFOIL plot of C_f, used to determine the point of boundary layer separation, at $Re = 100{,}000$ and $\alpha = 0°$. 100

3.24 XFOIL plot of C_f, used to determine the point of boundary layer separation, at $Re = 100{,}000$ and $\alpha = 5°$. The yellow and blue lines represent the airfoil suction and pressure surfaces respectively. 100

3.25 XFOIL plot of u/U_∞, used to determine the point of maximum velocity in the boundary layer, at $Re = 100{,}000$ and $\alpha = 0°$. 101

4.1 Sensitivity diagram (shown in dB, for various focus angles, in degrees) for a 63 channel array (Arcondoulis spiral, shown in Figure 4.4). The source was a simulated 7 kHz plane wave, arriving from the 70° direction. 106
4.2 Acoustic beamforming schematic diagram. 108
4.3 Allowable room within the AWT to accommodate an acoustic beamformer, including the proposed airfoil location and scanning grid. 113
4.4 The Arcondoulis spiral microphone array design used in the AWT (microphone positions denoted by empty circles joined by a line) and the corresponding default logarithmic spiral (microphone positions denoted by filled circles). 118
4.5 Microphone array distributions and the corresponding simulated cross-spectral beamforming result, for a 4.5 kHz monopole source located 600 mm from the array centre. Units are in dB, normalised to the maximum cross-spectral pressure. The presented array types are (a) Grid, (b) Randomised, (c) Logarithmic spiral and (d) Arcondoulis spiral. 121
4.6 (a) The MSL of the arrays presented in Figure 4.5, over 2 kHz to 20 kHz in 50 Hz increments. (b) Differences in MSL values of the logarithmic and the Arcondoulis spirals. The labelled frequency partitions identify transition frequencies for the superiority of each array. 123
4.7 Comparisons between the acoustic source strengths obtained from DAMAS and the cross-spectral method for a simulated 2 kHz monopole source (a) at $X = 200$ mm, $Y = 100$ mm, 600 mm below the array surface, (b) Enlargement of (a), identifying the MASL from the DAMAS and cross-spectral methods. 125
4.8 Comparisons between the acoustic source strengths obtained from DAMAS and the cross-spectral method for a simulated 2 kHz monopole source (a) at $X = 0$ mm, $Y = 0$ mm, 600 mm below the array surface and (b) Enlargement of (a), identifying the MASL from the DAMAS and cross-spectral methods. 126

4.9 Sixty-three microphone beamformer array installed in the AWT. 127
4.10 The acoustic beamformer installed in the AWT for airfoil noise measurements. 128
4.11 Schematic diagram of the scanning grid used to analyse the acoustic source locations of a 67 mm NACA 0012 airfoil in the AWT. 129
4.12 Shear layer refraction schematic diagram. 131
4.13 Shear layer refraction schematic diagram, showing the net shift of the acoustic source location, δ for θ' equal to θ_0. 134
4.14 Coordinate system employed for the positioning of the small acoustic source. 136
4.15 (a) Experimental arrangement for the error analysis of the acoustic beamformer in the AWT. (b) The headphone speaker attached to the traverse arm. 137
4.16 Cross-spectral beamformer output at 3325 Hz for an acoustic source located at $X = 0$ mm, $Y = 100$ mm, $Z = 600$ mm. The acoustic pressure (dB) is normalised relative to the maximum cross-spectral value. Lines have been drawn at the identified source location to help identify the location estimation error relative to the true source. 138
4.17 Cross-spectral beamformer output at 3325 Hz for an acoustic source located at $X = 50$ mm, $Y = 50$ mm, $Z = 600$ mm. The acoustic pressure (dB) is normalised relative to the maximum cross-spectral value. Lines have been drawn at the identified source location to help identify the location estimation error relative to the true source. 139
4.18 X-direction cross-spectral beamformer output error for the white noise acoustic source for various locations in the X-direction. 141
4.19 Y-direction cross-spectral beamformer output error for the white noise acoustic source for various locations in the X-direction. 141
4.20 Total cross-spectral beamformer output error for the white noise acoustic source for various locations in the X-direction. 142

4.21 X-direction cross-spectral beamformer output error for the white noise acoustic source for various locations in the Y-direction. 142
4.22 Y-direction cross-spectral beamformer output error for the white noise acoustic source for various locations in the Y-direction. 143
4.23 Total cross-spectral beamformer output error for the white noise acoustic source for various locations in the Y-direction. 143
4.24 The acoustic beamformer placed in the anechoic chamber. 145
4.25 Acoustic beamforming estimate of source location and noise spectrum for a white noise source placed 600 mm from the array in line with the centre microphone in the anechoic chamber. 146
4.26 Acoustic beamforming estimate of source location and noise spectrum for a white noise source placed 600 mm from the array in line with the centre microphone in the AWT. 147

5.1 PSDs recorded at $\alpha = 0°$ and Re = 30,000 (blue), 40,000 (red) and 50,000 (black), identifying the beginning of a broadband hump and the emergence of tones with increasing Reynolds number. 151
5.2 PSDs at $\alpha = 0°$ and Re = (a) 50,000, (b) 75,000, (c) 100,000, (d) 125,000 and (e) 150,000. The blue and grey lines represent the NACA 0012 airfoil and the background noise with flow respectively. 154
5.3 PSDs at $\alpha = 1.58°$ and Re = (a) 50,000, (b) 100,000 and (c) 150,000. The blue and grey lines represent the NACA 0012 airfoil and the background noise with flow respectively. 155
5.4 PSDs at $\alpha = 3.16°$ and Re = (a) 50,000, (b) 100,000 and (c) 150,000. The blue and grey lines represent the NACA 0012 airfoil and the background noise with flow respectively. 159
5.5 Self-noise spectrogram at $\alpha = 1.58°$ and $Re \approx 30,000$ to 157,000. 161
5.6 Enlargement of Figure 5.5, identifying key features to assist in the visualisation of a ladder structure jump. 161

5.7 Self-noise spectrogram at $\alpha = 0°$ and $Re \approx 30,000$ to 157,000. 162

5.8 Measured primary tones at $\alpha = 0°$ (○) and 1.58° (□). Values of $101 \times U^{0.85}$ were added to fit the measured tones at $\alpha = 0°$. 163

5.9 Pattern showing where tonal noise is likely to occur for a NACA 0012 airfoil (adapted from Lowson et al., 1994). Black filled markers represent that a tone was present, grey filled markers represent that a weak tone was present and all unfilled markers represent that a tone was not present. Data sources: ○ ● ● (present study), △ ▲ (Paterson et al., 1973), ▽ (Arbey and Bataille, 1983), ■ □ (Desquesnes et al., 2007), ◆ (Lowson et al., 1994). The tonal envelope and the maximum tonal amplitude lines are from Lowson et al. (1994). 165

5.10 Tonal envelope, zoom-in of other tonal envelope plot, but with more present work data and including the tonal envelope based on obtained data from experiment. Black filled markers represent a strong tone, grey markers represent a weak tone, unfilled markers represent no tone. Data sources: ■ (Desquesnes et al., 2007). 166

5.11 MASL and PSD at $\alpha = 0°$ and $Re =$ (a) 50,000, (b) 100,000 and (c) 150,000. The empty circles indicate the MASL per frequency and the red lines represent the averaged MASL over 100 Hz bands. Black lines have been drawn at $x/C = 1$ and 0 to depict the airfoil leading and trailing edges respectively. 169

5.12 MASL and PSD at $\alpha = 1.58°$ and $Re =$ (a) 50,000, (b) 100,000 and (c) 150,000. The empty circles indicate the MASL per frequency and the red lines represent the averaged MASL over 100 Hz bands. Black lines have been drawn at $x/C = 1$ and 0 to depict the airfoil leading and trailing edges respectively. 170

5.13 MASL and PSD at $\alpha = 3.16°$ and $Re = 150{,}000$. TThe empty circles indicate the MASL per frequency and the red lines represent the averaged MASL over 100 Hz bands. Black lines have been drawn at $x/C = 1$ and 0 to depict the airfoil leading and trailing edges respectively. 171

5.14 Schematic diagram identifying the coordinate system employed during hot-wire anemometry experiments. 172

5.15 An illustration of the three surface configurations, clarifying the labelling of the upper, lower, suction and pressure surfaces. 173

5.16 Photo of the oil mixture pattern showing surface flow behaviour at $Re = 150{,}000$ and $\alpha = 0°$. LE, TE, S and R denote Leading Edge, Trailing Edge, Separation and Reattachment, respectively. 176

5.17 Photos of the oil mixture pattern showing surface flow behaviour, for $Re = 50{,}000$ to 150,000 and $\alpha = 0°$. S and R denote Separation and Reattachment, respectively. 177

5.18 Photos of the oil mixture pattern showing surface flow behaviour on the pressure surface, for $Re = 50{,}000$ to 150,000 at (a) $\alpha = 1.58°$ and (b) $\alpha = 3.16°$. S and R denote Separation and Reattachment, respectively. . . . 178

5.19 Photos of the oil mixture pattern showing surface flow behaviour on the suction surface of a NACA 0012 airfoil, for $Re = 50{,}000$ to 150,000 at (a) $\alpha = 1.58°$ and (b) $\alpha = 3.16°$. S and R denote Separation and Reattachment, respectively. 179

5.20 Phase difference between the flow and noise signals at $f = 100$ Hz to 10 kHz, $\alpha = 0°$ and (a) $Re = 50{,}000$, (b) $Re = 100{,}000$ and (c) $Re = 150{,}000$. Flow measurements were obtained 1 mm above the airfoil surface ($z/C = 0.015$) in 1 mm chordwise increments ($x/C = 0.015$) from the leading edge ($x/C = 1$) to the trailing edge ($x/C = 0$). 182

5.21 Phase difference between the flow and noise signals at Re = 50,000, $\alpha = 0°$ and (a) $f = 589$ Hz, corresponding to the primary tone and (b) $f = 680$ Hz corresponding to a secondary tone. Flow measurements were obtained 1 mm above the airfoil surface ($z/C = 0.015$) in 1 mm chordwise increments ($x/C = 0.015$) from the leading edge ($x/C = 1$) to the trailing edge ($x/C = 0$). 184

5.22 Phase difference between the flow and noise signals at Re = 100,000, $\alpha = 0°$ and (a) $f = 1426$ Hz, corresponding to the primary tone and (b) $f = 1640$ Hz corresponding to a secondary tone. Flow measurements were obtained 1 mm above the airfoil surface ($z/C = 0.015$) in 1 mm chordwise increments ($x/C = 0.015$) from the leading edge ($x/C = 1$) to the trailing edge ($x/C = 0$). 186

5.23 Phase difference between the flow and noise signals at Re = 150,000, $\alpha = 0°$ and $f = 2050$ Hz, corresponding to the primary tone. Flow measurements were obtained 1 mm above the airfoil surface ($z/C = 0.015$) in 1 mm chordwise increments ($x/C = 0.015$) from the leading edge ($x/C = 1$) to the trailing edge ($x/C = 0$). 187

5.24 Phase difference between the flow and noise signals at $f = 100$ Hz to 10 kHz, Re = 50,000 and $\alpha = 1.58°$ on the airfoil (a) pressure surface and (b) suction surface. Flow measurements were obtained 1 mm above the airfoil surface ($z/C = 0.015$) in 1 mm chordwise increments ($x/C = 0.015$) from the leading edge ($x/C = 1$) to the trailing edge ($x/C = 0$). . 188

5.25 Phase difference between the flow and noise signals at Re = 50,000, pressure surface for $\alpha = 1.58°$ and (a) $f = 607$ Hz, corresponding to the primary tone and (b) $f = 517$ Hz corresponding to a secondary tone. Flow measurements were obtained 1 mm above the airfoil surface ($z/C = 0.015$) in 1 mm chordwise increments ($x/C = 0.015$) from the leading edge ($x/C = 1$) to the trailing edge ($x/C = 0$). 190

5.26 Phase difference between the flow and noise signals at Re = 100,000, α = 1.58° pressure surface and f = 1463 Hz, corresponding to the primary tone. Flow measurements were obtained 1 mm above the airfoil surface (z/C = 0.015) in 1 mm chordwise increments (x/C = 0.015) from the leading edge (x/C = 1) to the trailing edge (x/C = 0). 191

5.27 Mean velocity profiles at α = 0° and Re = (a) 50,000 (b) 100,000 and (c) 150,000. Measurements were obtained in 0.2 mm increments (z/C = 0.003) from z/C = -0.075 to 0.075, y/C = 0 and at x/C = 0, -0.03, -0.075 and -0.15. 197

5.28 Coherence between the flow and noise signals at α = 0° and Re = (a) 50,000 (b) 100,000 and (c) 150,000. Measurements were obtained in 0.2 mm increments (z/C = 0.003) from z/C = -0.075 to 0.075 and x/C = y/C = 0. 200

5.29 Coherence between the flow and noise signals, measured at Re = 100,000 and α = 0° along the line of x/C = -0.015, z/C = 0 and y/b = -0.363 to 0.363. 202

5.30 Coherence between flow and noise, measured at Re = 50,000 and α = 0°. Measurements were obtained at y/C = 0 in z/C = 0.003 increments, from z/C = 0.015 to 0.15 at chordwise stations (a) x/C = 1 (leading edge), (b) x/C = 0.3, (c) x/C = 0.15 and (d) x/C = 0 (trailing edge). 204

5.31 Coherence between flow and noise, measured at α = 0°, z/C = 0.015, y/C = 0 along the airfoil profile from x/C = 0 to 1 and at Re = (a) 50,000, (b) 100,000 and (c) 150,000. 207

5.32 Coherence between flow and noise, measured on the pressure surface at α = 1.58°, z/C = 0.015, y/C = 0 along the airfoil profile from x/C = 0 to 1 and at Re = (a) 50,000, (b) 100,000 and (c) 150,000. 209

5.33 Coherence between flow and noise, measured on the suction surface at α = 1.58°, z/C = 0.015, y/C = 0 along the airfoil profile from x/C = 0 to 1 and at Re = (a) 50,000, (b) 100,000 and (c) 150,000. 210

5.34 Coherence values between flow and noise, measured at $\alpha = 0°$, $y/C = 0$ and $z/C = 0.015$, from $x/C = 1$ to 0. (a) $Re = 100{,}000$ and the black, red and blue lines represent 1426 Hz (primary tone), 1640 Hz (secondary tone) and 1233 Hz (secondary tone) respectively. (b) $Re = 150{,}000$ and the black, blue and cyan lines represent 2050 Hz (primary tone), 3108 Hz (secondary tone) and all other secondary tone frequencies (1738 Hz, 2395 Hz and 2780 Hz) respectively. 212

5.35 Coherence values between flow and noise, measured at $Re = 150{,}000$ and $\alpha = 1.58°$. Measurements were obtained at $y/C = 0$ and $z/C = 0.015$, from $x/C = 1$ to 0 on the (a) pressure surface and (b) suction surface. The black, red, blue and cyan lines represent 2898 Hz (primary tone), 3378 Hz (secondary tone), 3055 Hz (secondary tone) and all other secondary tone frequencies (2047 Hz, 2523 Hz, 2728 Hz, 3754 Hz and 4050 Hz) respectively. 214

5.36 PSDs of a NACA 0012 airfoil and with a trip on the upper airfoil surface, at $\alpha = 0°$ and a Reynolds number of (a) 50,000, (b) 75,000, (c) 100,000, (d) 125,000 and (e) 150,000. The blue, green and grey lines represent the untripped NACA 0012 airfoil, the tripped airfoil on the upper surface and the background noise with flow respectively. 217

5.37 PSDs of a NACA 0012 airfoil and with a trip on both airfoil surfaces, at $\alpha = 0°$ and a Reynolds number of (a) 50,000, (b) 75,000, (c) 100,000, (d) 125,000 and (e) 150,000. The blue, green and grey lines represent the untripped NACA 0012 airfoil, the tripped airfoil on both surfaces and the background noise with flow respectively. 220

6.1 Schematic diagram of the dual acoustic feedback loops at $Re = 100{,}000$ and $\alpha = 1.58°$. Values of $n = 5$ and 8 used in the feedback model on both the pressure and suction surfaces predict tone frequencies 1493 Hz and 1498 Hz on the airfoil pressure and suction surfaces respectively. . . . 238

6.2 Proposed acoustic feedback model, in two consecutive stages (a) and (b). The acoustic feedback occurs back and forth from (a) to (b). 246

Abstract

Airfoils in low-to-moderate Reynolds number flows produce a series of tones that can be annoying to the human ear and potentially impede the design of fans, compressors, helicopter rotors and unmanned air vehicles. Despite extensive studies, there is still little consensus between the various proposed noise generation mechanisms. A majority of previous studies provided evidence for existence for an acoustic feedback mechanism that was responsible for the generation of tones. Disparity exists between studies regarding the lengths of the feedback paths and the acoustic processes that produce these tones. Some studies also assert that an acoustic feedback mechanism does not exist.

This thesis describes a series of experiments which were performed in a small-scale anechoic wind tunnel to investigate airfoil tonal noise generating mechanisms, using a NACA 0012 airfoil at angles of attack of 0°, 1.58° and 3.16° and Reynolds numbers 50,000 to 150,000. Experiments included single microphone measurements, acoustic beamforming, hot-wire anemometry and surface flow visualisation techniques. Single microphone measurements revealed that a strong primary tone was present with several weaker secondary tones, superimposed on a broadband spectrum. Acoustic beamforming was used to locate the acoustic source at the trailing edge. Hot-wire anemometry was used to characterise the flow properties near the airfoil surface, such as points of maximum velocity, boundary layer heights and wake velocity profiles. The phase differences between the acoustic signals and velocity fluctuations near the airfoil surface were used to measure the convective velocity

of disturbances in the boundary layer. Points of instability and phase change in the boundary layer were also investigated using hot-wire anemometry. Surface flow visualisation tests revealed locations of boundary layer separation and reattachment.

A dual acoustic feedback model was proposed, where feedback processes acted independently on the airfoil pressure and suction surfaces. A model proposed by Arbey and Bataille (1983) was adapted such that the feedback lengths were between the acoustic source at the trailing edge and the points of boundary layer separation on the pressure and suction surfaces. At non-zero angles of attack, acoustic feedback mechanisms existed on the airfoil suction and pressure sides simultaneously. For each Reynolds number and angle of attack, both surfaces generated tones within a feedback loop. The tones that were closely matched on both surfaces produced an acoustic superposition. Tones were generated on both airfoil surfaces independently and the tones with the same or similar frequencies constructively interfered, thus explaining the strong primary tone magnitude. The primary tone possessed near exact frequencies on both surfaces, whereas the secondary tones had weak or large differences in frequencies between both surfaces, causing little or no superposition, and thus explaining their diminished magnitude relative to the primary. Using this model, good agreement was achieved between the experimentally obtained and predicted tone frequencies.

Acknowledgments

This thesis is dedicated to my late father, Dr. Demetrius Arcondoulis. His passion to understand the universe and physical processes around us inspired me to pursue a career of science and engineering. My father would always explain mathematics, physics and astronomy to me as a child that in turn developed my thirst for knowledge and an inquisitive mind. I extend my gratitude to my mother, Barbara Arcondoulis and my sister, Katherine Arcondoulis, for their ongoing support and motivation throughout my candidature.

I am truly grateful for my supervisory panel, Assoc. Prof. Con Doolan, Assoc. Prof. Anthony Zander and Dr Laura Brooks. Their insight into acoustic processes and aerodynamics made my research journey clear and kept me on track. Their patience and understanding of my sporting commitments was also very much appreciated. I would also like to acknowledge the School of Mechanical Engineering at The University of Adelaide for making this research possible and for the opportunity to further my education.

I extend my sincere gratitude toward Mr Silvio De Ieso and Mr Norrio Itsumi for their insight and tireless work in the electronics workshop. Without their efforts, the construction of a 63 channel microphone array would not have been possible. I would also like to thank Dr Danielle Moreau for her assistance during the surface flow visualisation tests in the AWT and advice regarding hot-wire anemometry procedures.

Chapter 1

Introduction and Motivation

Airfoils produce tonal and broadband noise in low-to-moderate Reynolds numbers in the range 50,000 $< Re <$ 200,000. There are many important engineering applications that exhibit this behaviour, including micro-wind turbines, compressor and cooling fans, small unmanned air vehicles and submarines. The tonal and broadband noise observed under these flow conditions is said to be produced at the trailing edge of the airfoil (Brooks et al., 1989). An unstable boundary layer containing quadrupole noise sources diffracts at the trailing edge, forming a cardioid pressure distribution (Ffowcs Williams and Hall, 1970; Sandberg et al., 2008). Certain acoustic frequencies emitted due to this diffraction process are said to be amplified, via an acoustic feedback mechanism near the trailing edge (Arbey and Bataille, 1983; Nakano et al., 2006; Kingan and Pearse, 2009; Chong and Joseph, 2009). There exists considerable disparity in the explanations for this mechanism, as discussed in Chapter 2.

The tonal noise component is the greatest focus of this research, as even relatively low magnitude tonal noise can be irritating to the human ear, with prolonged exposure leading to hearing damage and ill psychological health. Passchier-Vermeer and Passchier (2000) discuss that there is sufficient scientific evidence that noise exposure can induce hearing impairment, hypertension and ischemic heart disease,

annoyance, sleep disturbance and decreased school performance. Bies and Hansen (2003) also discuss the psychological effects of tonal noise and the negative impacts it has on social behaviour, work efficiency and sleep, and its ability to affect speech recognition and communication. These health and psychological implications impede the use of engineering applications that exhibit excessive aeroacoustic noise in populated areas.

Mike Rann (former premier of South Australia) in April 2008 pushed for the installation of micro-wind turbines in the Adelaide Central Business District. At a similar time, South Australia Education Minister Jane Lomax-Smith announced that micro-wind turbines would be fitted to SA schools, as part of a Rann Government initiative to help "green" state schools and preschools. Much study is required to determine the aeroacoustic noise mechanisms surrounding the wind turbines before they are installed. Studies of micro-wind turbines in London showed that at a distance of five metres from the blades, a total sound pressure level (SPL) of 52 dB was measured when the wind speed was at 7 m/s. This has been identified as a potential problem for large-scale deployment within domestic areas (Mid Wales Energy Agency, 2005).

Computer cooling fan noise levels are sufficiently low to avoid hearing damage, yet the irritation and psychological effect of this noise warrants further research into the governing aeroacoustic mechanism. Marine propellers, hydrofoils and other submarine components exhibit transitional and turbulent boundary layers (Blake, 1975) and thus exhibit similar noise characteristics at low-to-moderate Reynolds number. The Australian Department of Defence plans to have a more potent and heavier maritime force by the mid-2030s and replace and expand the current fleet of six Collins class submarines with a more capable class of submarine (Defence White Paper, 2016). Significant investigations into the flow generated noise of these submarines will be required, to minimise the overall SPL of the submarine and produce acoustic signatures that are less likely to be detected.

While investigations of fans and propeller geometries assist in specific industrial

problems, they do not directly assist in determining the fundamental aspects of noise generation mechanisms, as each part has specific noise problems to address due to its unique geometry. Understanding the fundamental tonal noise generating mechanisms will provide an improved basis for future research in noise reduction of all airfoil shaped bodies in low-to-moderate Reynolds number flows.

1.1 Research aims

The overall aim of this research was to understand the fundamental mechanisms responsible for tonal noise generation of an airfoil at low-to-moderate Reynolds number. To understand the processes and mechanisms that produce tones, a unique combination of experiments were performed in an anechoic wind tunnel to analyse the local flow and acoustic conditions. A NACA 0012 airfoil profile was chosen for all of the experiments in this research to allow a comparison with published numerical and experimental results.

1.2 New research and results

The feasibility of an acoustic feedback mechanism was evaluated using a novel combination of experimental techniques, including acoustic beamforming, hot-wire anemometry and surface flow visualisation. The results provide evidence for the existence of two simultaneous feedback mechanisms, on the airfoil pressure and suction surfaces. The feedback length was found to occur between the point of boundary layer separation on the airfoil pressure and suction surfaces and the trailing edge, where the maximum acoustic source strength was located. Previous research suggested that the feedback loop originated at other locations, such as the point of maximum velocity on the airfoil surface (Arbey and Bataille, 1983). In addition, only one other study suggested that a dual feedback mechanism existed (Desquesnes et al., 2007) and others suggested that if a feedback mechanism existed, it occurred only on one airfoil surface (Longhouse, 1977). Other research suggested that a feedback mechanism was not required to observe the measured tones and that most of the noise could be attributed to facility effects (Nash et al., 1999; Tam and Ju, 2011).

All of the parameters used to derive and compare acoustic feedback models in this research were obtained via experimental methods. The convective disturbance velocity was an important parameter in determining the validity of an acoustic feedback process and was calculated using simultaneous hot-wire anemometry and microphone measurements. Previous research assumed that the convective disturbance velocity did not vary with Reynolds number and angle of attack (Arbey and Bataille, 1983), yet this study showed otherwise. The points of boundary layer separation on the airfoil surface were obtained using a surface flow visualisation technique, using a mixture of oil and talcum powder.

An acoustic beamformer was designed and manufactured in-house specifically for the anechoic wind tunnel. A unique arrangement of microphones in a phased array, namely the “Arcondoulis spiral”, was installed in the wind tunnel above the

airfoil trailing edge. This was done to improve the array response and beamformer output for the testing conditions and spatial requirements. Acoustic beamforming was used to determine the maximum acoustic source strength location. For all flow conditions, this was shown to be at the airfoil trailing edge.

Using varying feedback lengths provided reasonable agreement between predicted and measured tones. The best agreement was made using a dual feedback mechanism involving the points of boundary layer separation on the airfoil suction and pressure surfaces. This model also accounted for the variation of tonal noise frequencies with Reynolds number and angle of attack. These results showed that the overall measured noise was sensitive to the disturbance of at least one surface boundary layer, and the relative magnitude change due to boundary layer trips agreed with the proposed feedback model.

From the experimental results and subsequent analysis, there was considerable evidence to show that a dual acoustic feedback mechanism was responsible for the tonal noise generation of airfoils at low-to-moderate Reynolds number.

Chapter 2

Literature Review

This chapter provides a detailed overview of airfoil tonal noise generation at low-to-moderate Reynolds numbers. Despite significant research in this field, there is still controversy surrounding the mechanisms responsible for tonal noise generation and even the measured noise itself. Many of the studies performed to date present results for an airfoil at particular Reynolds numbers and angles of attack, making flow and noise comparisons with other studies difficult. Furthermore, experiments performed in different facilities presented different acoustic spectra for similar flow conditions, leading to investigations of facility effects on the measured noise. Even further disparity was introduced when numerical studies were used to investigate airfoil flow and noise, leading to differing conclusions regarding tonal noise mechanisms.

The majority of the studies investigated proposed that the tones associated with an airfoil in low-to-moderate Reynolds number flows were produced by an acoustic feedback mechanism. This mechanism was generally said to exist between the trailing edge (noise source location) and a point of receptivity on the airfoil chord, yet there is no consensus on either of these locations. Other studies suggested that the measured tones were a product of vortex shedding processes near the trailing edge and acoustic interactions with the experimental facility. Numerical studies have provided support for both cases.

2.1 Historical overview

Research into the tonal noise of airfoils at low-to-moderate Reynolds numbers began when Paterson et al. (1973) performed experiments with various airfoil profiles, flow speeds and angles of attack. They observed a single tone possessing a frequency dependence with Strouhal number and concluded that vortex shedding processes were responsible for its generation. Only a year later, Tam (1974) dismissed this explanation and proposed that the tonal frequency only coincidentally followed a trend with Strouhal number. They stated that measured noise was not due to vortex shedding or vortex shedding alone and that an acoustic feedback mechanism was responsible for the measured tone. Nearly a decade later and with the assistance of significant advances in data acquisition technology, Arbey and Bataille (1983) observed that the measured noise was not only a single tone, but it consisted of a series of tones and a broadband contribution. They proposed a different acoustic feedback model between the point of flow separation and the trailing edge (that they believed to be the noise source location) to accommodate these additional tones. Others agreed with the existence of an acoustic feedback model, but proposed different points of acoustic receptivity along the airfoil chord and the location of the noise source (including Nakano et al., 2006; Desquesnes et al., 2007; Kingan and Pearse, 2009; Chong and Joseph, 2009; Sandberg et al., 2010).

Acoustic feedback models were proposed at either zero or non-zero angle of attack flow behaviour (not both), thus making data and feedback models difficult to compare between wider Reynolds number and angle of attack regimes. Experimental studies that possessed the same or similar flow conditions were conducted in facilities with different reflective properties, resulting in differing acoustic spectra that were difficult to explain. Further controversy was introduced when Nash et al. (1999) proposed that the measurement of secondary tones was due to the acoustic interaction of a single tone (produced by vortex shedding processes) with experimental facility walls and surfaces. This theory was widely neglected until Tam and

Ju (2011) supported some of these claims using numerical methods.

As computational power increased over the past decade, many more publications of numerical analyses were presented. Numerical simulations provide flexibility in the range of problems to be analysed without concern of practical issues in a wind tunnel, yet the evaluation of acoustic pressures using numerical techniques such as Large Eddy Simulations (LES) and Direct Numerical Simulations (DNS) can be sensitive to flow errors (Wang, 1998). The radiated noise from an aeroacoustic source can contain very low energy relative to the unsteady flow. Thus small errors in the unsteady flow field can lead to significant errors in the acoustic pressure evaluation (Wang, 1998). In addition, even with significant advances in computational power, DNS and LES simulations remain computationally expensive. Furthermore, some studies supported an acoustic feedback mechanism using DNS (Desquesnes et al., 2007; Sandberg et al., 2010) and others opposed its existence in certain flow conditions (Tam and Ju, 2011).

There is significant controversy in this field of aeroacoustics and much more research is required to conclusively explain the tonal noise generating process of an airfoil at low-to-moderate Reynolds number.

2.2 Characteristics of airfoil self-noise

Arbey and Bataille (1983) revealed that at low-to-moderate Reynolds numbers, airfoil self-noise generally consisted of a series of acoustic tones superimposed on a broadband contribution. A representation of their acoustic spectra obtained at an angle of attack of zero degrees, $\alpha = 0°$, and at Reynolds numbers, Re, of approximately 107,000 and 371,000 are presented in Figures 2.1a and 2.1b respectively. At both Reynolds numbers there existed a primary tone frequency, $f_{n,max}$, and a series of secondary tone frequencies, f_n. The broadband contribution, namely a "broadband hump", occurred over a wider frequency range and was centred about frequency f_s.

The two spectra plots in Figure 2.1 possess similarity, in that a number of discrete tones exist within the frequency range of a broadband hump. The relative magnitudes of the tones between the two flow conditions differ significantly. In Figure 2.1a, the primary tone $f_{n,max}$ possessed a much greater relative magnitude to the secondary tones than at the flow conditions in Figure 2.1b. The frequency range of the broadband hump at the higher Reynolds number was greater than the lower Reynolds number, but smaller in maximum amplitude.

By inspection of Arbey and Bataille's (1983) data, the number of tones, the frequency spacing between tones, and the relative magnitudes of tones with respect to other tone magnitudes were seen to be Reynolds number dependent. Further inspection of their data revealed that there existed a Reynolds number that maximised the magnitude of $f_{n,max}$. Therefore at a certain Reynolds number and assuming all other flow parameters were held constant, the mechanism(s) responsible for tonal noise generation reached a saturation point. All of Arbey and Bataille's (1983) experiments were conducted at $\alpha = 0°$ and thus the influence of angle of attack on the tonal properties of the noise could not be ascertained from their data.

Chong and Joseph (2009) also observed a series of tones and a broadband hump using a NACA 0012 airfoil in a wind tunnel. The acoustic spectra from two of their experiments at $\alpha = 0°$, flow speed $U = 15$ m/s ($Re = 149{,}000$) and $\alpha = 4.2°$, $U = 54$ m/s ($Re = 536{,}500$) are shown in Figures 2.2a and 2.2b respectively. Comparing the airfoil self-noise broadband contributions with Arbey and Bataille (1983) was difficult, due to the different Reynolds numbers, angles of attack and experimental facilities. It should be noted that in Figures 2.1a and 2.2a the same number of tones were observed (five). While the flow conditions were not identical, the Reynolds numbers were relatively close ($Re = 107{,}000$ and $149{,}000$) and in both cases $\alpha = 0°$.

In all of the presented spectra by Arbey and Bataille (1983), it was observed that $f_{n,max} = f_s$. Chong and Joseph's (2009) result in Figure 2.2b showed that this was not necessarily the case. Making observations of the relative change of noise

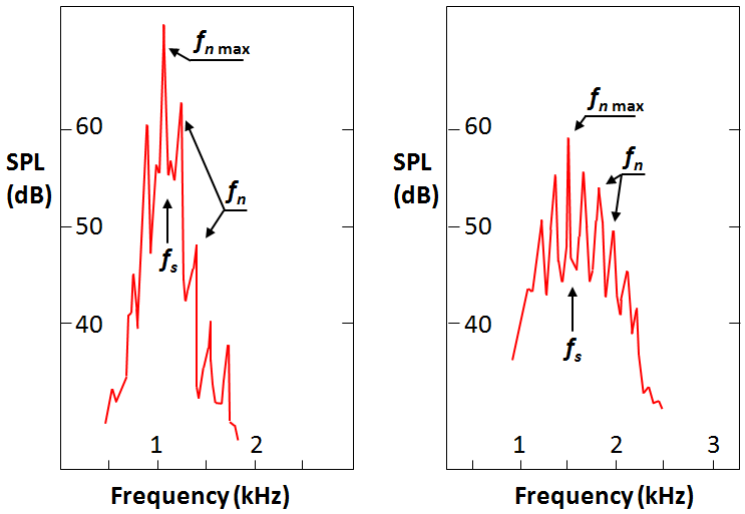

Figure 2.1: Representations of the experimentally obtained acoustic spectra obtained by Arbey and Bataille (1983), using a NACA 0012 airfoil, at $\alpha = 0°$ and at (a) $Re = 107{,}000$, chord $C = 80$ mm, $U = 20.2$ m/s and (b) $Re = 371{,}000$, $C = 160$ mm, $U = 35$ m/s.

behaviour with increasing Reynolds number and angle of attack was difficult within Chong and Joseph's (2009) data, as each flow case possessed different Reynolds numbers and angles of attack.

Nash et al. (1999) performed experiments in a hard-walled wind tunnel and repeated them with acoustic treatment in the wind tunnel. The acoustic spectra obtained using a 300 mm chord NACA 0012 airfoil at $\alpha = 3°$, $U = 23.4$ m/s ($Re = 459{,}000$) and $\alpha = 4°$, $U = 26.1$ m/s ($Re = 518{,}500$) are presented in Figures 2.3a and 2.3b respectively. Interestingly, a broadband hump was not observed. At both flow conditions, there existed a series of discrete tones, with a greater number of them present at a higher Reynolds number and angle of attack, consistent with Chong and Joseph (2009).

Nash et al. (1999) claimed that by acoustically treating their wind tunnel, all secondary tones were eradicated and that they were generated solely due to

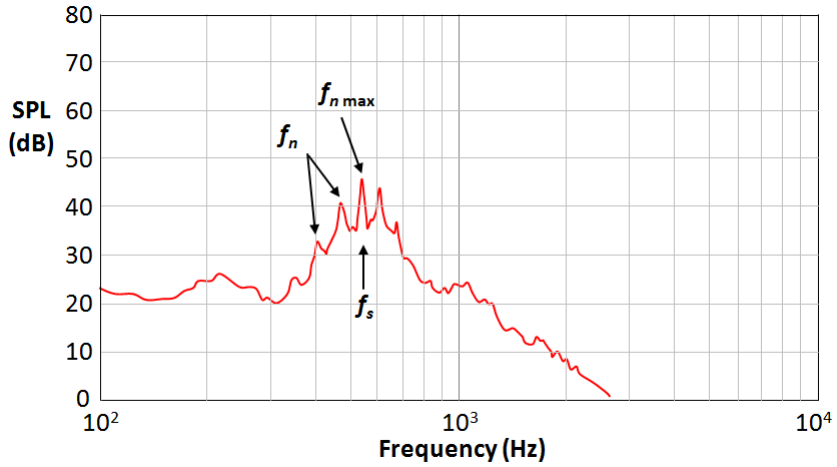

(a)

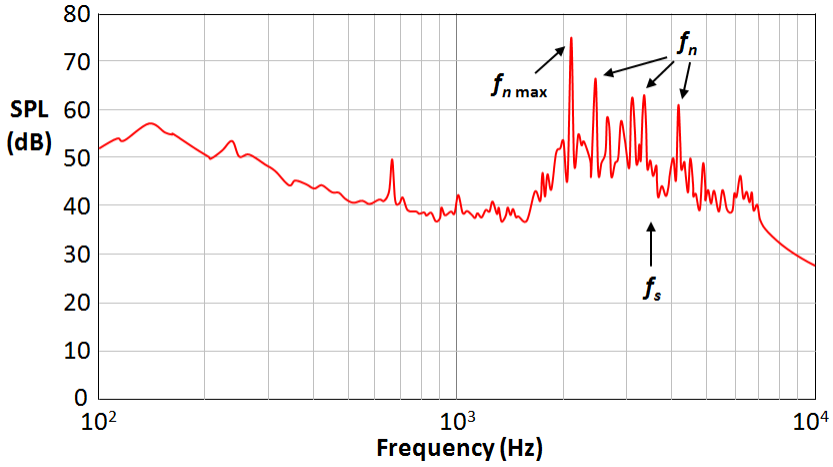

(b)

Figure 2.2: Representations of the experimentally obtained acoustic spectra obtained by Chong and Joseph (2009), using a NACA 0012 airfoil, $C = 150$ mm and at (a) $\alpha = 0°$, $U = 15$ m/s, $Re = 149{,}000$ and (b) $\alpha = 4.2°$, $U = 54$ m/s, $Re = 536{,}500$.

acoustic resonances and interactions within the experimental facility. Tam and Ju (2011) used DNS and supported Nash et al.'s (1999) claim of a single tone at low-to-moderate Reynolds number. Their acoustic spectra of a NACA 0012 airfoil at $Re = 400{,}000$ and $\alpha = 0°$ is presented in Figure 2.4, where only a single tone was present. The results of Nash et al. (1999) and Tam and Ju (2011) provided controversy as to what the true airfoil self-noise actually was and whether the series of secondary tones, f_n and even the broadband hump, f_s were facility induced or not. These tonal noise generating mechanisms are discussed further in Section 2.3.7.

In Figure 2.3, there appears to be little or no airfoil self-noise broadband contribution. This may be due to high broadband noise levels within the wind tunnel exceeding the broadband hump contribution, as no discussion was presented regarding the background wind tunnel noise during operation. Tam and Ju (2011) also reported no broadband contribution, possibly due to their numerical methods, or that the broadband hump reported by others was only due to the wind tunnel background noise or other facility-related sources. Kingan and Pearse (2009) claim that this broadband noise is associated with Tollmein-Schlicting (T-S) waves. Broadband noise-only recordings occurred when the Reynolds number was increased excessively, causing any tonal noise generating mechanisms to cease. Alternatively, much smaller Reynolds numbers did not produce any tones and only a small broadband contribution was observed. The amplitude and frequency range of the broadband noise hump was shown to vary with Reynolds number and angle of attack (Arbey and Bataille, 1983; Nakano et al., 2006).

By comparing and collating the data of studies to date, there existed few flow cases that were directly comparable. Almost all of the flow cases possessed a unique Reynolds number and angle of attack combination and in the case where the Reynolds numbers were comparable, the experiments were performed at different flow speeds due to different airfoil chords. Desquesnes et al. (2007) furthered the work of Paterson et al. (1973), Arbey and Bataille (1983), Nash et al. (1998) and Lowson et al. (1994, 1998) and collated experimentally and numerically obtained

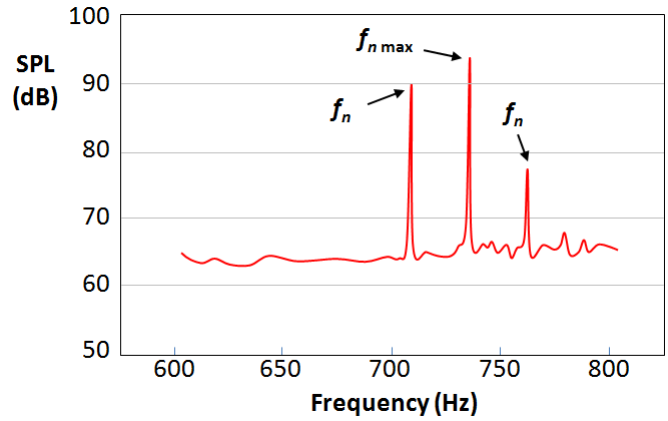

(a)

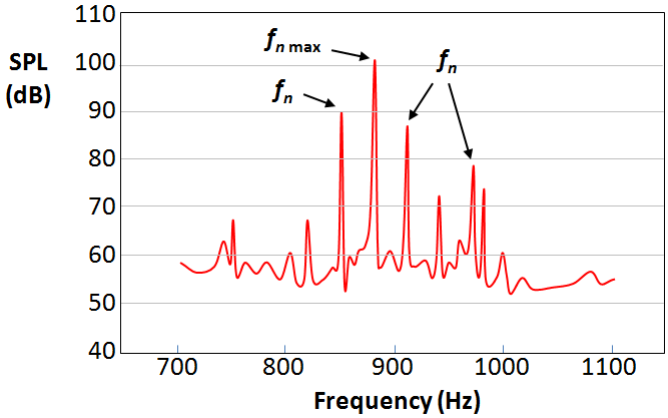

(b)

Figure 2.3: Representations of the experimentally obtained acoustic spectra obtained by Nash et al. (1999), using a NACA 0012 airfoil, $C = 300$ mm and at (a) $\alpha = 3°$, $U = 23.4$ m/s, $Re = 459{,}000$ and (b) $\alpha = 4°$, $U = 26.1$ m/s, $Re = 518{,}500$.

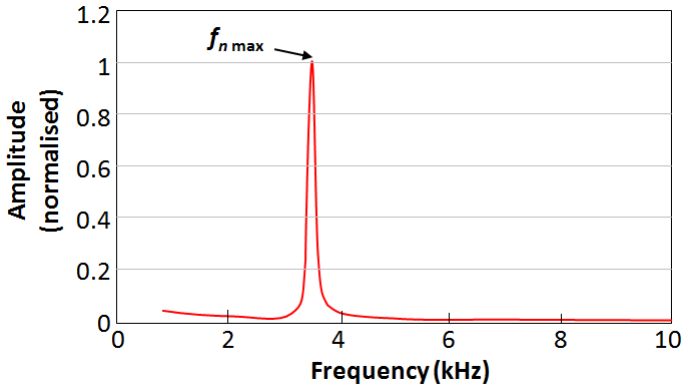

Figure 2.4: Representations of the acoustic spectra obtained using DNS by Tam and Ju (2011), using a NACA 0012 airfoil, $Re = 400{,}000$ and $\alpha = 0°$.

tonal noise data for a NACA 0012 airfoil, as presented in Figure 2.5. Lowson et al. (1998) produced a window of Reynolds numbers and angles of attack for which tones are predicted to occur, namely a tonal envelope. The proposed tonal envelope in Figure 2.5 conflicted with some of the presented data. At $Re = 400{,}000$ and $\alpha = 0°$, Arbey and Bataille (1983) did not reveal a tone via experiment, yet Lowson et al. (1994) predicted that this flow condition should exhibit a tone. McAlpine et al. (1999) experimentally showed that tones were not present at $\alpha = 0°$ and $Re = 160{,}000$ and 340,000, also contradicting the tonal envelope. There is also a lack of experimental and simulated data for flow conditions at $\alpha < 5°$ and $Re > 200,000$. Charts of this type for other airfoil profiles have not been found in the literature.

Using NACA 0012 and 0018 profiles over $Re = 800{,}000$ to 2,200,000, Paterson et al. (1973) observed that small increases in flow velocity, U, increased the frequency of $f_{n,max}$ by a factor of $U^{0.8}$. At certain flow velocities, $f_{n,max}$ would suddenly increase or "jump", creating a new 0.8 power relationship with velocity. This overall pattern of increasing frequency with respect to $U^{0.8}$ for a given velocity range formed a "ladder structure". Across a range of Reynolds numbers and various angles of attack,

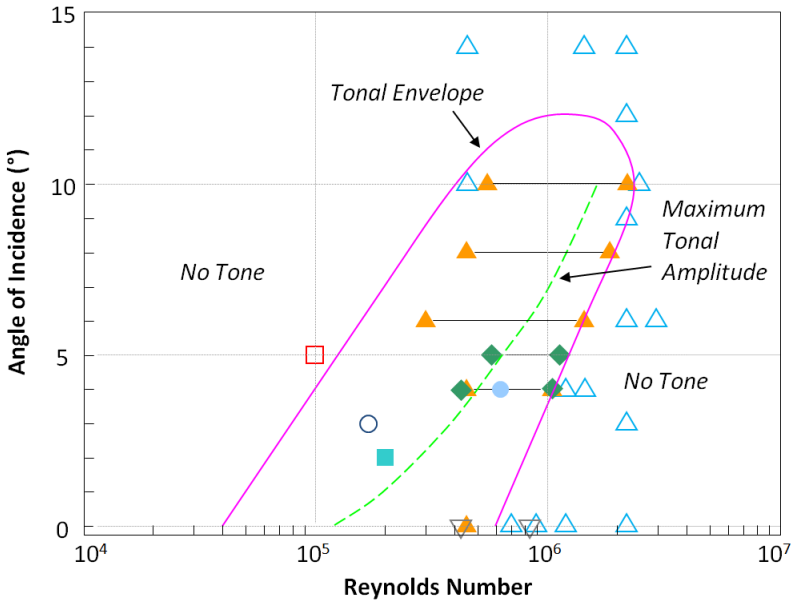

Figure 2.5: Pattern showing where tonal noise is likely to occur for a NACA 0012 airfoil (adapted from Lowson et al., 1994). Filled markers represent that a tone was present, whilst unfilled markers represent that a tone was not present. Data sources: △ ▲ (Paterson et al., 1973), ▽ (Arbey and Bataille, 1983), ■ □ (Desquesnes et al., 2007), ◆ (Lowson et al., 1994). The tonal envelope and the maximum tonal amplitude lines are from Lowson et al. (1994).

a $U^{1.5}$ curve of best fit was shown to agree with $f_{n,max}$, as provided by

$$f_{n,max} = \frac{0.011U^{1.5}}{\sqrt{C\upsilon}} \tag{2.1}$$

where υ is the kinematic fluid viscosity.

The ladder structure can be observed in Arbey and Bataille's (1983) data, presented in Figure 2.6. They collated all of their measured tones and drew lines through the primary tones, with a $U^{0.8}$ dependence, that abruptly ended at certain flow speeds (and thus Reynolds numbers), forming the ladder structure. The centre frequency of the broadband hump, f_s, was also presented and follows a $U^{1.5}$ dependence. A ladder structure was observed by many others (including Tam, 1974; Nash

et al., 1999; Nakano et al., 2006; Desquesnes et al., 2007; Chong and Joseph, 2009; Plogmann et al., 2013 and Probsting et al., 2014 & 2015). Moreau et al. (2014) also observed a ladder structure during experiments conducted in an anechoic wind tunnel of a wall-mounted finite airfoil.

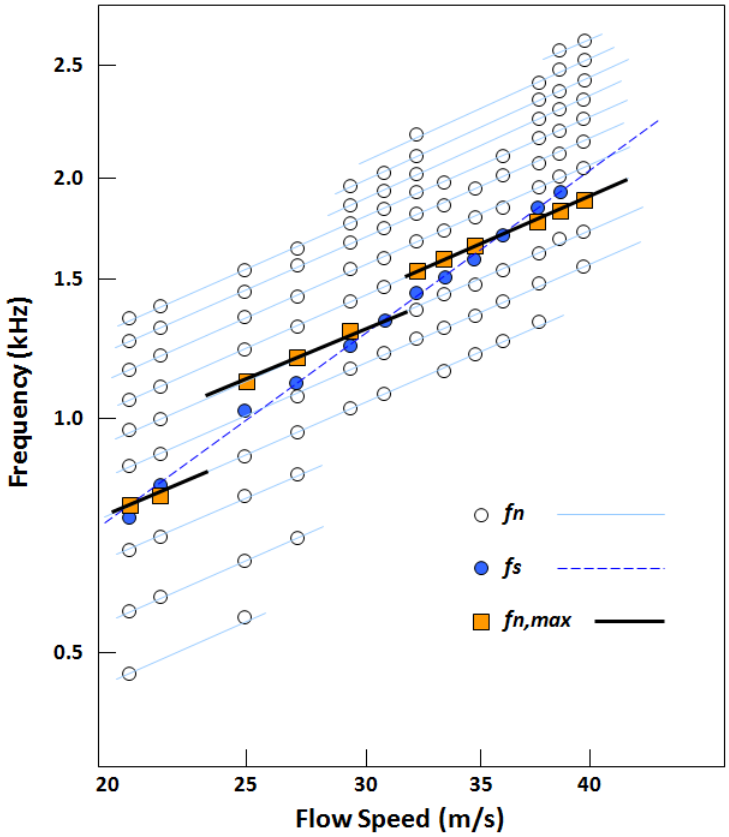

Figure 2.6: Ladder-type evolution of the primary tone, $f_{n,max}$, for a NACA 0012 airfoil with $C = 160$ mm. Adapted from Arbey and Bataille (1983).

2.3 Low-to-moderate Reynolds number airfoil flow and noise mechanisms

2.3.1 Boundary layer development

To understand the noise generating mechanisms, the nature of the flow around the airfoil surface first needs to be understood. For an airfoil placed in uniform flow, the flow remains attached to the airfoil past the leading edge along the chord. The Reynolds number, the airfoil chord and profile determines whether and/or where the flow separates or remains attached. Laminar boundary layer separation often occurs when an adverse pressure gradient opposes the freestream flow direction (O'Meara and Mueller, 1987). The laminar separated shear layer is highly unstable and causes transition to turbulence to occur at a point immediately downstream of the point of separation. If the Reynolds number is adequately low, the separated shear layer is turbulent and does not reattach to the airfoil surface. At higher Reynolds numbers the turbulent separated shear layer reattaches to the airfoil surface, forming a turbulent boundary layer between the point of reattachment and the trailing edge. These flow behaviours are identified in Figure 2.7.

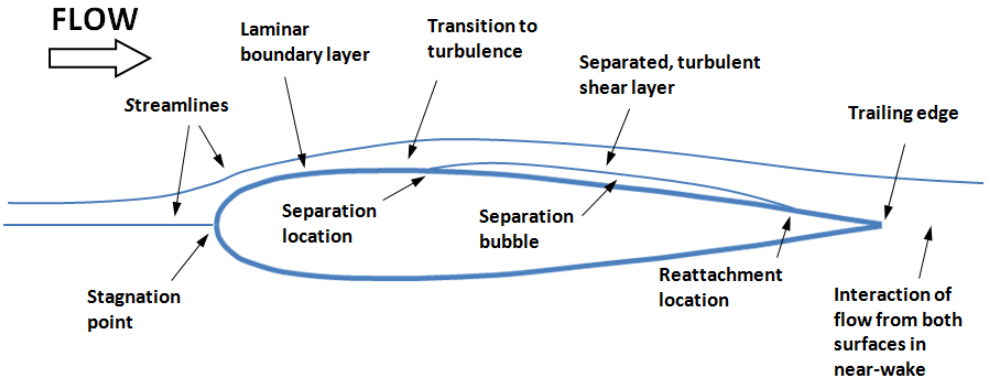

Figure 2.7: Schematic diagram of a the typical flow behaviour around an airfoil, at low-to-moderate Reynolds number.

Sandberg et al. (2008) performed DNS of a NACA 0012 airfoil at $Re = 50{,}000$ for several angles of attack. They showed that the a laminar boundary layer remained attached to a point where the flow became separated from the airfoil surface, creating an unstable shear layer. The unstable shear layers from the suction and pressure surfaces interacted past the trailing edge, forming a highly turbulent wake with a complex flow structure. Sandberg et al. (2008) also showed that at non-zero angles of attack, the boundary layers on each airfoil surface grew and became unstable at different distances along the chord. The boundary layer on the suction side of the airfoil became highly unsteady and separated from the airfoil, forming an unstable shear layer. The separation took place much further upstream than at zero angle of attack, resulting in a highly turbulent shear layer at the trailing edge. The pressure surface boundary layer remained laminar along the entire chord. Boutilier and Yarusevych (2012) used hot-wire anemometry to measure velocity profiles from the surface of a NACA 0018 airfoil and demonstrated that laminar boundary layer transition occurred much closer to the leading edge with increasing angle of attack.

Laminar-to-turbulent transition in the boundary layer is caused by the amplification of background disturbances in the pressure and velocity fields within an unstable frequency band (Rist et al., 1996). These disturbances may be initiated by surface roughness, vibration or by an external stimulus, such as an incoming vortical structure or acoustic waves interacting with the boundary layer (Jones et al., 2010). The disturbances generally grow and interact, eventually resulting in a saturation of disturbance growth and the creation of instability waves within the boundary layer. A primary instability is defined as an instability wave that grows exponentially within the boundary layer that can be either an absolute or a convective primary instability (Gaster 1963, 1968). The growth of T-S waves within the laminar boundary layer is an example of a convective instability. The mechanism by which bluff body vortex shedding is initiated is an example of an absolute instability (Hannemann and Oertel, 1989). The understanding of primary instability growth is important in predicting the location of laminar boundary layer transition

to turbulence.

In order to simulate and sustain turbulent flow behaviour in the separated shear layer, Sandberg et al. (2008) needed to introduce artificial excitation of T-S waves in the laminar boundary layer. Their flow conditions were at low Reynolds numbers, but their flow Mach number was unrealistically high to sustain the T-S wave excitation. The effects of these conditions on the separated shear layer, flow field near the trailing edge and the resulting trailing edge noise spectra are unknown.

2.3.2 Separation bubbles

A separation bubble is defined as the region of recirculating flow between the flow separation and reattachment points on the surface of a rigid body, as depicted in Figure 2.8. If the separated shear layer reattaches to an airfoil forming a separation bubble, the flow properties of the reattachment can vary depending on the airfoil profile and Reynolds number. Balser and Fazel (2010) discussed that in some cases the reattachment can exist with a rapid breakdown to turbulence with little or no vortex shedding formation. In other cases, however, the turbulent shear layer is an unsteady flow process where large scale vortex structures are shed into the turbulent boundary layer. This phenomenon is also known as bubble flapping and has been observed using DNS (Pauley et al., 1990) and measured using flow visualisation (Brendel and Mueller, 1986). The mechanism causing separation bubble flapping remains under investigation. Jones et al. (2008) proposed that the bubble flapping occurs at a frequency below the primary Kelvin-Helmholtz instability (Rist and Maucher, 2002; Jones et al., 2010) and that this behaviour can be attributed to vortex shedding. Jones et al. (2010) suggest that the bubble flapping is caused by an acoustic feedback mechanism; a topic discussed at length in Section 2.3.6.

Using smoke-wire visualisation, Boutilier and Yarusevych (2012) investigated the shear layer development of a NACA 0018 airfoil at Re = 100,000. For the airfoil surface at zero and non-zero angles of attack they identified that the flow both sepa-

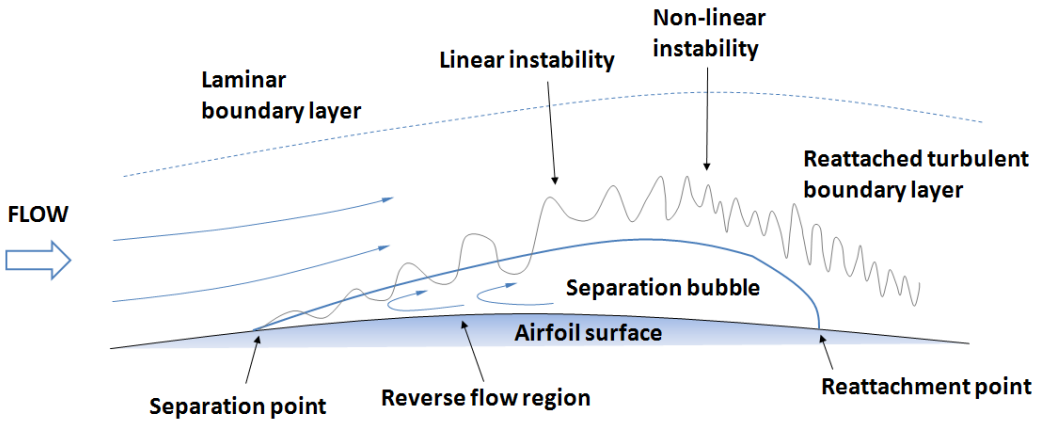

Figure 2.8: Schematic diagram of a laminar separation bubble and surrounding flow characteristics, adapted from Dovgal et al. (1994).

rated and reattached, creating a separation bubble along the chord. As the angle of attack was increased the separation bubble was observed further upstream, exhibiting higher disturbance growth rates and possessing a decreased length. Sandberg et al. (2008) showed using DNS that the separated shear layer did not reattach to the airfoil surface at Re = 50,000. This Reynolds number was half that investigated by Boutilier and Yarusevych (2012), and hence may be insufficient for flow reattachment.

Separation bubbles have been recorded near the trailing edge. Nakano et al. (2006) identified a laminar separation bubble, $x/C = 0.05$ in size, on the pressure side of a NACA 0018 airfoil near the trailing edge using Particle Image Velocimetry (PIV), at Re = 160,000 and $\alpha = 6°$. The streamlines from this investigation are depicted in Figure 2.9. Figures 2.9a - c correspond to 0 to 400 micro-seconds, at which the separation bubble developed into and remained at its maximum size (Nakano et al., 2006).

Nash et al. (1999) showed using smoke visualisation on a NACA 0012 airfoil pressure surface at $Re = 465{,}000$ and $\alpha = 3°$ that there existed a separated boundary layer near the trailing edge. The formation of an instability near the trailing edge

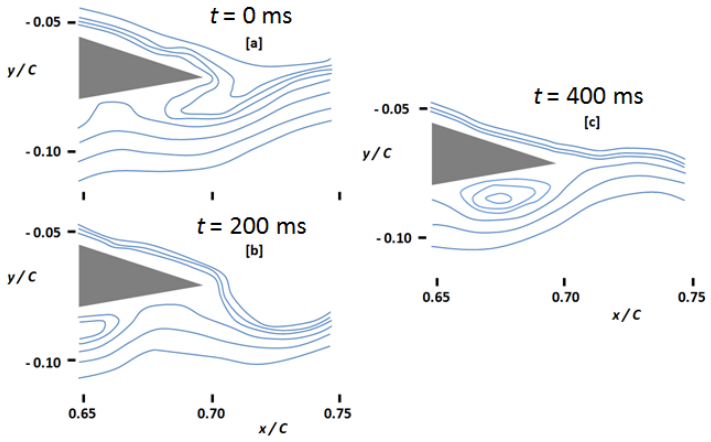

Figure 2.9: Streamline plot obtained using PIV of a laminar separation bubble at the trailing edge of a NACA 0018 airfoil placed at Re = 160,000 and $\alpha = 6°$. Adapted from Nakano et al. (2006). Images (a), (b) and (c) are in order of time, corresponding to 0, 200 and 400 micro-seconds respectively. Note that the pressure side of the airfoil is the lower side and flow is from left to right. Note that x/C = -0.3 and 0.7 denote the airfoil leading and trailing edge respectively, as defined by Nakano et al., (2006).

rolled up into a vortex that shed downstream of the trailing edge. Kingan and Pearse (2009) showed using XFOIL (Drela, 1989) that separation occurred near the trailing edge for flow cases where laminar boundary layer instability noise was produced, at both zero and non-zero angles of attack of a NACA 0012 airfoil. Plogmann et al. (2013) and Probsting et al. (2014) showed the existence of separation bubbles near the trailing edge at non-zero angles of attack on the airfoil pressure surface, using the Coherent Particle Velocity (CPV) method and PIV respectively.

In summary, separation bubbles were shown to occur near the trailing edge on the airfoil pressure surface, only for cases where the airfoil angle of attack was non-zero. Separation bubbles were measured mid-chord for airfoils placed at both zero and non-zero angles of attack and on the airfoil suction side only. For zero angle of attack flow cases, the locations of laminar boundary layer separation and shear layer

reattachment were only documented for the airfoil upper surface and it is assumed that this behaviour was symmetric about the airfoil centre line and mirrored on the lower surface.

2.3.3 Flow in the wake region

Understanding the coherent flow structures and vortex shedding processes in the airfoil wake may help explain the noise generating mechanisms at low-to-moderate Reynolds number (Yarusevych et al., 2009). Nakayama (1987) described that in the region near the wake centreline and immediately downstream of an airfoil trailing edge at $\alpha = 0°$, the interaction of the boundary layers from the upper and lower surfaces created an intense mixing zone where the flow changed rapidly with increased turbulence intensity and shear stress. Yarusevych et al.'s (2009) investigations showed that the coherent structures in the separated shear layer and airfoil wake were strongly Reynolds number dependent. For a NACA 0025 airfoil at $\alpha = 0°$ and $Re = 100{,}000$, wake vortices formed in the near-wake region and were shed on the upper and lower sides of the turbulent wake in an alternating manner. They suggested that the wake vortex shedding was caused by near-wake instability.

Tam and Ju (2011) used DNS for a NACA 0012 airfoil and displayed a vortical structure in the airfoil wake at $\alpha = 0°$ and $Re = 200{,}000$ and also showed unsteady near-wake motion and vortex shedding in regions further downstream of the near-wake. Yarusevych et al. (2003, 2004, 2008) investigated the flow behaviour in the wakes of airfoils by comparing the mean velocity profiles immediately aft of the trailing edge for $\alpha = 0°$, 5° and 10° and at $Re = 57{,}000$, 100,000 and 150,000. Yarusevych et al. (2003) discussed that the width of the airfoil wake increased with angle of attack, supported by the results of Sandberg et al. (2008). Yarusevych et al. (2003) also observed that the vertical location of the minimum velocity did not depend significantly on the angle of attack at $Re = 57{,}000$ and 100,000 and that increased turbulence within the boundary layer separation on the airfoil pressure

surface governed the wake formation and structure.

Chong and Joseph (2009) showed using PIV with a NACA 0012 airfoil that at a small distance aft of the trailing edge at $Re = 150{,}000$, there existed a small, distinct localised area of velocity fluctuations that were not predicted by others using DNS (Sandberg et al, 2008; Tam and Ju, 2011) and experiments (Yarusevych 2009, 2012). As the angle of attack increased from 0° to 2°, the localised velocity fluctuations moved closer to the trailing edge. When the angle of attack was increased to 5°, this localised velocity fluctuation disappeared, due to the reduction of adverse pressure gradient and boundary layer perturbation on the airfoil pressure surface with increasing angle of attack. The boundary layer on the suction surface underwent an earlier transition to instability, reducing the inflectional profile near the trailing edge and thus the amplification of the instability waves. When the instabilities from both surfaces of the airfoil interacted near the trailing edge, the reduced coherence of the resulting vortex shedding lost its periodicity and thus decreased the intensity of the velocity fluctuations.

Sandberg et al. (2008) provided evidence of a reverse flow region within the wake, under both laminar and turbulent flow conditions. Using a NACA 0012 airfoil at $\alpha = 0°$ and $Re = 50{,}000$, a reverse flow region existed between $1.008 < x/C < 1.05$, where $x/C = 1$ represented the trailing edge. Other thinner airfoils, NACA 0006 and NACA 0008, did not display a reverse flow region. Their explanation was that the flow was oscillating at the wake frequency between the upper and lower surfaces of the airfoil at the trailing edge. They were unclear as to why this behaviour was present for this airfoil but not for the others investigated in their paper, suggesting that the influence of the airfoil profile on the flow behaviour in the wake region was not fully understood. There is also no experimental data to verify this result.

It is clear that there are inconsistencies between the various studies of flow structures in the airfoil wake at low-to-moderate Reynolds number and that the simulated results do not always agree with experiments. The flow in the wake region is important for understanding the generation of tonal noise, yet there is no

general consensus on the flow structures in this area nor are there comprehensive studies of the relationship between the flow and noise.

2.3.4 Broadband noise generation

The presence of a finite flat plate edge in a turbulent flow results in a large increase in the existing noise within that fluid at low Mach numbers (Ffowcs Williams and Hall, 1970). Turbulent eddies that are close to the trailing edge are much more powerful sources of sound than eddies far from the edge. Ffowcs Williams and Hall (1970) showed that the greatest acoustic intensity is achieved when an eddy is located at the trailing edge. The acoustic intensity of an eddy located away from the trailing edge decreases relative to the third power of distance.

Ffowcs Williams and Hall (1970) discussed the acoustic pressure pattern that is directed from the sharp edge. The noise sources in the boundary layer are represented as quadrupoles that can be considered as a pair of dipoles whose major axes are mutually orthogonal. Five quadrupoles are drawn so that the major axis of one of the dipole pairs of each quadrupole is oriented towards the sharp edge. When a wave from a dipole encounters the edge, a diffracted wave is produced that travels back towards the quadrupole with opposite phase. This diffracted wave combines with outgoing waves from the other side of the dipole (that has similar phase to the diffracted wave) to create a more efficient source of sound than a free quadrupole. One side of the quadrupole is thus made an efficient radiator of sound and contributes to the cardioid directivity pattern commonly associated with trailing edge noise (Howe, 2006). Figure 2.10 shows the areas of acoustic superposition around the edge of the half plane.

The geometric differences between an infinitely thin flat plate and a 2-D symmetric (non-cambered) airfoil are the variation in thickness along the chord of the airfoil. Since both infinitely thin flat plates and most airfoils have a sharp trailing edge, it has been argued that the diffraction process at the trailing edge is the same

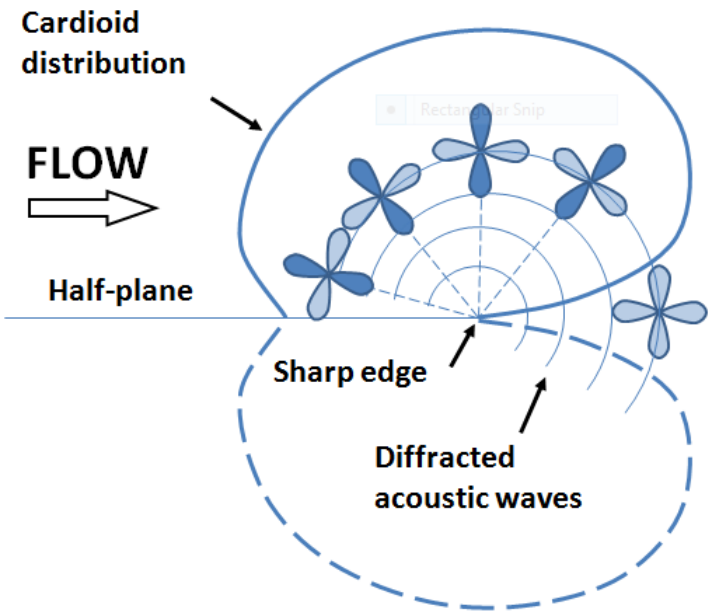

Figure 2.10: Cardioid directivity pattern of the noise emitted from eddies in various locations relative to a sharp edge.

for both geometries. Experimental measurements made by Paterson et al. (1973) for turbulent flow over a NACA 0012 airfoil showed that the flat plate theory yields reasonable results for finite thickness airfoil geometries. Sandberg et al. (2008) observed a cardioid pressure pattern at the trailing edge and found that the acoustic pressure distribution for a NACA 0012 airfoil using DNS was on average within 2 dB of their analytical acoustic analogy. The flow and noise behaviour of a plate with a sharp edge provides an introduction to the flow behaviour of an airfoil near its trailing edge. The diffraction process at the trailing edge causes a broadband noise contribution, but this process alone cannot explain the observed tonal noise that can occur when airfoils are in low-to-moderate Reynolds number flows.

2.3.5 Noise source location

There is general agreement that broadband noise is generated from the airfoil trailing edge, yet the acoustic source location responsible for tonal noise at low-to-moderate Reynolds number is still uncertain. Recent technological advances have helped alleviate some of the uncertainty of this acoustic source location. Gaudriot et al. (1982) claimed that the source of acoustic waves radiating from within the boundary layer was located at the airfoil trailing edge, using an acoustic mirror technique (Grosche et al., 1977). A more advanced acoustic imaging technique known as acoustic beamforming has been used extensively in commercial applications, such as wing sections, wind turbine blades and airfoils at significantly higher Reynolds numbers (Brooks and Humphreys, 2003, 2004; Oerlemans et al., 2008). Geyer et al. (2010) used acoustic beamforming to investigate broadband noise sources of a porous airfoil at $Re = 400{,}000$ to 800,000 and noted maximum acoustic source strengths at the trailing edge. Nakano et al. (2006) suggested there were several locations downstream of the trailing edge responsible for noise production. Tam (1974) and Chong and Joseph (2009) showed similar results but only of a single velocity fluctuation location that they claim was the origin of tonal noise production.

Using DNS Sandberg et al. (2008) observed that the pressures on the airfoil upper and lower surfaces were 180° out of phase and that the radiated acoustic pressure waves at low angles of attack were predominantly from a pressure source at the trailing edge. At higher angles of attack, an acoustic pressure wave was created at the leading edge, interfering with the acoustic waves generated at the trailing edge. The acoustic pressure above and below the airfoil was not completely out of phase in this case, due to the interaction of different boundary layers from the pressure and suction surfaces.

2.3.6 Acoustic feedback models

There have been many explanations why airfoils in low-to-moderate Reynolds number flows produce tonal noise. Tam (1974) proposed that a feedback process was responsible for amplifying the noise created by a diffraction process at the airfoil trailing edge (Ffowcs Williams and Hall, 1970). Tam (1974) showed that as the laminar boundary layer becomes unstable, T-S waves became amplified as they travelled downstream. The boundary layer instabilities passed the trailing edge into the wake, causing lateral vibrations that emitted an upstream-propagating acoustic wave and thus reinforcing the original disturbance. A schematic of the feedback loop proposed by Tam (1974) is shown in Figure 2.11.

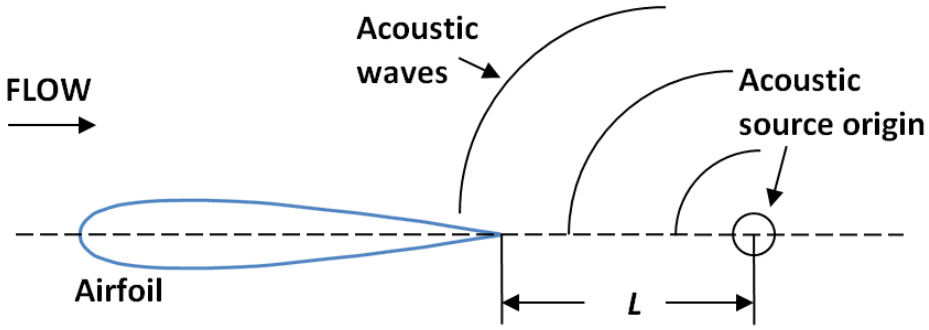

Figure 2.11: Schematic diagram identifying the important features of the proposed acoustic feedback mechanism by Tam (1974). The empty circle represents the proposed acoustic source origin and the arc lines represent acoustic waves travelling upstream. L represents the distance of the acoustic source origin to the feedback loop origin.

Longhouse (1977) proposed a different feedback mechanism that shared some similarities with Tam's (1974) model, claiming that the instabilities in the laminar boundary layer on the suction surface were indeed T-S waves and their interactions with the trailing edge generated acoustic waves, not a point in the wake. These acoustic waves radiated upstream and the instabilities in these waves reinforced with the T-S waves, completing a feedback mechanism.

Arbey and Bataille (1983) agreed in some aspects with Tam (1974) and Longhouse (1977), in that the existence of regularly spaced discrete tonal frequencies was linked with an acoustic feedback mechanism. Their explanation differed from that of Tam (1974) in both the feedback loop closing point and where the acoustic source was located relative to the trailing edge. Arbey and Bataille (1983) suggested that broadband noise was generated via a diffraction process at the trailing edge (Ffowcs Williams and Hall, 1970) that caused out-of-phase acoustic waves to radiate upstream. They proposed that the point of maximum flow velocity on the airfoil surface was the first point of instability in the laminar boundary layer. If the acoustic wave and the velocity fluctuation frequencies were in phase at this location, the velocity fluctuations would become amplified (Tam, 1974; Archibald, 1975). These velocity fluctuations then propagated downstream, thus closing the feedback loop, as depicted in Figure 2.12.

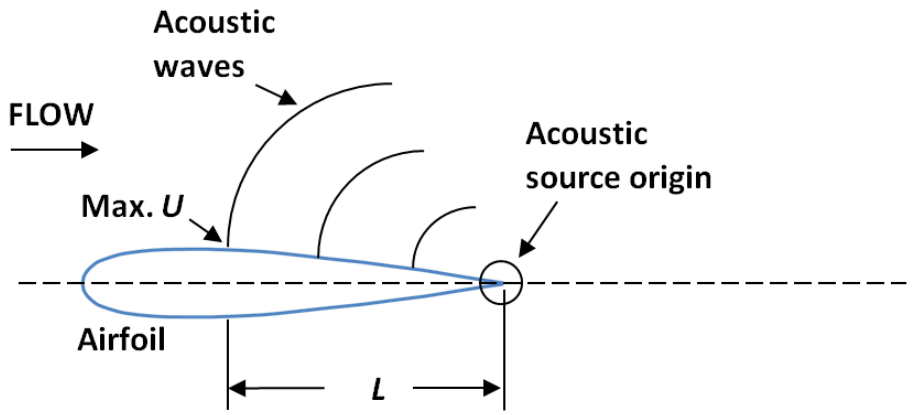

Figure 2.12: Schematic diagram identifying the important features of the acoustic feedback mechanism proposed by Arbey and Bataille (1983). The empty circle represents the proposed acoustic source origin and the arc lines represent acoustic waves travelling upstream. L represents the distance of the acoustic source origin to the feedback loop origin.

Arbey and Bataille (1983) derived a feedback loop model and proposed that each tone observed in the noise spectrum, f_n (Hz), could be measured using an equation that was rearranged to

$$f_n = \frac{C_r}{L}(n + 0.5)\left(1 + \frac{C_r}{C_0 - U}\right)^{-1} \tag{2.2}$$

where L is the feedback loop length, C_r is the convective disturbance velocity, C_0 is the speed of sound and n is a positive integer.

In Arbey and Bataille's (1983) model, the feedback length, L, is the distance between the point of maximum velocity on the airfoil chord and the trailing edge, that does not vary with Reynolds number. Therefore the feedback loop length they employed was constant for all flow conditions for each angle of attack. Via interpretation of Arbey and Bataille's (1983) graphical data, they achieved agreement within 3% or better between the predicted and experimentally measured tones at $\alpha = 0°$. As they were not able to compare experimental data at non-zero angle of attack, it is possible that a different acoustic feedback mechanism existed at non-zero angle of attack. Kingan and Pearse (2009) created a theoretical model of laminar boundary layer instability noise incorporating the theory of tone selection by Arbey and Bataille (1983), yet their prediction errors were greater than Arbey and Bataille (1983). Brooks et al. (1989) derived an expression for determining the peak frequency of a NACA 0012 airfoil due to laminar instability that provided good agreement with the measured primary tones reported by Arbey and Bataille (1983), but did not provide information regarding the secondary tone frequencies and magnitudes. Their SPL data was presented in one-third octave bandwidths, possibly causing the secondary tones to not be present in their results.

Arbey and Bataille's (1983) model was numerically sensitive to its parameters. No studies show a dependence or relationship of C_r/U with Reynolds number, angle of attack or airfoil profile. Boutilier and Yarusevych (2012) showed that the convective disturbance velocity fitted within the approximate range of $0.3 < C_r/U < 0.5$, consistent with a linear stability analysis performed using simulated separated

shear layer profiles (Dovgal et al., 1994). Boutilier and Yarusevych (2012) suggested that the convective disturbance velocity within the separated shear layer was dependent on the distance of the shear layer core from the airfoil surface, as well as the maximum reverse flow speed.

Desquesnes et al. (2007) using DNS results proposed that tonal noise is produced by a feedback loop involving a separation bubble on the pressure surface near the trailing edge. The existence of this recirculation bubble had previously been identified as a necessary condition for the tonal noise phenomenon to occur (Lowson et al, 1994). Desquesnes et al. (2007) proposed that a secondary feedback loop exists on the suction surface, explaining that boundary layer separation rapidly occurs creating an unstable shear layer with T-S instability waves that interact with the trailing edge, forming a dipolar acoustic source in the near wake. They suggested that acoustic waves then travel upstream along the airfoil chord and generate an acoustic feedback loop, as shown in Figure 2.13. Their research was performed at non-zero angles of attack and whether the main and secondary feedback loop lengths were equal at $\alpha = 0°$ was unknown. The validity of Desquesnes et al.'s (2007) proposed feedback model at $\alpha = 0°$ requires further investigation.

Jones et al. (2010) proposed a feedback model that originates from a disturbance created at the leading edge that becomes amplified by instability waves at some point downstream. Broadband noise radiates from the trailing edge due to diffraction processes (Ffowcs Williams and Hall, 1970) that radiate upstream above the shear layer. Selected frequencies of the acoustic waves are reinforced at the leading edge closing the feedback loop. Ikeda et al. (2012) also proposed that a feedback loop exists between the airfoil leading and trailing edges, but have little data to verify their proposition.

Plogmann et al. (2013) investigated tonal noise generation of a NACA 0012 airfoil via experiment using CPV. They observed the typical ladder-structure behaviour of the primary tone and claimed that an acoustic feedback loop exists on the airfoil pressure surface. They conjectured that if a secondary feedback loop on

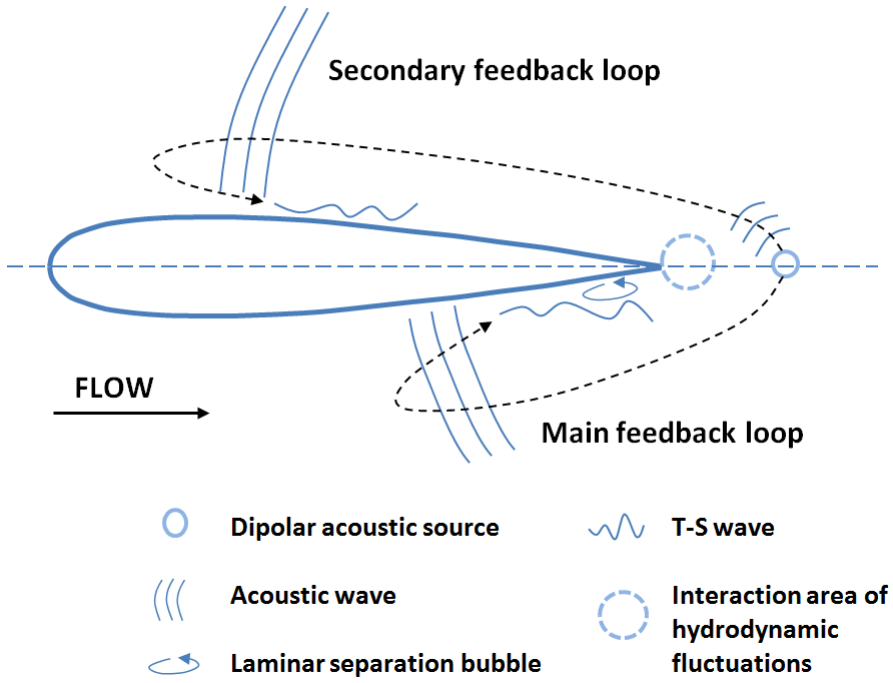

Figure 2.13: Schematic diagram of the tonal noise mechanisms proposed by Desquesnes et al. (2007).

the suction surface exists, then it has no significant influence on the measured tones.

In other applications, an acoustic feedback model was proposed to explain the tonal noise observed with a cavity on one airfoil surface. Schumacher et al. (2013) adapted the acoustic feedback model of Arbey and Bataille (1983) to provide evidence that an acoustic feedback mechanism exists between the downstream edge of the cavity and the trailing edge. Varying the cavity location and width affected the number of tones and tone frequency spacing, consistent with the acoustic feedback mechanism presented by Arbey and Bataille (1983).

The details of acoustic feedback mechanisms, if they exist, are uncertain. The feedback mechanisms reviewed here differed in their proposed acoustic source location and feedback loop length, L. Tam's (1974) value of L is between the trailing edge and the noise source at a fixed distance downstream of the trailing edge. In

Arbey and Bataille's (1983) model, L is the distance between the trailing edge and the point of maximum velocity on the airfoil surface. Desquesnes et al. (2007) proposed that L exists between the boundary layer on the airfoil pressure side and the noise source at some location downstream of the trailing edge. Despite the different parameters in each of these models, all of the acoustic feedback mechanisms investigated here contended that an acoustic wave radiated upstream from its source and became positively reinforced at some point along the airfoil chord.

2.3.7 Non-feedback related models

There is no conclusive evidence to suggest that the tone-producing mechanisms are due to an acoustic feedback mechanism or a combination of vortex shedding and an acoustic feedback mechanism. Insufficient bandwidth in acoustic measurements prevented Paterson et al. (1973) observing a series of secondary tones, leading to a theory of vortex shedding processes. While it has been shown by many in some DNS and experimental studies that secondary tones are present, the theory of vortex shedding has not been totally disregarded. It is possible that the primary acoustic tone is totally or partially generated via vortex shedding and the secondary tones by an acoustic feedback mechanism or other process.

Lowson et al. (1994) and Nash et al. (1999) suggested that an acoustic feedback mechanism is not necessary to observe tonal noise. They explained that amplification of T-S instabilities takes place within the laminar boundary layer and the separated shear layer. Using flow visualisation techniques they show that this separated flow region near the trailing edge forms vortices that are then shed downstream of the trailing edge producing a single tone. Nash et al. (1999) proposed that the existence of a separated boundary layer at the trailing edge would contradict the noise frequency prediction models produced by Paterson et al. (1973), Fink et al. (1976) and Arbey and Bataille (1983), that assumed the boundary layer at the trailing edge remains attached.

Nash et al. (1999) measured primary and secondary tones via experiment in a hard-walled wind tunnel for $Re > 200,000$ at non-zero angles of attack. They proposed that their observed secondary tones were generated by the interaction of the broadband and tonal noise within their testing facility. By testing the airfoil in a quasi-anechoic environment, they were able to eliminate all secondary tones and only observed a single primary tone. Using DNS, Tam and Ju (2011) supported this theory, showing that a NACA 0012 airfoil at $\alpha = 0°$ and Re = 200,000 to 500,000 there existed only a primary tone. They concurred with Nash et al. (1999) that an acoustic feedback mechanism does not occur at $\alpha = 0°$ and that any other tones observed via experiment at this flow condition are due to facility effects. Tam and Ju (2011) did not eliminate the possibility of secondary tone measurements at non-zero angle of attack measurements and thus Tam and Ju's (2011) study only partially supports Nash et al.'s (1999) theory. In addition, Tam and Ju (2011) do not negate the possibility of acoustic feedback mechanisms at non-zero angles of attack, whereas Nash et al. (1999) did.

Probsting et al. (2015) revealed via experiment using PIV and acoustic measurements that at non-zero angles of attack, tonal noise generation was dominated by processes on the suction surface at lower Reynolds numbers (approx. 30,000) and conversely at higher Reynolds numbers (approx. 230,000), dominated by processes on the pressure surface. They claim that a dual acoustic feedback mechanism (feedback loops on both the pressure and suction surfaces) are not necessary to observe tonal noise.

Another proposed tonal noise mechanism that does not involve acoustic feedback was discussed by Moreau et al. (2011). They measured tones from a flat plate in moderate Reynolds number flows at $\alpha = 0°$. They claimed that vortex shedding was responsible for the tonal noise, due to the location of hydrodynamic fluctuations downstream that possessed strong coherences with the tonal noise.

2.4 Research gaps

There are many research gaps in this field of low-to-moderate Reynolds number airfoil aeroacoustics. There is no clear consensus regarding the characteristics of the typical acoustic spectra of a NACA 0012 airfoil, for various Reynolds numbers and angles of attack. Some experimental results and numerical simulations display different numbers of tones, varying relative magnitudes of tones within the acoustic spectra and differing broadband contributions. There does not exist a generalised discussion of the occurrence of tones and their associated sound pressure levels for airfoils of varying angles of attack and Reynolds number within 50,000 $< Re <$ 200,000. The primary tone frequency can be estimated using a fitted equation to real data (Paterson et al., 1973), but there is still no formal method for determining the angle of attack and Reynolds number that causes the greatest tonal sound pressure level.

There does not exist a complete database detailing relative tonal frequencies and magnitudes for a specific airfoil profile, at zero and non-zero angles of attack and a range of low-to-moderate Reynolds numbers. The impact of the airfoil profile on tonal noise generation has not as yet been fully investigated as most studies focussed on a single airfoil profile, for varying Reynolds numbers and angles of attack, without comparing the results of the same flow conditions for different airfoil profiles. There exists limited data for the locations along the airfoil chord where instabilities begin to form and the points of flow separation and reattachment, for various angles of attack and Reynolds number. There is disparity in the existence of separation bubbles, both mid-chord and near the trailing edge. Some simulations and experiments displayed separated shear layer reattachment, yet others in similar flow conditions did not.

There is no clear agreement regarding the noise generation mechanism(s). The studies supporting an acoustic feedback mechanism share little consensus on the start and end points of the feedback loop lengths. Some studies showed that the

acoustic source is at the trailing edge, whereas others suggest it is slightly downstream. There is uncertainty as to whether a single or multiple feedback loop system exists at non-zero angles of attack and if feedback processes are indeed responsible for tonal noise generation at zero angle of attack. There is evidence showing that a feedback mechanism does not necessarily exist at zero angle of attack, yet there are discrepancies within these theories.

There is little experimental data to verify the results of DNS and LES numerical simulations. Thus there is a need to obtain further experimental data to both validate the results of numerical simulations as well as provide a correlation with the airflow in the immediate vicinity of an airfoil. There is also a need to verify the use of analytical acoustic analogies for airfoils of significant thickness.

There are a plethora of research gaps in this field, many of which cannot be addressed in a single thesis. The primary gap to be addressed in this thesis is the feasibility of an acoustic feedback mechanism. To address this large gap, smaller gaps will be studied, such as the feedback loop(s) start and closing points, the acoustic source location and the influence of angle of attack on the measured noise and the mechanisms responsible for generating it.

2.5 Hypothesis

From the reviewed literature and the majority of the evidence provided, it was hypothesised that an acoustic feedback mechanism is responsible for tonal noise generation for an airfoil at low-to-moderate Reynolds number. The feedback loop of this said mechanism is between the noise source location (trailing edge) and the point of boundary layer separation on both the suction and pressure surfaces. The distance between boundary layer separation and the trailing edge seems an ideal feedback length, as it varies with Reynolds number and angle of attack and these distances are unique on the airfoil pressure and suction surfaces. A depiction of the hypothesised feedback model is shown in Figure 2.14.

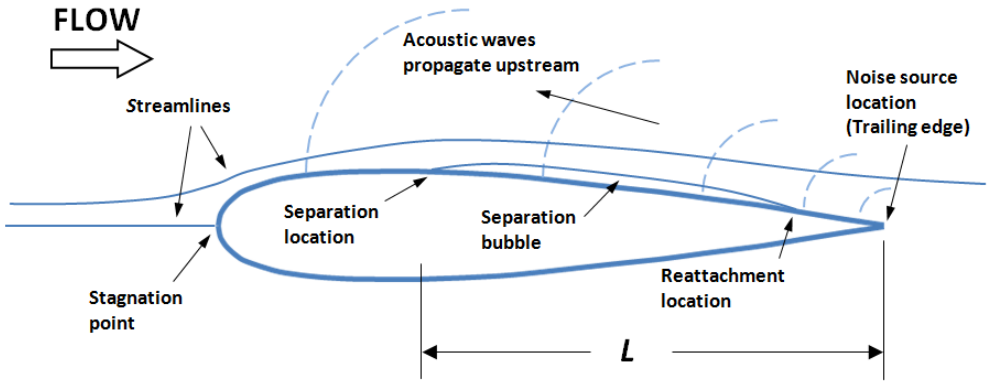

Figure 2.14: Hypothesised acoustic feedback model, where L represents the distance between the trailing edge (noise source) and point of boundary layer separation.

Arbey and Bataille's (1983) model is still the most accurate tonal noise prediction model to date and was thus chosen as a starting point for investigation. By using this model and employing feedback lengths other than those used by Arbey and Bataille (1983), deeper insight was made into the validity of each feedback length and the model itself. It was hoped that a more accurate tonal noise prediction model could be achieved using a feedback length from the point of boundary layer separation to the trailing edge.

Chapter 3

Single Microphone and Flow Measurement Methods

This chapter details the experimental methods and testing conditions used to measure the self-noise and important flow features of a 67 mm chord (275 mm span) NACA 0012 airfoil at low-to-moderate Reynolds number and varying angles of attack. Only single microphone and flow measurement methods are considered in this chapter. Acoustic beamforming, a multi-channel noise source location method, is discussed in Chapter 4.

3.1 Anechoic Wind Tunnel (AWT)

The Anechoic Wind Tunnel (AWT) is a low-speed open-circuit wind tunnel designed for scale model testing, located in the Sir Edward Holden Laboratory at The University of Adelaide. The anechoic chamber of the AWT has approximate dimensions of 1.4 m × 1.4 m in width and 1.6 m in height, inclusive of acoustic wall treatments. A schematic diagram of the AWT viewed from above is shown in Figure 3.1. The AWT was used for all of the airfoil-related experiments in this study.

A centrifugal fan generates flow that passes through a silencer located on a

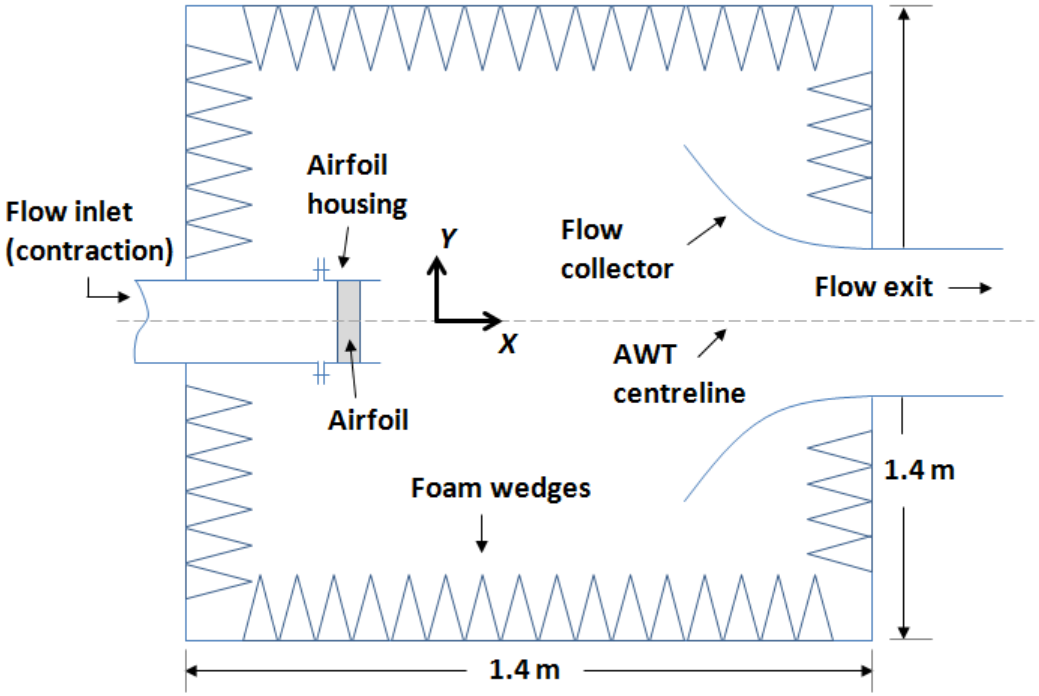

Figure 3.1: AWT facility, viewed from above. Note in the coordinate system shown, Z is positive in the downward direction.

mezzanine level above the AWT. The flow then travels downward, passes through a flow straightener and travels through a contraction outlet into a test section. The contraction outlet has an area of 75 mm (height) × 275 mm (spanwise width) as shown in Figure 3.2. The flow then enters the chamber where it interacts with a test piece (e.g. airfoil) and is then received by a collector at the opposite end. The flow exits the AWT into the laboratory via a collector that possesses an outlet area of 400 mm × 400 mm. Figure 3.3 shows the AWT viewed through the door opening.

The walls were acoustically treated with foam wedges that have a pyramid shape to minimise acoustic reflections during aeroacoustic tests. Each of the wedges has a square base of 100 mm × 100 mm and are 300 mm in length, base-to-tip. The base of the wedges cover as much of the AWT wall surfaces as practically possible, with the exception of the floor (covered in thick sheets of 50 mm thick flat foam)

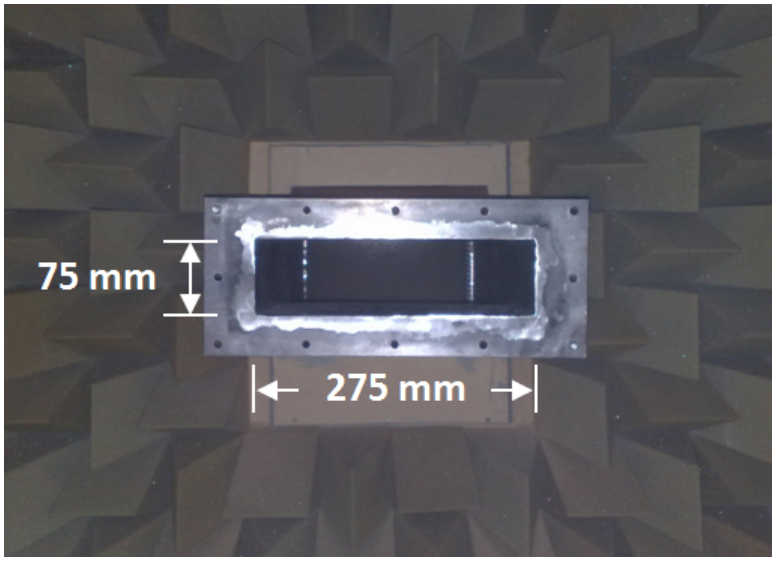

Figure 3.2: AWT contraction outlet. Flow direction is out of the page.

and the collector (no acoustic treatment). These modifications have made the AWT a near reflection-free acoustic environment for frequencies greater than 200 Hz, as determined using both white-noise speaker tests and background noise measurements, detailed in Leclerq et al., (2007). Note that the airfoil self-noise frequencies of interest are greater than 200 Hz, ascertained from preliminary experiments.

3.1.1 Contraction outlet velocity

The AWT contraction outlet speed is a function of the rotational fan speed driving the airflow. A calibration was performed between the rotational fan speed (Hz) and the outlet speed (m/s) for each experiment, using a pitot-probe placed at the centre of the contraction outlet. The pitot-probe pressure was measured using a barotron, where the difference between the atmospheric conditions within the tunnel and the pressure of the pitot-probe was evaluated. The contraction outlet speed was calculated using this pressure differential for a range of operational fan speeds and a linear trendline was created to fit the data.

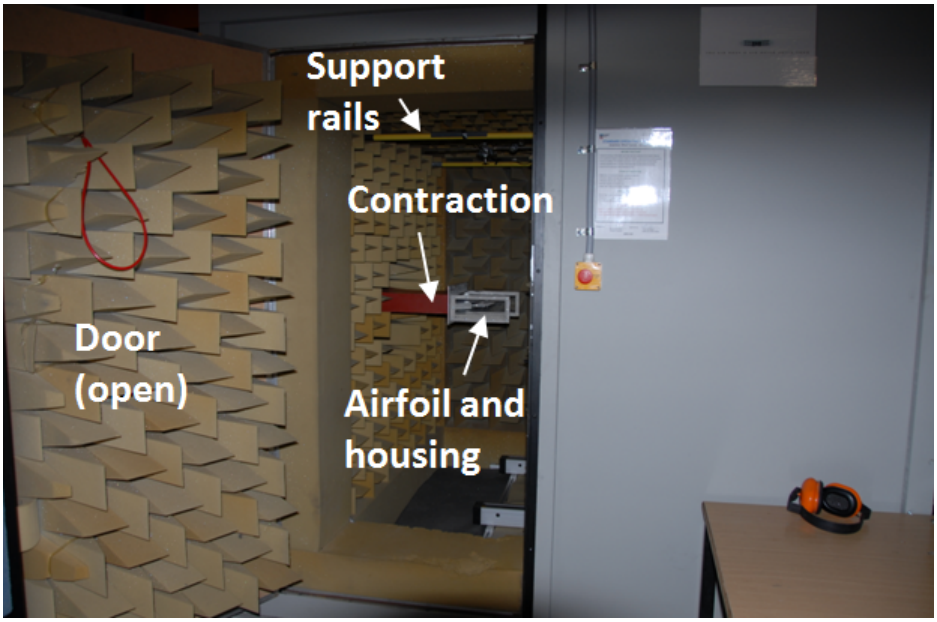

Figure 3.3: AWT facility, viewed from outside.

3.1.2 Boundary layer development and turbulence intensity

As the flow passed through the contraction toward the test section in the AWT, a boundary layer developed along the contraction walls and decreased the usable area for wind tunnel testing. A hot-wire anemometry probe (refer to Section 3.2.6 for use and procedures of hot-wire anemometry) was used to quantify the wind tunnel boundary layer heights, flow uniformity and turbulence intensity at the AWT contraction. One-hundred measurements were obtained in 2.75 mm and 0.75 mm increments over a series of lines that spanned the contraction width (275 mm) and height (75 mm) respectively. The line coordinates are represented by Y = -10 mm, 0 mm and 10 mm and Z = -10 mm, 0 mm and 10 mm as depicted in Figure 3.4. Flow velocity measurements were obtained at a flow speed of 22.54 m/s, corresponding to a Reynolds number of 100,000 with a 67 mm airfoil chord at the time of testing. The details of the data acquisition are provided in Section 3.2.6.2.

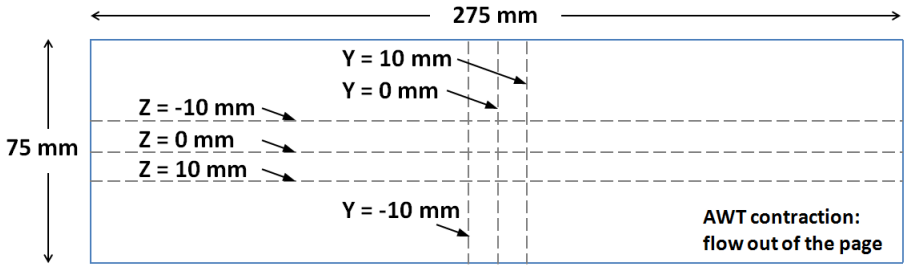

Figure 3.4: Hot-wire probe paths used to measure mean velocity and turbulence intensity at the outlet of the AWT contraction.

Figure 3.5 presents the mean velocity profiles across the AWT contraction outlet, measured along the spanwise direction. Along the $Z = 0$ mm line, it can be observed that $u/U \simeq 0.99$ at Y = -125 + 2×2.75 mm = -119.5 mm and at Y = 125 mm - 3×2.75 mm = 116.75 mm. Thus the total usable working area was defined between Y = -119.5 mm and 116.75 mm. The flow distribution at the contraction was skewed in the vertical direction, as shown in Figure 3.6. Along the airfoil centreline ($Y = 0$), $u/U = 1.008$ at Z = -20 mm, $u/U = 1$ at $Z = 0$ mm and $u/U = 0.99$ at $Z = 20$ mm, where u is the local velocity and U is the velocity obtained at $Y = Z = 0$ (at the centre of the contraction outlet). The velocity values at the airfoil centreline were slightly greater than below the centreline. Within the usable area of the test section, the non-uniformity of the mean velocity was less than 1%.

Turbulence intensities were calculated along the lines shown in Figure 3.4 and are presented in Figures 3.7 and 3.8 for constant Z and Y respectively. The turbulence intensity was calculated as the standard deviation of the time varying velocity signal divided by its mean, multiplied by 100. Along the contraction span and within ±100 mm of the centre, the turbulence intensity was 0.75% or less. Outside of this range near the contraction walls, the turbulence intensity was much greater, in excess of 2% and thus measurements in this range during experiments were not considered. Thus the effective span for testing purposes was 200 mm at a Reynolds number of 100,000 for a 67 mm chord airfoil.

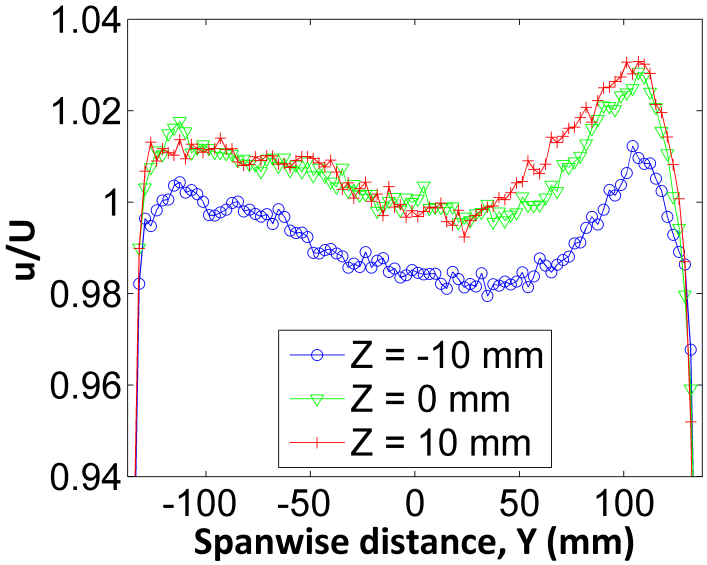

Figure 3.5: Mean velocity profiles across the AWT contraction outlet. Measurements displayed are along the spanwise direction, at $X = 0$.

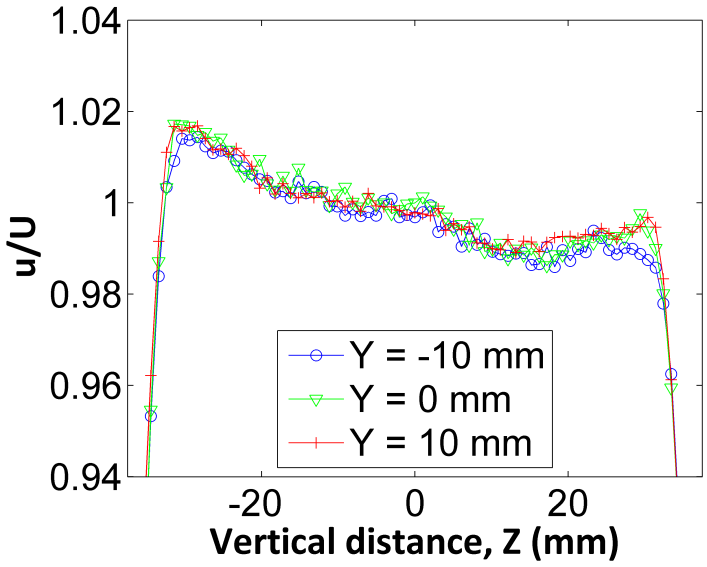

Figure 3.6: Mean velocity profiles across the AWT contraction outlet. Measurements displayed are along the vertical direction, at $X = 0$.

The turbulence intensity of the AWT is higher than the other experimentally based studies discussed in this thesis. Values of 0.1% or less are quoted in several studies (Chong and Joseph, 2009; Yarusevych et. al, 2009; Geyer et al, 2010). Despite the higher turbulence intensity in the AWT, it has not affected the acoustic results. The hydrodynamic disturbances in the freestream are too large to have significant impacts on the development of a transitional boundary layer on the airfoil surface.

3.2 Experimental methods and arrangements

This section is categorised into single microphone tests, surface flow visualisation tests, boundary layer trip tests and hot-wire anemometry tests. All of the hot-wire anemometry tests were performed simultaneously with single microphone tests, allowing the investigation of the coherence between flow and acoustic signals. Surface flow visualisation tests were performed with and without boundary layer trips. The acoustic signals of all boundary layer trip tests, with the exception of the surface flow visualisation test, were measured using a single microphone. A schematic diagram showing the experimental set-up for experiments using a microphone and hot-wire anemometry is shown in Figure 3.9.

The airfoil was secured in a custom-made housing that provided an interface between the flow contraction and the airfoil, as shown in Figure 3.10. The housing was designed so that it can be easily installed and removed from the contraction. It was constructed of a metallic frame with thick Perspex sheets that were attached to the frame using screws at each spanwise end, to support the airfoil. The airfoil was secured to the Perspex sheets using a rod protruding through the airfoil along its axis of maximum thickness. The rod had a tight secure fit into a circular hole on each Perspex sheet that prevented the airfoil from rotating or vibrating during experiments. To simulate an angle of attack condition, the airfoil was rotated by hand, using enough force to overcome the friction of the fit of the rod into the Perspex

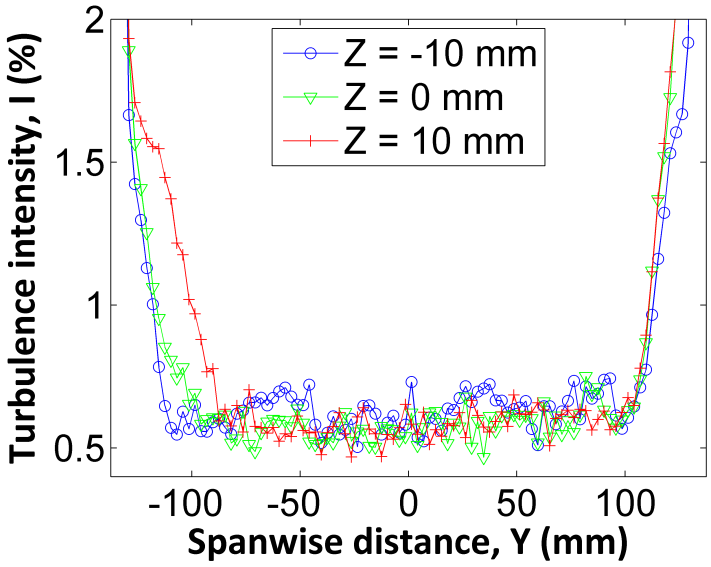

Figure 3.7: Turbulence intensity profiles across the AWT contraction outlet. Measurements displayed are along the spanwise direction.

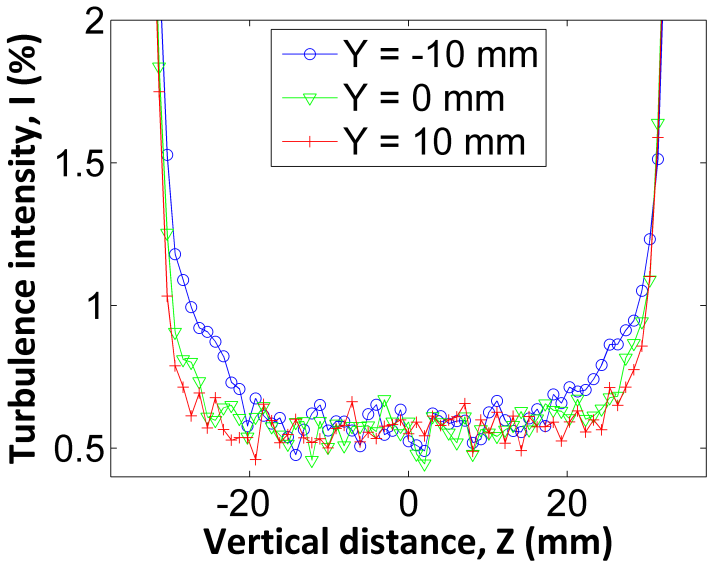

Figure 3.8: Turbulence intensity profiles across the AWT contraction outlet. Measurements displayed are along the vertical direction.

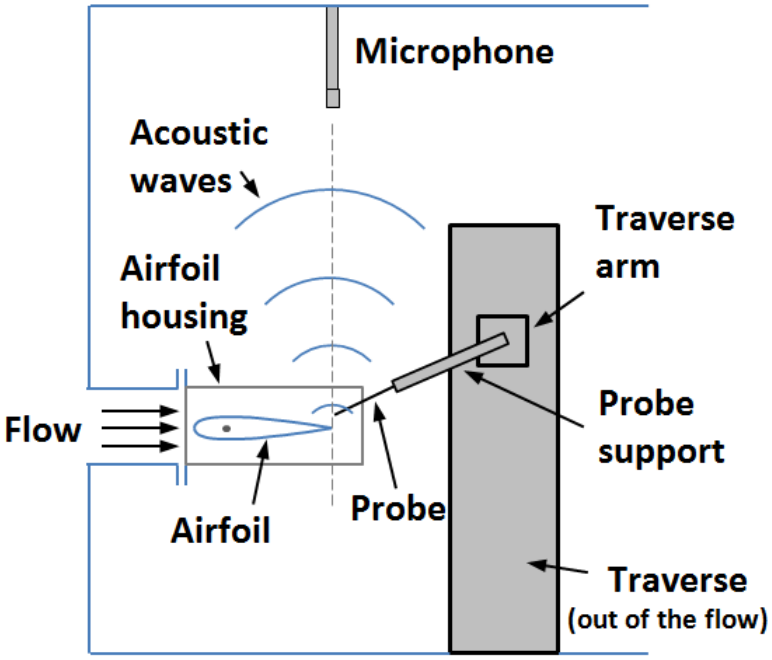

Figure 3.9: Schematic diagram showing the microphone and hot-wire probe locations during airfoil self-noise experiments in the AWT.

hole. Markers on the Perspex sheet identified rotational angles corresponding to 0°, 5° and 10°.

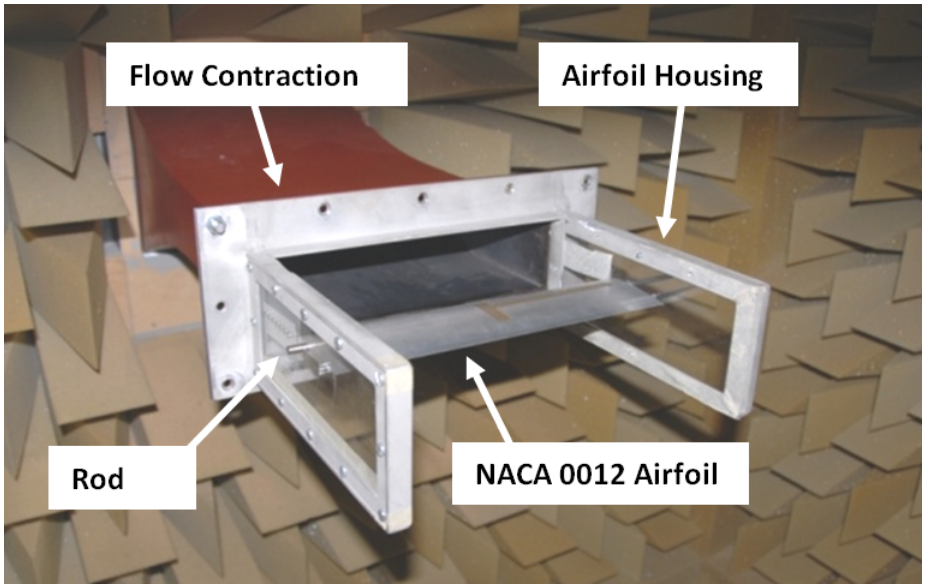

Figure 3.10: NACA 0012 airfoil secured to the AWT contraction.

3.2.1 Reynolds number and angle of attack

Based on the flow speed capabilities of the AWT under varying atmospheric conditions, the upper Reynolds number limit for testing was chosen to be 150,000. This was a near-maximum Reynolds number that could be consistently achieved in the AWT under all environmental conditions, as discussed in Section 3.1.1. The lower Reynolds number limit for testing was initially determined by previous research detailed in the Literature Review. Sandberg et al. (2008) showed that NACA 0012 airfoils at Reynolds numbers as low as 50,000 produce tonal noise but little experimental data was found at this Reynolds number or lower. Many of the studies in the Literature Review presented results for Reynolds numbers of 100,000 and greater, that provided motivation to seek the lower bounds of Reynolds number flows that produced airfoil tonal self-noise.

To determine a suitable lower Reynolds number limit, preliminary experiments were performed. The airfoil was installed in the AWT at $\alpha = 0°$ and the flow speed was slowly increased from rest. Between Reynolds numbers of approximately

30,000 to 35,000, tonal noise was first noticed, yet the signal-to-noise ratio above the broadband airfoil self-noise and the AWT background noise was poor. With increasing Reynolds number the signal-to-noise ratio markedly improved and a lower Reynolds number limit of 50,000 was selected. Flow measurements at Reynolds numbers of 50,000 to 150,000 presented adequate signal-to-noise ratios, allowing clear identification of the airfoil self-noise spectrum characteristics. At the lowest tested Reynolds number of 50,000, the measured broadband noise exceeded the background noise by 10 dB or greater for frequencies less than 1 kHz. At non-zero angles of attack, similar signal-to-noise ratios were observed for all Reynolds numbers as at $\alpha = 0°$, with the exception of the $\pm 10°$ geometric angles of attack.

As discussed in Section 2.3.6, the airfoil angle of attack had a significant impact on the production of tonal noise. To investigate the effect of angle of attack, the airfoil was placed at three geometric angles of attack during testing, 0°, 5° and 10°. The angle 5° was chosen arbitrarily to provide a non-zero angle of attack case. Preliminary acoustic tests in the AWT showed that tonal noise was observed for a range of Reynolds numbers at this angle of attack. At a 10° geometric angle of attack, tones were not measured at lower Reynolds numbers but only near the limits of the AWT maximum flow speed. Angles of attack greater than 10° were investigated and no tonal noise was observed over a wide range of flow speeds. Therefore two angles of attack, 5° and 10°, were selected for further investigation.

The operating conditions were:

- Reynolds numbers: Re = 50,000, 100,000 and 150,000
- Geometric angles of attack: $\alpha = 0°$, $\pm 5°$ and $\pm 10°$.

Some additional single microphone, hot-wire anemometry and surface flow visualisation tests were performed at Reynolds numbers of 75,000 and 125,000 in addition to the operating conditions listed. This assisted in visualising acoustic and flow trends with increasing Reynolds number.

3.2.2 Angle of attack correction

Since the AWT jet height was finite, two-dimensional correction factors were applied to determine the true effect of the airfoil angle of attack (Brooks et al., 1989). Generally, the true angle of attack is less than the geometric angle of attack for small jet height testing environments. This is due to flow curvature and deflection of the flow downstream that does not occur in a near infinite jet (Brooks et al., 1989).

The correction factor is

$$\alpha = \frac{\alpha'}{\zeta} \tag{3.1}$$

where α is the true angle of attack, α' is the geometric angle of attack, and the correction factor ζ is given by

$$\zeta = (1 + 2\sigma)^2 + \sqrt{12\sigma} \tag{3.2}$$

and

$$\sigma = \frac{\pi^2}{48}\left(\frac{C}{H}\right)^2 \tag{3.3}$$

where C is the airfoil chord length (67 mm) and H is the height of the jet within which the airfoil is placed (75 mm). Thus the actual angles of attack presented in this research are calculated as

- $0°$ (geometric) is $\alpha = 0°$ (true)
- $5°$ (geometric) is $\alpha = 1.58°$ (true)
- $10°$ (geometric) is $\alpha = 3.16°$ (true)

Only the true angle of attack, α, will be stated hereafter throughout this thesis.

3.2.3 Single microphone tests

A single microphone was placed in the acoustic far field to determine the power spectral density (PSD) of the self-noise of an airfoil placed in uniform flow. PSDs were obtained using a Brüel & Kjær (B&K) 1/2" free-field microphone (Model No. 4190) that was capable of obtaining acoustic measurements between 6.3 Hz and 20 kHz, with a dynamic range of 14.6 dB to 146 dB. A free-field microphone type was selected as appropriate for noise measurements within an anechoic environment. The microphone signal was amplified by a B&K 2829 power supply connected to mains power.

The background airflow noise was recorded with the airfoil housing components (except for the airfoil) attached to the contraction outlet as shown in Figure 3.10. This ensured that any noise produced from flow interaction with the housing was not attributed to airfoil self-noise. The speeds investigated (that varied slightly with environmental conditions) were approximately 11.3, 17.0, 22.6, 28.3 and 33.9 m/s, corresponding to Reynolds numbers of 50,000, 75,000, 100,000, 125,000 and 150,000 for an airfoil with a 67 mm chord.

3.2.3.1 Data acquisition

The microphone data were collected using an NI DAQ card (BNC-2110), using a MATLAB DAQ interface, at a sampling frequency of 50 kHz for a duration of 4 seconds. For convenience, the data were filtered using a MATLAB script. The data were passed through a digital low pass filter of 22.7 kHz (corresponding to approximately the sampling frequency of 50 kHz divided by 2.2, as per the Nyquist criterion) and a digital high pass filter of 50 Hz. To convert the data from the time domain into the frequency domain, a Fast Fourier Transform (FFT) algorithm was applied to the data. The pwelch function in MATLAB estimated the PSD of the input time series data using Welch's averaged modified periodogram method of spectral estimation. The data was segmented into 8 sections of equal length and

each segment was windowed with a Hamming window of equal length of the segment. The PSD (Pa/Hz) was presented with a frequency bandwidth of 1 Hz. The PSD was converted into a Sound Pressure Level (dB/Hz) (SPL) by

$$SPL = 10\log_{10}\left(\frac{PSD}{(20\times 10^{-6})^2}\right) \tag{3.4}$$

The acoustic data are presented as SPL throughout this thesis.

It was important to find the shortest adequate sampling time to minimise the time spent in the AWT and data storage over the large number of repeated experiments performed. The shortest adequate sampling time was defined as the shortest sampling time during an experiment that yielded tonal noise measurements within ±1 Hz and ±2 dB error of a PSD obtained using a much longer sampling time. Consider the following hypothetical example; a sampling time of 20 seconds is employed in which a 1440 Hz tone with magnitude 67 dB is measured. Repeating the experiment with identical conditions but with only a 4 second sampling time produces a 1441 Hz tone with magnitude 65 dB. This suggests that the shorter 4 second sampling time is adequate, within ±1 Hz and ±2 dB error bounds.

With this understood measure of adequacy, preliminary experiments were performed with an airfoil in place at $Re = 100{,}000$ and $\alpha = 0°$. At this flow condition the measured PSDs displayed several tones and broadband noise. These PSDs were obtained using 20 second sampling times and the tonal noise peak frequencies and magnitudes were obtained. Data were then obtained with a shorter sampling time of 10 seconds and the recorded tonal frequencies and magnitudes were measured within 1 Hz and 1 dB, respectively. A further decrease of the sampling time to 4 seconds yielded similar results, with 1 Hz and 1 dB errors, respectively. Decreasing the sampling time even further to 3 seconds resulted in errors greater than 1 Hz and 2 dB. Thus a sampling time of 4 seconds was arrived at based on this trial and error process.

3.2.3.2 Microphone calibration

A piston-phone (B&K, type 4228) was used to calibrate the microphone. The microphone was inserted into the piston-phone head that emitted a 1 Pa tone at 1 kHz. The measured spectrum from the piston-phone consisted of a 122 dB, 1 kHz tone and negligible broadband noise. The measured time series acoustic pressure was then multiplied by a factor so that it scaled to 1 Pa at 1 kHz. This factor was then applied to the entire time series acoustic signal obtained via data acquisition. The microphone was calibrated for every experiment, once per day of acoustic testing. The data acquisition process used is detailed in Section 3.2.3.1.

3.2.3.3 Microphone placement

The microphone was placed 600 mm (± 2 mm) above the airfoil trailing edge, centred with the mid-span point of the airfoil. This ensured that the microphone was placed well outside of the free jet shear layer region, avoiding problems of microphone self-noise due to airflow. Determining the optimum downstream (Y-component) location of the microphone required consideration of the nature of the noise (whether it possessed monopole, dipole or quadrupole directivity), the flow speed and a calculation of the effect of the shear layer on the acoustic waves.

The shear layer at the edge of the wind tunnel free jet potential core caused refraction of acoustic waves. The effect of this was taken into account when placing the microphone in the AWT and a representative calculation was performed using the method detailed in Chapter 4, Section 4.5.2. For a noise source placed in the jet at mid-height under 40 m/s flow conditions, it was calculated that the acoustic waves will be shifted approximately 45 mm downstream of the noise source at 600 mm above the plane of the airfoil trailing edge. This result indicated the approximate maximum magnitude of shear layer refraction expected during testing. A 45 mm shift of acoustic wave propagation is significant; therefore, for all acoustic tests the microphone was placed 600 mm above the trailing edge height and the

appropriate distance downstream of the trailing edge, based on the expected shear layer refraction distance due to the AWT contraction flow speed.

3.2.4 Surface flow visualisation

Locations of boundary layer transition, separation and reattachment were obtained using surface flow visualisation by spreading a fluid mixture over the airfoil upper surface. Thompson and Lotz (2002) and Traub (2011) investigated the effects of boundary layer trips on boundary layer transition, separation and reattachment on an airfoil using a mixture of titanium dioxide, kerosene, linseed oil and oleic acid. A similar in-house fluid mixture was developed using commonly accessible materials; a mixture of talcum powder and linseed oil. This fluid mixture was spread across a portion of the span of the upper airfoil surface.

Initially only the oil was applied to the airfoil surface in the AWT. This was impractical as the oil alone was not very distinct in photographs and much of it sprayed off the airfoil surface causing inconvenience. Small amounts of talcum powder were added to the same amount of oil used in the previous test that allowed clearer photographs of the results and also decreased the amount of sprayed oil mixture at the same flow speed. The point of separation was measured to be the same as the oil-only case (within 1 mm) via inspection of both photographs and quantifying the distance of the leading edge to the point of flow separation.

Through trial and error, an optimum ratio of powder to oil was obtained. The quantity of oil used per test was approximately 20 mL that was carefully poured onto the airfoil. A toothbrush was used to distribute the oil over a portion of the airfoil span used for testing. Talcum powder was mixed into the oil using a toothbrush until the entire mixture was a light yellow colour and non-transparent. Further increases in talcum powder, while increasing the luminosity of the mixture, excessively increased the flow viscosity, which caused the oil mixture to spread unevenly along the airfoil chord, affecting the local flow conditions near the airfoil surface.

For each flow visualisation test images were captured using a digital camera positioned at the top of the airfoil housing and aimed at the airfoil surface. The lens of the camera was centred with the airfoil mid-chord and angled downward from the horizontal to ensure that the airfoil span was captured. Flow separation and reattachment locations were estimated by identifying the locations where the fluid mixture transitioned from being attached to being removed from the airfoil surface. These locations were measured on each photograph, scaled relative to the airfoil chord length and converted into physical distances. An example surface flow visualisation test is shown in Figure 3.11.

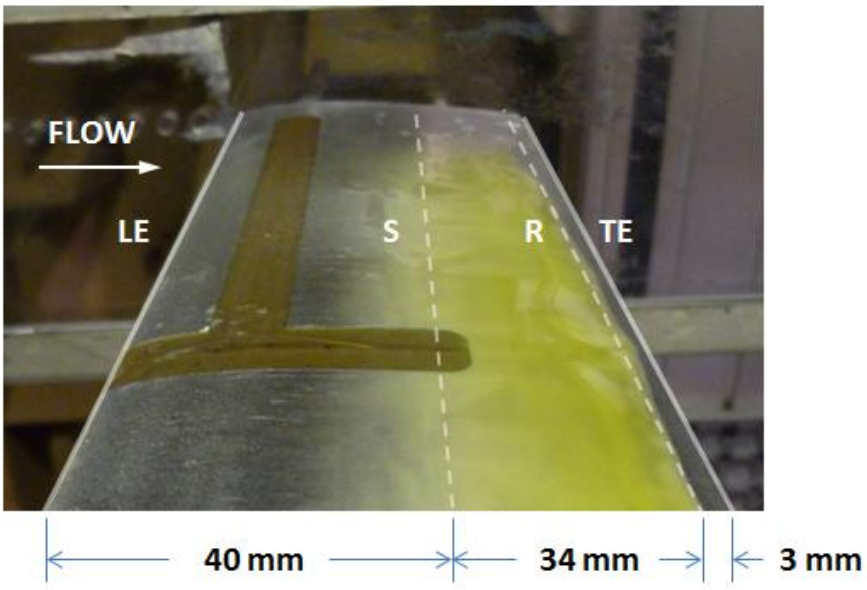

Figure 3.11: Photos of fluid patterns showing surface flow behaviour for a NACA 0012 airfoil, at Re = 150,000 and $\alpha = 0°$. LE, TE, S, and R denote Leading Edge, Trailing Edge, Separation and Reattachment, respectively.

Estimating the point of separation was susceptible to visual judgement. Care was taken in scaling the point of observed separation relative to the airfoil chord. Some flow visualisation tests were difficult to evaluate as the fluid mixture did not possess a sharp clear line on the airfoil surface at points of flow separation and

reattachment. In these scenarios, the point of flow separation was estimated to within ±1 mm. Relative to an airfoil chord of 67 mm, a 2 mm error corresponds to a 3% relative error.

During preliminary tests the lines on the airfoil surface representing flow separation and reattachment did not vary with time. The lowest investigated Reynolds number of 50,000 required the greatest settling time of approximately 30 seconds. To visualise how the boundary layer developed and the points of flow separation and reattachment varied with increasing flow speed, the fluid mixture was spread over a portion of the airfoil span while the flow was off. The AWT fan was set to gradually increase from rest to maximum flow speed and the camera recorded a video of the motion of the mixture with increasing flow speed. This helped reveal any unsteady flow behaviour as well as identify flow separation and reattachment points between the tested Reynolds numbers.

3.2.5 Boundary layer trips

Interrupting the boundary layer on an airfoil surface was achieved using a trip line that rapidly transitioned the laminar boundary layer into a turbulent boundary layer. Doing this on only one airfoil surface created a turbulent boundary layer or separated shear layer on the tripped surface and a laminar or transitional boundary layer on the untripped surface. This helped provide insight as to whether one airfoil surface or both contributed to tonal noise generation mechanisms.

Fishing line with a diameter of 0.42 mm (0.6% of a 67 mm airfoil chord) was used as a trip line. This was securely fastened across the span of the airfoil at both ends using adhesive tape, ensuring that the line did not bow and/or flap relative to the airfoil surface during flow conditions. The fishing line was attached 7 mm downstream of the airfoil leading edge, as shown in Figure 3.12. This distance corresponded to approximately 10% of the airfoil chord.

Three boundary layer trip configurations were investigated. A trip line was

separately placed on the upper surface alone, on the lower surface alone and on both surfaces. Each of these configurations were compared with the same airfoil without any trips. A surface flow visualisation test was also performed when the airfoil was tripped only on the upper surface. PSDs were obtained using a B&K 1/2" microphone as detailed in Section 3.2.3.1.

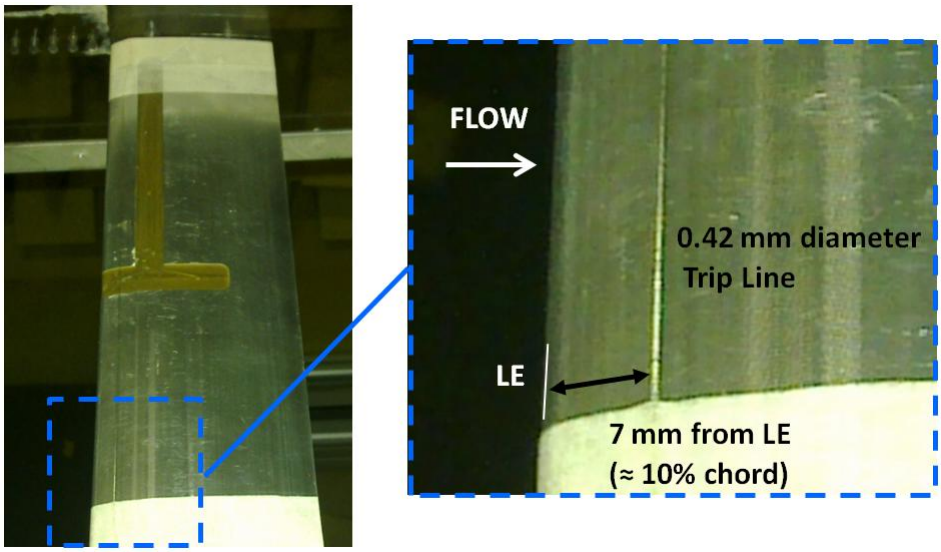

Figure 3.12: Trip line attachment on the upper surface of a NACA 0012 airfoil in the AWT. LE denotes Leading Edge.

3.2.6 Hot-wire anemometry

A hot-wire probe is a sensitive wire placed normal to a flow direction to determine flow velocity components. The wire is heated and the convective cooling of the wire determines the airflow velocity, based on the electrical resistance of the wire. Hot-wire probes can also determine fluctuating velocity components at high spatial resolution. If a hot-wire probe is used to obtain data simultaneously with a single microphone, the coherence between the fluctuating velocity and the acoustic signal can be measured that can be used to calculate the velocity of acoustic disturbances in the boundary layer and locations of separated shear layers.

Hot-wire anemometry was used in this research over other flow measuring devices such as PIV and Laser Doppler Anemometry (LDA). The set-up and running costs of a hot-wire anemometry system are much lower than the aforementioned techniques and it is faster to set-up in a wind tunnel facility. The probe head is also small allowing it to be placed in close proximity to sharp edges and flat surfaces, such as the airfoil trailing edge and the contraction outlet walls. Hot-wire anemometry can obtain velocity signals with excellent frequency resolution, in small measurement volumes and possesses excellent signal-to-noise ratios.

3.2.6.1 Apparatus specifications

The probes used in this research were TSI Miniature Straight Probes (Model No. 1260A) comprising a single cylindrical shape. The diameter of the probe body supporting the wire filament sensor (6 μm diameter) was 1.5 mm, oriented at 90° to the flow direction. The wire was connected to the probe in an in-line configuration, so that the cylindrical length of the probe body was in the same direction as the flow causing minimal flow interference. TSI recommended the use of the probe in flow conditions under 300 m/s; well above of the range of flow speeds investigated here. A photograph of one of the probes is shown in Figure 3.13. The probe was carefully plugged into a dual sensor probe support (Model 1155 Standard Probe

Support). The length of the shaft was 6 in (approx. 152 mm) allowing the probe head to measure the local flow field without bluff body interference caused by the probe support. The support used in this research is shown in Figure 3.14.

Figure 3.13: TSI 1260A hot-wire probe used for flow measurements.

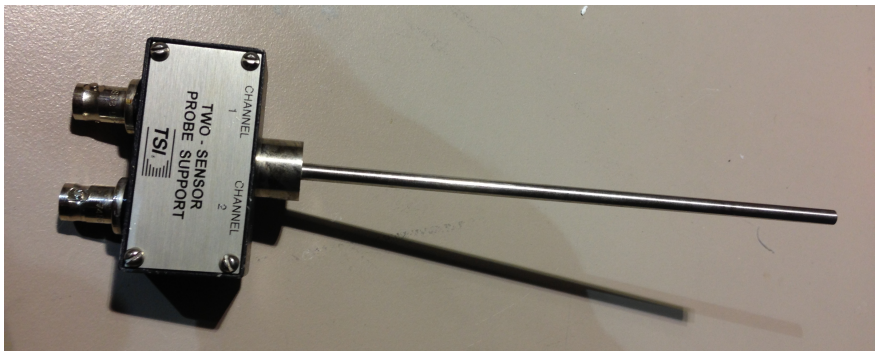

Figure 3.14: The TSI probe holder connected to the traverse lever arm and used to secure the probe.

The probes were powered using a TSI IFA300 Constant Temperature Anemometer (CTA). A BNC cable connected the probe support to the CTA box and the

CTA transferred the analog temperature fluctuation signal of the wire filament to a NI DAQ. The CTA box possessed a frequency response of up to 250 kHz that well exceeded the required sampling frequency. The TSI software package, ThermalPro, was used for the interface between the probes and the PC. The data from ThermalPro was acquired and processed using an in-house MATLAB script to obtain mean velocities, fluctuating velocity components and spectral velocity maps.

3.2.6.2 Data acquisition

The hot-wire data were collected via a 24-bit NI DAQ card using a MATLAB DAQ interface at a sampling frequency of 50 kHz for 4 seconds. A similar procedure to that discussed in Section 3.2.3.1 was used to determine the shortest adequate sampling time. An error of 0.1 m/s or less was deemed acceptable and was consistently achieved with a 4 second sampling time. The preliminary experiments were conducted at the contraction outlet without an airfoil in place and 1 mm downstream of the trailing edge of the airfoil, at Re = 100,000 and $\alpha = 0°$. Sampling times less than the single microphone measurements were not considered, to ensure that coherence measurements between the two could be obtained.

After the analog-to-digital conversion stage, a low pass filter was applied at a frequency of 20 kHz within ThermalPro. The data were then passed through a digital band pass filter of 100 Hz to 12 kHz using an in-house MATLAB script. Conversion of the data from the time domain into the frequency domain was performed in an identical manner as for the acoustic data discussed in Section 3.2.3.1.

3.2.6.3 Probe calibration

The probe was calibrated against a known flow speed to accurately measure the flow velocity. The first step was to determine the resistance in the probe and probe cables. The probe cable resistance was constant and independent of the probe measurement. To measure the cable resistance, the resistance of the probe support

was obtained by fitting the support with a shorting probe. Once the cable resistance was recorded, the hot-wire probe was carefully connected to the probe support to measure the resistance of the probe in still conditions. The operating resistance for the probe during tests was the probe resistance in the no-flow condition multiplied by 1.7. The probe support was then attached to the TSI Model 1127 Air Velocity Calibrator, as shown in Figure 3.15. The calibrator had a turbulence intensity of 0.3% and velocity accuracy of 0.5%, as cited by TSI. The typical quantification error of the velocity measurements is inversely proportional to $2^{no.bits+1} = 2^{25}$. The input range of the system is ±5 volts, thus making the quantification error in the order of microvolts (10^{-6} V).

The height of the probe was adjusted so that the probe wires were approximately 1 mm above the air outlet of the calibrator. The calibrator was fed pressurised air from a compressed air source. By measuring the differential in pressure between the atmosphere and the flow onto the hot-wire probe, the flow velocity at the probe was calculated using Bernoulli's equation. Data were obtained from the barotron and the hot-wire probe at a sampling frequency of 10 kHz for 6 seconds. The measured voltage from the probe was plotted against the flow velocity measured via the barotron and a calibration chart was created. An example calibration chart is presented in Figure 3.16.

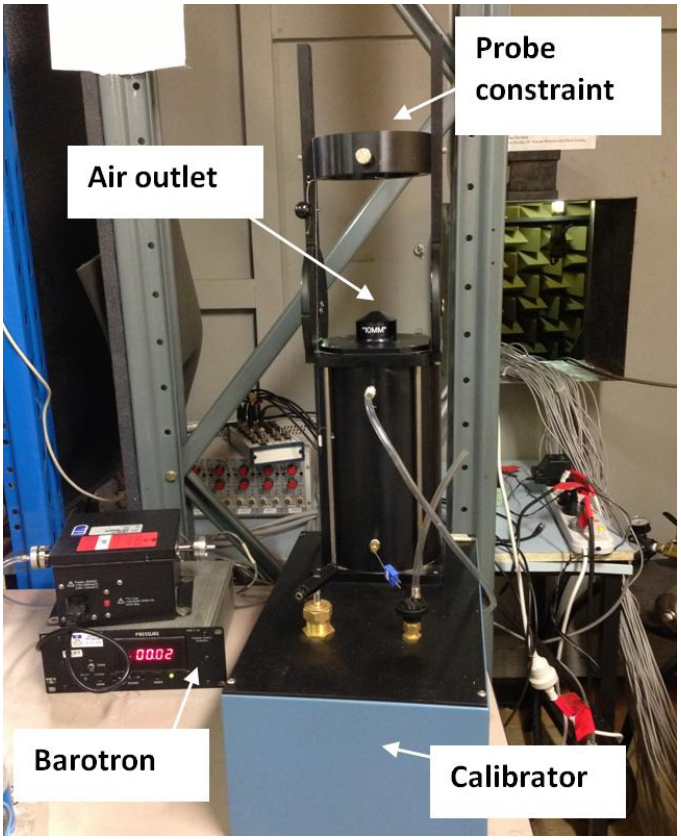

Figure 3.15: The TSI Model 1127 Air Velocity Calibrator used for calibration of the the hot-wire probes used in the AWT.

The relationship between the probe voltage and the flow velocity was non-linear, therefore several pressure measurements using the calibrator were used to fit a smooth, reliable curve. Based on trial-and-error, 17 points were used to fit a 5^{th} order polynomial calibration curve. A command called "polyfit" in MATLAB was used to determine the coefficients of the polynomial to fit the data using a least-square method. This polynomial equation was used to determine the flow velocity during subsequent data acquisition scripts within MATLAB, based on the measured voltage of the hot-wire probe.

By observation of Figure 3.16, it can be seen that the 5^{th} order polynomial

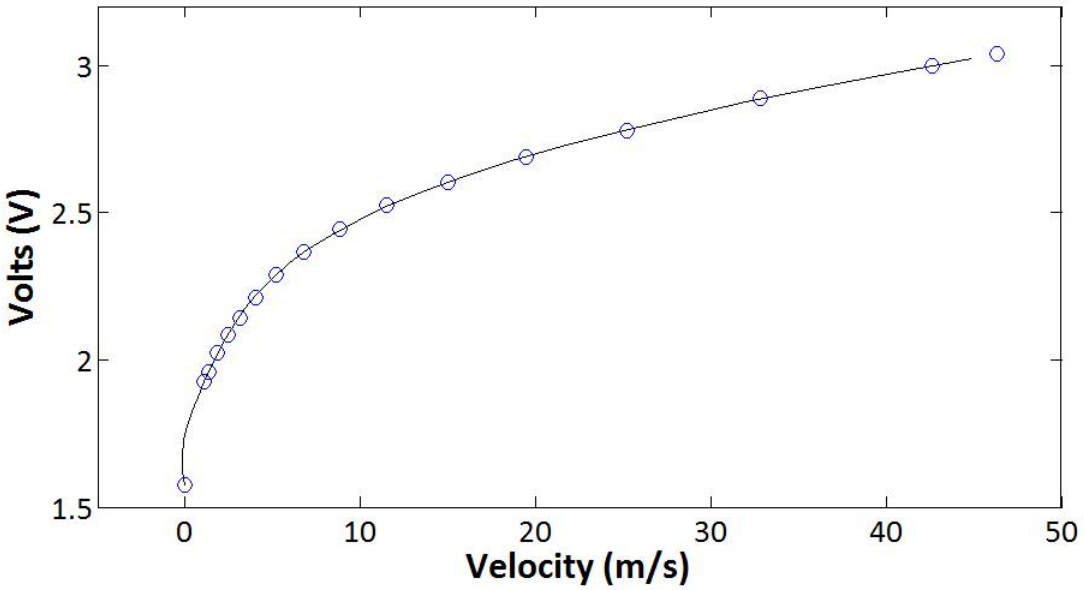

Figure 3.16: An example calibration chart between the hot-wire probe voltage and the measured flow speed through the calibrator. The fitted line represents the calibration curve.

provided an accurate fit to the data. By inspecting the data, the greatest error in the calibration model occurred for a voltage of 2.52 V, where the true flow speed was 14.1 m/s and the predicted flow speed using the model was 14.0 m/s. This represents an upper bound to the estimation error of 1.3%. All of the other data points exhibited errors less than 1%.

As a confirmation of the calibration process and to ensure that the probe was correctly attached to the probe holder, the probe was secured at the same location as the pitot-probe was placed when previously calibrating the AWT (discussed in Section 3.1.1) with the AWT airflow on. The probe always gave the same velocity reading as the pitot-probe (to within 0.1 m/s) unless it was incorrectly fitted to the probe holder. In that situation, the probe holder would be reattached and a data acquisition would be reattempted until the hot-wire and pitot-probe readings matched. If this could not be achieved then the probe was likely damaged and was

replaced.

The probes had a tendency to drift over extended periods of data acquisition. As a check, after a few hours of continuous data acquisition, the probe would be placed in the pitot-probe position during calibration and the measured mean velocity would be checked against the pitot-probe value. In all situations where this was performed, the measured mean velocity of the AWT flow before and after extensive periods of data acquisition were within 0.5 m/s. It should be noted that the CTA system automatically applied temperature compensation.

3.2.6.4 Probe placement

Various hot-wire probe configurations were required to obtain local flow properties, such as boundary layer height, locations of concentrated velocity fluctuations near the airfoil surface and in the wake, and coherences between the acoustic and flow signals along the airfoil span and chord.

The AWT contained a DANTEC traverse (see Figure 3.17) possessing the capability to place an object within 7.5 μm precision. The hot-wire probe holder was secured to a rigid steel lever arm attached to the traverse body. This ensured accurate positioning of a hot-wire probe in the flow relative to a known origin, such as the airfoil trailing edge. The rigidity of the lever arm also ensured that any flow induced vibration of the hot-wire probe was minimised. The lever arm allowed the proximity of a hot-wire probe and probe support near the airfoil without flow interference by the traverse.

The traverse was controlled via an in-house MATLAB script run from a separate PC located next to the AWT. It was set to slowly move in fixed increments relative to a known distance, thus allowing the automated measurement of velocity data near the airfoil surfaces. For every test the probe holder was angled downward with a fixed angle of 20° below the horizontal, so that the probe holder and traverse arm would have a low impact on the flow. As a preliminary test, the freestream velocity

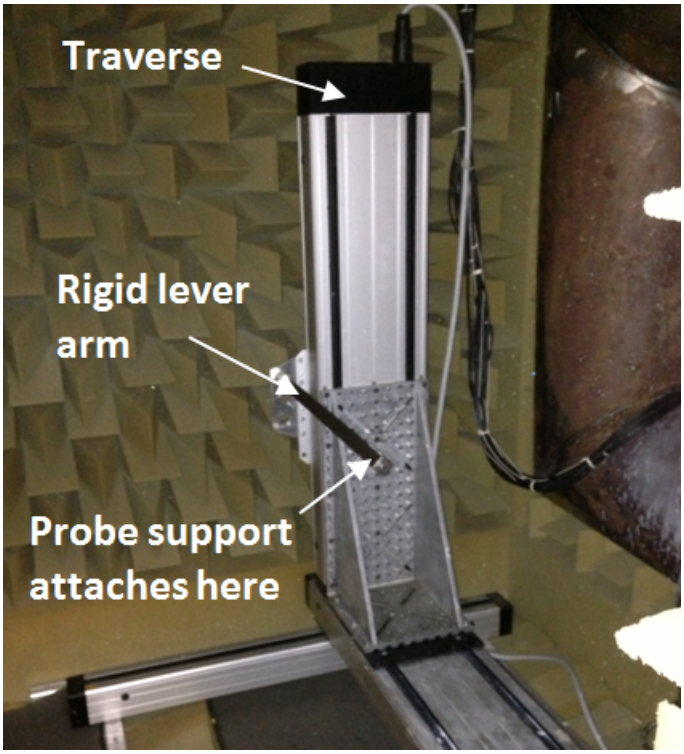

Figure 3.17: The DANTEC traverse inside the AWT.

was measured with a 0° and 20° probe angle and agreement was met within 0.1 m/s of a 22.54 m/s flow speed (i.e., 0.4%).

Throughout the experiments the probe was placed as close as 1 mm to the airfoil surface. Therefore care was taken when attaching the probe to the holder, as well as ensuring the traverse operations did not cause any collisions with the airfoil or the housing structure. An example of a hot-wire anemometry test in the AWT is shown in Figure 3.18, where the probe was located near the airfoil trailing edge.

Hot-wire measurements were obtained in a spanwise direction downstream of the trailing edge as depicted in Figure 3.19. Measurements were obtained in 2 mm spanwise increments, at locations of 1 mm, 2 mm, 5 mm and 10 mm downstream of the trailing edge.

To measure the height of the boundary layer and/or the separated shear layer

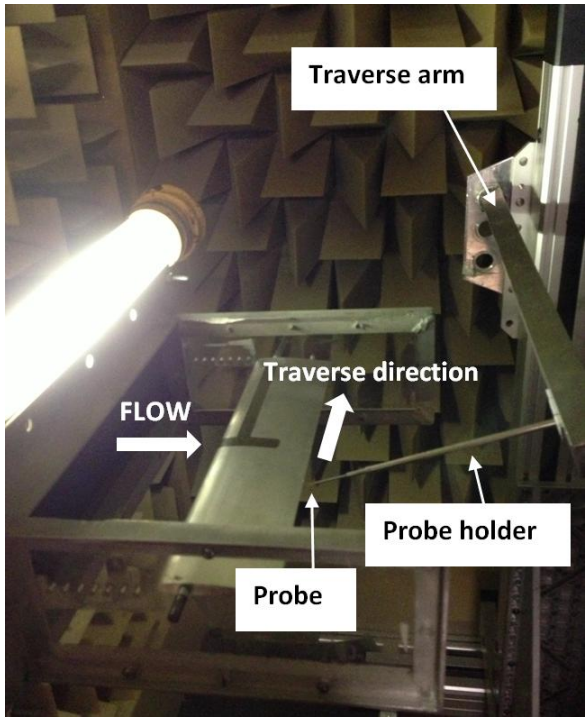

Figure 3.18: A hot-wire probe in a span-wise test configuration in the AWT.

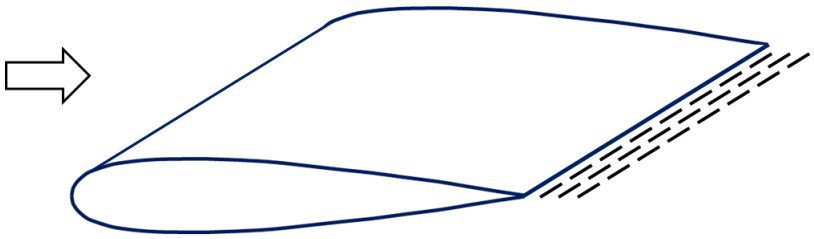

Figure 3.19: Schematic diagram of the hot-wire path used to measure the coherence between the measured acoustic signal and power spectrum of the velocity fluctuation signal in the wake.

on the upper airfoil surface, the hot-wire probe was placed 1 mm above the trailing edge. Measurements were obtained by the probe along a vertical path away from the airfoil surface, as depicted in Figure 3.20. The probe was then returned back to 1 mm above the airfoil surface at the trailing edge. It was then traversed 1 mm

upstream, ensuring it followed the airfoil profile and remained 1 mm above the airfoil surface. This process was repeated to obtain velocity profiles from the trailing edge to 10 mm upstream of the trailing edge in 1 mm increments. From 10 mm to 60 mm upstream of the trailing edge, measurements were obtained in 10 mm increments in the chordwise direction.

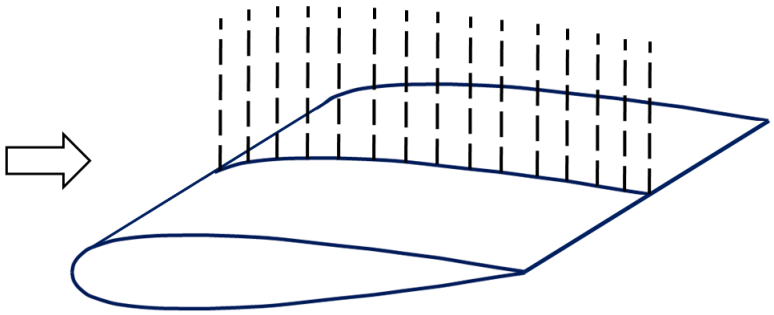

Figure 3.20: Schematic diagram of the hot-wire path used to measure velocity profiles from the airfoil surface into the free-stream flow region along the airfoil chord.

To measure vertical wake profiles at the trailing edge and downstream of it, the hot-wire probe was placed 25 mm below the trailing edge height and moved 50 mm in the vertical direction. This is depicted in Figure 3.21. The probe was moved vertically in 1 mm increments. Tests were performed in the same manner 1 mm, 2 mm, 5 mm, 10 mm, 20 mm, 50 mm and 100 mm downstream of the trailing edge. The coherence between the acoustic and flow signals was calculated at each measurement location for each velocity profile in the wake.

A hot-wire probe was traversed at a fixed height above the airfoil surface from the trailing edge to the leading edge, as depicted in Figure 3.22. A single microphone was used to measure the acoustic signal and obtain the coherence between the flow and acoustic signals. By inspection of the phase between the flow and acoustic signals, the convective disturbance velocity was estimated. This procedure is presented in Section 5.1.5.

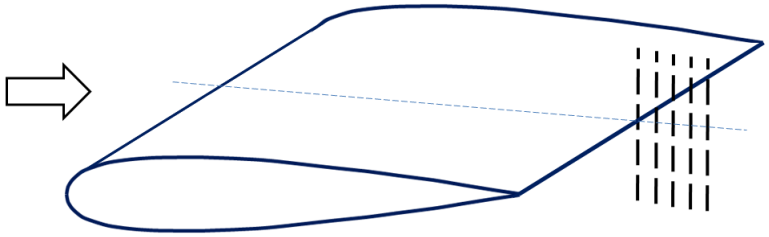

Figure 3.21: Schematic diagram of the hot-wire path used to measure near-wake velocity profiles and coherence between the measured acoustic signal and power spectrum of the velocity fluctuation signal in the near-wake.

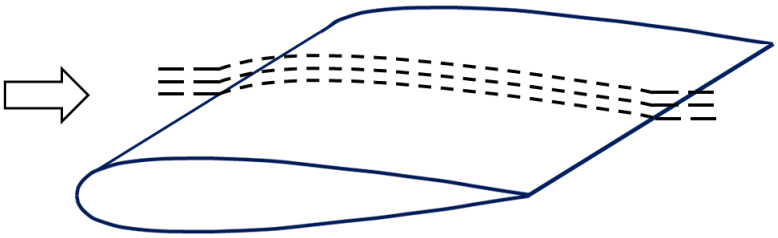

Figure 3.22: Schematic diagram of the hot-wire path used to measure the coherence between the measured acoustic signal and power spectrum of the velocity fluctuation signal near the airfoil surface along the length of the airfoil chord.

3.3 XFOIL method

XFOIL (Drela, 1989) is a widely used 2-D potential flow solver that can be used to determine pressure distributions and flow velocities around an airfoil surface. For the purposes of this study, it was used to verify surface flow visualisation tests (points of boundary layer separation and reattachment) and hot-wire anemometry data (points of maximum velocity in the boundary layer).

Points of boundary layer separation were identified in XFOIL where values of the coefficient of friction, C_f, were equal to zero. For the example of Re = 100,000 and $\alpha = 0°$, the point of boundary layer separation was found to be $x/C = 0.63$, as can be observed in Figure 3.23. At non-zero angles of attack, XFOIL provided data for both the pressure and suction surfaces. The results for C_f at Re = 100,000 and $\alpha = 5°$ are presented in Figure 3.24. It can be seen that the pressure surface, labelled in blue and the letter "B" in the legend (where B represents bottom-surface) has $C_f = 0$ at $x/C = 0.92$. This represents that the boundary layer remains attached up to this point of separation and it then remains detached past the trailing edge ($x/C = 1$). The suction surface, labelled in yellow and the letter "T" in the legend (where T represents top-surface) has $C_f = 0$ at $x/C = 0.13$ and 0.38. This can be identified as boundary layer separation at $x/C = 0.13$ and reattachment at $x/C = 0.38$, forming a separation bubble between these two points. The reattached boundary layer remains attached from $x/C = 0.38$ to the trailing edge ($x/C = 1$).

The point of maximum velocity in the boundary layer was identified as the chordwise location that possesses the maximum value of the u/U_∞ plot within $0 \leq x/C \leq 1$. An example plot for Re = 100,000 and $\alpha = 0°$ is presented in Figure 3.25, where the maximum value of u/U_∞ is located at $x/C = 0.1$. The same procedure was performed at non-zero angles of attack, where values of u/U_∞ were obtained on both the pressure and suction surfaces.

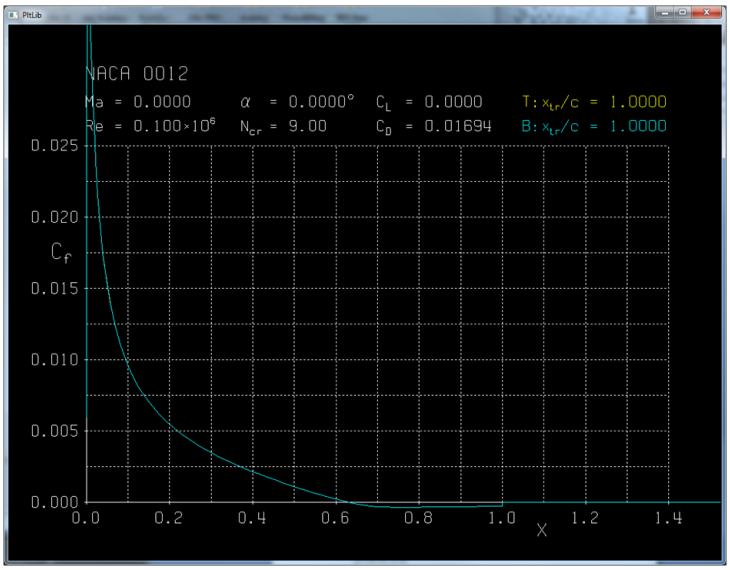

Figure 3.23: XFOIL plot of C_f, used to determine the point of boundary layer separation, at Re = 100,000 and $\alpha = 0°$.

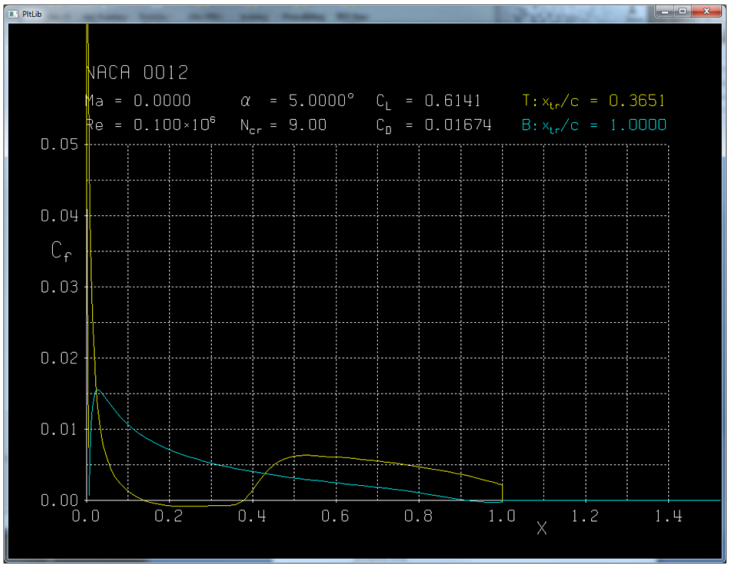

Figure 3.24: XFOIL plot of C_f, used to determine the point of boundary layer separation, at Re = 100,000 and $\alpha = 5°$. The yellow and blue lines represent the airfoil suction and pressure surfaces respectively.

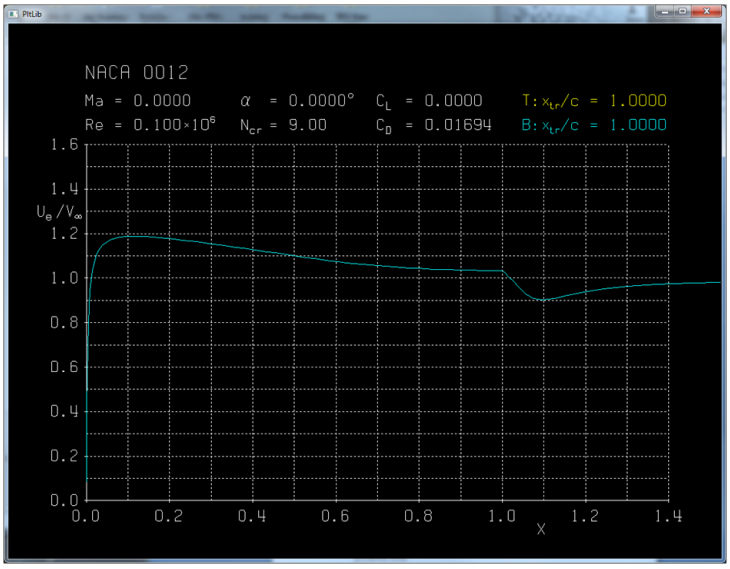

Figure 3.25: XFOIL plot of u/U_∞, used to determine the point of maximum velocity in the boundary layer, at $Re = 100{,}000$ and $\alpha = 0°$.

3.4 Summary

The experimental techniques used in this research have been summarised in this chapter. Experiments using an airfoil in the AWT were conducted over a range of Reynolds numbers (50,000 to 150,000) and angles of attack (0°, 1.58° and 3.16°) to investigate the flow and tonal noise of the airfoil. Table 3.1 provides a summary of the experiments performed in this study and the labelling of terms are defined in the table. A example entry of "SM, HW, AC" states that single microphone measurements were obtained simultaneously with hot-wire anemometry along the airfoil chord, and an example entry of "SM" states that single microphone measurements were obtained only.

The location of the acoustic source relative to the trailing edge is an important property needed to investigate the processes responsible for the generation of tones. This was evaluated using acoustic beamforming, introduced in the following chapter.

Table 3.1: Summary of experiments. All non-zero angle of attack tests were performed on both the airfoil pressure and suction surfaces.

	Angle of attack, α°					
Re		0°		1.58°		3.16°
50,000	SM	SM, HW, AC	SM	SM, HW, AC	SM	SM, HW, AC
	BF	SM, HW, VP	BF	SM, HW, VP	BF	
	SM, T	SM, HW, W				
	SFV		SFV		SFV	
75,000	SM		SM		SM	
	BF		BF		BF	
	SM, T					
	SFV		SFV		SFV	
100,000	SM	SM, HW, AC	SM	SM, HW, AC	SM	SM, HW, AC
	BF	SM, HW, VP	BF	SM, HW, VP	BF	
	SM, T	SM, HW, W				
	SFV		SFV		SFV	
125,000	SM		SM		SM	
	BF		BF		BF	
	SM, T					
	SFV		SFV		SFV	
150,000	SM	SM, HW, AC	SM	SM, HW, AC	SM	SM, HW, AC
	BF	SM, HW, AC	BF	SM, HW, VP	BF	
	SM, T	SM, HW, W				
	SFV		SFV		SFV	

Key:
SM = single microphone, BF = acoustic beamforming, HW = hot-wire anemometry, SFV = surface flow visualisation, AC = airfoil chord, VP = vertical profile, W = airfoil wake, T = trip-line.

Chapter 4

Acoustic Beamforming

4.1 Beamforming review

Beamforming is a signal processing technique used in radio astronomy, seismology and acoustics, for directional signal transmission or reception. Prior to the development of acoustic beamforming, the "acoustic mirror" technique was used in aeroacoustic testing, where a large concave elliptic mirror and an associated microphone were positioned in the acoustic far field (Kendall, 1977; Groshe et al., 1977; Schlinker, 1977). This technique was shown to be capable of locating individual sound sources relatively accurately; however, it needed to be physically shifted to detect sound sources of different locations. Also, in order to investigate sound sources at frequencies less than 2 kHz, excessively large mirrors were required (Brooks et al., 1998).

Microphone directional arrays such as radar antenna arrays and U.S. Navy hydrophone arrays were used for the detection of submarines as early as World War II (Elliot, 1966; Burdic, 1984). Acoustic beamforming been used successfully for the study of airfoil trailing edge noise (Brooks and Humphreys, 2006a; Dobrzynksi et al., 2008; Fisher et al., 2008) and other aeroacoustic tests, such as on aircraft landing gear and fuselage noise (Brusniak, 2008; Dobrzynksi et al., 2008).

4.2 Beamforming theory and algorithms

When a plane wave radiates towards a non-coplanar surface, each location on the surface receives the wave with a different acoustic phase. This is due to differences in the propagation distance of the wave to each point. If microphones are placed on this non-coplanar surface, they will detect this unique acoustic magnitude and phase. A beamforming algorithm will scan a defined area of space to locate and determine the strength of any noise sources. The direction of each area scan is called the focus direction. When the focus direction coincides with the incoming noise, a noise source is then detected (Brüel & Kjær, 2004). Figure 4.1 is a sensitivity diagram that shows an example plane wave noise source distribution.

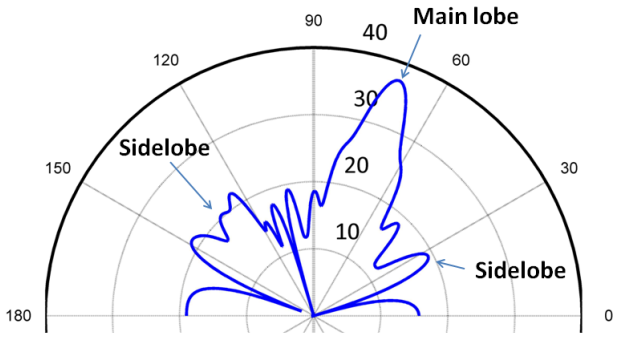

Figure 4.1: Sensitivity diagram (shown in dB, for various focus angles, in degrees) for a 63 channel array (Arcondoulis spiral, shown in Figure 4.4). The source was a simulated 7 kHz plane wave, arriving from the 70° direction.

The incident wave is non-coplanar with the microphone array plane, resulting in a sensitivity diagram that shows a noise source at an angle from the perpendicular axis of the array. Note that the "main lobe", corresponding to the incoming wave source magnitude and direction, is not the only signal presented in Figure 4.1. There exist other signal patterns in other directions of noticeable magnitude called "sidelobes". These are false spatial aliasing images that can reduce the quality of the source pressure distribution (Underbrink, 2002; Brüel & Kjær, 2004; Dougherty, 2005; Brooks and Humphreys, 2006a,b).

The sensitivity diagram acts as a test for the microphone array pattern, showing the effectiveness of the array to isolate a single incident wave (Brüel & Kjær, 2004). While an effective array design can reduce sidelobe images from sensitivity diagrams, the ability of the array to localise a source is not quantified from this measure alone. Improvements in the quality of the beamformer output have been achieved using beamforming techniques and algorithms over a 2-D plane. These methods include delay and sum, cross-spectral and deconvolution techniques, such as DAMAS (Brooks and Humphreys; 2006a), which is further detailed in Section 4.2.2. The delay and sum and cross-spectral algorithms produce the same output, yet due to the matrix-structure of the cross-spectral method, uncorrelated noise can be removed from the output, as discussed in the following section. The mathematical representation of the cross-spectral method in the following section is adapted from Brüel & Kjær (2004) and Brooks and Humphreys (2006a).

4.2.1 Cross-spectral method

Both the delay and sum and cross-spectral beamforming algorithms require measurements of both pressure magnitude and phase (expressed as a complex number) at each microphone. These data are processed first in the beamforming algorithm, in a cross-spectral matrix (C) defined as

$$C = \{p(f)p'(f)\}' \tag{4.1}$$

where p represents a vector of complex pressures in the frequency domain for each microphone, f represents the beamforming frequency and the prime represents the complex conjugate.

A beamforming output is computed over a planar area of space at a known distance from the array, referred to as the z-distance. This area is generally positioned in line with the centre of the microphone array. The area is evenly discretised into a grid of $NX \times NY$ data points, where NX and NY represent the number of grid lines

in the x and y directions respectively. Only square grids were used in this research and thus $NX = NY$. Various planar surfaces above and below the trailing edge can also be analysed during post-processing if desired. Figure 4.2 shows a schematic of the beamforming configuration, the placement of the microphones and two points of a grid area to be analysed (the grid would contain $NX \times NX$ data points, in the order of thousands of points).

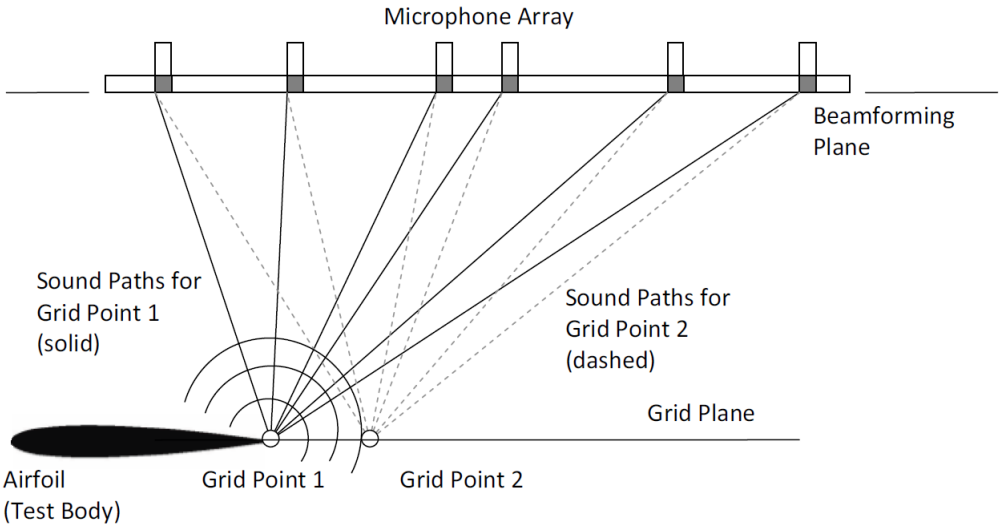

Figure 4.2: Acoustic beamforming schematic diagram.

Steering vectors ($\widehat{v}$) are used to scan the area of space under investigation for noise sources. The steering vectors contain the unique distances of each grid point in the area of investigation to each microphone, m. It is assumed that the wave is emitted from the acoustic source as a spherical wave (i.e., a monopole source). The steering vectors for the m^{th} microphone are defined as

$$v(m) = a(m)\frac{r_m(m)}{r_c(m)}\exp\left[\frac{-j2\pi f r_m(m)}{c}\right] \tag{4.2}$$

$$\widehat{v} = [v(1)v(2)\cdots v(M)] \tag{4.3}$$

where a represents a shear layer refraction correction term (Brooks and Humphreys, 2006a), r_m is the distance from the grid point to the microphone location, r_c is the distance from the grid point to the array centre and c is the speed of sound. The variable m ranges from 1 to M, where M is the total number of microphones in the array. The delay and sum beamforming output (Y) is computed using

$$Y(\widehat{v}) = \frac{(\widehat{v}')^T \left\{ diag_1(w) \left[C \right] diag_1(w)^T \right\} (\widehat{v}')}{\left(\sum_{m=1}^{M} w(m) \right)^2 - \left(\sum_{m=1}^{M} w(m) \right)} \tag{4.4}$$

where w represents a microphone shading vector and T denotes a matrix transpose. Microphone shading allows each microphone pressure magnitude to be adjusted during calibration. Some of the values of w can be set to zero to eliminate microphones, saving computational time and data acquisition. The "diag_1" function is the creation of a diagonal matrix, where the diagonal elements are the elements of the row vector to which the function is applied.

The cross-spectral beamforming output (Y) is computed using

$$Y(\widehat{v}) = \frac{(\widehat{v}')^T \left\{ diag_1(w) \left[C - diag_2(C) \right] diag_1(w)^T \right\} (\widehat{v}')}{\left(\sum_{m=1}^{M} w(m) \right)^2 - \left(\sum_{m=1}^{M} w(m) \right)} \tag{4.5}$$

where the "diag_2" function sets the matrix elements to zero, except along the diagonal.

The cross-spectral algorithm is primarily the same as the delay and sum algorithm, except the cross-spectral matrix diagonal terms are removed as shown in Equation 4.5. This eliminates microphone self-noise, which is auto-correlated noise between each microphone.

4.2.2 DAMAS

Brooks and Humphreys (2006a) derived a deconvolution algorithm called DAMAS (Deconvolution Approach for the Mapping of Acoustic Sources) that further refines the noise source distribution output. DAMAS helps remove the uncertainty of lo-

cating and quantifying noise sources by significantly removing sidelobe distributions and refining the source location area. The DAMAS solution scheme is derived by solving the following matrix equation

$$AX = Y \tag{4.6}$$

where Y is the delay and sum or cross-spectral output and X is the DAMAS solution to be solved. The matrix X contains only the true noise sources responsible for the values of Y (Brooks and Humphreys, 2006a). Both matrices X and Y are square and have dimension $NX \times NX$. The matrix A is defined as

$$A_{n,ns} = \frac{(\widehat{v}_n')^T \left\{ diag_1(w) \left[G_{ns} - diag_2(G_{ns}) \right] diag_1(w)^T \right\} (\widehat{v}_n)}{\left(\sum_{m=1}^{M} w(m) \right)^2 - \left(\sum_{m=1}^{M} w(m) \right)} \tag{4.7}$$

where n and ns are independent variables that range from 1 to N, where N is the total number of grid points in the area of investigation (equivalent to $(NX+1)^2$). Note that $N \neq NX^2$; $NX+1$ gridlines are required for NX locations. The G matrix is defined as a steering vector matrix array

$$G_n = \begin{bmatrix} (v(1)^{-1})\, v(1)^{-1} & \cdots & (v(1)^{-1})\, v(M)^{-1} \\ \vdots & \ddots & \vdots \\ (v(M)^{-1})\, v(1)^{-1} & \cdots & (v(M)^{-1})\, v(M)^{-1} \end{bmatrix}_n \tag{4.8}$$

Due to its low rank, the A matrix is generally unable to be directly inverted. Brooks and Humphreys (2006a) developed an iterative scheme to invert the A matrix and thus determine the DAMAS noise source pressures. This inversion procedure is defined by

$$A_{n,1}X_1 + A_{n,2}X_2 + \cdots + A_{n,N}X_N = Y \tag{4.9}$$

$$X_n = Y_n - \left[\sum_{ns-1}^{n-1} A_{n,ns}X_{ns} + \sum_{ns=n+1}^{N} A_{n,ns}X_{ns} \right] \tag{4.10}$$

$$X_n^{(i)} = Y_n - \left[\sum_{ns-1}^{n-1} A_{n,ns} X_{ns}^{(i)} + \sum_{ns=n+1}^{N} A_{n,ns} X_{ns}^{(i-1)} \right] \tag{4.11}$$

where the superscript i denotes the iteration number of the solution scheme.

The DAMAS solution scheme is unfortunately computationally expensive, sometimes taking several hours to compute on a standard PC for even small array sizes. This technique requires many matrix inversion iterations, where the A matrix dimensions can be as high as 2601×2601 (Brooks and Humphreys, 2006a). According to Brooks and Humphreys (2006a) the number of required solution iterations is dependent on the complexity of the noise sources. They claim for most aeroacoustic tests that 5000 iterations is adequate for convergence of their solution scheme.

4.3 Beamformer design

In the design of typical hard-walled wind tunnels, little consideration is generally given to acoustic testing. This can make the design and optimisation of an acoustic beamforming array quite difficult, due to reflected noise between the array and walls (Underbrink, 2002). Fortunately the AWT possesses anechoic treatment, simplifying the array design process. The optimal array design for an aeroacoustic testing facility (Underbrink, 2002) is dependent upon various parameters, including frequencies of investigation, size of area of investigation, allowable dimensions of the array, distance of the array to the noise sources, distance between noise sources under investigation and the maximum allowable sidelobe levels. Many of these parameters are driven by spatial and budget constraints.

4.3.1 DAQ constraints

The number and quality of microphones available was mainly governed by budget constraints. While the size of the AWT restricts the diameter of the array and hence the number of microphones, the allowable budget also limited this to a large extent.

The cost of individual microphones (Lectrets) used was insignificant compared to the cost of the required data acquisition hardware. The DAQ for the AWT consisted of an NI PXI-1042Q Chassis, with four PXI-4496 DAQ cards. Each card was capable of storing 16 channels of data, thus allowing the acquisition of 64 channels of synchronous data.

From a theoretical beamforming standpoint, it is desirable to use as many microphones as possible, yet in a logarithmic spiral array design, it is recommended that the number of microphones used is an odd number. This prevents any redundancies for the unique spacing between the microphones in the array (Underbrink, 2002). Thus the total number of microphones chosen for use was 63, provided that they can be accommodated in the space within the AWT, which is assessed in Section 4.3.2. An added benefit of using 63 microphones is that a spare channel is available on the 64-channel DAQ. The spatial constraints are discussed in the following section.

4.3.2 Spatial constraints

Prior to designing the beamforming array, the allowable area over which microphones can be placed must be determined. This area influences the number of microphones that can be fit into a confined plane. The array was installed near the AWT ceiling to prevent interaction with other instrumentation. The ceiling surface is a 1.4 m $\times$ 1.4 m square area and acoustic foam wedges on the AWT walls fills some of this area. Near the ceiling two rigid parallel rods run in the same direction as the flow and are located approximately 300 mm inboard from the outer edge of the acoustic foam wedges. Thus, the final allowable dimension for the plate containing the array (assuming the existing beams are used to support the array and are 50 mm thick) is 1.4 m - 2 $\times$ 300 mm - 2 $\times$ 50 mm = 700 mm. This value was set as the maximum allowable array size and thus the maximum allowable theoretical distance between any two microphones within the array. These distances are depicted in a schematic diagram shown in Figure 4.3.

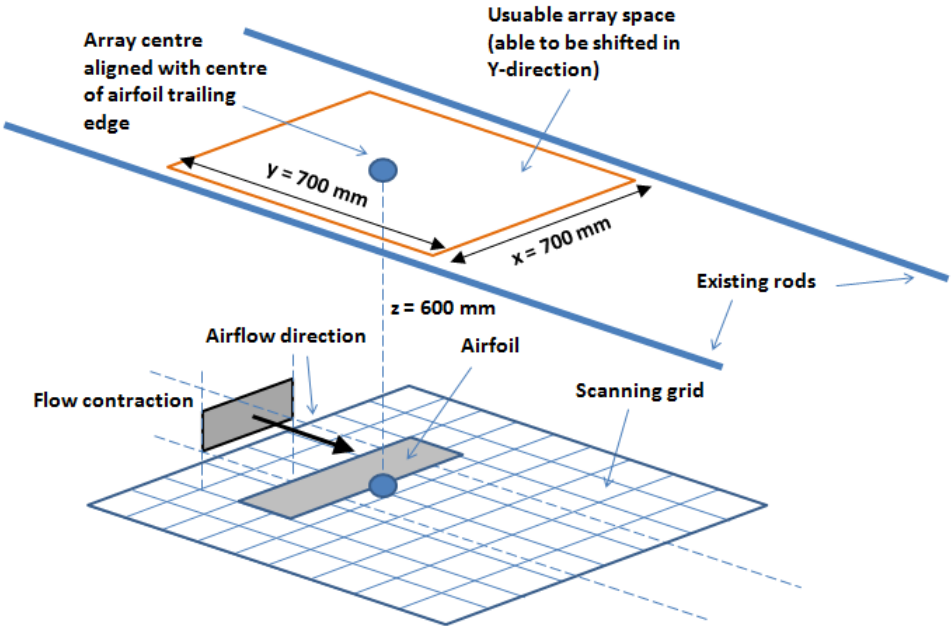

Figure 4.3: Allowable room within the AWT to accommodate an acoustic beamformer, including the proposed airfoil location and scanning grid.

The size of the AWT and the locations of the beams were the driving factors for the array size. Consideration was also given to the weight of the array, as well as the ability to feed microphone-to-amplifier cables from the array upper surface out of the AWT with sufficient cable relief. As a check prior to manufacture and assembly, a Finite Element Analysis was performed on the array assembly, including the simulated masses of the microphones, Perspex sheet, aluminium rods and supports. The maximum deflection of the array was estimated to be 12 mm at the geometric array centre and the maximum stress levels were significantly less than the yield stresses of the materials. The maximum deflection of 12 mm, if treated as an error in distance, represented 2% of 600 mm.

An important spatial factor was the distance of the array centroid (corresponding to the centroid of the microphone array pattern) to the location of the expected acoustic source locations; i.e., the z-distance. Beamforming theory suggests that

smaller z-distances allow greater source resolution, assuming that the z-distance is the only parameter of investigation. Excessively minimising the z-distance results in other acoustic problems, being that the microphones may be placed in the acoustic near field, depending on the source frequency, as well as possible interaction of the array with the flow field.

Considering the fixed location of the contraction outlet, the location of the beams near the AWT ceiling, as well as the relatively wide range of frequencies to be investigated, it was decided to keep the beamformer array at a distance of 600 mm from the centreline of the AWT flow contraction. Note that for an airfoil at non-zero angle of attack, the distance of the trailing edge to the array was slightly different than if the airfoil were placed at $\alpha = 0°$. Therefore accommodations for the change in z-distance were accounted for in the beamforming algorithm when investigating airfoil noise at non-zero angles of attack.

4.4 Array type comparison

This section describes simulations that were used to compare the performance of a variety of microphone arrays. A monopole source was simulated as a spherical wave that propagated toward the microphone array, such that each microphone location detected a unique pressure magnitude and phase that were then input into Equation 4.1. Equations 4.2 to 4.11 were then computed.

4.4.1 Logarithmic spirals

Simply employing a large number of microphones does not guarantee a desirable sidelobe distribution and beamwidth. Quite often the quality of the sidelobe distribution comes at the expense of beamwidth and vice-versa. The quality of the sidelobe magnitudes and beamwidth is dependent upon the number of unique spacings between each of the microphones in the array. To achieve an optimised balance

between sidelobe distribution and beamwidth, it is recommended that the microphones be distributed by means of a randomisation pattern or a type of spiral pattern (Underbrink, 2002). Logarithmic spirals were investigated, as they possess the highest number of unique spacings between microphones as compared to other array types of the same size and number of microphones (Underbrink, 2002).

The parametric equations for the coordinates (x and y) of a logarithmic spiral are

$$x(m) = a\cos(\theta(m))\exp(b\theta(m)) \tag{4.12}$$

$$y(m) = a\sin(\theta(m))\exp(b\theta(m)) \tag{4.13}$$

where a and b are coefficients that affect the overall size of the spiral and how rapidly the arms of the spiral expand from the centre respectively. The angle $\theta(m)$ is defined as

$$\theta(m) = \left(\frac{(m-1)\varphi n}{M}\right) \tag{4.14}$$

where φ is the spiral sweep angle (i.e. $\varphi = 2\pi$ represents one spiral revolution) and n is the number of sweeps of φ.

Logarithmic spiral array designs were investigated simulating 63 microphones in a 700 mm × 700 mm square area. The beamwidth and sidelobes of the beamformer output were compared for each array design for a range of frequencies for a monopole source located 600 mm from the array centre, simulating the expected airfoil noise in the AWT. The cross-spectral beamformer algorithm was employed for the comparison analysis.

The arrays were varied in microphone distribution by changing the parameters n, a and b. The beamformer outputs of different arrays were qualitatively compared for fixed monopole sources and frequencies per instance. Increasing the distribution of microphones near the centre of the array decreased the beamwidth of the

monopole main lobe for higher frequencies, at the compromise of increased sidelobe magnitudes. Therefore, the design process was an optimisation task between minimising array beamwidth and sidelobe levels over the range of frequencies expected from low-to-moderate Reynolds number airfoil flows in the AWT.

Most of the analysed array designs presented adequate resolution of the noise source, displaying a defined main lobe with little sidelobe interference. Unfortunately many of these arrays were larger than a square metre in size. Some of the array designs that displayed excellent noise source resolution at higher noise frequencies were invalid practically, as the theoretical microphone locations were too close to each other causing potential physical interference. Thus the optimisation task involved keeping many of the microphones closer to the array centre (improving higher frequency performance) while keeping some microphones near the 700 mm square area perimeter (improving lower frequency performance).

Increasing the parameter n resulted in pushing the arms of the spirals closer together. This resulted in better resolution of acoustic sources at higher frequencies. Forcing the spiral arms closer together also minimised the overall array size compromising the ability of the array to perform adequately at lower frequencies. Parameters a and b dictate how far the spiral arms extend and increasing a and b resulted in increasing total array size. Parameter a acts as an overall scaling multiplier of the total array size; that is, the array pattern is unchanged but the distance of each microphone from the array centre, if the first microphone is located at the geometric origin, is multiplied by a. This parameter was useful in dictating the overall array size, if a potential array pattern design required magnitude scaling. The parameter b is included within the exponential term in the parametric coordinates. Thus, changes to b resulted in an exponential increase of microphone-to-array centre distances, for increasing m (whereas increasing a results in a linear increase of microphone-to-array centre distances).

4.4.2 Arcondoulis spiral

A modification to the default logarithmic spiral equation was introduced to ensure that 63 microphones could be placed in a 700 mm × 700 mm square area while densely populating the centre of the array. This was done by "squashing" the spiral pattern in the direction of the furthest microphone from the array centre by introducing an additional multiplicative factor to Equations 4.12 and 4.13. The Arcondoulis spiral coordinates (x' and y') are created by including scaling factors that are a function of m, such that

$$x'(m) = \left[\frac{(m + \epsilon_x M)}{M}\right] a\cos(\theta(m))\exp(b\theta(m)) \tag{4.15}$$

$$y'(m) = \left[\frac{(m + \epsilon_y M)}{M}\right] a\sin(\theta(m))\exp(b\theta(m)) \tag{4.16}$$

where ϵ_x and ϵ_y are coefficients that determine the "squashing" of the spiral in the x and y directions respectively. In this case, m ranges from 2 to M and $x(1) = y(1) = 0$, to ensure that a microphone is located at the origin. Effectively, the spiral size coefficient is no longer constant and now a function of the number of microphones. In the case of the Arcondoulis array presented here, the parameters were

$a = 0.03$, $b = 0.06$, $n = 6$, $\varphi = 2\pi$, $M = 63$, $\epsilon_x = \epsilon_y = 0.9$.

Four microphones located closest to the array centre do not fit Equations 4.15 and 4.16. This is due to the nature of both the Arcondoulis and the logarithmic spirals, that do not possess an element at or near the geometric origin. These microphones were manually shifted toward the array centre to ensure that a smooth, continuous pattern of microphones was generated. This also helped achieve sufficient clearance between each microphone location near the array centre. The coordinates of the Arcondoulis spiral array used in the AWT are provided in Appendix A. The final array design is shown in Figure 4.4, including the default logarithmic spiral pattern spanning the same area for comparative purposes.

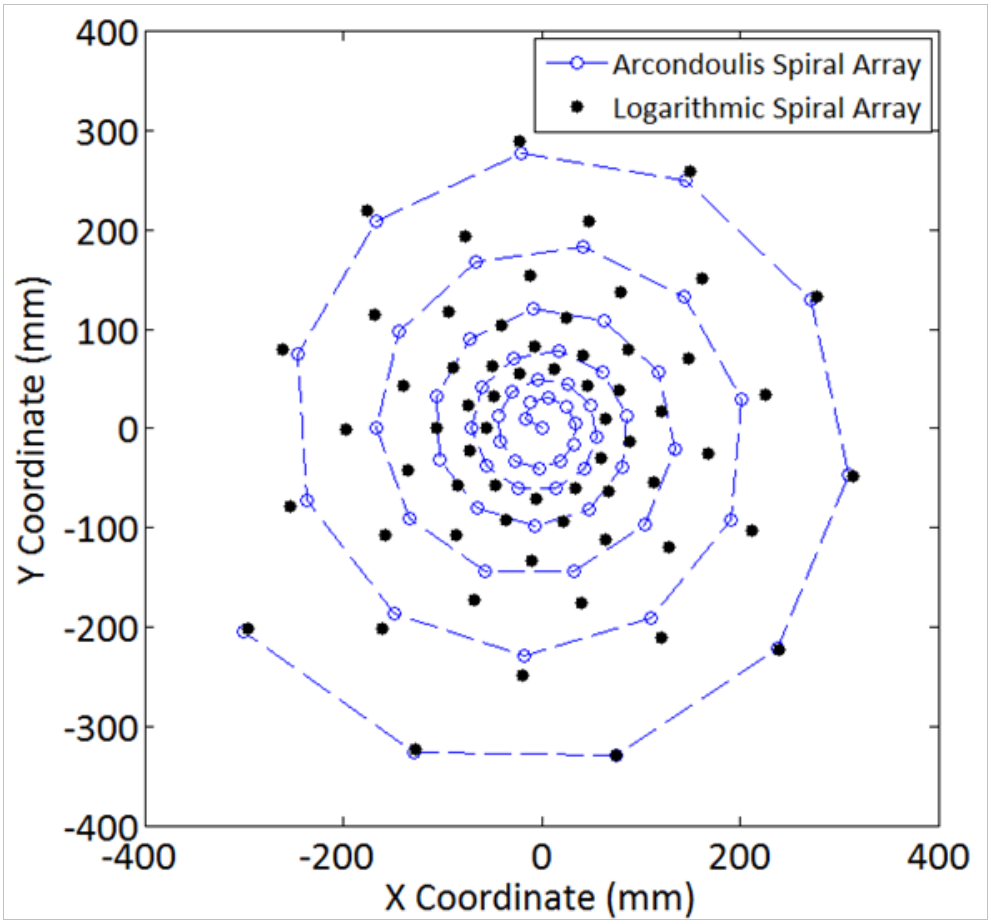

Figure 4.4: The Arcondoulis spiral microphone array design used in the AWT (microphone positions denoted by empty circles joined by a line) and the corresponding default logarithmic spiral (microphone positions denoted by filled circles).

Note the differences in the spirals in Figure 4.4; the Arcondoulis spiral contains a denser population of microphones near the centre as desired. It also expands more rapidly than the original logarithmic spiral after the spiral arm has made three turns about the centre. This ensures that the same spiral area is covered with a greater percentage of microphones near the array centre.

4.4.3 Maximum sidelobe levels

One method of comparing the performance of an array relative to another is to measure the magnitude of the greatest sidelobes, known as the Maximum Sidelobe Level (MSL). An array that possesses a smaller value of MSL is said to have better sidelobe characteristics. It is important that the sidelobes are as small in magnitude as possible, to ensure that they are not mistaken for true noise sources during experiments. In certain aeroacoustic testing regimes sidelobe images resulting from multiple noise sources may interfere, potentially resulting in the inability to identify true and false noise sources. The superposition of a sidelobe with a true noise source may adversely affect the accuracy of the true noise source location and magnitude. Reducing sidelobe levels or even removing them from the beamformer output can provide negative effects on the beamformer output. Excessive suppression of sidelobes often results in an increased main lobe width and decreased resolution of the noise source. Thus one must exercise caution in designing a beamformer array and decide whether the main lobe width or the magnitude and distribution of sidelobes is of greater importance in the beamformer application. For this research and most aeroacoustic experiments, a balance of both is desired.

An MSL analysis was performed to exhibit the beamformer output characteristics of the Arcondoulis spiral relative to other array types. An algorithm was written to detect the MSL by calculating the maximum cross-spectral image output that excluded the main lobe area. The main lobe was defined as the area from the maximum amplitude (normalised to 0 dB) to the base of the lobe (measured at -50 dB from the maximum). Grid, random, logarithmic spiral and Arcondoulis spiral arrays were compared. To ensure that the comparisons were fair, each of the arrays possessed the same number of microphones (63) that covered the same 700 mm × 700 mm area. A noise source was simulated at a z-distance of 600 mm from the array, the same as the AWT experimental conditions. The source was placed at coordinates $x = y = 0$ mm, directly in-line with the array centre microphone. The scanning grid was 1000 mm × 1000 mm, ensuring the entire main lobe width and

the sidelobes of greatest magnitudes were measured.

An arbitrary noise source frequency of 4.5 kHz was selected, to ensure that the arrays possessed sidelobes and that their main lobe widths differed. At lower frequencies, some of the arrays possessed no sidelobes at all, and at higher frequencies the comparison became unrealistic as the frequencies were outside the expected range of the experiments. Figure 4.5 displays the arrays and their beamformer outputs for grid, random, logarithmic spiral and Arcondoulis spiral arrays over a 1000 mm × 1000 mm scanning grid, respectively.

The grid array result shown in Figure 4.5a located the source correctly but there were significant sidelobes (-20 dB with respect to the main lobe) within 100 mm of the centre of the scanning grid. The randomised array performance shown in Figure 4.5b was inferior, as there were stronger distributions of sidelobes (-15 dB with respect to the main lobe).

The logarithmic spiral array beamformer output shown in Figure 4.5c displays a better distribution of sidelobe levels than the grid and randomised arrays. While there are still sidelobes present, they are considerably lower in magnitude (-35 dB re main lobe) compared with the grid and randomised outputs (-20 dB and -15 dB respectively). The Arcondoulis spiral output possesses the best sidelobe characteristics from the array designs investigated. As observed from Figure 4.5d, there are no visible sidelobes (although there are sidelobes with magnitudes -50 dB relative to the main lobe). The width of the main lobe of the Arcondoulis spiral is equal to the width of the main lobe of the logarithmic spiral from 0 dB to -25 dB. Below a magnitude of -25 dB, the main lobe of the Arcondoulis spiral widens (i.e., the same noise magnitude is distributed over a greater area). This is generally not desirable in beamforming applications that require the identification of a single isolated source. In the investigation of aeroacoustic applications (such as airfoil trailing edge noise) the noise may consist of multiple sources, corresponding to either several main lobes or a large superimposed main lobe in the beamformer output. In either case, the location of the trailing edge noise sources can be identified with greater resolution

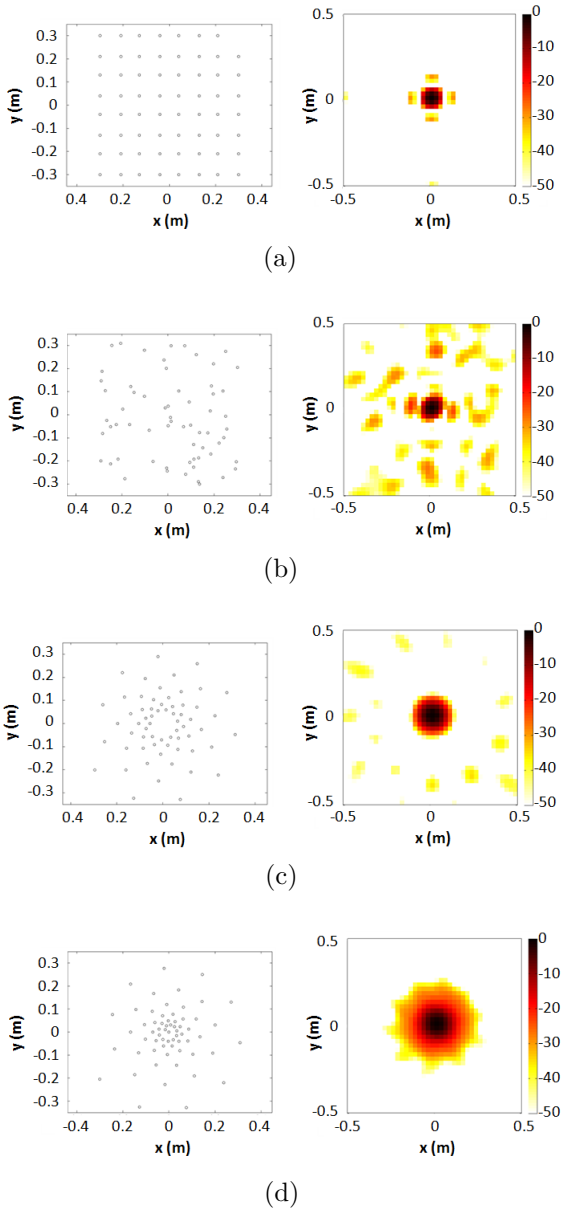

Figure 4.5: Microphone array distributions and the corresponding simulated cross-spectral beamforming result, for a 4.5 kHz monopole source located 600 mm from the array centre. Units are in dB, normalised to the maximum cross-spectral pressure. The presented array types are (a) Grid, (b) Randomised, (c) Logarithmic spiral and (d) Arcondoulis spiral.

using DAMAS.

To compare the array performances over a wider range of noise source frequencies, the MSL for each array was calculated for source frequencies of 2 kHz to 20 kHz, in 50 Hz increments, as displayed in Figure 4.6. The Arcondoulis spiral had superior sidelobe characteristics to all of the other array types for frequencies less than 4.84 kHz, as observed in Figure 4.6a. Some arrays at lower frequencies possessed no sidelobes in the cross spectral output. The random array presented superior results to the other array types over some very small frequency ranges, centred at approximately 12.3 kHz and 18.2 kHz. Both the logarithmic and Arcondoulis spirals performed better than other arrays, but this was frequency dependent. To investigate this further, the differences between the normalised MSL values of the logarithmic and Arcondoulis spirals were calculated and are presented in Figure 4.6b. As observed from Figure 4.6b, the Arcondoulis spiral sidelobe characteristics were superior to the logarithmic spiral for $f \leq 4.84$ kHz and 12.36 kHz $\leq f \leq$ 20 kHz. For 7.53 kHz $\leq f \leq$ 12.36 kHz, no spiral had consistently superior sidelobe characteristics over the other. By calculating the average MSL for each frequency investigated within 7.53 kHz $\leq f \leq$ 12.36 kHz, one can determine which array possesses better sidelobe characteristics over this range. This average was showed that the Arcondoulis spiral was slightly superior in this frequency range.

4.4.4 Comparison of cross-spectral and DAMAS techniques

Due to the much greater computational requirements of using DAMAS as compared to the cross-spectral method, an investigation was performed to determine whether the maximum acoustic source location (MASL) as determined by both methods was comparable. In experimental testing cases where only the MASL was required, there could be significant time savings if the cross-spectral method presented the same MASL as DAMAS. Simulations were performed at various locations on a scanning

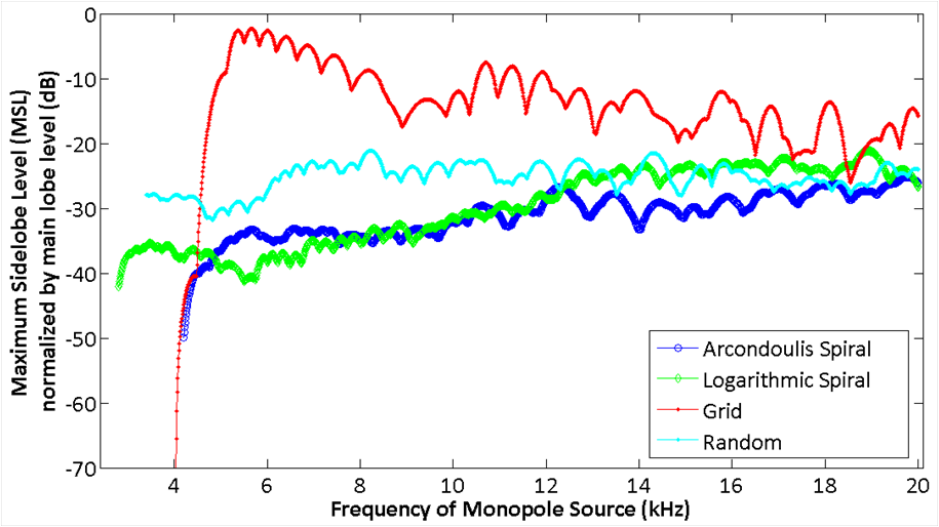

(a)

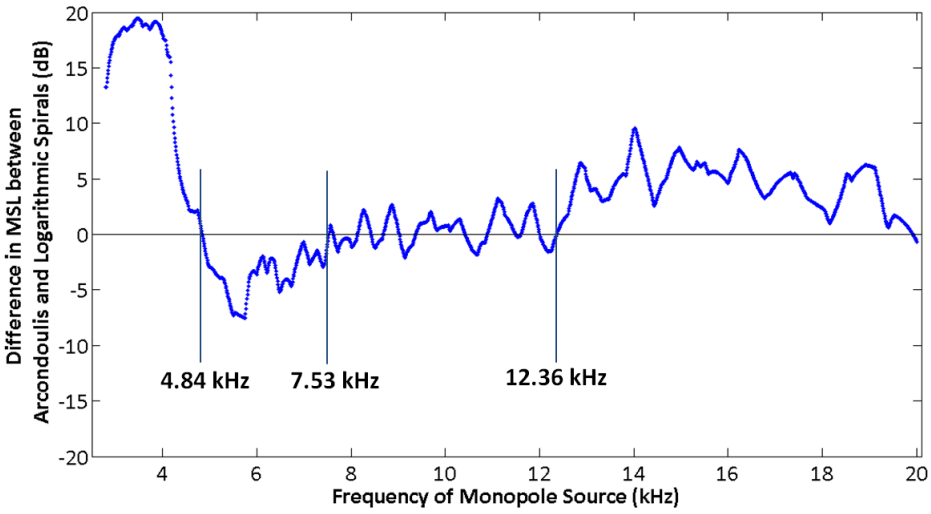

(b)

Figure 4.6: (a) The MSL of the arrays presented in Figure 4.5, over 2 kHz to 20 kHz in 50 Hz increments. (b) Differences in MSL values of the logarithmic and the Arcondoulis spirals. The labelled frequency partitions identify transition frequencies for the superiority of each array.

grid plane 600 mm below the array centre. Two scenarios are presented in Figures 4.7 and 4.8, where the simulated source was at $X = 200$ mm, $Y = 100$ mm and $X = 0$ mm, $Y = 0$ mm, respectively. Five hundred (500) iterations of the A-matrix (Brooks and Humphreys, 2006a) were performed in the DAMAS algorithm that converged to within approximately 2 dB ref 20×10^{-6} Pa. The scanning grid consisted of $NX = 30$ grid lines and the monopole source possessed a frequency of 2 kHz. The simulations showed that for both source locations, the MASL was the same using both the cross-spectral and DAMAS methods. To help visualise the results, they are presented as acoustic pressures at each grid point N, where $N = (NX + 1)^2$. Other simulated source locations were tested that consistently showed that all simulated monopole sources within a 1000 mm $\times$ 1000 mm scanning grid were estimated at the same locations using both the DAMAS and cross-spectral methods.

4.5 Beamformer experiments

An array was manufactured with 63 Lectret microphones in the pattern of the Arcondoulis spiral, with coordinates provided in Appendix A. Holes were laser-cut into a Perspex sheet to accommodate snap-lock connections that secured the microphones. The microphone array was suspended in the AWT by connecting the Perspex sheet with screws to aluminium rods. The ends of these rods were fitted with aluminium C-sections, which rested onto existing cylindrical beams in the AWT. The array was located 600 mm above the plane of the mid-height of the AWT flow contraction (z-direction). The array location was adjusted so that the X and Y coordinates of the centre microphone of the array were the same as the spanwise centre of the airfoil trailing edge. The array installed in the AWT is depicted in Figure 4.3 and shown in Figure 4.9.

For beamforming experiments the airfoil was secured in the AWT as discussed in Section 3.2. The centre of the airfoil span was located in line with the array centre microphone, in the X-direction (spanwise direction). The array was placed 600 mm

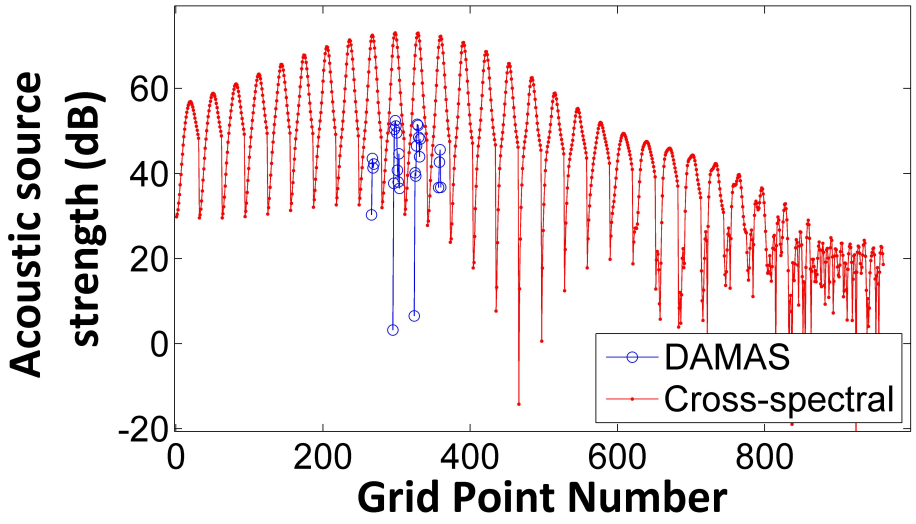

(a)

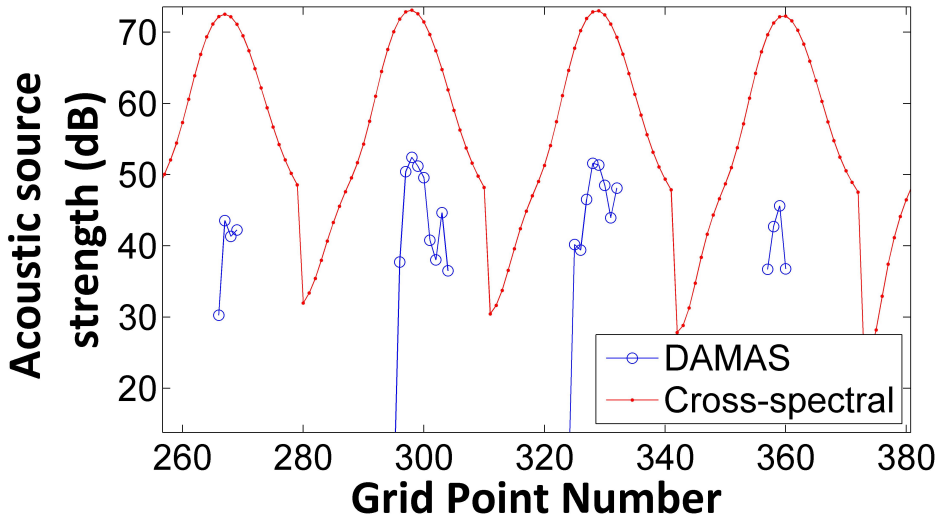

(b)

Figure 4.7: Comparisons between the acoustic source strengths obtained from DAMAS and the cross-spectral method for a simulated 2 kHz monopole source (a) at $X = 200$ mm, $Y = 100$ mm, 600 mm below the array surface, (b) Enlargement of (a), identifying the MASL from the DAMAS and cross-spectral methods.

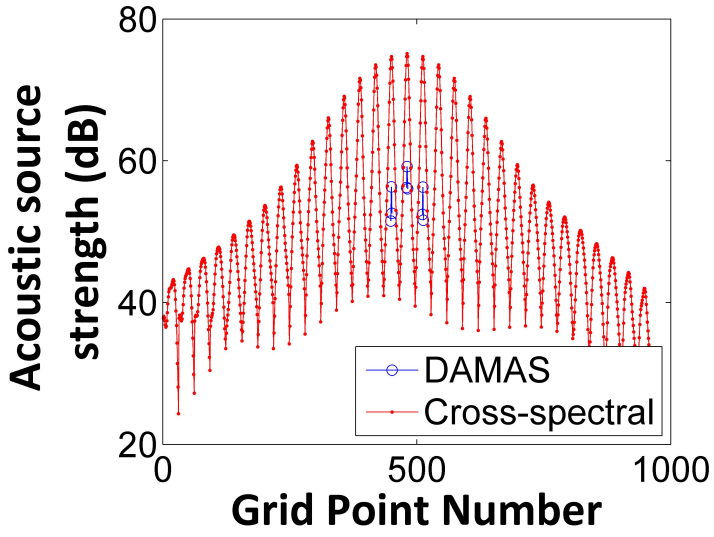

(a)

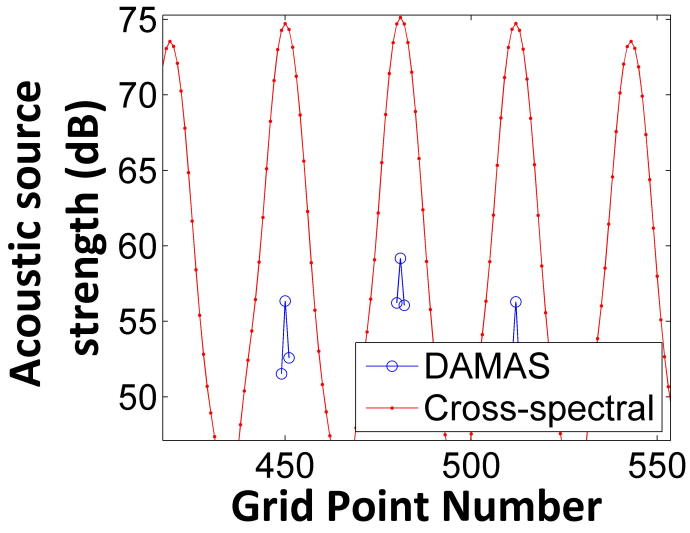

(b)

Figure 4.8: Comparisons between the acoustic source strengths obtained from DAMAS and the cross-spectral method for a simulated 2 kHz monopole source (a) at $X = 0$ mm, $Y = 0$ mm, 600 mm below the array surface and (b) Enlargement of (a), identifying the MASL from the DAMAS and cross-spectral methods.

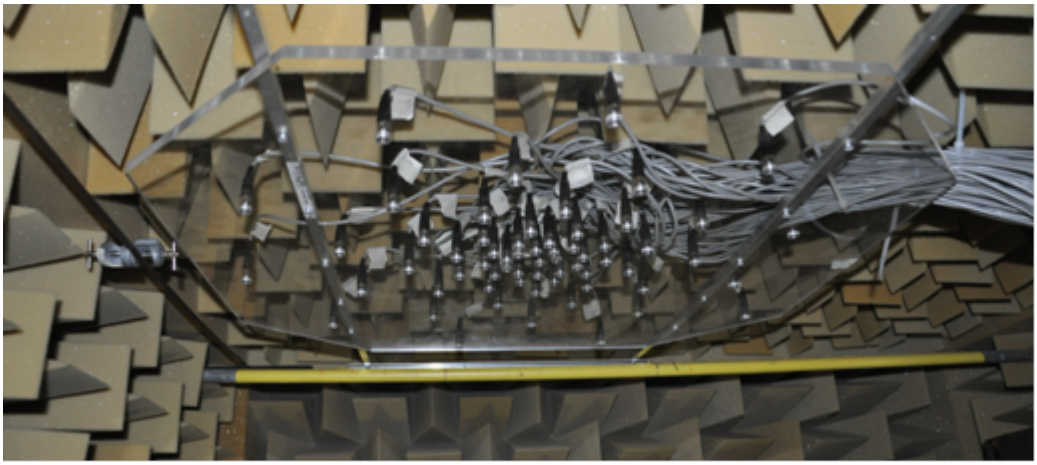

Figure 4.9: Sixty-three microphone beamformer array installed in the AWT.

above the plane of the AWT jet mid-height, which corresponded to the height of the airfoil trailing edge at $\alpha = 0°$. To minimise the effect of the shear layer (and knowing that the maximum acoustic source location would be either at the trailing edge or in its vicinity) the centre of the acoustic beamformer was aligned with the airfoil trailing edge, in the Y-direction (chordwise direction). This also made post-processing of data more convenient as the acoustic source location results were presented relative to the airfoil trailing edge, corresponding to $Y = 0$ mm. The placement of the acoustic beamformer in the AWT is shown in Figure 4.10.

Preliminary experiments using an airfoil in place revealed that broadband noise was observed at frequencies below 500 Hz. At these frequencies, the signal-to-noise ratio was typically low (at most 5 dB greater than the background noise) and the beamformer resolution was poor. For frequencies between approximately 3 kHz to 4 kHz, the array microphones did not possess a flat response, due to acoustic effects within their housing within the array. Beamforming results were thus presented for 500 Hz $\leq f \leq$ 3 kHz.

The scanning grid and its location within the AWT are depicted in Figure 4.11. The scanning grid for the airfoil was set at 180 mm × 180 mm to cover the entire

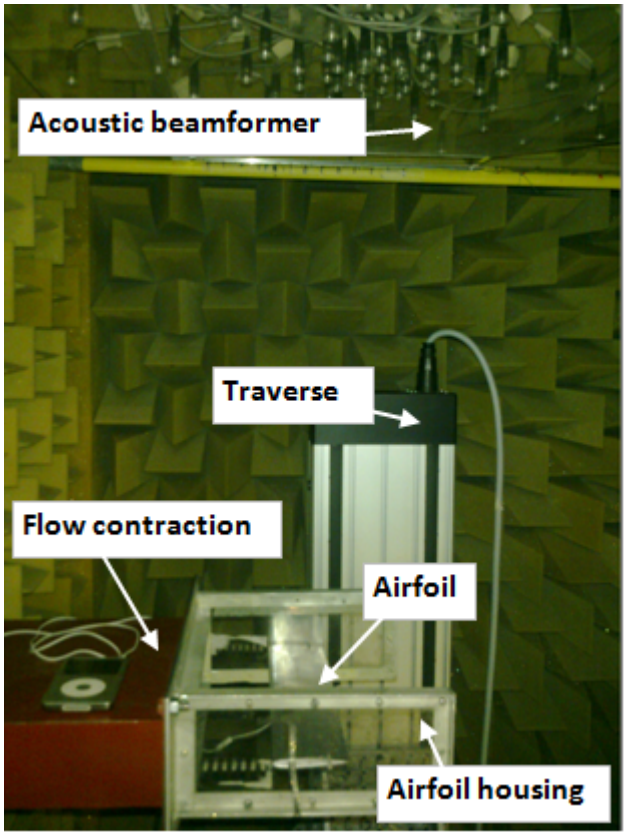

Figure 4.10: The acoustic beamformer installed in the AWT for airfoil noise measurements.

airfoil chord, as well as upstream and downstream locations. The airfoil span is 275 mm, meaning that the entire airfoil span is not encompassed within the scanning grid, thus any noise generation mechanisms near the side edges are not seen in the beamformer output. The scanning grid contains 50 × 50 grid spacings (created by $NX = 50$ scanning grid lines, corresponding to $N = 51 \times 51 = 2601$ scanning grid points). Thus a scanning grid of 180 mm × 180 mm possesses a grid resolution of 180 mm / 50 = 3.6 mm.

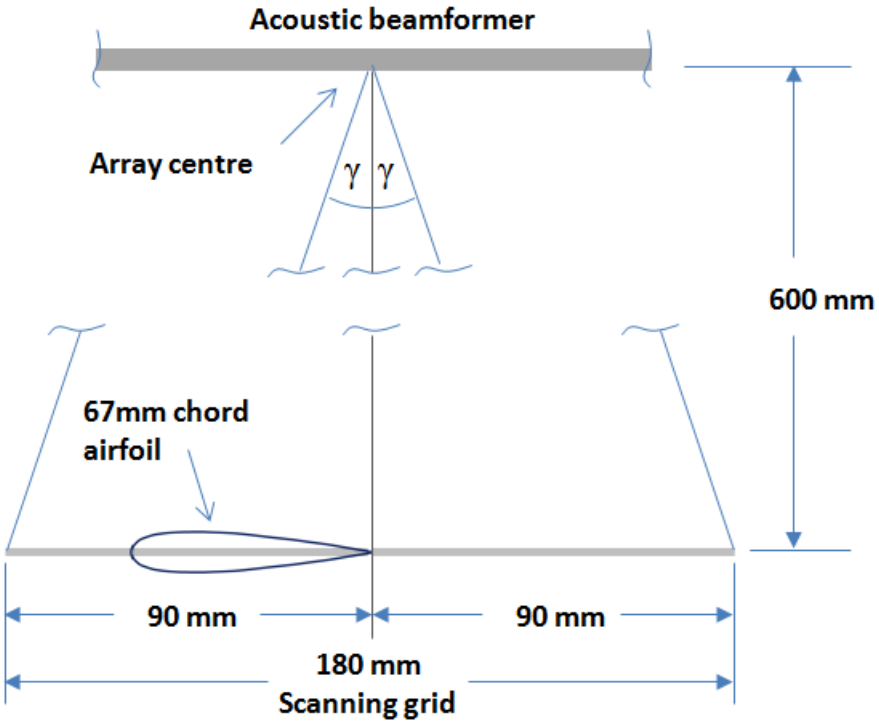

Figure 4.11: Schematic diagram of the scanning grid used to analyse the acoustic source locations of a 67 mm NACA 0012 airfoil in the AWT.

4.5.1 Data acquisition

A MATLAB DAQ interface with the NI PXI system was used to collect the data at a sampling frequency of 2^{15} Hz for 5 seconds. The data were converted into Pascals, band-pass filtered between 50 Hz and 10 kHz and passed through the inbuilt MATLAB FFT algorithm. These data were used to form the cross-spectral matrix. The autospectra were removed from the cross-spectral matrix prior to commencing the cross-spectral beamforming algorithm.

The sampling time of 5 seconds was justified in a process similar to that discussed in Section 3.2.3.1. The results of one sampling time to another were analysed by comparing their cross-spectral outputs. The frequency of the greatest beamformer magnitude was calculated for both cases and compared. This corresponds to the

frequency at which the cross-spectral output displayed the greatest magnitude. For sampling times of 20, 10 and 5 seconds, this remained the same for a preliminary experiment with an airfoil in place at $Re = 100{,}000$ and $\alpha = 0°$. This frequency also matched the measurement of the single microphone preliminary tests as expected.

In the cross-spectral output, the location of the maximum acoustic source location was shown to be the same for the aforementioned flow condition and sampling times. This suggests that a sampling time of 5 seconds was sufficient to accurately locate the maximum acoustic source strength. The cross-spectral output patterns were also visually compared for different sampling times, based on the number of cells within the scanning grid that possessed acoustic source terms or none (or less than the threshold of -20 dB). This provided a comparison of the beamformer resolution for various sampling times. Again, the sampling time had a negligible impact on the sidelobe magnitudes as well as the resolution of the acoustic source (i.e., how many scanning grid cells the acoustic source covered, within -20 dB of the maximum magnitude). It should be noted that at sampling times less than 5 seconds (such as 2 and 3 seconds) the experiments were not repeatable with the same flow conditions and many of the cross-spectral outputs were nonsensical.

4.5.2 Shear layer refraction

The airfoil is located in the centre of the AWT jet and thus the noise that is emitted from the airfoil surfaces or trailing edge must travel through half the AWT jet height before arriving at a microphone. This causes the acoustic waves to experience refraction and thus they do not propagate to the same location as would be expected in still conditions. A correction was applied to allow for this refraction effect and to understand the true location of the acoustic source. The acoustic refraction process is illustrated in Figure 4.12.

The following is a rearrangement of the equations for shear layer refraction in an open jet. Amiet (1977) derived three equations with three unknowns, requiring an

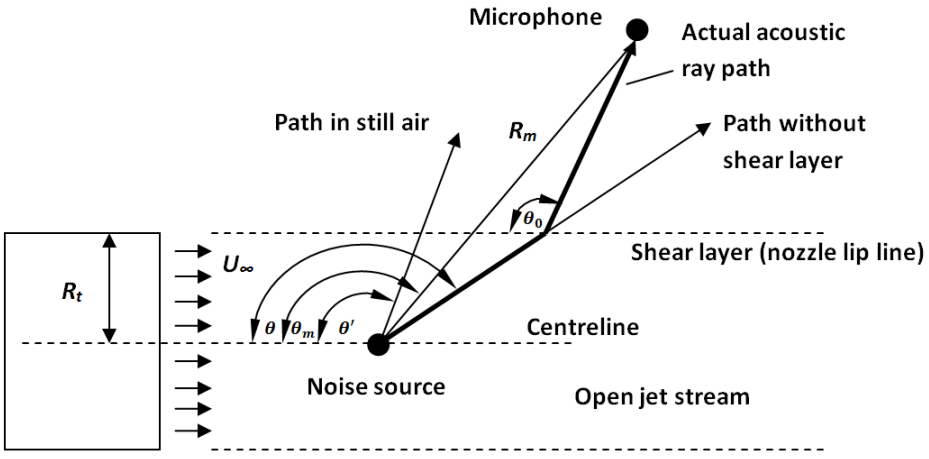

Figure 4.12: Shear layer refraction schematic diagram.

implicit solution. The rearrangement was done in this study to make the integration of the mathematics into the beamforming algorithm more convenient. Brooks and Humphreys (1998) provided a different approach to dealing with these equations in their beamforming code; however, the following approach was deemed the most convenient for implementation in a beamforming algorithm, as discussed in detail in Section 4.5.3.

From consideration of the geometry

$$R_m \cos(\theta_m) = R_t \cot(\theta) + (R_m \sin(\theta_m) - R_t) \cot(\theta_0) \tag{4.17}$$

where R_m, θ_m and R_t are defined in Figure 4.12.

Using known microphone locations within the AWT and the jet height, Equation 4.17 provided a geometric relationship between the acoustic path (that would exist in still air) and the true acoustic path (in moving air). The derived relationship between θ and θ' (Amiet, 1977) was provided by

$$\cot(\theta) = \frac{\cos(\theta') - M_0}{\sin(\theta')} \tag{4.18}$$

where M_0 is the open-jet Mach number.

Assuming that the speeds of sound within the moving airflow and still air were equivalent (i.e. c_t and c_0 are equal), then

$$U_{tr} = U_\infty - \frac{c_t}{\cos(\theta')} = -\frac{c_0}{\cos(\theta_0)} \tag{4.19}$$

where U_{tr} is the trace velocity. Dividing by c_t results in

$$M_0 = \frac{1}{\cos(\theta')} - \frac{c_0/c_t}{\cos(\theta_0)} \tag{4.20}$$

$$= \frac{1}{\cos(\theta')} - \frac{1}{\cos(\theta_0)} \tag{4.21}$$

This equation was further rearranged to provide an expression for θ_0 where

$$\theta_0 = \cos^{-1}\left\{\left(\frac{1}{\cos(\theta')} - M_0\right)^{-1}\right\}. \tag{4.22}$$

Equation 4.17 was manipulated to yield

$$A_1 = \cot(\theta) + A_2\cot(\theta_0), \tag{4.23}$$

where

$$A_1 = \left(\frac{R_m}{R_t}\right)\cos(\theta_m) \tag{4.24}$$

$$A_2 = \left(\frac{R_m}{R_t}\right)\sin(\theta_m) - 1 \tag{4.25}$$

Substituting Equation 4.18 into Equation 4.23 yielded

$$A_1 = \frac{\cos(\theta') - M_0}{\sin(\theta')} + A_2\cot(\theta_0). \tag{4.26}$$

Substituting Equation 4.22 into Equation 4.26 gave

$$A_1 - \frac{\cos(\theta') - M_0}{\sin(\theta')} - A_2\cot\left\{\cos^{-1}\left(\frac{\cos(\theta')}{1 - M_0\cos(\theta')}\right)\right\} = 0 \tag{4.27}$$

Finally, using the defined expressions for A_1 and A_2 yielded

$$\left(\frac{R_m}{R_t}\right)\cos(\theta_m) - \frac{\cos(\theta') - M_0}{\sin(\theta')} - \left\{\left(\frac{R_m}{R_t}\right)\sin(\theta_m) - 1\right\}\cot\left\{\cos^{-1}\left(\frac{\cos(\theta')}{1 - M_0\cos(\theta')}\right)\right\} = 0. \tag{4.28}$$

Equation 4.28 contains only one unknown variable, θ', and was solved iteratively to within a convergence of 10^{-6} radians. Equations 4.22 and 4.18 were then used explicitly to determine the remaining required angles θ_0 and θ, respectively.

4.5.3 Shear layer refraction approximation method

The shear layer refraction beamforming algorithm by Brooks and Humphreys (1998) modified the beamformer output to account for the shear layer refraction at each scanning grid point. To save computational resources, the calculated shear layer refraction at the centre microphone due to an acoustic source directly beneath it was computed. This offset value was applied to the entire beamformer output, resulting in a "net shift" of the image in the direction of the flow. This method, compared to the shear layer refraction beamforming algorithm by Brooks and Humphreys (1998) that effectively calculates Equation 4.28 for every point on the scanning grid, showed little difference in the computation of the maximum acoustic source locations. The maximum source location was found to be at the same scanning grid point using both methods.

The difference between θ' and θ_0 is very small for values of θ' close to 90°. By approximating that $\theta' = \theta_0$, then the acoustic path in still air is parallel to the actual acoustic ray path once it has passed through the shear layer, as depicted in Figure 4.13. The offset between the two acoustic rays, δ, corresponds to the net shift of the acoustic source location on the scanning grid.

Using trigonometry and geometric constructions, the following equation was de-

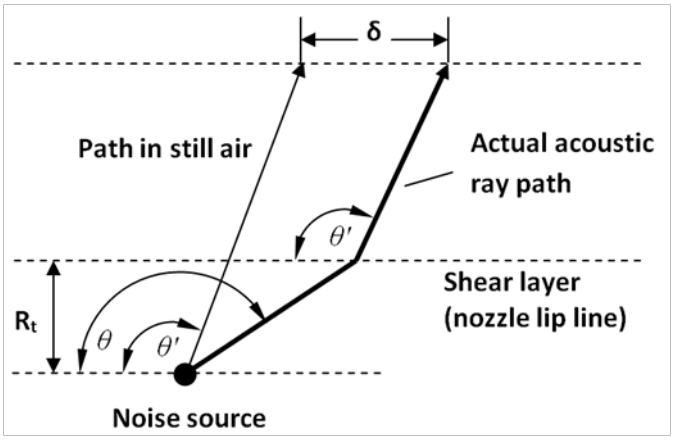

Figure 4.13: Shear layer refraction schematic diagram, showing the net shift of the acoustic source location, δ for θ' equal to θ_0.

rived

$$\delta = R_t \left[\tan(\theta - \frac{\pi}{2}) - \tan(\theta' - \frac{\pi}{2}) \right] \tag{4.29}$$

allowing δ to be solved knowing θ and θ'.

The values of δ were calculated in an iterative manner using Equations 4.28 and 4.29. The convergence value of the iterative scheme was 10^{-6} metres. The equations were used for the flow speeds corresponding to the experiment Reynolds numbers as presented in Table 4.1. For completeness, the corresponding values of θ' - θ_0 are included to support the validity of the assumption that led to the derivation of Equation 4.29. The terms Upstream Limit and Downstream Limit correspond to the locations of the upper and lower bounds of a 180 mm × 180 mm scanning grid, placed 600 mm below the array. The angle between the vertical axis and the scanning grid upper bounds was calculated via trigonometry as 8.3°.

The results in Table 4.1 show that for a Reynolds number of 150,000 (where the greatest shift of the beamformer image occurs), a 3.7 mm shift of the beamforming image from the centre of the scanning grid is required to account for the effect of the shear layer. The upstream and downstream edges of the scanning grid at

Table 4.1: Shift of beamformer image (δ) and θ' - θ_0 due to shear layer refraction for each test case.

Re	Upstream Limit		Directly above (90°)		Downstream Limit	
	δ (mm)	θ' - θ_0 (°)	δ (mm)	θ' - θ_0 (°)	δ (mm)	θ' - θ_0 (°)
50,000	1.25	0.04	1.23	0.00	1.24	0.04
75,000	1.87	0.06	1.85	0.00	1.87	0.06
100,000	2.49	0.08	2.46	0.00	2.49	0.08
125,000	3.11	0.11	3.08	0.00	3.11	0.09
150,000	3.74	0.13	3.70	0.00	3.73	0.11

this Reynolds number require a 3.74 mm and a 3.73 mm shift respectively. The estimated source locations at the extremities of the scanning grid were accurate within 3.74 mm - 3.70 mm = 0.04 mm for the Reynolds number 150,000 case due to shear layer behaviour only. For all Reynolds number cases, the values of θ' - θ_0 are small, showing that the geometric approximation shown in Figure 4.13 has a negligible effect on the beamformer output. For practicality, the entire beamformer image was shifted by the directly above (90°) value for all flow cases.

4.6 Error analysis

An error analysis was performed to determine the accuracy of the beamformer output. This determined the expected error of the beamformer in estimating the acoustic source location in X and Y coordinates. This was considered to be very important; the investigation of a potential acoustic feedback mechanism between two points on or near the airfoil surface relies heavily on an accurate determination of the acoustic source locations.

To perform the positional error analysis, both white and tonal noise were emitted from a single headphone speaker (Apple iPhone 4s headphones). This was achieved by uploading a series of acoustic audio files onto an iPod and playing one of the files (either a tone or white noise) on repeat during the experiment. This provided a small

noise source of approximately 15 mm in diameter. The z-distance was held constant at 600 mm, while the acoustic source location was varied within a horizontal plane using a traverse. The uncertainty of the array output in both X and Y locations were estimated. The coordinate system employed for the placement of the small acoustic source is shown in Figure 4.14. The experimental arrangement is shown in Figure 4.15.

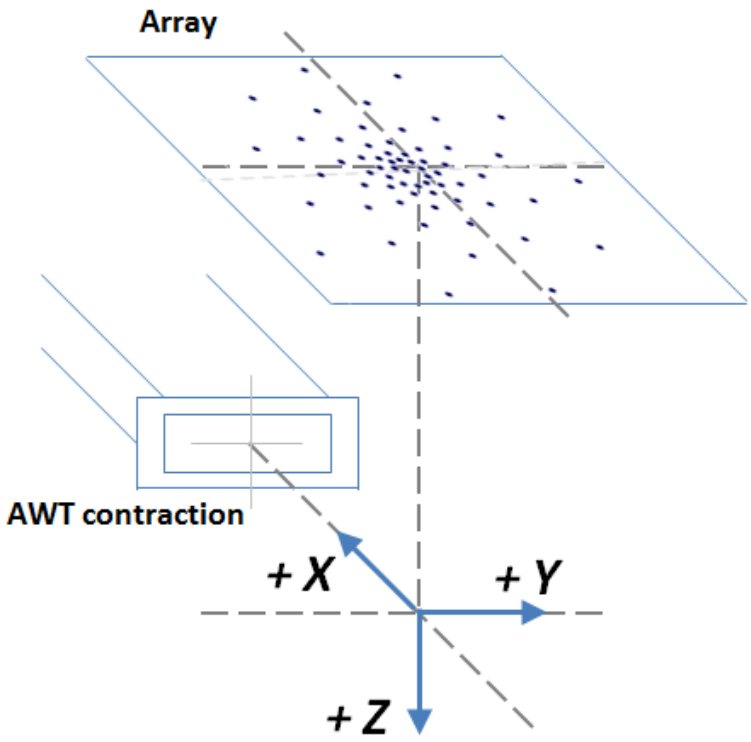

Figure 4.14: Coordinate system employed for the positioning of the small acoustic source.

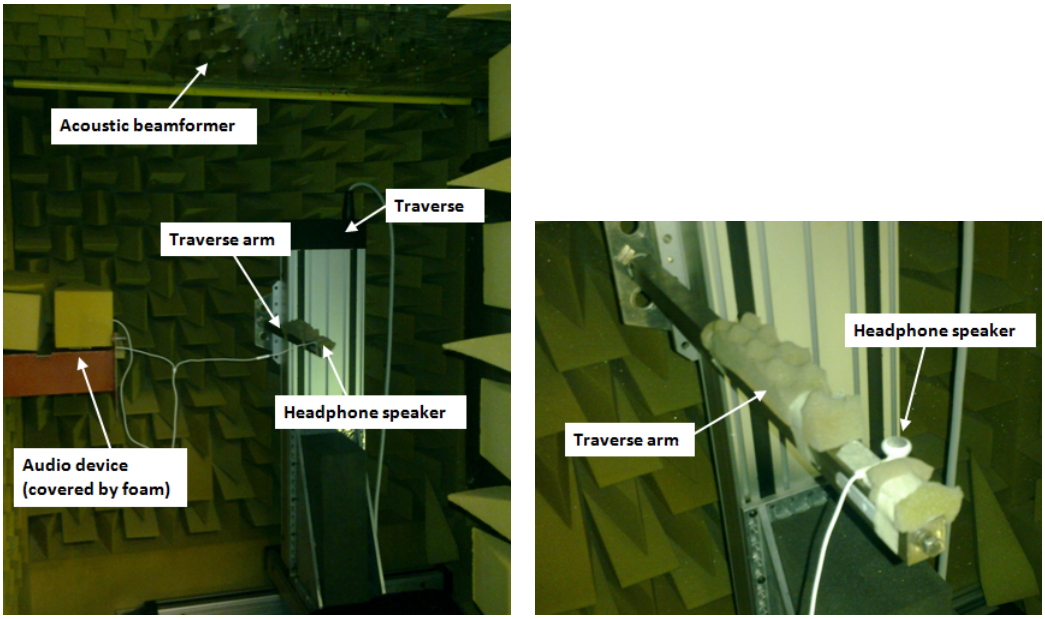

(a) (b)

Figure 4.15: (a) Experimental arrangement for the error analysis of the acoustic beamformer in the AWT. (b) The headphone speaker attached to the traverse arm.

4.6.1 Error calculation method

The source location calculated by the beamformer was taken to be the grid point location on the scanning grid possessing the maximum cross-spectral output. It was assumed that the headphone speaker radiated only in a vertical direction towards the array and that the maximum cross-spectral output location corresponded to the geometric centre of the headphone speaker. The headphone speaker was aligned with the vertical axis by placing a laser alignment device pointing vertically at the speaker location and ensuring that the laser light projected onto the centre of the array centre microphone.

The error of the source location estimation was calculated as the difference between the beamformer location and the true source location of the speaker (located by the traverse). An example of the beamformer error in estimating the acoustic

source location at $X = 0$ mm, $Y = 100$ mm is shown in Figure 4.16. The true source location was $X = 0$ mm, $Y = 100$ mm and the beamformer calculated the maximum cross-spectral location at $X = 9$ mm, $Y = 108$ mm. Thus the beamformer located the acoustic source with an error of 9 mm in the X direction and 8 mm in the Y-direction.

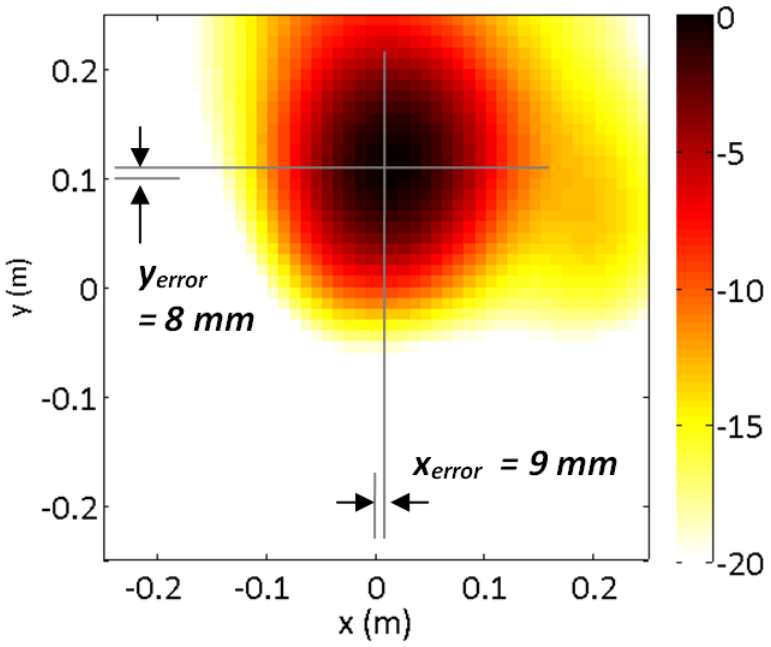

Figure 4.16: Cross-spectral beamformer output at 3325 Hz for an acoustic source located at $X = 0$ mm, $Y = 100$ mm, $Z = 600$ mm. The acoustic pressure (dB) is normalised relative to the maximum cross-spectral value. Lines have been drawn at the identified source location to help identify the location estimation error relative to the true source.

Figure 4.16 shows that the error in the X and Y directions were different. Due to the asymmetric nature of the microphone array about both the X and Y axes, the errors in orthogonal directions were not expected to be equal. Thus, for each source location tested, both the X and Y errors were computed.

Figure 4.17 displays the beamformer output for the acoustic source located at $X =$ -50 mm, $Y = 50$ mm. It was important to see how accurately the beam-

former would locate a source with non-zero X and Y components. The error in the Y-direction was measured as 16 mm, twice the error of a source located at $Y = 100$ mm. It is anticipated that the error increase was due to the inclusion of an X component of the source location. The error in the X direction was 8 mm, thus the total error was calculated as $(X_{error}^2 + Y_{error}^2)^{\frac{1}{2}} = 18$ mm.

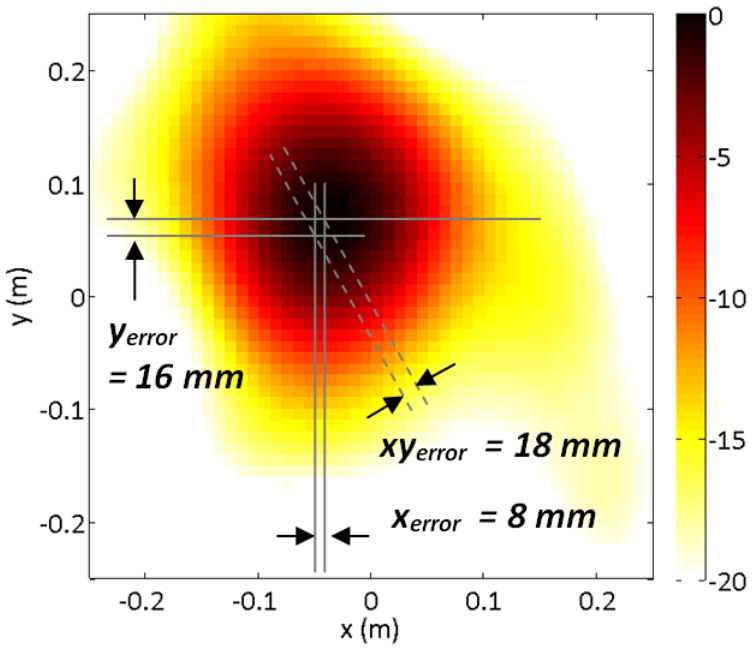

Figure 4.17: Cross-spectral beamformer output at 3325 Hz for an acoustic source located at $X = 50$ mm, $Y = 50$ mm, $Z = 600$ mm. The acoustic pressure (dB) is normalised relative to the maximum cross-spectral value. Lines have been drawn at the identified source location to help identify the location estimation error relative to the true source.

4.6.2 Beamformer error maps

The overall error performance of the beamformer was estimated by emitting a white noise source from the headphone speaker. The beamformer estimated location was calculated for frequencies in 5 Hz increments, between 2 kHz and 5 kHz. The scanning grid was refined to $NX = 100$ (i.e., 101 × 101 scanning grid points) and the scanning grid size was 0.3 m × 0.3 m. This resulted in a spacing of 3 mm between the grid lines. By increasing the scanning grid resolution, the discretisation error of the beamformer map due to the scanning grid was minimised.

The error of the estimated source location was averaged over a 100 Hz bandwidth, so that an X error, Y error and a total error was estimated for 2 kHz to 2.1 kHz, 2.101 kHz to 2.2 kHz and so on, up to 5 kHz. Contour plots of the error magnitude were produced with 30 bands (of 100 Hz bandwidth) and with 17 measurement locations spread independently along the X and Y axes

- $X = 0$ mm with Y = [0, 10:5:60, 70, 80, 100, 120, 150] mm,
- $Y = 0$ mm with X = [10:5:60, 70, 80, 100, 120, 150] mm.

Plots were produced for the X_{error}, Y_{error} and total error for the source location placed along the X and Y axes and are presented in Figures 4.18 through 4.23.

Figure 4.18 shows that along the X-axis of the scanning grid the greatest beamformer X_{error} was 40 mm, located near the scanning grid origin (directly beneath the array centre). Other than at near the scanning grid origin at approximately 3.4 kHz, the X_{error} was less than 25 mm across the entire scanning grid. The values of Y_{error} in Figure 4.19 were less than the values of X_{error} being 20 mm or less, with a maximum located at the scanning grid origin for a frequency of 2.1 kHz. The total error plot along the X-axis, displayed in Figure 4.20, closely resembles the X_{error} plot as the X_{error} values were overall greater than the Y_{error} values.

The X_{error} along the Y-axis displayed in Figure 4.21 was greatest for frequencies between 2 kHz and 2.2 kHz, with a maximum error of 60 mm located at the origin.

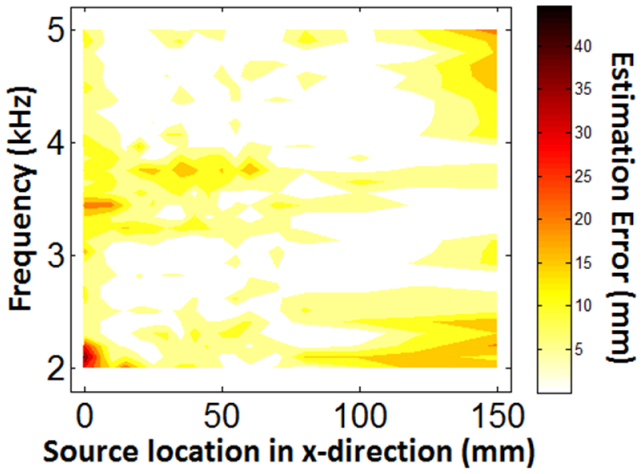

Figure 4.18: X-direction cross-spectral beamformer output error for the white noise acoustic source for various locations in the X-direction.

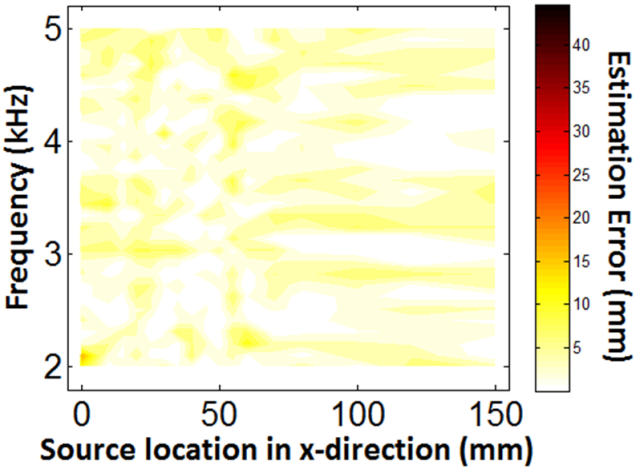

Figure 4.19: Y-direction cross-spectral beamformer output error for the white noise acoustic source for various locations in the X-direction.

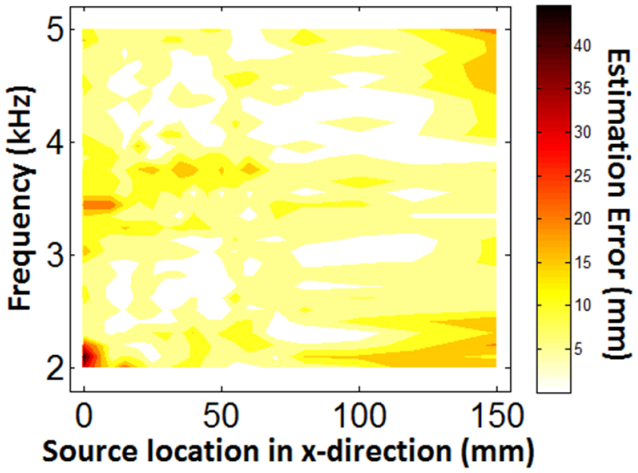

Figure 4.20: Total cross-spectral beamformer output error for the white noise acoustic source for various locations in the X-direction.

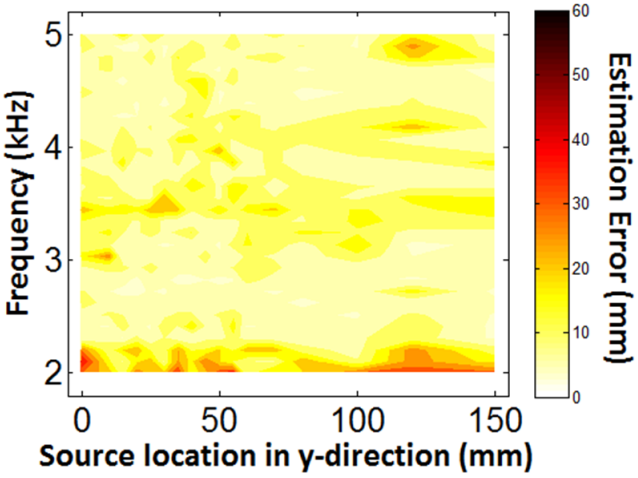

Figure 4.21: X-direction cross-spectral beamformer output error for the white noise acoustic source for various locations in the Y-direction.

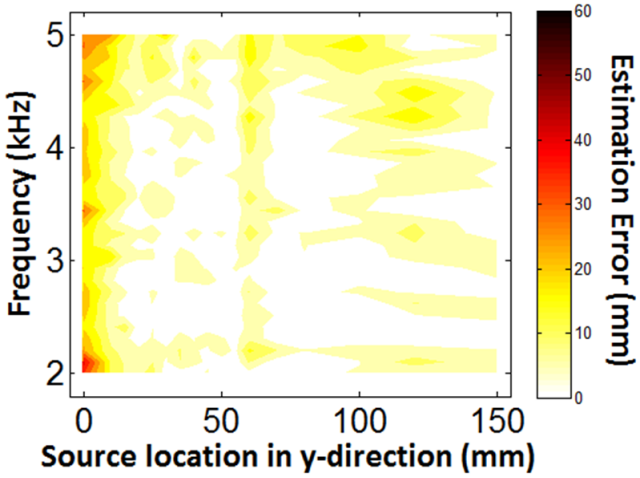

Figure 4.22: Y-direction cross-spectral beamformer output error for the white noise acoustic source for various locations in the Y-direction.

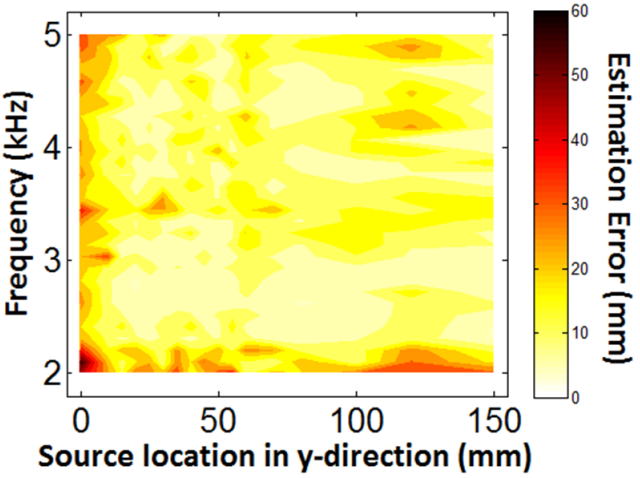

Figure 4.23: Total cross-spectral beamformer output error for the white noise acoustic source for various locations in the Y-direction.

Other local maxima were located at 35 mm at a frequency of 3.5 kHz and at 120 mm at a frequency of 4.8 kHz. The Y_{error} along the Y-axis displayed in Figure 4.22 shows that the greatest error existed at or near the origin, with a maximum magnitude of 50 mm. The errors were significantly less away from the origin.

The beamformer X_{error} was much greater than the Y_{error} on average in the AWT. This may have been due to a stronger standing wave mode between the walls of the AWT in the X-direction as there were no openings or interruptions to the acoustic wave propagation. In the Y-direction, the flow collector may have acted as an opening and thus the standing waves in the Y-direction were not as strong. The effect of standing waves in the AWT is further discussed in Section 4.6.3.

For airfoil tests in the AWT, the Y-distance corresponded to the chordwise direction and the X-distance corresponded to the spanwise direction. It will be shown in Chapter 6 that the Y-component of the noise source location was of greatest importance (i.e., the down/upstream noise location relative to the airfoil trailing edge).

4.6.3 AWT standing waves

There was some concern as to whether the beamformer output was negatively affected by facility effects. The AWT contains some reflective surfaces, being the flow collector near the outlet, the body of the traverse, the flow contraction and the Perspex sheet housing the microphone array. From preliminary tests, the AWT chamber is not anechoic below 200 Hz. The AWT surfaces reflect acoustic waves and it was thought that weak acoustic standing waves may form within the AWT. As discussed in Section 4.6.2, the estimation error of the beamformer varied with frequency and source location. It was unclear as to whether this measurement uncertainty was due to standing wave effects, beamformer measurement errors or a combination of both.

To determine the baseline performance of the beamformer without any reflective

surfaces in the vicinity of noise sources, it was tested in the anechoic chamber at The University of Adelaide. The chamber has dimensions 4.75 m × 3.90 m × 3.94 m and is effectively anechoic for frequencies greater than 100 Hz. The walls are acoustically treated with rock wool wedges and the floor is constructed of a relatively open aluminum lattice. Beneath the lattice, there are thick layers of foam to help minimise reflections. For the beamformer tests, 100 mm thick layers of foam were placed on top of the lattice in areas where acoustic reflections could influence the beamformer output. Figure 4.24 shows the acoustic beamformer placed in the anechoic chamber in its test configuration.

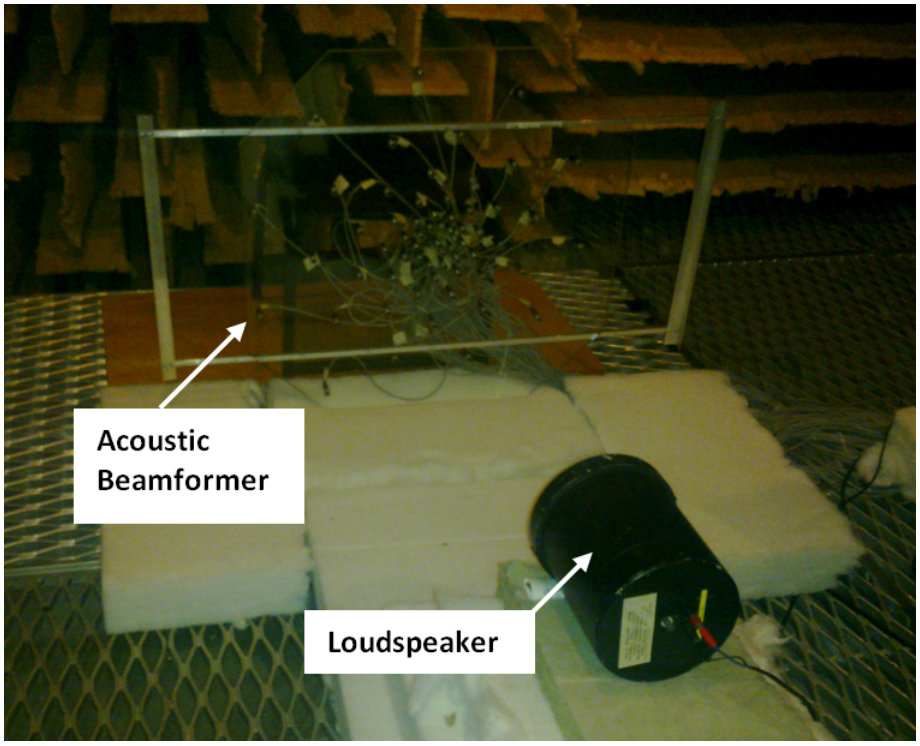

Figure 4.24: The acoustic beamformer placed in the anechoic chamber.

A white noise signal was input into a loudspeaker placed 600 mm from the array in line with the centre microphone. A white noise source was specifically used in this study to see if the beamformer estimations varied with frequency. Figure 4.25 shows

the beamformer output, identifying the maximum acoustic source location for each frequency between 500 Hz and 3 kHz and the measured noise spectrum from the array centre microphone. The beamformer located the loudspeaker centre to within 5 mm of its actual location for frequencies between 1 kHz to 3 kHz. Between approximately 500 Hz and 750 Hz, the beamformer estimated the loudspeaker location to within 10 mm of its actual location.

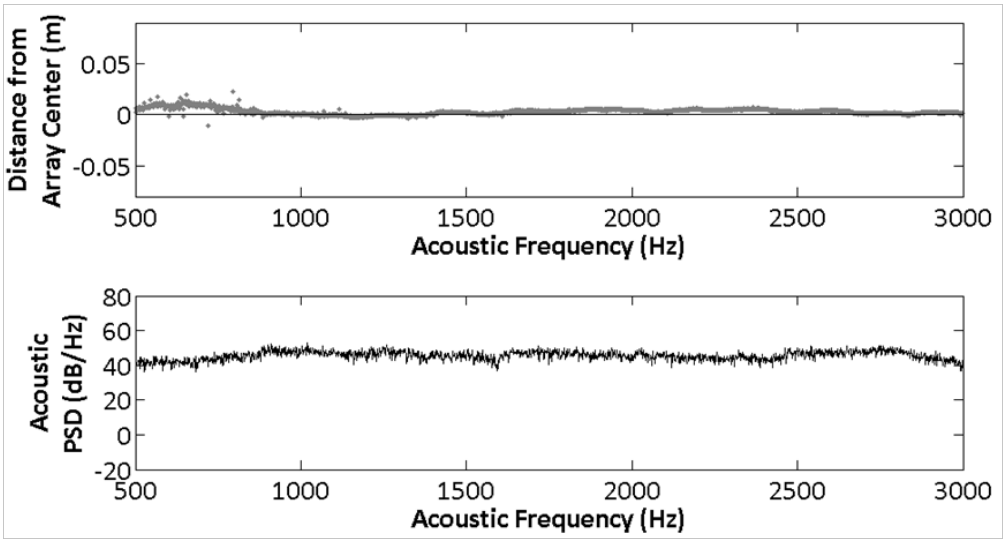

Figure 4.25: Acoustic beamforming estimate of source location and noise spectrum for a white noise source placed 600 mm from the array in line with the centre microphone in the anechoic chamber.

The same loudspeaker was used to project white noise into the AWT and was placed 600 mm directly beneath the centre microphone of the microphone array, pointed upward. Figure 4.26 shows the resulting beamformer output. The mean acoustic spectral density magnitude in this frequency range was 40 dB. The minimum and maximum values within this range were 30 dB and 48 dB respectively. The differences in the measured spectra shown in Figures 4.25 and 4.26 were possibly due to the effects of standing or spurious reflected waves within the AWT.

Figure 4.26 shows that the estimated acoustic source location of the loudspeaker

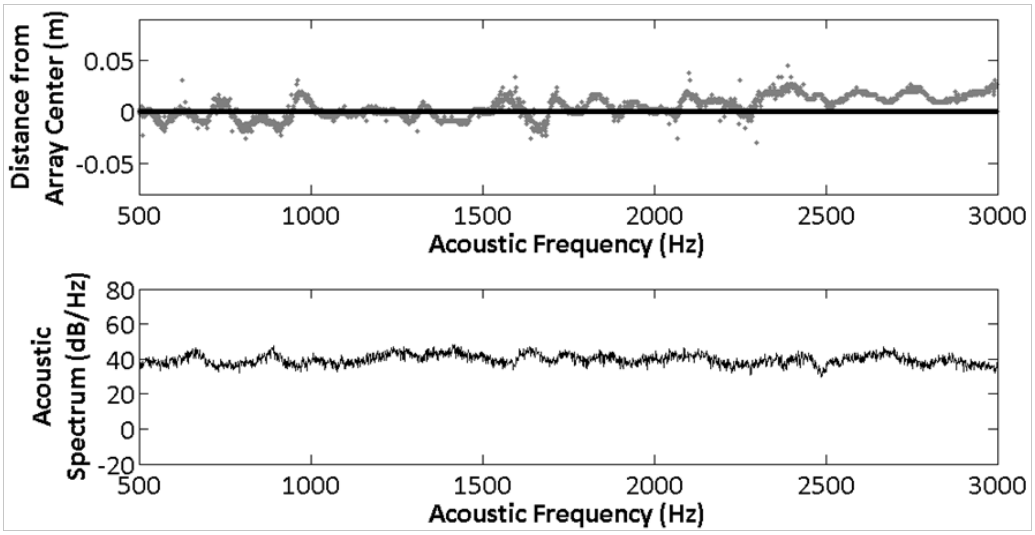

Figure 4.26: Acoustic beamforming estimate of source location and noise spectrum for a white noise source placed 600 mm from the array in line with the centre microphone in the AWT.

varied with frequency, unlike the results obtained in the anechoic chamber shown in Figure 4.25. It was proposed that weak standing waves were formed in the AWT that moved the apparent location of maximum acoustic strength away from the loudspeaker location. The standing waves may have caused a superposition of acoustic energy at a location away from the loudspeaker that was detected by the beamformer.

Table 4.2 provides the mean value and the standard deviation of the loudspeaker location for five equispaced frequency ranges over 500 Hz to 3 kHz for measurements in the AWT and anechoic chamber. The standard deviation of the anechoic chamber results were much lower than the AWT results for all frequencies. The differences in standard deviation values between the AWT and the anechoic chamber measurements show that having some reflective or partially reflective surfaces within a testing facility can affect the ability of an acoustic beamformer to accurately locate acoustic sources.

Table 4.2: Beamformer estimation error for a white noise source in the AWT and the anechoic chamber.

Frequency range (Hz)	AWT		Anechoic chamber	
	Mean value (mm)	Standard deviation (mm)	Mean value (mm)	Standard deviation (mm)
500-999	3.0	9.5	5.8	3.9
1000-1499	2.2	4.8	0.0	1.4
1500-1999	4.2	8.8	3.4	1.5
2000-2499	11.0	9.1	4.3	1.0
2500-2999	15.6	4.9	2.2	1.1

4.7 Summary of beamforming methods

An acoustic beamformer was designed and installed in the AWT for aeroacoustic tests. Sixty-three (63) microphones were arranged in a unique logarithmic spiral configuration, namely the Arcondoulis spiral. The array was located 600 mm above the airfoil location and the centre microphone was aligned with the spanwise centre of the airfoil trailing edge. Preliminary tests using the beamformer revealed that weak standing and/or spurious waves occurred during aeroacoustic tests. An error analysis revealed that the estimation errors of the array were greater in the X-direction as compared to the Y-direction, likely due to standing wave modes in the X-direction.

The effects of shear layer refraction on the beamformer image were taken into account via an approximation method. Using Amiet's (1977) shear layer refraction model, the entire beamformer image is shifted by the amount a wave is refracted directly beneath the array centre microphone. This was shown to be an accurate approximation assuming the noise source of interest is near the centre of the scanning grid.

Chapter 5

Experimental Results

This chapter contains the experimental results obtained in the AWT using the NACA 0012 airfoil arrangement presented in Chapter 3. Analysis of these results provided the measured noise and its source location, the flow field around the airfoil and the coherence between the flow field and acoustic data.

This chapter has been separated into two sections to help differentiate the experimental results pertinent to a potential acoustic feedback mechanism and those related to AWT facility effects on the measured noise. Section 5.1 contains experimentally obtained parameters required to investigate an acoustic feedback mechanism. Section 5.2 presents the influences of facility effects and a boundary layer trip line on the measured tones.

5.1 Acoustic feedback mechanism parameters

This section provides the necessary data to perform an acoustic feedback analysis. The following parameters were obtained via experiment: primary and secondary tones; candidate start and end points of a feedback loop; and convective disturbance velocities. The integration of these parameters into feedback models is presented in Chapter 6.

5.1.1 Primary and secondary tones

This section presents the acoustic results obtained at Re = 50,000, 100,000 and 150,000. To observe the change in measured noise with increasing flow speed, PSDs recorded at Re = 75,000 and 125,000 were presented at $\alpha = 0°$ but not at $\alpha = 1.58°$ and 3.16°. It should be noted that the three aforementioned Reynolds numbers captured all of the unique tonal noise measurements within this range (i.e., the PSDs at Reynolds numbers between those investigated displayed similar characteristics with no more or fewer tones than at the presented Reynolds numbers). At $\alpha = 3.16°$, no tonal noise was recorded for all Reynolds numbers investigated.

Tonal noise measurements were obtained via numerous tests. The primary tone observed for Re = 100,000 and $\alpha = 0°$ was recorded each time with varying atmospheric conditions, ranging from 17° to 32° Celsius. Over twenty measurements of this tone were obtained over this time period, giving a mean of 1426 Hz and a standard deviation of 3.4 Hz. The standard deviation relative to the mean was small, showing that the measurement of the primary tone at Re = 100,000 and $\alpha = 0°$ was repeatable for all atmospheric conditions. This result was indicative of the repeatability of the noise characteristics at other angles of attack and Reynolds numbers. There did not appear to be any significant correlation between tone frequency and temperature.

At $\alpha = 0°$ and $Re \leq 30,000$ no tones and only weak broadband noise were recorded that barely exceeded the background noise. Increasing the flow speed to approximately Re = 40,000 resulted in a significant change in the measured noise and the beginning, so to speak, of the unique low-to-moderate Reynolds number noise characteristics. The broadband noise increased in magnitude due to the increased flow speed but a portion of the broadband noise across a specific frequency range increased disproportionately, producing a "broadband hump". Increasing the flow speed to Re = 50,000 resulted in the emergence of three discrete tones from the broadband hump. The strongest of the tones, namely the primary tone, possessed a similar frequency as the peak of the broadband hump (also the centre frequency

of the broadband hump). This broadband hump was observed to vary with flow speed between approximately 200 Hz and 800 Hz, thus possessing a 600 Hz range. The other two tones, both weaker in magnitude than the primary, were measured in the same frequency range as the broadband hump, one at a lower frequency than the primary tone, the other at a higher frequency. The change in measured noise from Re = 30,000 to 40,000 can be observed in Figure 5.1 and the PSD recorded at Re = 50,000 is presented in Figure 5.2a.

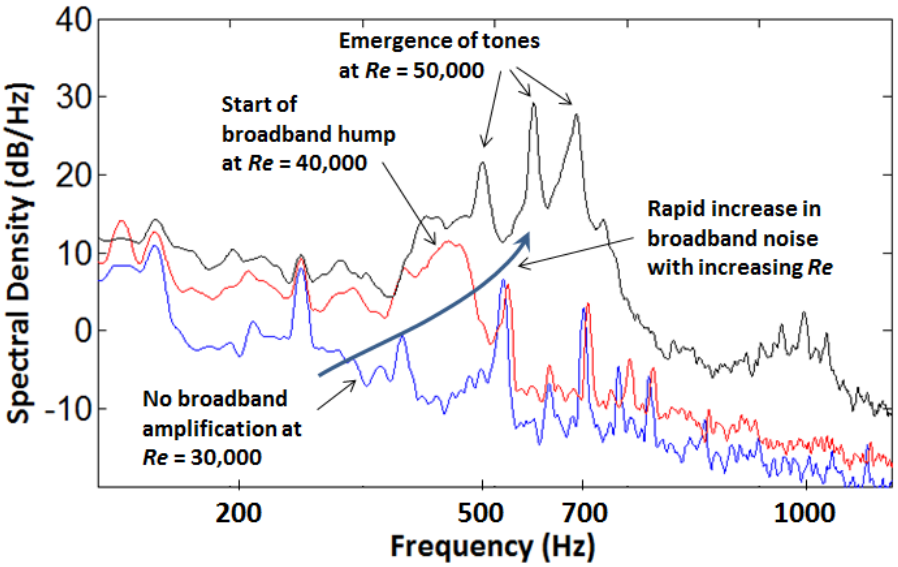

Figure 5.1: PSDs recorded at $\alpha = 0°$ and Re = 30,000 (blue), 40,000 (red) and 50,000 (black), identifying the beginning of a broadband hump and the emergence of tones with increasing Reynolds number.

Increasing Re to 75,000 caused these tones to become more narrowband and increase in both magnitude and frequency. The centre frequency of the broadband hump increased to 1500 Hz, measured between 500 Hz to 2 kHz. This change in measured noise can be observed by comparing Figures 5.2a and 5.2b that present Re = 50,000 and 75,000 respectively. At Re = 100,000, a second broadband hump with a superimposed tone was observed. This broadband hump was centred at

approximately 2.5 kHz, as shown in Figure 5.2c. This broadband contribution corresponded to the primary harmonic of the flow induced tonal and broadband noise. It was evident from these PSDs that the increase in Reynolds number contributed to the higher frequency noise, as there was negligible noise at frequencies greater than 2 kHz at $Re = 50{,}000$. From the Reynolds numbers investigated, $Re = 100{,}000$ possessed the strongest tonal magnitudes. Nash et al. (1998) predicted that a NACA 0012 airfoil at $\alpha = 0°$ should present maximum tonal amplitudes at $Re \approx 110,000$ (observed from Figure 2.5). That prediction closely matches the experimental data acquired in this study.

The results at $Re = 100{,}000$ possess similarities with a spectral density plot of Arbey and Bataille (1983). They investigated a NACA 0012 airfoil via experiment at $\alpha = 0°$ and flow speeds between approximately 20 to 35 m/s. Only one of their flow cases was comparable to the Re range investigated in this research. Arbey and Bataille (1983) used an 80 mm chord airfoil at $\alpha = 0°$ and a 20.2 m/s flow speed. Assuming standard atmospheric conditions, this corresponds to $Re = 107{,}000$. They detected seven tones, between approximately 750 Hz to 1715 Hz. Their primary tone was the third lowest frequency tone at approximately 1070 Hz. The two strongest secondary tones were those adjacent to the primary tone (the second lowest and fourth lowest frequency tones). The noise characteristic of the two strongest secondary tones being the tone either side of the primary tone was in agreement with the results of this current study. The strongest secondary tones were 12 dB weaker than the primary. In the present work, the secondary tones were approximately 20 dB weaker than the primary tone.

The four weakest tones (at the lowest frequency and the three highest frequencies) measured by Arbey and Bataille (1983) possessed much smaller magnitudes than the primary and stronger secondary tones. The strongest of these four tones was 23 dB less than the primary tone and 12 dB less than the strongest secondary tones. By observing Figure 5.2c, the only measured noise approximately 20 dB less than the primary tone magnitude were the secondary tones. Thus it was observed

that Arbey and Bataille (1983) recorded stronger secondary tones relative to the primary tone than in the present research.

Increasing Re to 125,000 and 150,000 produced higher frequency tones that can be observed by comparing Figures 5.2d and 5.2e respectively. At Re = 125,000, the PSD appeared similar to Re = 100,000 with a small decrease in primary tone magnitude but little change in secondary tone magnitudes. At Re = 150,000, the secondary tones weakened by approximately 5 dB relative to Re = 125,000 and only the primary tone possessed a distinct tone above the broadband hump. At this higher flow speed relative to the other Reynolds numbers investigated, there was a significant increase in the broadband noise contribution. This caused the higher frequency secondary tones to possess a smaller amplitude relative to the broadband noise. There were an increased number of tones present in the measured spectrum at Re = 150,000 than at Re = 125,000.

The PSDs recorded at $\alpha = 1.58°$, shown in Figure 5.3, shared similarities to $\alpha = 0°$, up to and including Re = 125,000. The primary and secondary tone frequencies increased slightly and the number of secondary tones at each Reynolds number was the same as $\alpha = 0°$. This suggests that increasing α to 1.58° had only a small effect on any tonal noise generation mechanisms, for such a Reynolds number range and airfoil profile. Comparing Re = 150,000 to 100,000, the primary tone was more narrowband and possessed a smaller magnitude, and the secondary tones were much smaller in magnitude. Increasing the Reynolds number and/or the angle of attack (from $\alpha = 0°$ to 1.58°) caused the primary tone frequency to increase. The increase in primary tone frequency at $\alpha = 0°$ with respect to flow speed followed the $U^{1.5}$ prediction presented by Paterson et al. (1973) and Arbey and Bataille (1983). The ratio of the primary tone frequency between $\alpha = 0°$ to 1.58° with respect to Reynolds number was not constant, nor did there exist a trend with increasing Reynolds number. This showed that increases in the primary tone frequency were dependent on both the Reynolds number and angle of attack, not just one of those parameters alone.

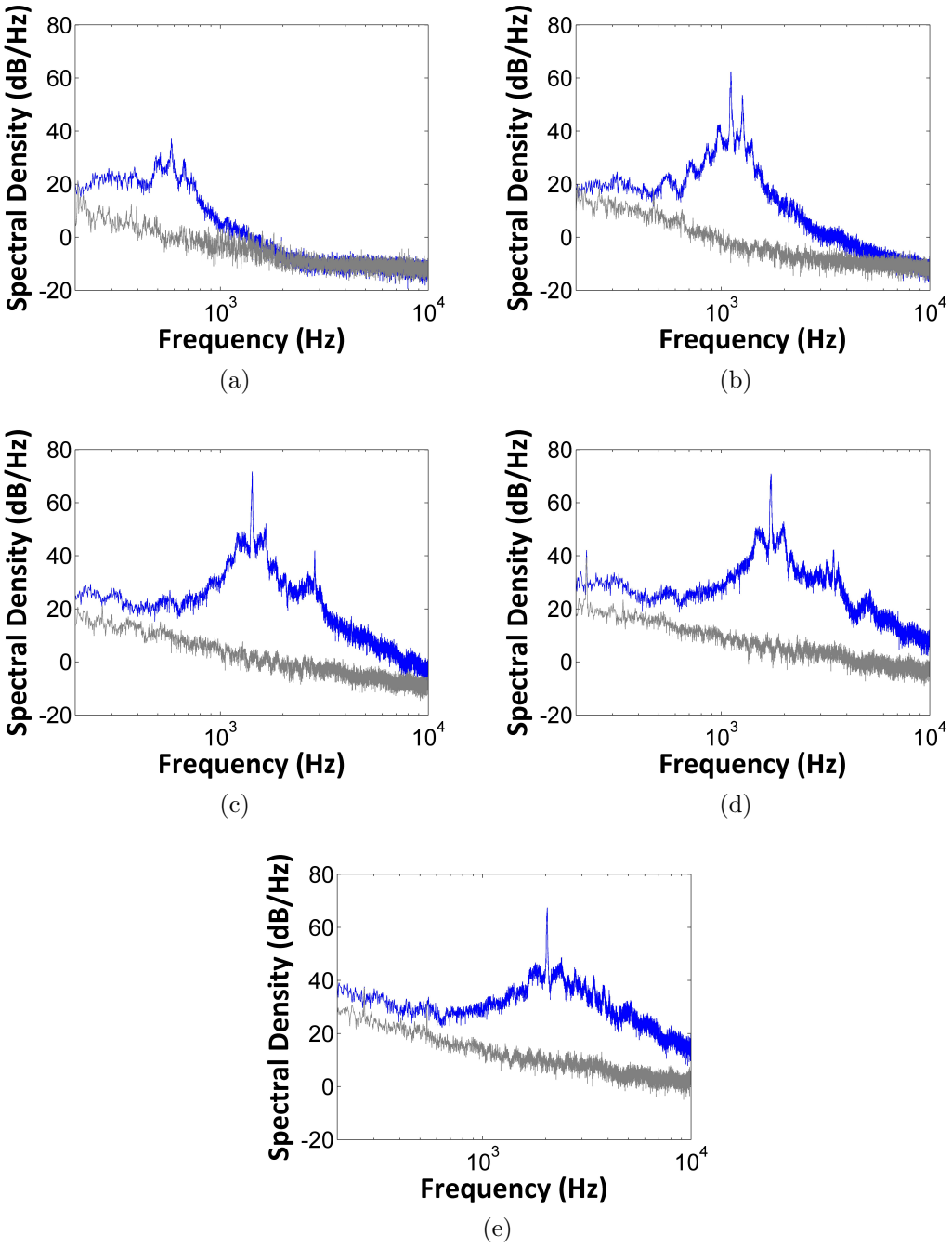

Figure 5.2: PSDs at $\alpha = 0°$ and $Re =$ (a) 50,000, (b) 75,000, (c) 100,000, (d) 125,000 and (e) 150,000. The blue and grey lines represent the NACA 0012 airfoil and the background noise with flow respectively.

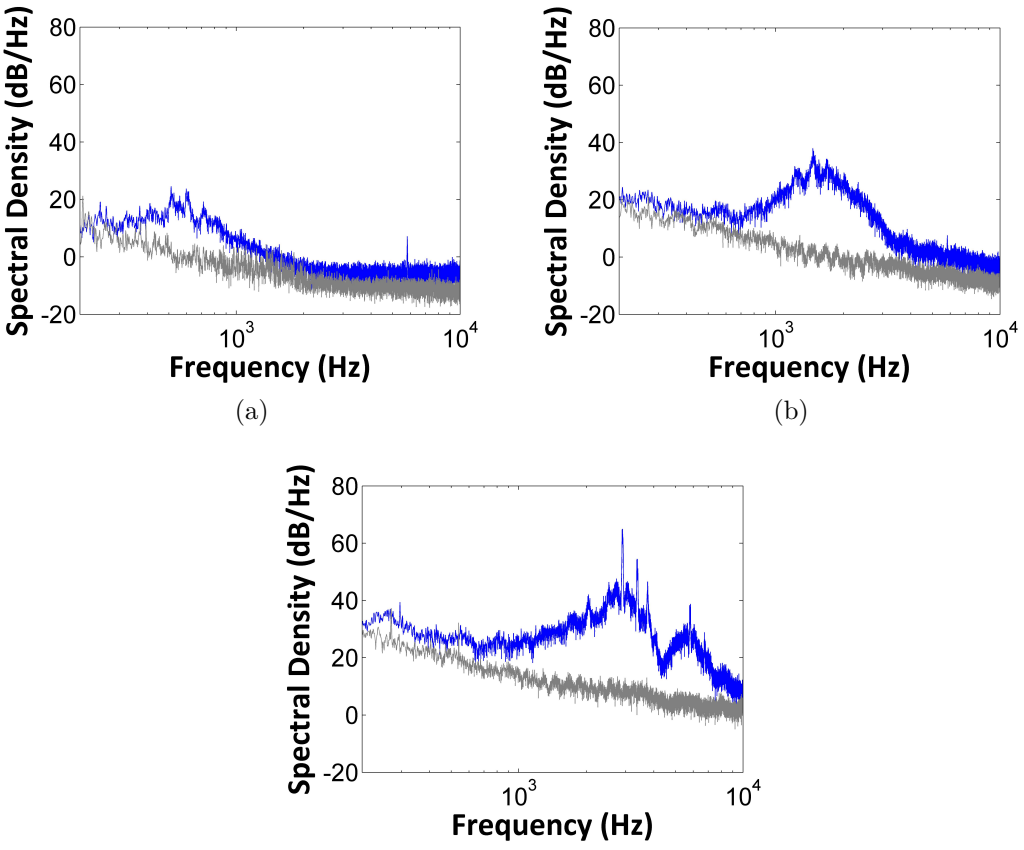

Figure 5.3: PSDs at $\alpha = 1.58°$ and Re = (a) 50,000, (b) 100,000 and (c) 150,000. The blue and grey lines represent the NACA 0012 airfoil and the background noise with flow respectively.

Table 5.1: Primary tone frequencies for $\alpha = 0°$ and ±1.58°.

Re	Primary Tone Frequency (Hz)	
	0°	±1.58°
50,000	589	607
100,000	1426	1463
150,000	2050	2898

Table 5.2: Secondary tone frequencies for $\alpha = 0°$ and ±1.58°.

Re	Secondary Tone Frequencies (Hz)	
	0°	±1.58°
50,000	505, 680, 756	517, 713
100,000	1233, 1640	1236, 1701, 1862, 2035
150,000	1738, 2395, 2780, 3108	2047, 2523, 2728, 3055, 3378, 3754, 4050

Tables 5.1 and 5.2 list the primary and secondary tones at $\alpha = 0°$ and 1.58° respectively. Only the tones recorded at $Re = 50{,}000$, 100,000 and 150,000 are listed, as only they were considered for tonal noise mechanism analysis in the following chapter. There were no obvious trends in the number of tones and their magnitude with respect to Reynolds number and angle of attack. At $Re = 50{,}000$, 150,000 and $\alpha = 0°$, there existed three secondary tones whereas at $Re = 100{,}000$ and $\alpha = 0°$ there existed only two secondary tones. The results also indicate that for the same Reynolds number, increasing $\alpha = 0°$ to 1.58° produces a different number of secondary tones.

The differences in the measured tone frequencies for a given flow condition were calculated and tabulated in Table 5.3. To explain how these values were calculated,

consider Re = 100,000 and $\alpha = 0°$: the tones were 1233 Hz, 1426 Hz and 1640 Hz. The differences in the measured tones were 1426 Hz - 1233 Hz = 193 Hz and 1640 Hz - 1426 Hz = 214 Hz; these values are presented in Table 5.3 in their appropriate cell. The number of entries per cell in Table 5.3 was the number of measured tones minus one. The standard deviation between the differences per Reynolds number was included to show the magnitude of the differences and to assist in the comparison between $\alpha = 0°$ and $\pm 1.58°$. At $\alpha = 0°$ the tones were relatively equispaced, as can be observed from the low standard deviation between the tone frequency differences. With the exception of Re = 50,000, the standard deviations for $\alpha = 1.58°$ were much greater than at $\alpha = 0°$.

Arbey and Bataille (1983) predicted that tones generated by their acoustic feedback mechanism should be equispaced at $\alpha = 0°$. At Re = 107,000 their tones were spaced apart by an average of approximately 160 Hz, with a standard deviation of 23 Hz. It should be noted that they did not perform any experiments at non-zero angle of attack flow conditions and the accuracy of their feedback model at non-zero angles of attack is discussed further in the following chapter. Based on the significant differences in the $\alpha = 0°$ and $\pm 1.58°$ values in Table 5.3, it is possible that Arbey and Bataille's (1983) explanation for equispaced tone frequencies at $\alpha = 0°$ is not adequate at non-zero angles of attack.

The noise measurements recorded at $\alpha = 3.16°$ differed significantly from $\alpha = 0°$ and 1.58°. Across Re = 50,000 to 150,000, no distinct tonal behaviour was detected. At Re = 50,000, the broadband hump observed in the PSD barely exceeded the background noise, as observed in Figure 5.4. The broadband hump frequency range and magnitude increased with Re. By observation of Figure 5.4c, the broadband noise distribution resembled the noise observed during the commencement of tonal noise production, similar to $Re \approx 40,000$ at $\alpha = 0°$. It was hypothesised that at higher Reynolds numbers for this angle of attack, the small peak centred at approximately 3 kHz would increase in magnitude with increasing flow speed, from which tones would emerge, based on the acoustic spectra obtained at 4° and 4.2° by

Table 5.3: Difference between tone frequencies (Hz), for $\alpha = 0°$ and ±1.58°. The standard deviations between the difference values are presented in brackets.

Re	Difference between tone frequencies (Hz)			
	0°	Standard Deviation	±1.58°	Standard Deviation
50,000	84, 91, 76	(7.5)	90, 106	(11.3)
100,000	193, 214	(17.7)	227, 238, 161, 173	(38.4)
150,000	312, 345, 385	(36.6)	476, 205, 170, 157, 323, 376, 296	(117.1)

Chong and Joseph (2009) and Kingan and Pearse (2009) respectively. Unfortunately, the limitations of the maximum AWT flow speed prevented consistent measurements at $Re > 150,000$. According to Nash et. al (1998), for a NACA 0012 airfoil, tones should be present at this angle of attack at 80,000 ≤ Re ≤ 900,000. While this present work disagrees with the lower Reynolds number limit of 80,000, it is highly likely that tones would become present at some Reynolds number > 150,000.

5.1.2 Ladder structure

To evaluate the behavioural change of the measured noise with flow speed, the AWT was operated at maximum flow speed capacity, being 35.4 m/s. Noise measurements were obtained in the same manner as the previous section, but the DAQ was recording throughout the entire experiment, with the addition of a hot-wire probe at the contraction outlet to measure flow speed. The AWT fan was turned off, causing the contraction outlet flow speed to slowly decrease non-linearly with time. At the instant the fan was turned off, the measured Reynolds number was 157,000. Over a period of approximately 100 seconds, the contraction outlet flow speed decreased to zero. These tests were performed at $\alpha = 0°$ and 1.58°.

Continuous changes of the tonal frequencies, magnitudes and number of tones

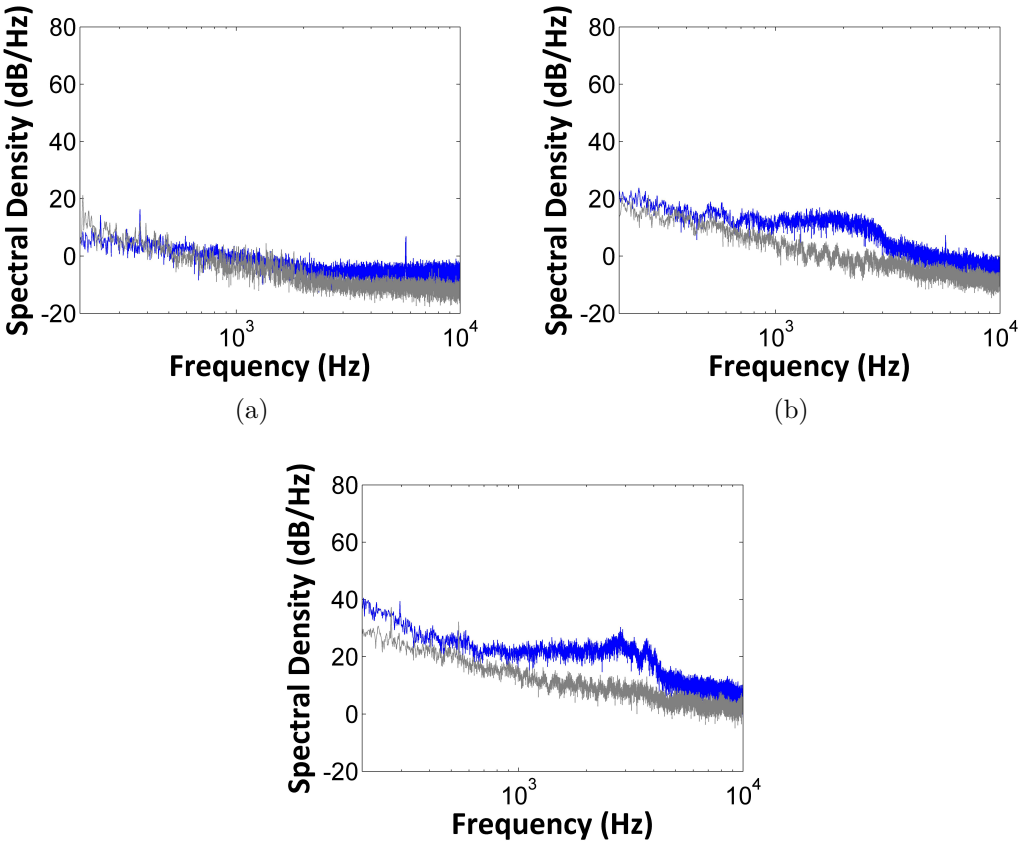

Figure 5.4: PSDs at $\alpha = 3.16°$ and Re = (a) 50,000, (b) 100,000 and (c) 150,000. The blue and grey lines represent the NACA 0012 airfoil and the background noise with flow respectively.

with respect to Reynolds number were observed and provided deeper insight into the development of the tones with Reynolds number. The data are presented in a spectrogram plots shown in Figure 5.5 for $\alpha = 1.58°$. Note that the x-axis representing Re is non-linear. This is due to the non-linear decrease in AWT fan speed with time during the measurements.

The results obtained at $\alpha = 1.58°$ are presented prior to these for $\alpha = 0°$, as some critical features are more obvious at this angle of attack and thus helped explain

the observed behaviour at $\alpha = 0°$. The spectrogram plot displayed in Figure 5.5 reveals the ladder structure measured at $\alpha = 1.58°$. At 100,000 $\leq Re \leq$ 120,000, there exists a primary tone, clearly greater in magnitude than the secondary tones. Above $Re \approx 125,000$, the secondary tone with the highest frequency increased in magnitude, surpassing the previous primary tone magnitude, making it the "new" primary tone at this Reynolds number. Further increases in Re caused the secondary tone magnitudes to increase, none of which surpassed the primary tone, even up to the AWT flow speed limit (Re = 157,000). The transition of a secondary tone, sufficiently increasing in magnitude to surpass the "previous" primary tone and thus causing an apparent jump in primary tone frequency, was what formed a "ladder structure". This explained the sudden change in primary tone frequency. A new tone at a higher frequency did not emerge at a higher flow speed; that tone was recorded at lower flow speeds as a secondary tone and gained magnitude with increased flow speed, overtaking the previous primary tone. In fact, if all of the tones were simply regarded as tones without the labelling of primary and secondary, the observed behaviour was one tone increasing in magnitude while the other diminished. To assist further visualisation of a ladder structure jump, an enlargement of a portion of Figure 5.5 is provided in Figure 5.6 with key features labelled.

The data for $\alpha = 0°$ were interpreted with a clearer understanding of the ladder structure process after the analysis of the $\alpha = 1.58°$ results. From Figure 5.7, which shows the results for $\alpha = 0°$, the tonal noise magnitudes were diminished at the maximum Reynolds number. At $Re \geq 150,000$, some weaker magnitude tones become apparent. From the observed ladder structure behaviour in Figure 5.5, it was most likely that these weaker tones marked the initiation of a ladder structure jump from the lower Reynolds number tones. Unfortunately higher Reynolds numbers were not able to be achieved to verify this prediction experimentally. Interestingly though, the peak tonal noise magnitudes occurred at $Re \leq 150,000$ and the next ladder step did not possess strong tone magnitudes as observed in Figure 5.5 (i.e., the transition from a secondary tone into the new primary tone was not obvious).

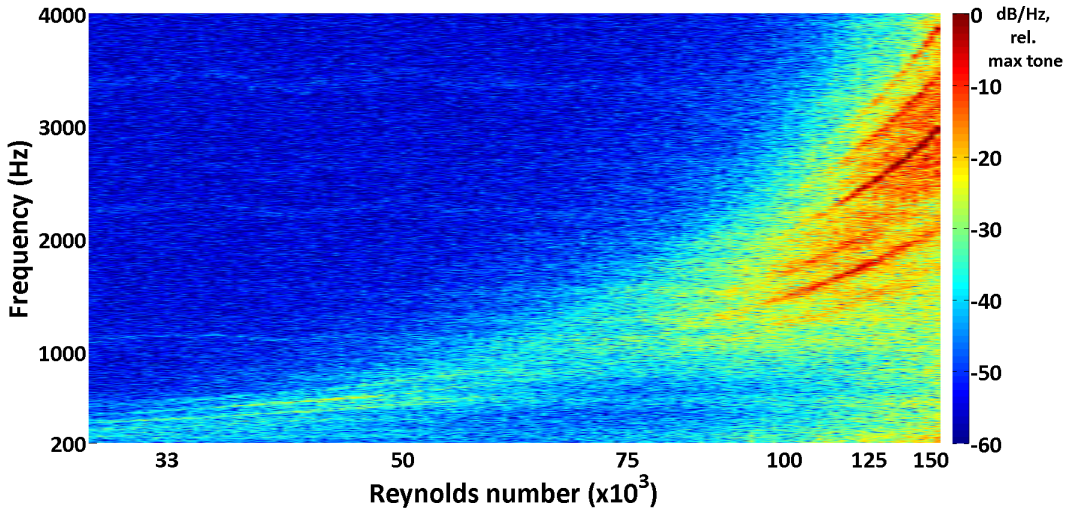

Figure 5.5: Self-noise spectrogram at $\alpha = 1.58°$ and $Re \approx 30,000$ to 157,000.

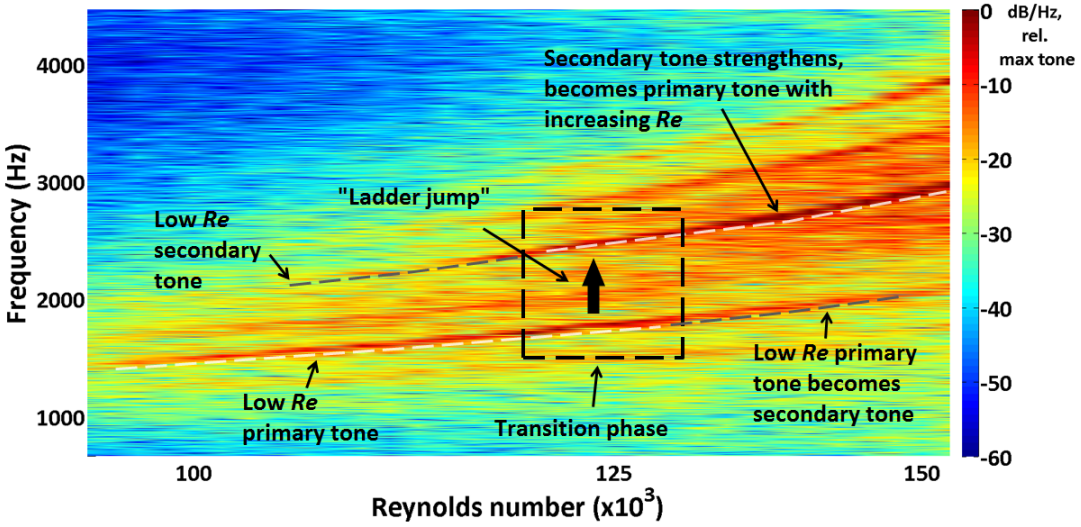

Figure 5.6: Enlargement of Figure 5.5, identifying key features to assist in the visualisation of a ladder structure jump.

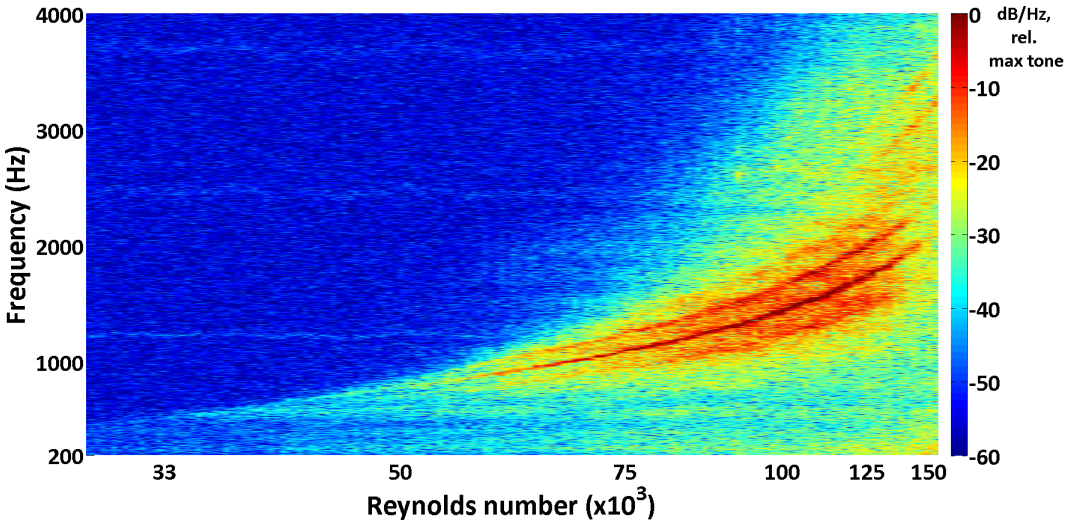

Figure 5.7: Self-noise spectrogram at $\alpha = 0°$ and $Re \approx 30,000$ to 157,000.

To quantify the behaviour observed in Figures 5.5 and 5.7, the primary tone frequencies were plotted against flow speed U as shown in Figure 5.8. Another data set was included, being $f = K \times U^{0.85}$, where $K = 101$ was chosen to best fit the tone frequencies. The 0.85 power relationship of frequency with flow speed was documented by Arbey and Bataille (1983), who showed that the primary tone frequency follows a $U^{0.85}$ dependency, but at a certain Reynolds number, the frequency suddenly increased forming a new $U^{0.85}$ dependency and thus the ladder structure. The primary tones at $\alpha = 1.58°$ demonstrated two steps of the ladder structure, as observed previously in Figure 5.5. The tones measured at $Re = 50{,}000$ to 100,000 constituted the first ladder step and the tones at $Re = 125{,}000$ and 150,000 the second step. Over a range of Reynolds numbers and angles of attack, the frequency dependency eventually fitted a $U^{1.5}$ curve, also measured by Paterson et al.(1973) and Arbey and Bataille (1983). The frequencies at $\alpha = 0°$ only fitted a single $U^{0.85}$ curve, because the Reynolds number was insufficient to see the next $U^{0.85}$ dependency. A more comprehensive data set from sources other than Arbey and Bataille (1983) was not available in this Reynolds number range.

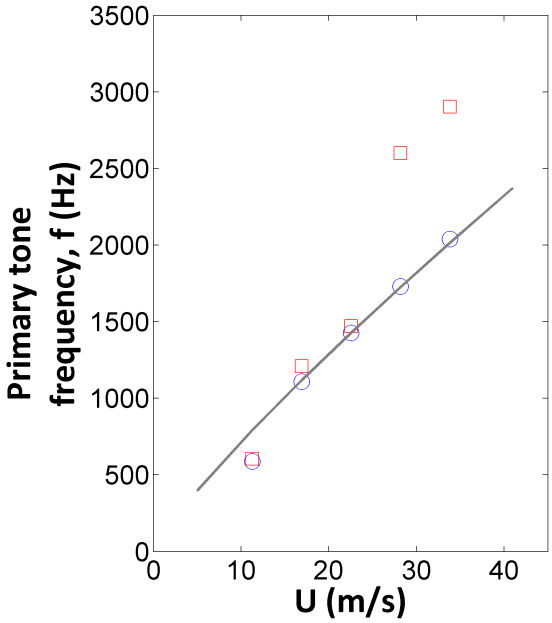

Figure 5.8: Measured primary tones at $\alpha = 0°$ (○) and 1.58° (□). Values of $101 \times U^{0.85}$ were added to fit the measured tones at $\alpha = 0°$.

5.1.2.1 Tonal noise envelope

All of the primary tones listed in Table 5.1 are presented in Figure 5.9, which also displays the tonal envelope predicted by Nash et al. (1998). This plot shows an extension of the data gathered by Nash et al. (1998) and presented in Figure 2.5, by including the data of the present study.

The data from the present study provided a reasonable fit with the tonal envelope in the region of $\alpha = 0°$ to 3.16° and Re = 20,000 to 200,000. The left side of the envelope suggests that for a smaller angle of attack, tones should occur at a lower Reynolds number (i.e., the left hand side of the envelope possesses a positive slope on a chart with Reynolds number as the x-axis and angle of attack on the y-axis). The primary tones recorded in this research showed that this was partially the case. Weak tones were detected at approximately Re = 40,000 for both $\alpha = 0°$ and 1.58°;

while tones were not detected at a lower Reynolds number at $\alpha = 0°$ than for $\alpha = 1.58°$. Nash et al.'s (1998) predicted envelope cut the x-axis (i.e., where the lower tonal limit existed for $\alpha = 0°$) at $Re = 40{,}000$, consistent with the present work. Their line of maximum tonal amplitude provided reasonable agreement with the present work at $\alpha = 0°$. The present work showed that the maximum primary tone magnitude was measured at $Re = 100{,}000$, in agreement with the Nash et al. (1998) prediction. The maximum tonal amplitudes at $\alpha = 1.58°$ and $3.16°$ cannot be compared, as these may have occurred at $Re > 157,000$.

At $\alpha = 3.16°$ tones were not recorded for $Re \leq 150,000$ and weak tones became apparent at the AWT limit of $Re \approx 157,000$. According to the predicted envelope of Nash et al. (1998), tones should have been measured for $Re \geq 80,000$. Nash et al. (1998) displayed insufficient data in this flow range to observe tonal behaviour in detail. To help clarify the comparisons between the present work and Nash et al. (1998), without speculation of tonal behaviour at higher angles of attack and Reynolds numbers, Figure 5.10 was provided.

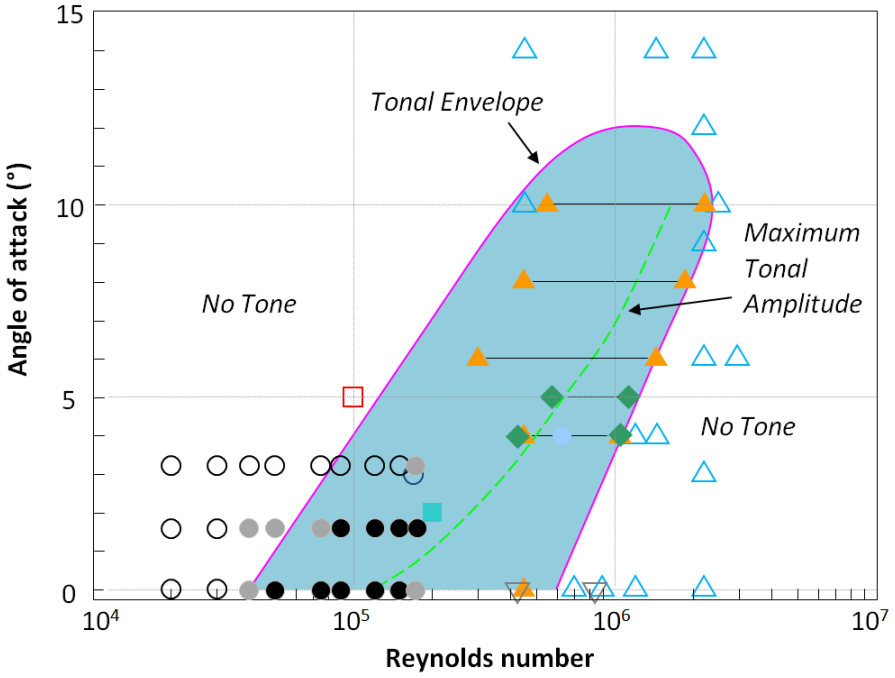

Figure 5.9: Pattern showing where tonal noise is likely to occur for a NACA 0012 airfoil (adapted from Lowson et al., 1994). Black filled markers represent that a tone was present, grey filled markers represent that a weak tone was present and all unfilled markers represent that a tone was not present. Data sources: ○ ● ● (present study), △ ▲ (Paterson et al., 1973), ▽ (Arbey and Bataille, 1983), ■ □ (Desquesnes et al., 2007), ◆ (Lowson et al., 1994). The tonal envelope and the maximum tonal amplitude lines are from Lowson et al. (1994).

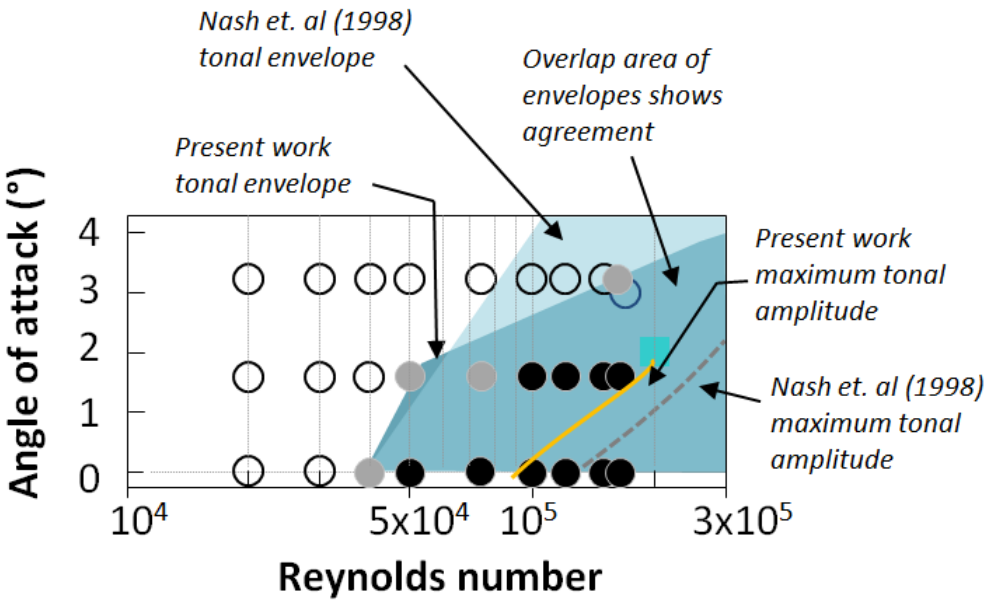

Figure 5.10: Tonal envelope, zoom-in of other tonal envelope plot, but with more present work data and including the tonal envelope based on obtained data from experiment. Black filled markers represent a strong tone, grey markers represent a weak tone, unfilled markers represent no tone. Data sources: ■ (Desquesnes et al., 2007).

5.1.3 Maximum acoustic source location

The acoustic beamformer was used to determine the Maximum Acoustic Source Location (MASL) of the airfoil self-noise for varying angles of attack and Reynolds numbers in the AWT. Understanding and quantifying this location was considered important, as it corresponds to the initiation point(s) of some of the proposed feedback loops discussed in the Literature Review. As discussed previously in Section 4.6.3, the ability of the acoustic beamformer to accurately locate a source in the AWT was affected by standing waves and was frequency dependent. This was taken into account when interpreting the beamformer output when the MASL was measured over a range of beamforming frequencies.

Figures 5.11 and 5.12 present the MASL and PSD for Re = 50,000, 100,000 & 150,000 and $\alpha = 0°$ and 1.58° respectively. The MASL values are presented in 2 Hz increments as empty red circles. The average of the MASL values over 100 Hz bands are displayed as dotted blue lines. At the three different Reynolds numbers, tones and broadband humps were generated at different frequencies and the PSDs are significantly different, yet the MASL patterns with respect to frequency are similar. The patterns are more defined (data less scattered) for frequencies possessing greater signal-to-noise ratios. The pattern also strongly resembles the pattern recorded with a white noise source in the AWT (shown in Figure 4.26) providing evidence that the MASL values were dominated by standing wave behaviour or other AWT facility effects.

The actual MASL values of airfoil self-noise were difficult to interpret. By comparing the white noise source tests performed in the anechoic chamber and the AWT (Figures 4.25 and 4.26), the standing wave pattern produced in the AWT could be observed and it served as a transfer function for beamformer outputs in the AWT. It was possible to do this, since the data recorded in the anechoic chamber possessed MASL values at or near $x = 0$. It was thus assumed that the pattern in the AWT was always observed for any noise source located 600 mm from the array with adequate signal-to-noise ratio. Recognising that this pattern would always occur

indicated consistency, yet it did not help estimate the true MASL values of an airfoil. However, the relative shift of the entire pattern in the x-direction (chordwise) direction, relative to the white noise pattern in Figure 4.26, was assumed to be indicative of the true x-direction shift of the MASL. By use of this assumption and via close observation of Figures 5.11 and 5.12, the MASL values of the airfoil for Re = 50,000, 100,000 and 150,000 at both $\alpha = 0°$ and 1.58° were deduced to be at the trailing edge, $x/C = 0$.

Figure 5.13 displays the MASL and PSD at Re = 150,000 and $\alpha = 3.16°$ that was an indicative result of all Reynolds numbers investigated at this angle of attack, on both the pressure and suction surfaces. The broadband noise possesses a low signal-to-noise ratio and the MASL values are scattered about the trailing edge line. These MASL values were as expected for broadband noise generating mechanisms produced at the airfoil trailing edge.

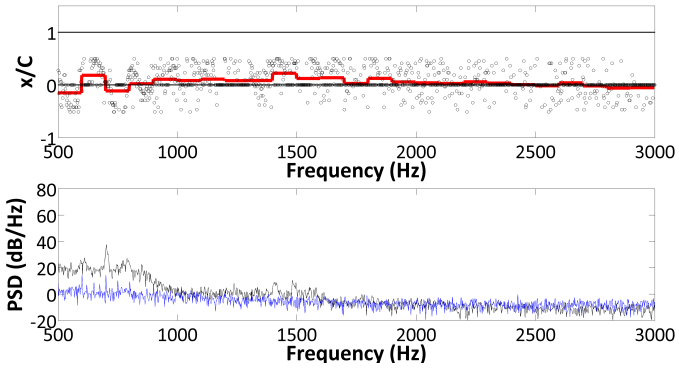

(a)

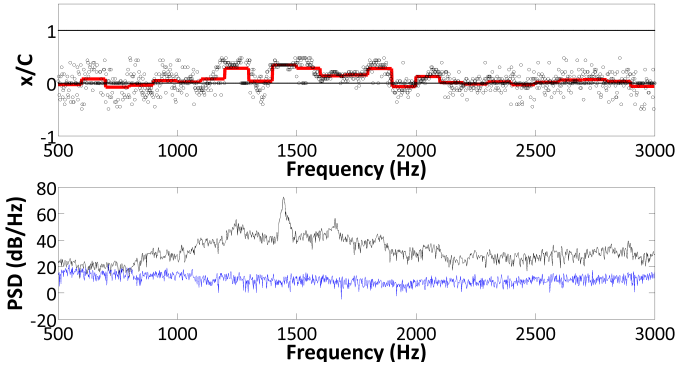

(b)

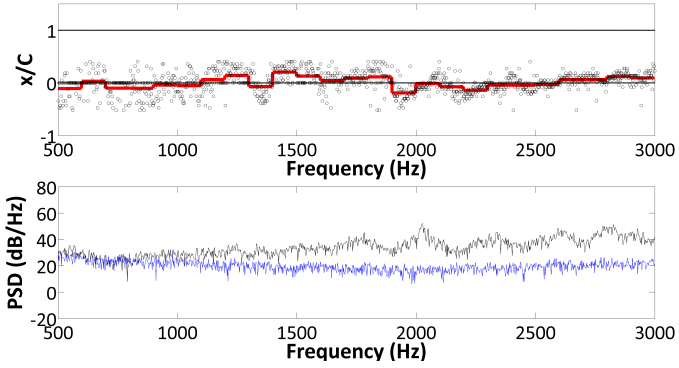

(c)

Figure 5.11: MASL and PSD at $\alpha = 0°$ and Re = (a) 50,000, (b) 100,000 and (c) 150,000. The empty circles indicate the MASL per frequency and the red lines represent the averaged MASL over 100 Hz bands. Black lines have been drawn at $x/C = 1$ and 0 to depict the airfoil leading and trailing edges respectively.

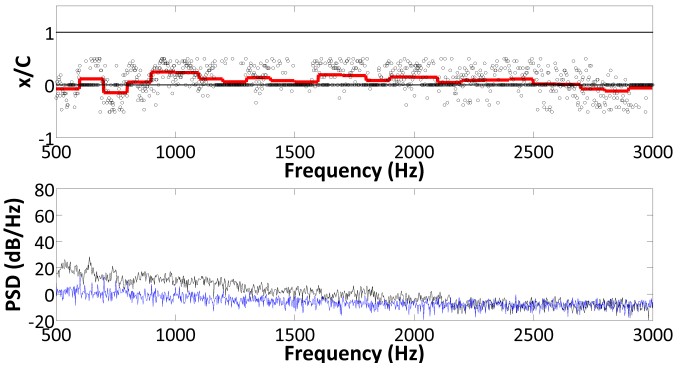

(a)

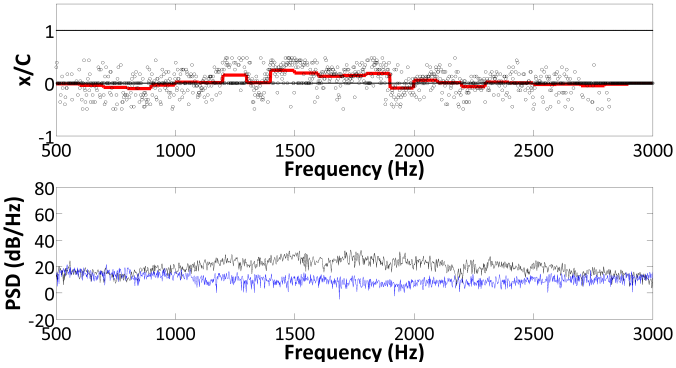

(b)

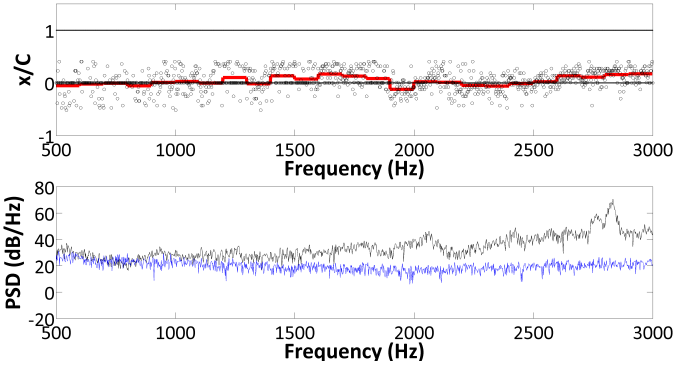

(c)

Figure 5.12: MASL and PSD at $\alpha = 1.58°$ and $Re =$ (a) 50,000, (b) 100,000 and (c) 150,000. The empty circles indicate the MASL per frequency and the red lines represent the averaged MASL over 100 Hz bands. Black lines have been drawn at $x/C = 1$ and 0 to depict the airfoil leading and trailing edges respectively.

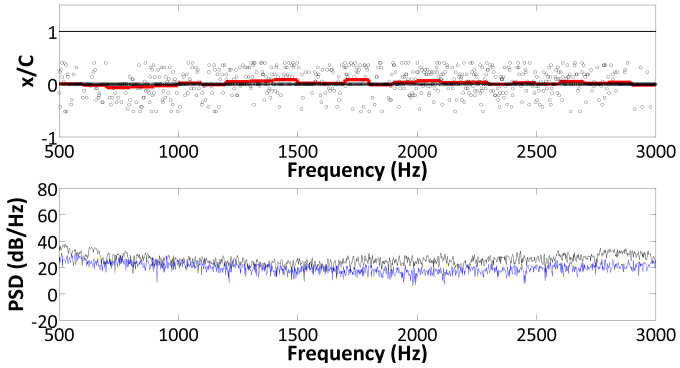

Figure 5.13: MASL and PSD at $\alpha = 3.16°$ and $Re = 150{,}000$. The empty circles indicate the MASL per frequency and the red lines represent the averaged MASL over 100 Hz bands. Black lines have been drawn at $x/C = 1$ and 0 to depict the airfoil leading and trailing edges respectively.

5.1.4 Feedback closing point candidates

The potential feedback loop(s) closing point(s) were estimated using hot-wire anemometry and surface flow visualisation. A suitable starting choice was to experimentally locate and verify the potential feedback loop closing points identified in the research discussed in the Literature Review. These locations included the point of maximum mean-velocity location as proposed by Arbey and Bataille (1983) and the point(s) of flow separation as proposed by Desquesnes et al. (2007). Other locations, inspired by data obtained in this present work, included locations of phase change and the origin of convective disturbance generation.

Throughout this section, the coordinate system shown in Figure 5.14 is used. The trailing edge is defined as $x/C = 0$, the leading edge as $x/C = 1$, the mid-span point of the airfoil as $y/C = 0$ and the airfoil surface as $z/C = 0$. The upper and lower surfaces are the airfoil surfaces whose normal vector faced up (skyward) and down (floor) respectively. This has no bearing on which surface is a pressure or suction surface. Figure 5.15 illustrates the labelling procedure.

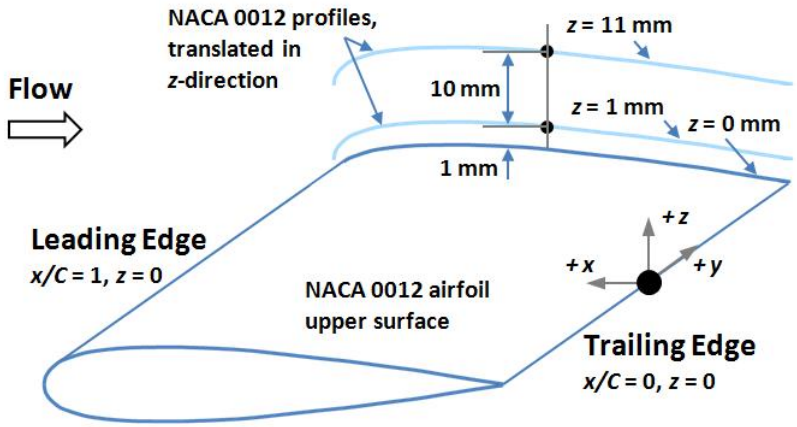

Figure 5.14: Schematic diagram identifying the coordinate system employed during hot-wire anemometry experiments.

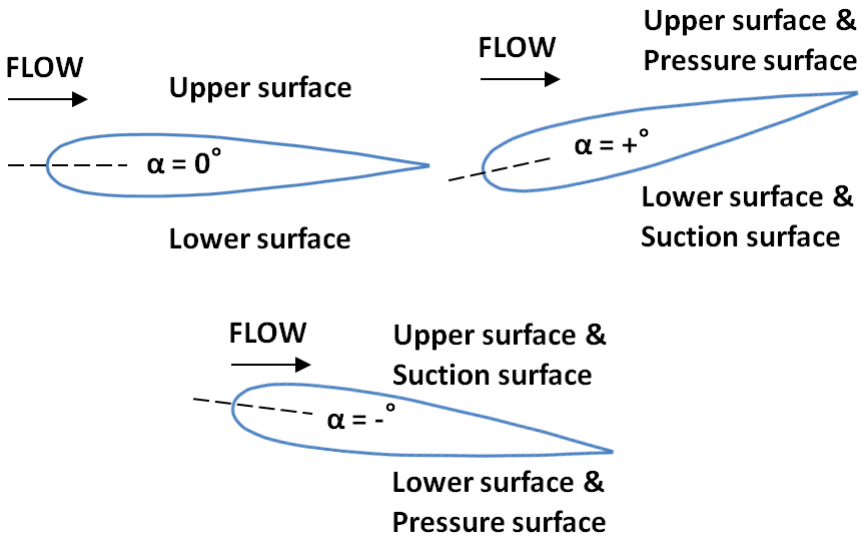

Figure 5.15: An illustration of the three surface configurations, clarifying the labelling of the upper, lower, suction and pressure surfaces.

5.1.4.1 Maximum mean velocity location

The Maximum Mean Velocity Location (MMVL) was identified by keeping the hot-wire probe 1 mm above the airfoil surface ($z/C = 0.015$), centred spanwise ($y/C = 0$) and moved from the leading to trailing edge ($x/C = 1$ to 0) in 1 mm increments ($x/C = 0.015$).

The measured mean velocity increased from the leading edge ($x/C = 1$) to the MMVL. At $\alpha = 0°$ the MMVL was measured at $x/C = 0.87$ for all Reynolds numbers. This agreed with the results of Arbey and Bataille (1983), who based their feedback analysis on a constant MMVL value of L_U for all Reynolds numbers investigated at $\alpha = 0°$. For their $Re = 107{,}000$ test, they used $L_U = 0.069$ m with a 0.080 m NACA 0012 airfoil chord. This corresponds to $x/C = 0.069/0.08 = 0.86$, providing good agreement with the present work ($x/C = 0.87$).

The MMVL was measured at $x/C = 0.94$ on the airfoil pressure surface at $\alpha = 1.58°$ for all Reynolds numbers investigated. On the suction surface, the MMVL

values were near-constant with Reynolds number. The minimum and maximum values were $x/C = 0.61$ and 0.67 at $Re = 50{,}000$ and 100,000 respectively. The average value of the three MMVL values was 0.64, with a standard deviation of 0.03. This gave a relative error of less than 5% for each measurement. The MMVL values obtained via experiment at $\alpha = 0°$ and 1.58° are listed in Table 5.4.

XFOIL (Drela, 1989) was used to determine the MMVL to provide a comparison with experimental data. As observed in Table 5.4, excellent agreement was achieved with the experimental data for $\alpha = 0°$ and on the pressure surface for $\alpha = 1.58°$. Differences in MMVL were observed only on the airfoil suction side at $\alpha = 1.58°$ with a maximum relative error of 10% at $Re = 100{,}000$. The errors at $Re = 50{,}000$ and 150,000 were 2% and 6% respectively.

The unsteady behaviour of boundary layer separation on the suction side, as observed during surface flow visualisation tests (introduced in Section 5.1.4.2) helped explain why the MMVL values on the suction side were not constant and the differences with the XFOIL results. The point of separation varied with time in a back-and-forth manner with a period of approximately 0.2 seconds.

Unfortunately, experimental data at non-zero angle of attack were not available to compare with the MMVL values measured here. Arbey and Bataille (1983) only performed experiments at $\alpha = 0°$ and other non-zero angle of attack experiments by others were performed at much higher Reynolds numbers than this present work. For completeness, measurements were obtained at $\alpha = 3.16°$, showing that the MMVL on the pressure side was at the leading edge, and on the suction side it possessed an average of $x/C = 0.53$ with a standard deviation of 0.05. Non-steady behaviour of boundary layer separation on the suction side was also observed at this angle of attack.

5.1.4.2 Flow separation and reattachment locations

Surface flow visualisation was used to detect flow separation and reattachment and qualitatively observe unsteady flow behaviour via video recording. An example

Table 5.4: Maximum mean velocity location (x/C), measured at $z/C = 0.015$. The stated angles are angles of attack, α.

Re	Maximum mean velocity location (experiment) x/C		
	0°	1.58°	-1.58°
50,000	0.87	0.94	0.61
100,000	0.87	0.94	0.67
150,000	0.87	0.94	0.64
	Maximum mean velocity location (XFOIL) x/C		
	0°	1.58°	-1.58°
50,000	0.87	0.94	0.60
100,000	0.87	0.94	0.60
150,000	0.87	0.94	0.60

result is presented in Figure 5.16 for Re = 150,000 and $\alpha = 0°$. The uniform flow interacted with the airfoil leading edge, forming a laminar boundary layer along a portion of the chord. As the boundary layer developed, the flow caused the oil mixture to collect 40 mm downstream ($x/C = 0.40$) of the leading edge, representing the point of flow separation, S. Near the trailing edge, the mixture was removed from the airfoil surface, representing a point of separated shear layer reattachment, labelled R. This occurred 3 mm from the trailing edge ($x/C = 0.05$).

A summary of the surface flow visualisation tests performed at $\alpha = 0°$ is presented in Figure 5.17. Flow separation was observed for all Reynolds numbers at $\alpha = 0°$. For increasing Reynolds numbers, the separation point occurred further downstream, but did not increase linearly with Reynolds number. At Re = 100,000 to 150,000 reattachment occurred close to the trailing edge.

Surface flow visualisation tests performed on the pressure surfaces at $\alpha = 1.58°$ and 3.16° are presented in Figures 5.18a and 5.18b respectively. For both angles of attack, both flow separation and reattachment were observed for all Reynolds numbers. As the Reynolds number increased, both the separation and reattachment

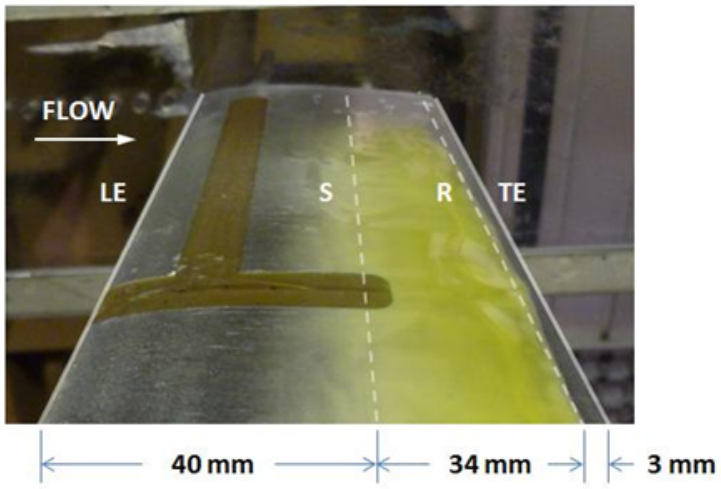

Figure 5.16: Photo of the oil mixture pattern showing surface flow behaviour at Re = 150,000 and $\alpha = 0°$. LE, TE, S and R denote Leading Edge, Trailing Edge, Separation and Reattachment, respectively.

locations moved further downstream. It can be observed that boundary layer separation occurred further downstream from the leading edge for the same Reynolds number flow than at $\alpha = 0°$, with Re = 50,000 being an exception. The distance of the point of separation and reattachment from the leading edge did not increase linearly with Reynolds number for both angles of attack.

On the suction surfaces at $\alpha = 1.58°$ and 3.16°, separation occurred rapidly after the leading edge and flow reattachment was observed further downstream, creating a mid-chord separation bubble. This was observed for both $\alpha = 1.58°$ and 3.16°, as displayed in Figures 5.19a and 5.19b respectively. At $\alpha = 3.16°$, the point of flow reattachment was observed to be further upstream than at $\alpha = 1.58°$. The point of flow separation at $\alpha = 3.16°$ moved only slightly downstream as the Reynolds number increased from 50,000 to 150,000. At $\alpha = 1.58°$, a more noticeable increase of separation distance from the leading edge was measured and the point of flow reattachment moved slightly downstream, as a result of increasing Reynolds number.

XFOIL (Drela, 1989) was also used to measure locations of boundary layer sep-

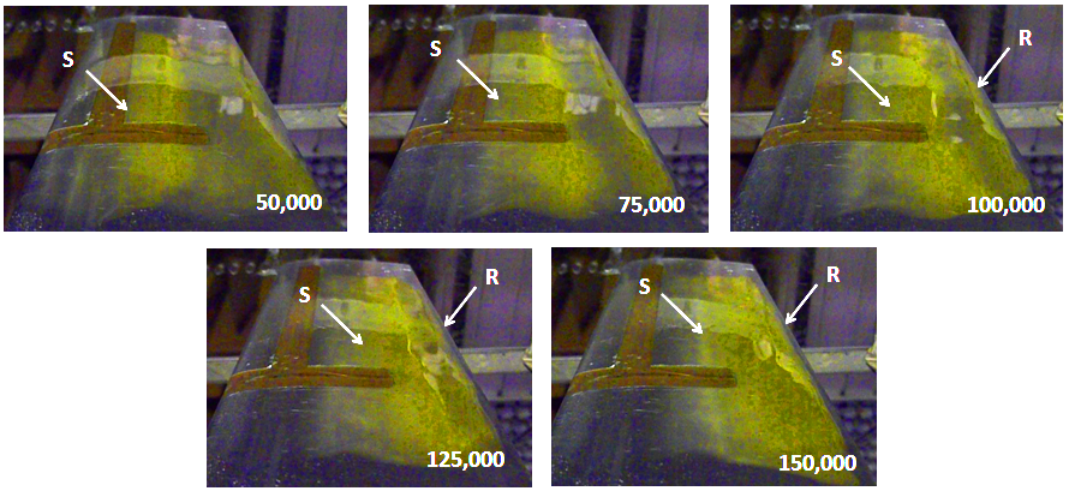

Figure 5.17: Photos of the oil mixture pattern showing surface flow behaviour, for Re = 50,000 to 150,000 and $\alpha = 0°$. S and R denote Separation and Reattachment, respectively.

aration and reattachment, providing a comparison with the experimental data. The points of boundary layer separation obtained via experiment and XFOIL are listed in Table 5.5. The points of reattachment were not listed here, as several of the flow cases did not display reattachment.

There are several explanations for the differences between the experimentally measured and XFOIL predicted separation locations in Table 5.5. One was the thickness of the oil mixture on the airfoil surface having a greater effect on the flow behaviour at lower Reynolds numbers. At higher Reynolds numbers, the freestream flow had greater kinetic energy and forced the mixture off the airfoil surface, thus decreasing the oil mixture thickness. This may explain why the differences between the experimental and XFOIL separation length data varied with respect to Reynolds number. Due to the differences in the experimental and XFOIL data, both were considered as viable feedback length candidates and were analysed in feedback analysis in the following chapter.

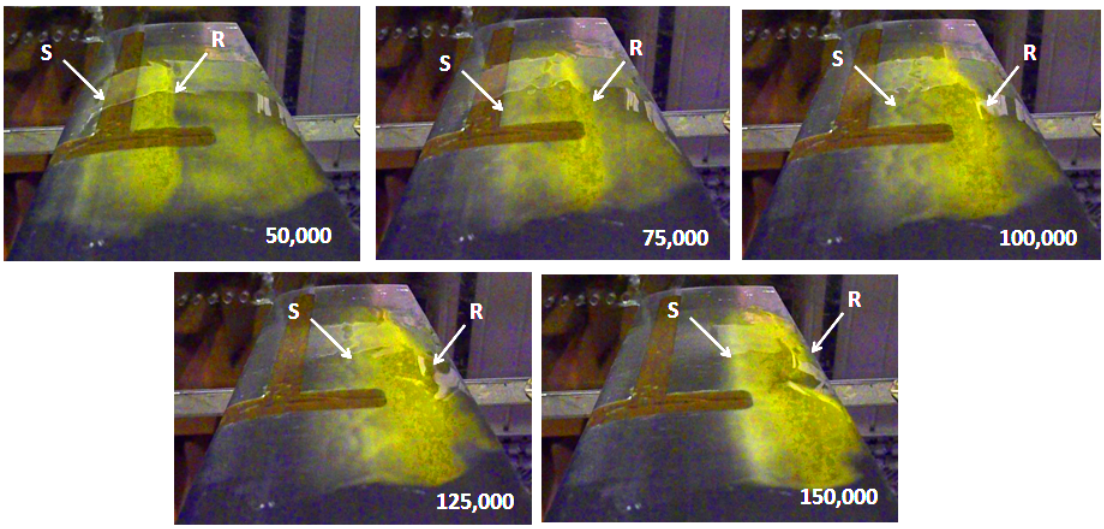

(a)

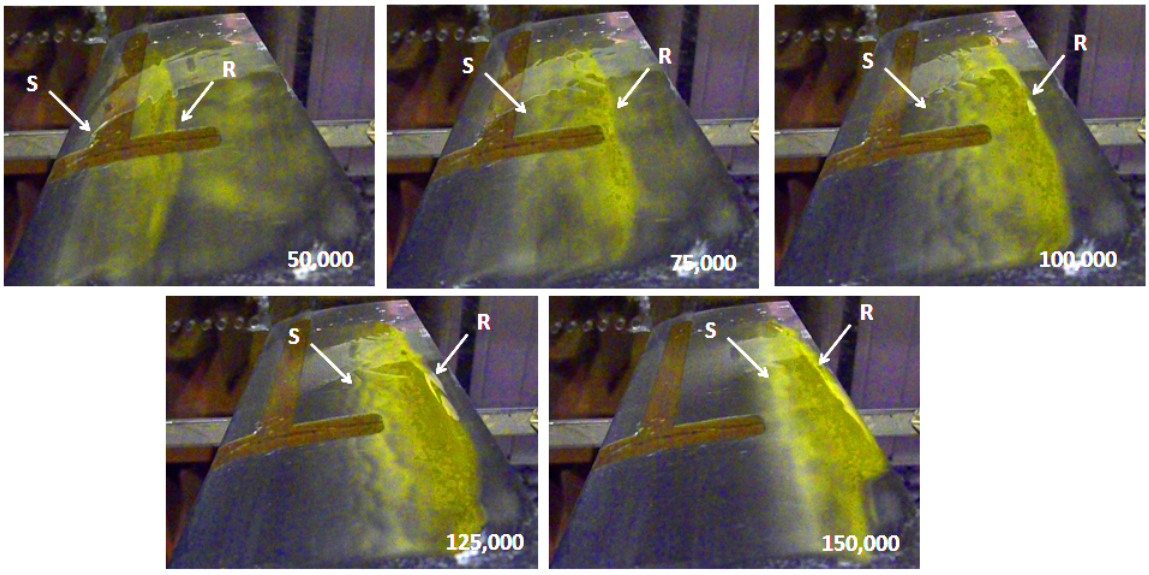

(b)

Figure 5.18: Photos of the oil mixture pattern showing surface flow behaviour on the pressure surface, for Re = 50,000 to 150,000 at (a) $\alpha = 1.58°$ and (b) $\alpha = 3.16°$. S and R denote Separation and Reattachment, respectively.

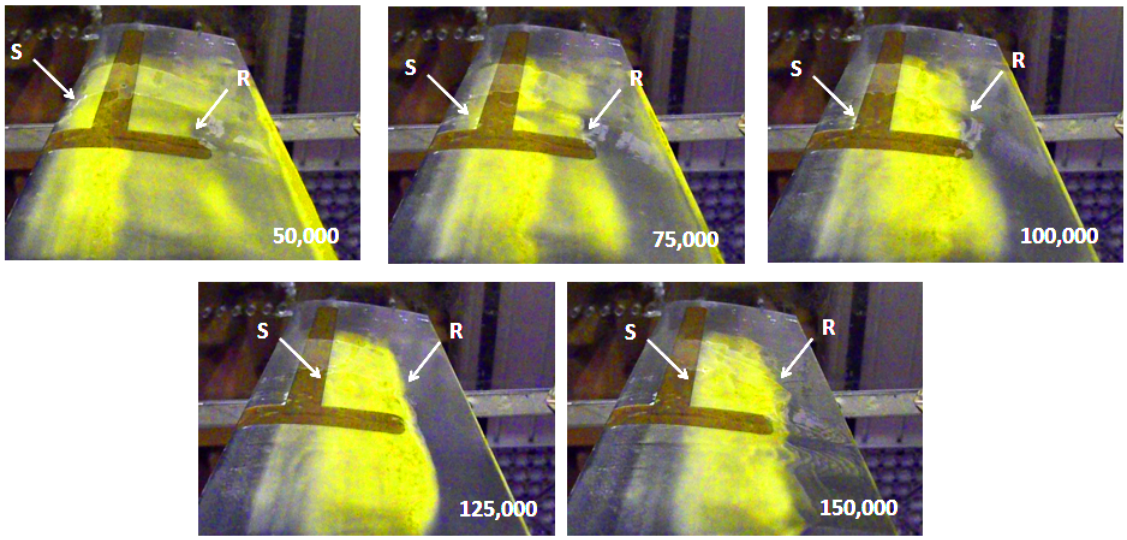

(a)

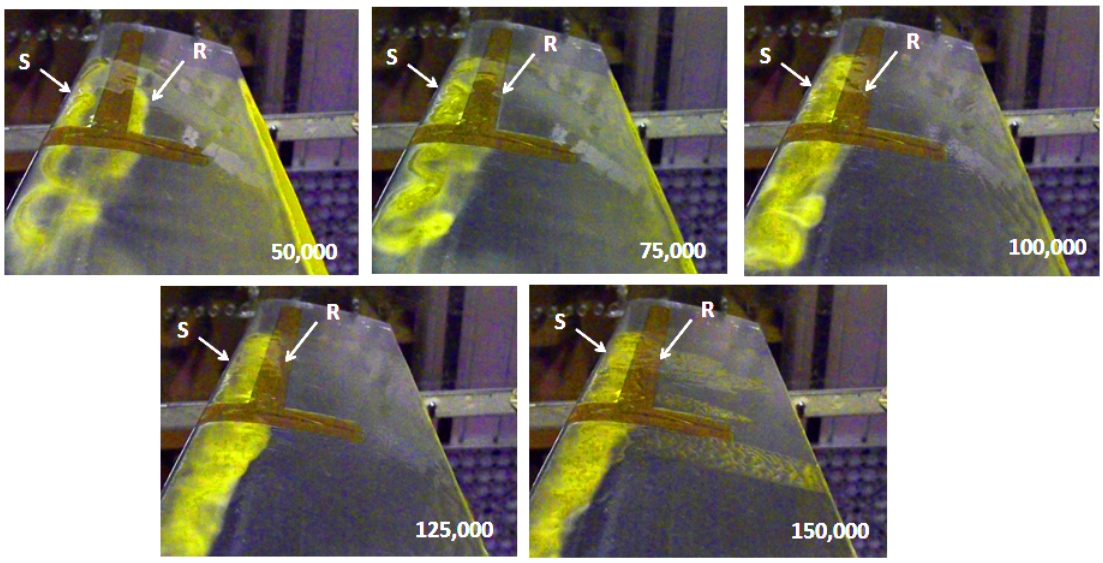

(b)

Figure 5.19: Photos of the oil mixture pattern showing surface flow behaviour on the suction surface of a NACA 0012 airfoil, for Re = 50,000 to 150,000 at (a) $\alpha = 1.58°$ and (b) $\alpha = 3.16°$. S and R denote Separation and Reattachment, respectively.

Table 5.5: Point of boundary layer separation from the airfoil surface (x/C). Positive and negative angles of attack represent the airfoil pressure and suction surfaces respectively.

Re	Location of boundary layer separation (experiment) (x/C)				
	0°	1.58°	-1.58°	3.16°	-3.16°
50,000	0.67	0.81	0.93	0.82	0.97
100,000	0.57	0.55	0.85	0.45	0.97
150,000	0.40	0.34	0.69	0.22	0.97
Re	Location of boundary layer separation (XFOIL) (x/C)				
	0°	1.58°	-1.58°	3.16°	-3.16°
50,000	0.69	0.90	0.90	0.80	0.97
100,000	0.63	0.88	0.85	0.71	0.97
150,000	0.63	0.84	0.81	0.51	0.97

5.1.4.3 Locations of change in phase difference and origin of convective disturbances

This section provides estimates of where abrupt changes in phase between flow and noise occurred and where convective disturbances originated. These locations were obtained by measuring the difference in phase between the flow signal obtained using hot wire anemometry 1 mm above the airfoil surface ($z/C = 0.015$) along the entire chord and the noise obtained by a microphone located in the acoustic far-field. The phase differences between flow and noise were displayed as phase plots along the airfoil chord, for a range of frequencies including tonal and broadband noise. They helped provide an overview of the relationship of phase difference with frequency and position on the airfoil chord. To help quantify the locations of changes in phase difference and origins of convective disturbances, data were plotted and analysed at individual primary and secondary tone frequencies.

The phase differences obtained at $\alpha = 0°$ and $Re = 50{,}000$, 100,000 and 150,000 are presented in Figure 5.20. In Figure 5.20a, the phase difference between the flow

and noise signals appeared to be near-constant along the airfoil length from $x/C = 1$ to $x/C \approx 0.3$, with no noticeable patterns in the phase difference from 500 Hz to 1000 Hz. This is the frequency range where the tones and the broadband hump were measured. The lines of constant phase corresponded to acoustic waves, as inferred from their slope corresponding to the speed of sound. At higher frequencies, the phase difference was random due to the low signal-to-noise ratio. In the tonal frequency range, a significant phase shift occurred at $x/C \approx 0.25$. The phase difference suddenly shifted from positive to negative and continued in this manner along the chord to the trailing edge. The phase differences at $0.25 \geq x/C \geq 0$, however, showed gradual changes of phase from positive to negative and were observed as an interference pattern. This interference wave pattern corresponded to a combination of convective disturbance waves (generated in the boundary layer as part of the transition process) and acoustic waves (from the trailing edge travelling upstream).

At $Re = 100{,}000$ a similar pattern was observed, as shown in Figure 5.20b. Constant phase differences were observed for certain frequencies in the tonal frequency range, to the origin of convective disturbances. The convective disturbance waves were observed at $x/C \approx 0.3$, slightly more upstream than at $Re = 50{,}000$. At $Re = 150{,}000$, convective disturbance wavelengths were observed further upstream at $x/C = 0.38$ as shown in Figure 5.20c and there also existed bands of constant phase difference within the tonal frequency range.

Data were presented at the primary and some secondary tone frequencies to quantify the locations of changes in phase difference and origins of convective disturbances. Figure 5.21 presents the phase differences at $Re = 50,000$ and $\alpha = 0°$ for both the primary tone (589 Hz) and a secondary tone (680 Hz). By observation of Figure 5.21a, the phase difference was relatively constant from the leading edge ($x/C = 1$) to $x/C = 0.33$, with the exception of a single point at $x/C = 0.96$. It was assumed that the result at $x/C = 0.96$ was an anomaly, most-likely due to the hot-wire probe contacting the airfoil surface during experiments.

Immediately downstream of $x/C = 0.33$, the phase difference changed suddenly

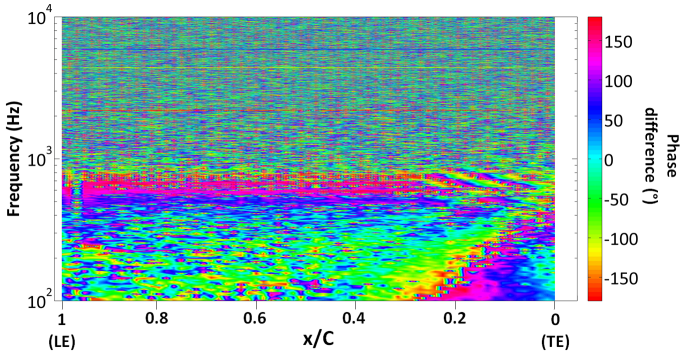

(a)

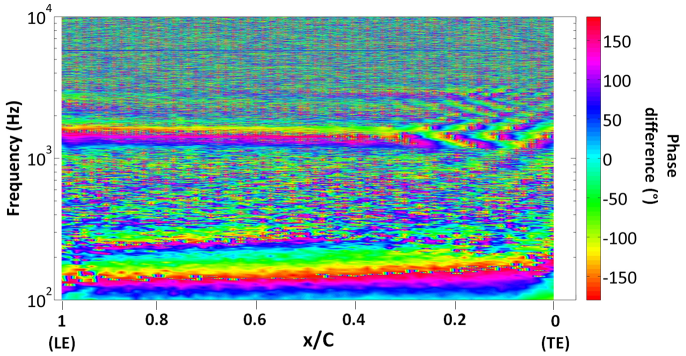

(b)

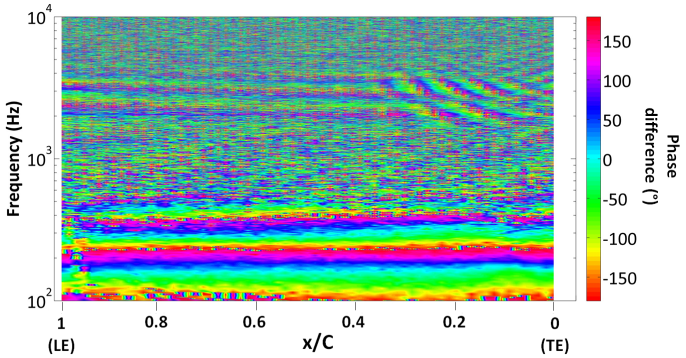

(c)

Figure 5.20: Phase difference between the flow and noise signals at $f = 100$ Hz to 10 kHz, $\alpha = 0°$ and (a) $Re = 50{,}000$, (b) $Re = 100{,}000$ and (c) $Re = 150{,}000$. Flow measurements were obtained 1 mm above the airfoil surface ($z/C = 0.015$) in 1 mm chordwise increments ($x/C = 0.015$) from the leading edge ($x/C = 1$) to the trailing edge ($x/C = 0$).

from approximately 145° at $x/C = 0.33$ to -180° at $x/C = 0.32$. This abrupt change in phase difference represented where 180° out-of-phase acoustic waves that propagated upstream from the trailing edge interacted with the boundary layer, as the velocity signal from the convective disturbance exceeded the acoustic wave signal. The phase difference was briefly near-constant further downstream of $x/C = 0.32$ until another phase shift occurred abruptly at $x/C = 0.22$ to approximately 160°, indicating an eddy convecting downstream. Thus the phase shift was first observed at $x/C = 0.32$.

Between $x/C = 0.2$ and the trailing edge, a convective disturbance wave pattern was observed. There existed three distinct phase change locations, at $x/C = 0.18$, 0.09, 0.02. The location furthest from the trailing edge indicated the origin of the convective disturbances at $x/C = 0.18$. The phase differences recorded at the secondary tone frequency of 680 Hz showed similar results to the primary tone. By observing Figure 5.21b, the phase difference was relatively constant from the leading edge ($x/C = 1$) to $x/C = 0.28$, with the exception of a single point again at $x/C = 0.96$. The location of phase shift was measured at $x/C = 0.27$. There existed two clear phase change locations at $x/C = 0.2$ and 0.1, indicating a strong convective wave propagating downstream and thus the suspected origin of convective disturbances was at $x/C = 0.2$. This was the point where the convective disturbance velocity signal exceeded the acoustic velocity signal and potentially the origin of the major convective disturbances in the boundary layer, where the convective waves became strong, indicating strong coupling.

Figure 5.22 presents the phase differences at $Re = 100,000$ and $\alpha = 0°$ for both the primary tone (1426 Hz) and a secondary tone (1640 Hz). For the primary tone of 1426 Hz, the abrupt change in phase difference occurred at $x/C = 0.46$ that can be observed in Figure 5.22a. There existed three clear phase change locations at $x/C = 0.3$, 0.19 and 0.11. The secondary tone result at 1640 Hz required more interpretation. In Figure 5.22b the convective wave was clearly defined, but the first phase change location (the first meaning the closest to the leading edge) was

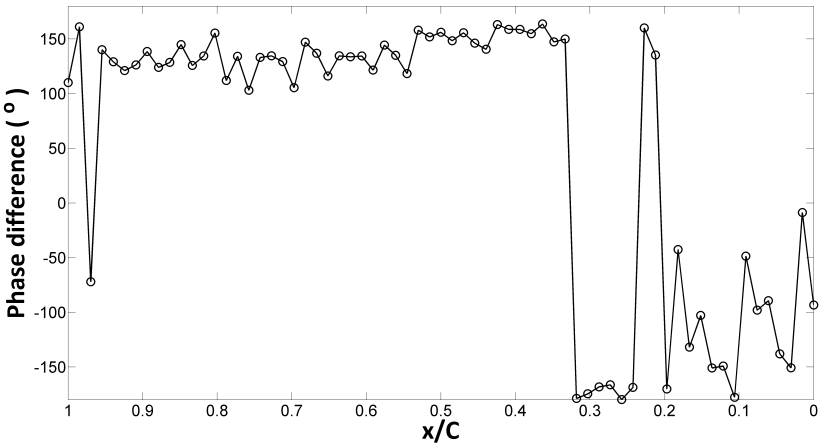

(a)

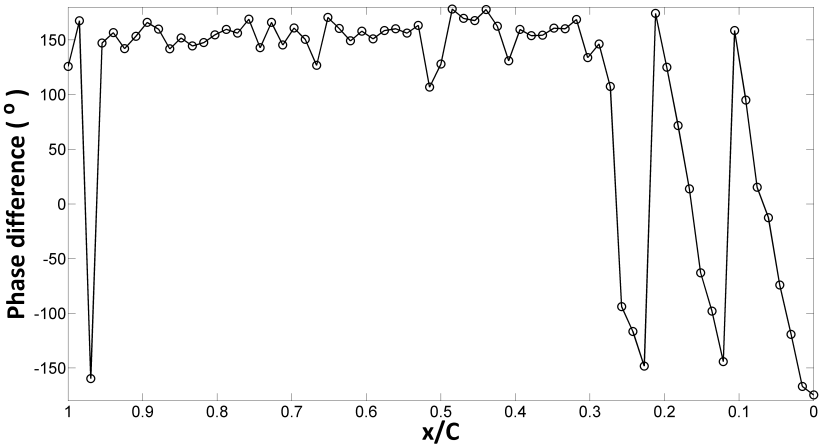

(b)

Figure 5.21: Phase difference between the flow and noise signals at $Re = 50,000$, $\alpha = 0°$ and (a) $f = 589$ Hz, corresponding to the primary tone and (b) $f = 680$ Hz corresponding to a secondary tone. Flow measurements were obtained 1 mm above the airfoil surface ($z/C = 0.015$) in 1 mm chordwise increments ($x/C = 0.015$) from the leading edge ($x/C = 1$) to the trailing edge ($x/C = 0$).

not immediately obvious. In addition, an abrupt phase shift did not occur prior to the convective waves, as observed for the primary tone. The phase difference gradually increased from -150° at the leading edge ($x/C = 1$) to approximately -60° at $x/C = 0.42$. At $x/C = 0.41$, the phase difference decreased to approximately -165° and thus this location was deemed the location of phase change. The first phase change location was at $x/C = 0.39$.

The phase differences at $Re = 150{,}000$, $\alpha = 0°$ and at the primary tone frequency of 2050 Hz are presented in Figure 5.23. Between $x/C = 1$ to 0.4, the phase difference gradually increased from approximately 25° to 170°, with three outlier values at $x/C = 0.71$, 0.57 and 0.44. The location of phase shift was harder to determine; it was either $x/C = 0.44$ or 0.38. Identifying data that were outliers or abrupt changes in phase was difficult, especially when the phase difference was not a smooth increase/decrease with respect to x/C. There were three or four phase change locations, with the initial phase change location estimated at $x/C = 0.34$ and the others at $x/C = 0.22$, 0.12 and 0.02.

The phase difference plots of the secondary tones at $Re = 150{,}000$ and $\alpha = 0°$ displayed phase shifts across the entire chord and the location of an abrupt phase difference change could not be determined (or it possibly occurred at the leading edge and phase shifts occurred along the airfoil chord). The convective wave pattern was very difficult to interpret.

The phase differences obtained at $Re = 50{,}000$ and $\alpha = 1.58°$ on both the pressure and suction surfaces are presented in Figure 5.24. The phase differences on the pressure surface are displayed in Figure 5.24a. The phase difference between the flow and noise signals resembled the convective wave patterns observed at $\alpha = 0°$ (presented in Figure 5.24a). At $\alpha = 1.58°$, the convective wave pattern occurred at $x/C = 0.55$, further upstream than at $\alpha = 0°$. There were four phase change locations observed between $x/C = 0.55$ and the trailing edge; this was also shown in Figure 5.25, identifying the phase differences at the primary tone frequency (607 Hz) and a secondary tone frequency (517 Hz). On the airfoil suction surface at $Re = 50{,}000$

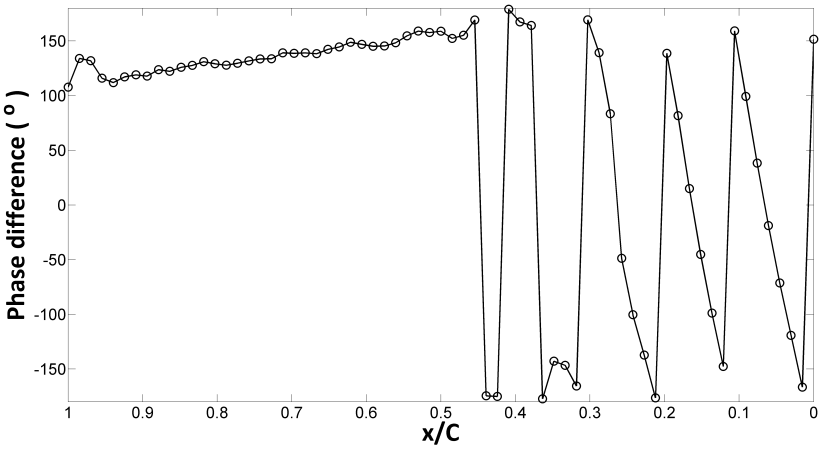

(a)

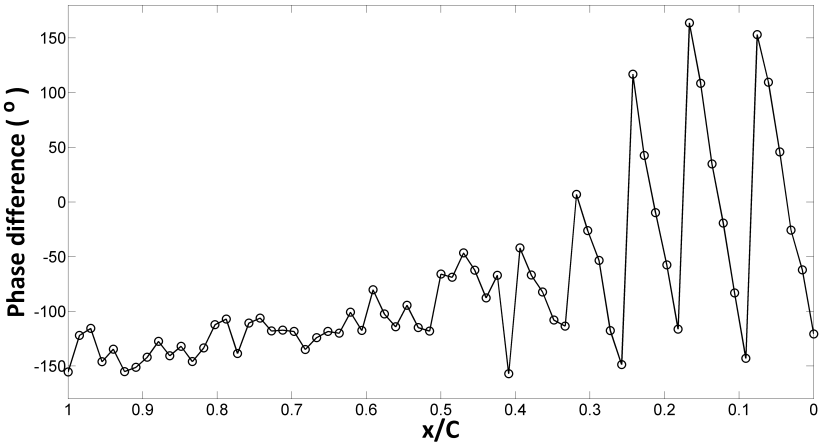

(b)

Figure 5.22: Phase difference between the flow and noise signals at $Re = 100,000$, $\alpha = 0°$ and (a) $f = 1426$ Hz, corresponding to the primary tone and (b) $f = 1640$ Hz corresponding to a secondary tone. Flow measurements were obtained 1 mm above the airfoil surface ($z/C = 0.015$) in 1 mm chordwise increments ($x/C = 0.015$) from the leading edge ($x/C = 1$) to the trailing edge ($x/C = 0$).

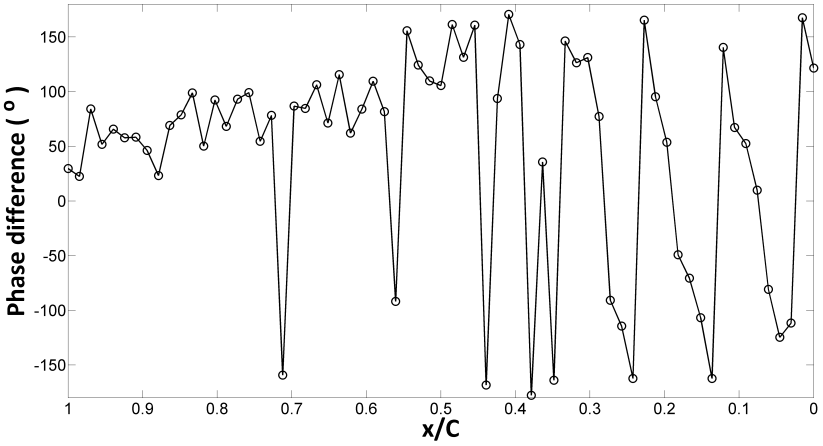

Figure 5.23: Phase difference between the flow and noise signals at Re = 150,000, $\alpha = 0°$ and $f = 2050$ Hz, corresponding to the primary tone. Flow measurements were obtained 1 mm above the airfoil surface ($z/C = 0.015$) in 1 mm chordwise increments ($x/C = 0.015$) from the leading edge ($x/C = 1$) to the trailing edge ($x/C = 0$).

and $\alpha = 1.58°$, there were no discernible convective wave patterns, as observed in Figure 5.24b. In the tonal noise frequency range, the phase difference was relatively constant along the airfoil chord.

The phase differences at $Re = 50{,}000$, on the pressure surface for $\alpha = 1.58°$ and at the primary tone frequency of 607 Hz are presented in Figure 5.25a. There were three clear convective wave peaks located at $x/C = 0.12$, 0.25 and 0.37. It was difficult to distinguish the peak at $x/C = 0.53$ as a convective wave peak and it was assumed that it was not. The negative phase difference values located at $x/C = 0.55$ and 0.77 were assumed to be rogue data (possibly due to misinterpretation of the MATLAB unwrap function) and it was assumed that they did not represent the location of abrupt phase change; this was located at $x/C = 0.46$, where the phase difference shifted from positive to negative prior to the development of convective waves.

At the secondary tone frequency of 517 Hz, three phase change locations can be

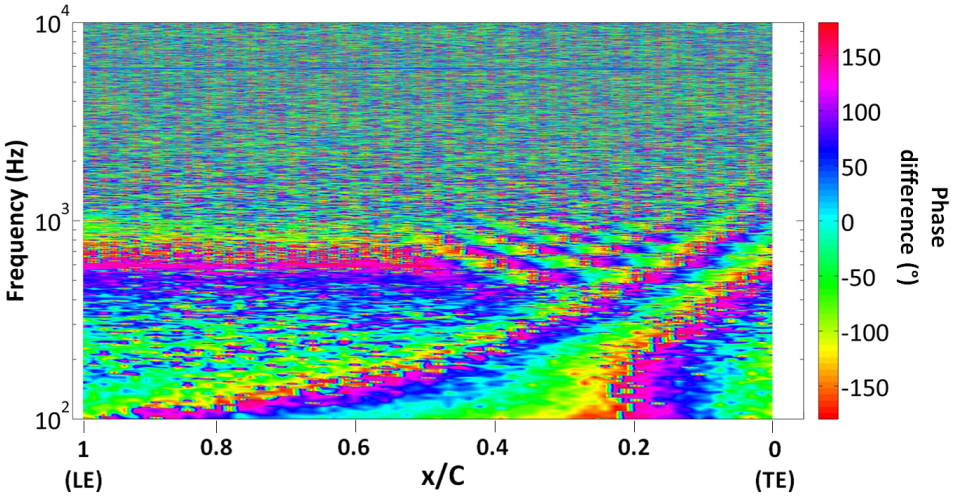

(a)

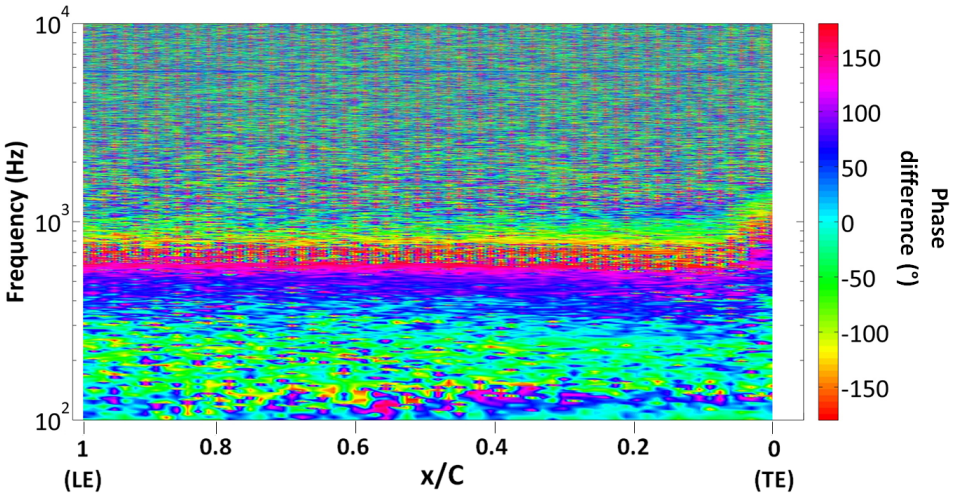

(b)

Figure 5.24: Phase difference between the flow and noise signals at $f = 100$ Hz to 10 kHz, $Re = 50{,}000$ and $\alpha = 1.58°$ on the airfoil (a) pressure surface and (b) suction surface. Flow measurements were obtained 1 mm above the airfoil surface ($z/C = 0.015$) in 1 mm chordwise increments ($x/C = 0.015$) from the leading edge ($x/C = 1$) to the trailing edge ($x/C = 0$).

observed in Figure 5.25b at $x/C = 0.03$, 0.18 and 0.33. An abrupt phase shift was not observed near the commencement of the convective waves, rather a gradual phase change between $x/C = 0.48$ to 0.35. Therefore it was assumed that the location of the phase shift was $x/C = 0.33$.

Increasing Re to 100,000 produced very different phase difference data, as presented in Figure 5.26 for the primary tone of 1463 Hz. From the leading edge to $x/C = 0.55$, the phase constantly shifted from positive to negative, as expected in the case of broadband or background noise. Between $x/C = 0.55$ and 0.25, there appeared to be some non-randomised formation and three phase change locations could be observed at $x/C = 0.45$, 0.36 and 0.26. There was no defined location of phase shift on the airfoil chord. This result was indicative of the phase differences observed at $Re = 100{,}000$ and 150,000 at $\alpha = 1.58°$, on both the pressure and suction surfaces. Note that for all Reynolds numbers investigated at $\alpha = 3.16°$, the phase difference between the flow and noise signal displayed no patterns or discernible phase shifts on both the pressure and suction surfaces.

The measured start of convective disturbance waves for the primary tone seemed to be a suitable candidate for feedback lengths in acoustic feedback analysis. These lengths possessed unique distances relative to the trailing edge at each Reynolds number and angle of attack which was ideal, yet in some cases values were not able to be detected. Table 5.6 lists the measured start of convective disturbances at $\alpha = 0°$ and $\pm 1.58°$. These values were obtained via the observation of the phase difference plots at single frequencies, as previously shown in this section. Values were not tabulated when convective wave patterns were not detected.

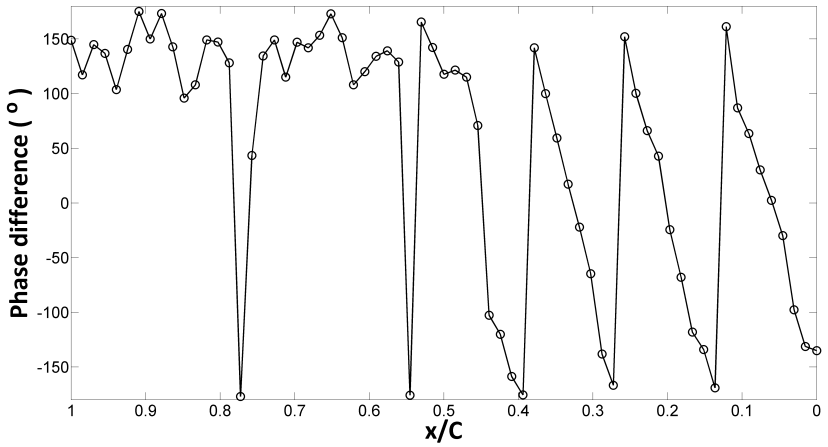

(a)

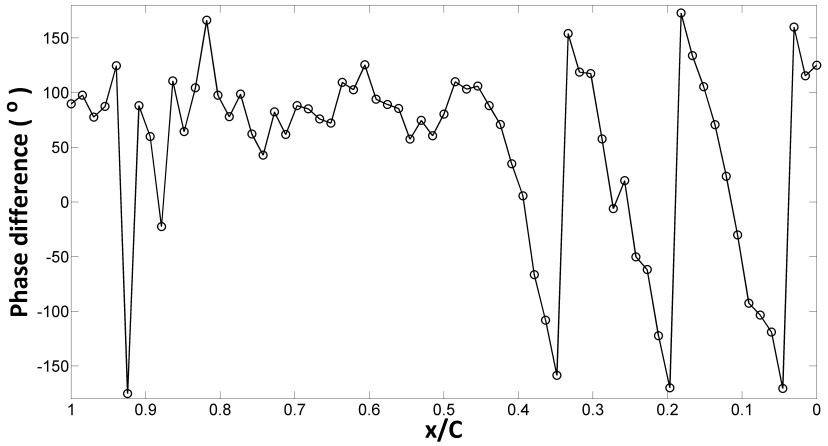

(b)

Figure 5.25: Phase difference between the flow and noise signals at $Re = 50,000$, pressure surface for $\alpha = 1.58°$ and (a) $f = 607$ Hz, corresponding to the primary tone and (b) $f = 517$ Hz corresponding to a secondary tone. Flow measurements were obtained 1 mm above the airfoil surface ($z/C = 0.015$) in 1 mm chordwise increments ($x/C = 0.015$) from the leading edge ($x/C = 1$) to the trailing edge ($x/C = 0$).

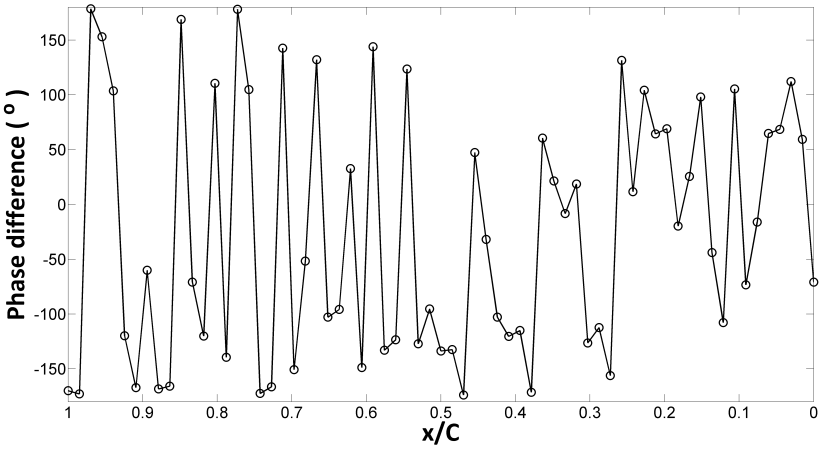

Figure 5.26: Phase difference between the flow and noise signals at Re = 100,000, $\alpha = 1.58°$ pressure surface and $f = 1463$ Hz, corresponding to the primary tone. Flow measurements were obtained 1 mm above the airfoil surface ($z/C = 0.015$) in 1 mm chordwise increments ($x/C = 0.015$) from the leading edge ($x/C = 1$) to the trailing edge ($x/C = 0$).

Table 5.6: Measured start of convective disturbances (x/C) for primary tones at $\alpha = 0°$ and ±1.58°. Positive and negative α denote the pressure and suction surfaces respectively.

Re	Origin of convective disturbances, x/C		
	0°	1.58°	-1.58°
50,000	0.18	0.37	n/a
100,000	0.30	0.45	0.12
150,000	0.34	n/a	n/a

5.1.5 Convective disturbance velocity

The previous section identified the convective disturbance waves by measuring the changes in phase between the flow and noise signals. This section provides calculations of the convective disturbance velocities for the airfoil at different Reynolds numbers and angles of attack.

The distance between the phase change locations corresponded to the convective disturbance wavelength, λ (m), for a tone frequency, f (Hz). The convective disturbance velocity, C_r (m/s), was calculated via

$$C_r = f\lambda \tag{5.1}$$

Using the data at Re = 100,000 and $\alpha = 0°$ for a primary tone frequency of 1426 Hz, there were three phase change locations at x/C = 0.11, 0.19 and 0.3. The wavelengths between these peaks were 0.3 - 0.19 = 0.11 and 0.19 - 0.11 = 0.08. The average of these two wavelengths was 0.095 and thus $\lambda = 0.095 \times 67$ mm = 6.4 mm. Using Equation 5.1 with f = 1426 Hz yielded $C_r = 1426 \times 6.4/1000$ = 9.1 m/s. The convective disturbance velocity is often presented in ratio form relative to the freestream velocity, $C_r/U_\infty = 9.1/22.54 = 0.40$. Table 5.7 lists the convective disturbance velocity ratios calculated using the primary tone frequencies at both $\alpha = 0°$ and the pressure surface at 1.58°, for Re = 50,000 to 150,000. Using the secondary tone frequencies helped provide some verification for values obtained using the primary tones as these results were within 5% of those calculated using the primary tones.

The evaluation of the convective disturbance velocity was very susceptible to measurement error of the phase change locations along the airfoil chord. Assuming an error of $x/C = 0.01$ in these estimations, this corresponded to a 0.01×67 mm = 0.67 mm error in wavelength estimation. Multiplying this value by a primary tone value of 589 Hz to 2050 Hz would yield an error of approximately 0.4 to 1.4 m/s in convective disturbance velocity. Thus the errors in the convective disturbance

Table 5.7: Convective disturbance velocity ratio, C_r/U_∞, for $\alpha = 0°$ and $\pm 1.58°$, calculated using the primary tone frequencies presented in Table 5.1.

Re	C_r/U_∞	
	$0°$	$\pm 1.58°$
50,000	0.44	0.46
100,000	0.40	0.46
150,000	0.41	0.40

velocity ratio would be approximately 0.04, which is a 10% relative error with respect to a value of 0.40.

5.1.6 Summary of feedback mechanism parameters

Experiments performed using a NACA 0012 airfoil in the AWT provided sufficient data to perform an acoustic feedback analysis, which is provided in the following chapter. The measured noise at $Re = 50{,}000$ to 150,000 at $\alpha = 0°$ and $1.58°$ displayed a series of tones superimposed on a broadband hump. The number and relative magnitudes of secondary tones varied with Re and α. At $\alpha = 3.16°$, tones were not observed. Acoustic beamforming revealed that the MASL was strongly influenced by a standing wave pattern in the AWT when the signal to noise ratio was high. Based on the averaged MASL over a range of frequencies and Reynolds numbers, it was deduced that the MASL was at the trailing edge for all flow conditions considered. A series of feedback length candidates were proposed via experiment, including the MMVL, location of convective disturbance origin and point of boundary layer separation. Rejected candidates included points of boundary layer reattachment and the locations of abrupt phase change between flow and noise, due to insufficient data. The convective disturbance velocity was calculated by measuring convective wavelengths in the phase difference between the flow and noise.

5.2 Investigation of facility effects

There has been discussion in the literature that facility effects may be responsible for the generation of secondary tones of airfoils at low-to-moderate Reynolds number (Nash et al., 1999; Tam and Ju, 2011). This section helps provide some insight into the feasibility of these propositions, by presenting experimental results that address these claims. The facility effects on the acoustic beamforming results were documented in Section 4.6.3, by illustrating the standing wave pattern in the beamformer output.

To help determine the causality between the flow and noise in the near wake and along the airfoil, the coherence between the two signals was obtained. Strong coherence between flow and noise would be expected for the primary and secondary tone frequencies, provided that the velocity fluctuations in the boundary layer are responsible (or at least partially responsible) for the generation of those tones. If the facility effects are solely responsible for the generation of secondary tones, then strong coherence between the flow and noise at these frequencies would not be observed.

Boundary layer trips were introduced to determine their impact on tonal noise generating mechanisms, by affecting the boundary layer development on a particular surface. Tests were performed with trips on one surface and on both surfaces. This determined the sensitivity of tonal noise generating mechanisms to boundary layer disturbances on one surface and the interaction of feedback mechanisms of both surfaces.

5.2.1 Effects of contraction walls and airfoil housing

This section details the effects of the AWT contraction walls and the airfoil housing on the tonal noise generation mechanisms. The development of the boundary layer in the AWT contraction and the airfoil housing prevented tonal noise generation along the entire airfoil chord, causing some finite spanwise effects. Additionally,

while the airfoil was placed in the housing with caution, there may have existed some error in the angle of attack. This is not to be mistaken with the angle of attack correction described in Section 3.2.2, which was a correction due to a finite jet height, and is not an error-based correction. Experiments in the near wake were performed to illustrate the impact on the flow.

5.2.1.1 On the angle of attack

To determine the actual angle attack that the airfoil was placed, velocity profiles obtained from below to above the plane of the airfoil were obtained at the trailing edge and further downstream, at $\alpha = 0°$. Tam and Ju (2011) proposed via DNS research that all secondary tones of a NACA 0012 airfoil measured at $\alpha = 0°$ would be due to facility effects and that experiments that revealed secondary tones at $\alpha = 0°$ could be due to relative skewness between the flow and the airfoil in the testing facility. Addressing these claims was important and could be achieved by measuring the vertical wake profiles and obtaining an understanding of the vertical skewness of the flow relative to the centreline of the AWT contraction and the trailing edge location.

Hot-wire anemometry measurements were obtained in 0.2 mm ($z/C = 0.003$) increments from z/C = -0.075 to 0.075 to obtain mean velocity profiles of the wake, in line with the trailing edge, $x/C = 0$, and further downstream at x/C = -0.03, -0.075 and -0.15. The mean velocity profiles obtained at $\alpha = 0°$ and Re = 50,000, 100,000 and 150,000 are presented in Figure 5.27. The z/C locations were measured relative to the airfoil trailing edge.

For all of the Reynolds numbers analysed at $\alpha = 0°$, the minimum mean velocity was located at $z/C = 0$. This was consistent with the minimum mean velocity location predicted by potential flow theory (XFOIL: Drela, 1989). With decreasing x/C (i.e., moving downstream) for all Reynolds numbers, the mean velocity increased in the range z/C = -0.02 to 0.02.

There existed some asymmetry between the mean velocity values above and

below the trailing edge. During the characterisation of the flow prior to experiments, the flow in the AWT contraction was slightly skewed in the z-direction, as presented in Section 3.1.2, Figure 3.6. This would have affected these mean velocity profiles, as even a slight asymmetry in freestream flow would affect the interaction of the boundary layers from each surface in the near wake.

Coherence measurements between the flow and noise data were obtained immediately downstream of the trailing edge (denoted as $x/C = 0$), mid-span $y/C = 0$ and in the same vertical range as the mean velocity measurements, z/C = -0.075 to 0.075. By identifying strong coherences near the trailing edge, the acoustic frequencies caused by velocity fluctuations could be determined. This helped understand whether the measured tones were caused by velocity fluctuations near the airfoil surface or other influences, such as facility effects. It also helped reveal whether the angle of attack error or AWT freestream flow angle error had any impact on the causality between measured velocity fluctuations and the tones. Figure 5.28 presents coherence values at Re = 50,000, 100,000 and 150,000 and $\alpha = 0°$.

From Figure 5.28a, there are four lines of moderate coherence (values up to 0.6) that represent the primary and secondary tones in the tonal frequency range, at Re = 50,000 and between 500 Hz and 800 Hz. The coherence weakened at approximately $z/C = 0$, corresponding to the region of minimum mean velocity. The first and second harmonics of the primary tone possessed strong coherences (values up to 0.8), observed away from the trailing edge. The broadband noise contribution at frequencies less than 500 Hz also possessed moderate coherence with the velocity fluctuations, thus showing that this broadband noise was flow induced. This was to be expected from the diffraction processes at the trailing edge that produce velocity fluctuations and broadband noise.

As discussed in Section 5.1.1, increasing Re from 50,000 to 100,000 at $\alpha = 0°$ produced stronger tones and an increased broadband hump magnitude and frequency range. These significant changes in the measured noise were observed in the coherence values in the wake, as shown in Figure 5.28b. The primary tone frequency at

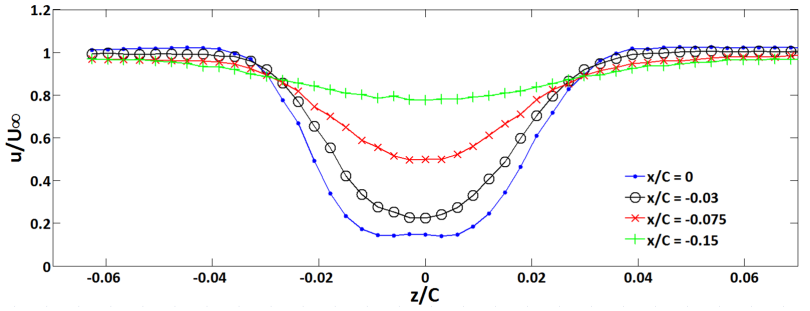

(a)

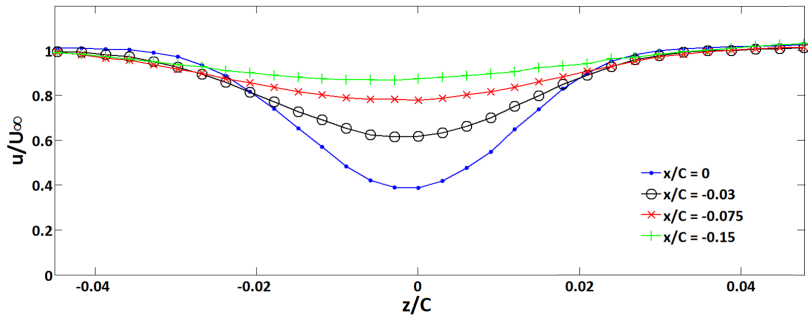

(b)

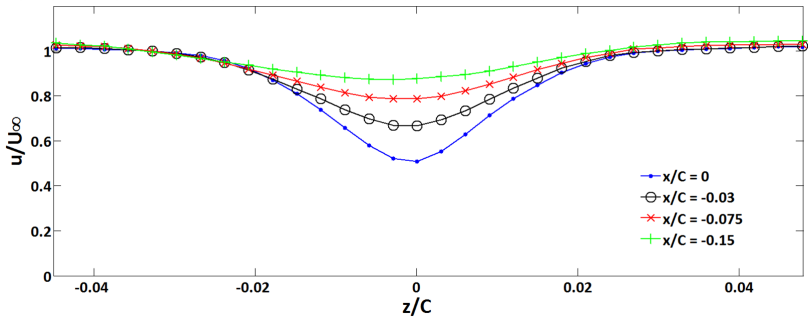

(c)

Figure 5.27: Mean velocity profiles at $\alpha = 0°$ and Re = (a) 50,000 (b) 100,000 and (c) 150,000. Measurements were obtained in 0.2 mm increments ($z/C = 0.003$) from z/C = -0.075 to 0.075, $y/C = 0$ and at x/C = 0, -0.03, -0.075 and -0.15.

1426 Hz displayed very strong coherence with the velocity fluctuations, at a value near 1. The secondary tones at frequencies 1233 Hz and 1640 Hz also possessed strong coherences, with values up to 0.7. The coherence for the secondary tones was at a maximum away from the trailing edge. Despite the secondary tones possessing a weaker coherence than the primary tone, the coherence values were still strong and therefore strong evidence existed to support the causation of secondary tones by velocity fluctuations near the trailing edge.

The broadband hump frequency range, other than that coinciding with the tone frequencies, showed near-zero coherence with the velocity fluctuations. This provided evidence that the mechanisms responsible for the noise constituting the broadband hump had no causality with the velocity fluctuations measured in the wake near the trailing edge. The broadband noise at frequencies less than 200 Hz showed moderate coherence for positive z/C values, but not below the trailing edge. The noise in this frequency range could only have been produced by the AWT freestream. This deduction was ascertained by comparing the PSDs of the airfoil self-noise and the background noise in Figure 5.2, where the airfoil self-noise barely exceeded the background for frequencies less than 500 Hz. Thus, the asymmetry of coherence above and below the trailing edge in this frequency range showed that this noise could not have been caused by the airfoil or any possible misalignment error and that it was produced by the AWT. Note that this did not eliminate the possibility of both the airfoil and/or the freestream flow being at a small non-zero angle of attack, as this explanation was only valid for noise with frequency approximately 500 Hz or less. In addition, the AWT is non-anechoic for frequencies less than 200 Hz, and the reflection of noise from the trailing edge to the AWT contraction and airfoil housing and acoustic beamformer may have affected the noise generation at 200 Hz or less.

The change in coherence values from Re = 100,000 to 150,000 were significant. At Re = 150,000, the coherence values of the tones were much weaker than at lower Reynolds numbers, as observed in Figure 5.28c. The primary tone frequency of 2050 Hz and the secondary tones showed weak-to-moderate coherences (values

up to 0.5) at $z/C \leq -0.05$ and $z/C \geq 0.05$ but negligible coherence outside these regions. Similarly to $Re = 100{,}000$, there existed moderate coherence of low frequency noise at frequencies approximately 250 Hz or less. The explanation provided at $Re = 100{,}000$ was also applicable at $Re = 150{,}000$. Note the change in coherence scale in Figure 5.28c; this was done to allow clear visibility of the weaker coherences at the tone frequencies. This change in scale also made the broadband coherences at lower frequencies appear stronger than at $Re = 100{,}000$ but they are similar.

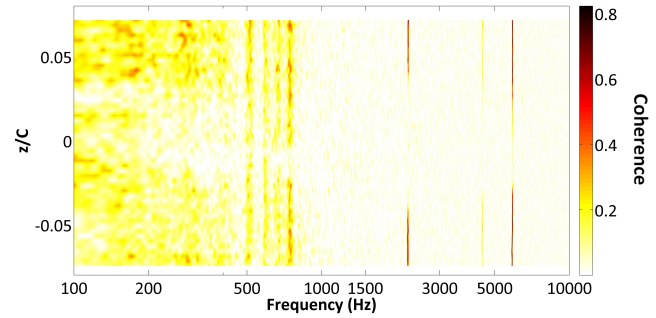

(a)

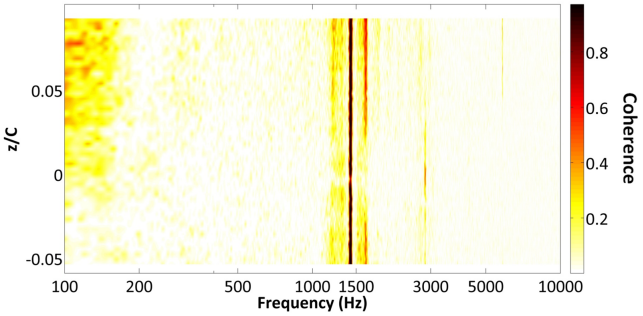

(b)

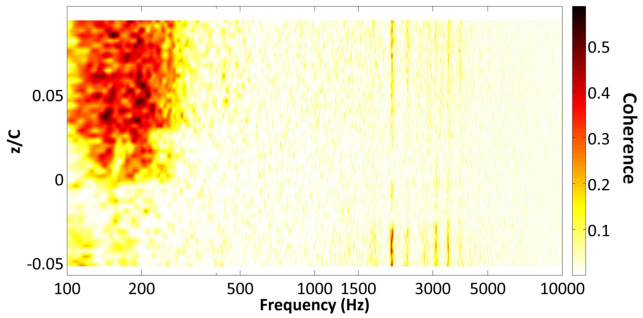

(c)

Figure 5.28: Coherence between the flow and noise signals at $\alpha = 0°$ and $Re =$ (a) 50,000 (b) 100,000 and (c) 150,000. Measurements were obtained in 0.2 mm increments ($z/C = 0.003$) from $z/C =$ -0.075 to 0.075 and $x/C = y/C = 0$.

5.2.1.2 Effects along the airfoil span

Hot-wire anemometry measurements were performed along the y-axis and immediately downstream of the trailing edge, x/C = -0.015 and $z/C = 0$. This illustrated the effects of airfoil housing side walls on the tonal noise generation mechanisms, near the ends of the airfoil span. Figure 5.29 revealed the coherence between the flow and noise signals at Re = 100,000 and $\alpha = 0°$ along y/b = -0.363 to 0.363, where b represents the airfoil span. This was done to help illustrate the portion of the airfoil span that possessed strong coherence with flow and noise. Using y/C may have been misleading, as the focus of this test was to determine the percentage of the span affected by the airfoil housing and AWT contraction boundary turbulence intensity, independent of the airfoil chord.

From $y/b = 0$ to 0.3, the primary tone frequencies exhibited coherence values greater than 0.8 and the secondary tone frequencies exhibited coherence values of 0.3 to 0.6. At distances greater than $y/b \approx 0.3$, both the primary and secondary tone coherence values decreased significantly. For tonal noise to occur, the freestream velocity must have a low turbulence intensity. Near the AWT contraction walls, the turbulence intensities were much higher than in the centre of the contraction, as shown in Figure 3.7. Therefore the tonal noise generation mechanisms between $y/b = 0.3$ to 0.5 (where $y/b = 0.5$ represents the end of the airfoil, attached to the housing) were affected by a combination of the turbulence intensity of the freestream flow and the interaction of the boundary layer with the housing side walls.

5.2.2 Coherence of primary and secondary tones along the airfoil chord

The coherence values between the flow and noise were obtained along the airfoil chord, to determine the chordwise stations that presented strong coherence at the primary and secondary tone frequencies. If strong coherences were observed at the secondary tone frequencies, it would provide evidence that those secondary tones

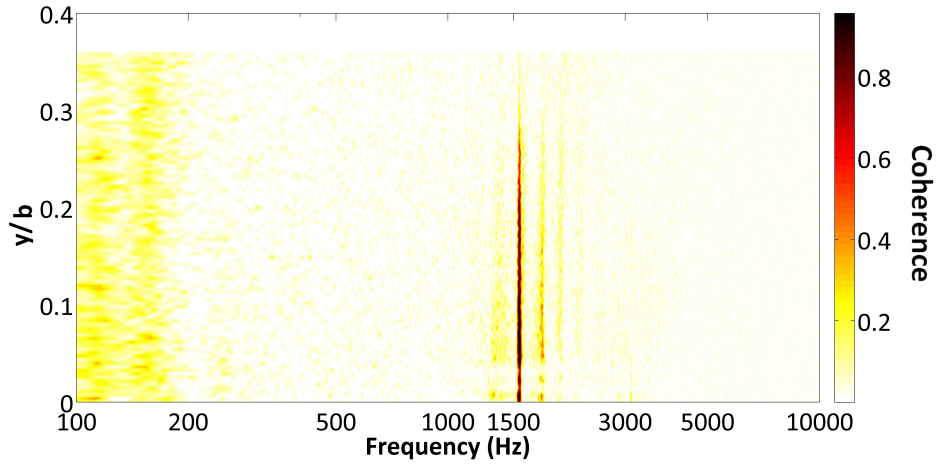

Figure 5.29: Coherence between the flow and noise signals, measured at Re = 100,000 and $\alpha = 0°$ along the line of x/C = -0.015, $z/C = 0$ and y/b = -0.363 to 0.363.

were generated by velocity fluctuations near the airfoil surface.

Figure 5.30 presents the coherence values at Re = 50,000 and $\alpha = 0°$ measured at four chordwise stations; $x/C = 1$ (leading edge), $x/C = 0.3$, $x/C = 0.15$ and $x/C = 0$ (trailing edge). Measurements were obtained from $z/C = 0.015$ to 0.15 in $z/C = 0.003$ increments, to determine the effect on the measured coherence in the z-direction at various stations along the airfoil chord.

From Figure 5.30a, the coherences of the primary (589 Hz) and secondary tones (505 Hz, 680 Hz and 756 Hz) at the leading edge possessed values of 0.6 or higher, from $z/C = 0.015$ to 0.1. The strongest coherence tone was at 680 Hz with a maximum value of 0.7. At $z/C > 0.1$ the coherences decreased markedly to values of 0.4 or less. Measurements obtained further downstream at $x/C = 0.3$ are presented in Figure 5.30b. These data revealed that the strongest coherence did not belong to the 680 Hz tone, but to the primary tone at 589 Hz. The coherence of the previously strong secondary tone at 680 Hz decreased markedly, from 0.7 to 0.4. The coherence of the secondary tone at 756 Hz increased significantly from 0.2 to 0.6. Similarly to

the coherence values at $x/C = 1$, the coherence values decreased at $z/C > 0.1$.

At $x/C = 0.15$, the order of tonal coherence strengths varied again from $x/C = 1$ and 0.3. From Figure 5.30c the maximum tonal coherence was observed at the highest secondary tone frequency of 756 Hz. The primary tone coherence at 589 Hz changed from the strongest tone coherence at $x/C = 0.3$ to the weakest tone coherence at $x/C = 0.15$. Similarly to the coherence values at $x/C = 1$ and 0.3, the coherence values decreased at $z/C > 0.1$. Stronger coherence at frequencies less than 300 Hz were observed, due to the proximity to the trailing edge, corresponding to the broadband noise from the AWT flow and broadband diffraction processes at the trailing edge.

At the trailing edge, $x/C = 0$, the maximum tonal coherence values were observed at $z/C > 0.03$, not near the airfoil surface, as observed for $x/C \geq 0.3$ in Figure 5.30d. Near the trailing edge the hot-wire measurements were obtained within the boundary layer, as it had developed over 1 mm ($z/C = 0.015$) in height at this location. The low coherence values near the trailing edge suggest that the velocity fluctuations within the boundary layer did not contribute to the measured noise. The strongest coherence tone was the highest frequency secondary tone at 756 Hz, from $z/C = 0.03$ to 0.15. The other tones possessed weaker coherences up to $z/C \approx 0.08$, where the coherence at 509 Hz increased. The primary tone at 589 Hz and secondary tone at 680 Hz increased in coherence values from $z/C \approx 0.1$, reaching values of 0.6 to 0.7.

The tonal coherence values with respect to the airfoil chord were more difficult to explain. From Figure 5.30, it appeared that none of the tones possessed strong coherence along the entire chord. The highest frequency tone at 756 Hz possessed strong coherence from $x/C = 0$ to 0.3 but not at $x/C = 1$. The primary tone at 589 Hz displayed strong coherence from $x/C = 0.3$ to 1, but not near the trailing edge. Therefore there were segments along the airfoil chord where velocity fluctuations were responsible for producing some tones but not others. This showed that the primary and secondary tones were generated and observed at the same location. Further tests were performed, at $z/C = 0.015$ along the airfoil chord, from $x/C = 0$

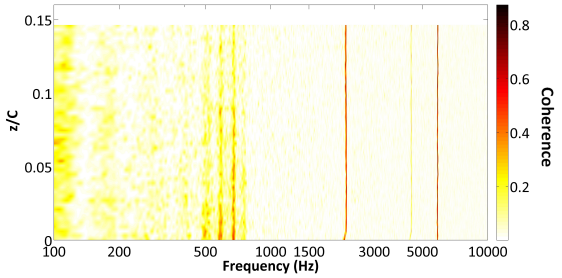

(a)

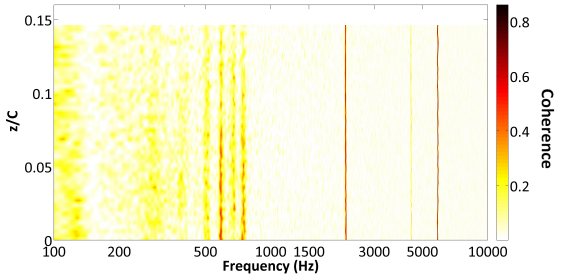

(b)

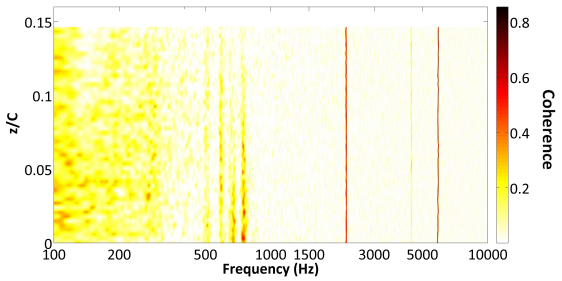

(c)

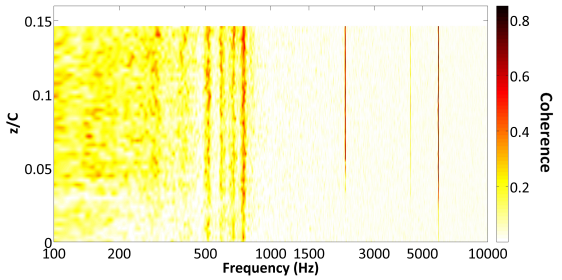

(d)

Figure 5.30: Coherence between flow and noise, measured at Re = 50,000 and $\alpha = 0°$. Measurements were obtained at $y/C = 0$ in $z/C = 0.003$ increments, from $z/C = 0.015$ to 0.15 at chordwise stations (a) $x/C = 1$ (leading edge), (b) $x/C = 0.3$, (c) $x/C = 0.15$ and (d) $x/C = 0$ (trailing edge).

to 1, for $\alpha = 0°$ and $Re = 50{,}000$, 100,000 and 150,000 to further understand the relationship of the tonal coherence with respect to the chord. The data are presented in Figure 5.31.

At $Re = 50{,}000$ and $\alpha = 0°$ the primary and secondary tones possessed a minimum coherence of approximately 0.2 along the airfoil chord and maxima of approximately 0.7, as presented in Figure 5.31a. For each acoustic tone, the coherence magnitude varied along the airfoil chord and the variation for each tone was unique. The tones with highest frequency possessed stronger coherence near the trailing edge than the lower frequency tones ($x/C = 0.1$ to 0.3) yet all of the tones possessed strong coherence near the leading edge ($x/C = 0.85$ to 1) with the exception of the rogue measurement at $x/C = 0.96$ where there was an abrupt change in coherence. It was assumed that this was caused due to accidental contact between the hot-wire probe and the airfoil surface during the traverse process from one chordwise station to the next. This abrupt change was not observed at other Reynolds numbers for the same angle of attack, strongly suggesting that the abrupt change is not due to highly localised flow behaviour. The harmonics of the primary tone at higher frequencies showed strong coherence with the flow for the entire chord length, with some weakening at $x/C = 0$ to 0.1.

As presented in Figure 5.31b, at $Re = 100{,}000$ the primary tone at 1426 Hz displayed very strong coherences along the entire chord, near unity at every chordwise measurement. The secondary tones possessed weaker coherences, with their maxima near the leading and trailing edges. The higher frequency secondary tone possessed stronger coherences than the lower frequency secondary tone. While the secondary tone coherences were not as strong as the primary tone, they still possessed some coherence along the entire chord, with values between 0.2 and 0.6. The coherence of the broadband hump frequency range was negligible, with the exception of the tonal frequencies. At frequencies less than 200 Hz, the broadband noise contribution provided strong coherence between $x/C = 0$ and 0.6. At $Re = 150{,}000$ and $\alpha = 0°$, the coherence values presented in Figure 5.31c differed significantly from $Re = 50{,}000$

and 100,000. There were weak coherences between $x/C = 0.1$ to 0.3 at the primary tone frequency of 2050 Hz. There existed very strong coherences for frequencies less than 300 Hz along the entire airfoil chord.

The variation of coherences along the chord were unique for each Reynolds number but some consistencies were observed. At $x/C = 0.1$ to 0.3, the strongest coherences were observed in the tonal frequency range for all Reynolds numbers. Local maxima were also observed near the leading edge and mid-chord the coherences were the weakest, with the exception of the primary tone frequency of 1426 Hz at $Re = 100{,}000$. Due to the significant differences in the coherence values for the tones at $Re = 50{,}000$ to 150,000 at $\alpha = 0°$, it was difficult to draw conclusions regarding whether the measured tones were produced from velocity fluctuations alone or they were influenced by facility effects of the AWT.

Figure 5.32 presents the coherence values at $z/C = 0.015$ along the airfoil chord, $x/C = 0$ to 1, for the pressure surface at $\alpha = 1.58°$ and $Re = 50{,}000$, 100,000 and 150,000. The coherences at $Re = 50{,}000$, shown in Figure 5.31a, possessed similarities with the results at $\alpha = 0°$, in that all of the tones at some point along the airfoil chord showed some strong coherence. Interestingly, the strongest coherence values were observed mid-chord on the pressure surface at $\alpha = 1.58°$, whereas they were present near the leading and trailing edges at $\alpha = 0°$.

There existed negligible coherence between the flow and noise signals on the airfoil pressure surface at $Re = 100{,}000$ and $\alpha = 1.58°$, as observed in Figure 5.31b. This result was unexpected, considering the strong coherence along the entire airfoil chord at this Reynolds number and $\alpha = 0°$. This result showed that the measured tonal noise was not produced by the velocity fluctuations measured by the hot-wire anemometry probe at $z/C = 0.015$. It is possible that the velocity fluctuations responsible for the tones existed further from the airfoil pressure surface than $z/C = 0.015$ and were thus not detected. In addition, the primary tone magnitude relative to the broadband hump at this flow condition was relatively low compared to $\alpha = 0°$ and the velocity fluctuations that were required to produce tonal noise were

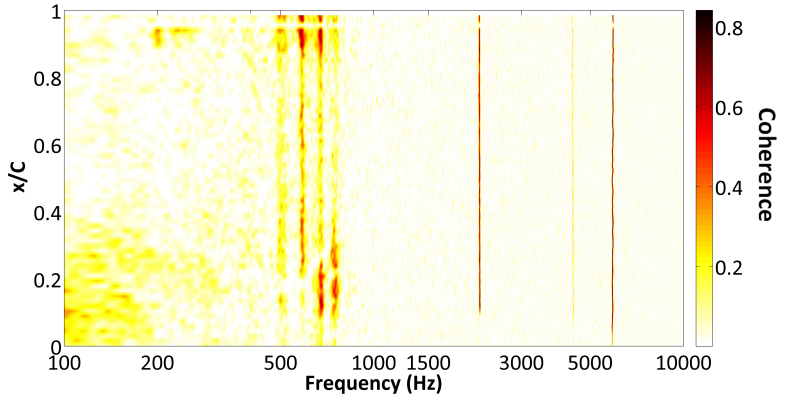

(a)

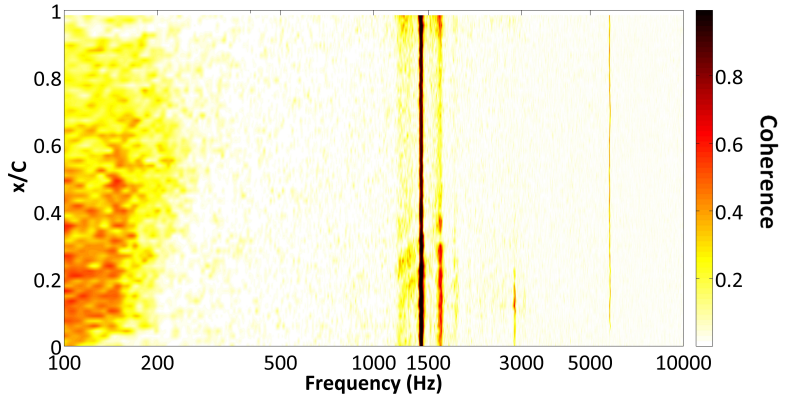

(b)

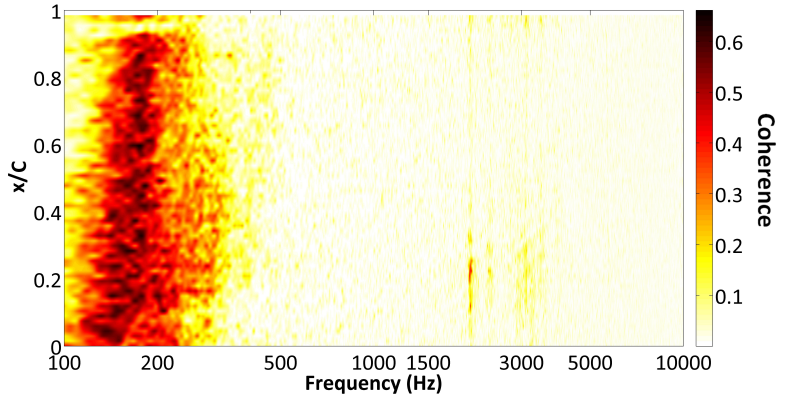

(c)

Figure 5.31: Coherence between flow and noise, measured at $\alpha = 0°$, $z/C = 0.015$, $y/C = 0$ along the airfoil profile from $x/C = 0$ to 1 and at $Re =$ (a) 50,000, (b) 100,000 and (c) 150,000.

significantly weaker in magnitude and thus produced weaker coherences between them.

From Figure 5.32c, there existed strong coherence values along the entire pressure surface at $Re = 150{,}000$ and $\alpha = 1.58°$ for the primary tone, and weak-to-moderate coherence values for the secondary tones near the leading and trailing edges. This Reynolds number displayed the strongest primary tone magnitude at this angle of attack and the strong coherence values along the chord reflect the causality between the velocity fluctuations that were responsible for generating this noise.

Figure 5.33 presents the coherence values at $z/C = 0.015$ along the airfoil chord, $x/C = 0$ to 1, for the suction surface at $\alpha = 1.58°$ and $Re = 50{,}000$, 100,000 and 150,000. By observation of Figure 5.33a, at $Re = 50{,}000$ all of the tones possessed moderate-to-strong coherence values of 0.5 to 0.7 along the entire chord, with the exception near the trailing edge, from $x/C = 0$ to 0.1.

The coherence values on the suction surface were negligible along the chord at $Re = 100{,}000$ as shown in Figure 5.33b. Therefore, at $Re = 100{,}000$ and $\alpha = 1.58°$, there was negligible coherence between the flow and noise on both airfoil surfaces.

The coherence values at $Re = 150{,}000$ on the suction surface were similar to those on the pressure surfaces, yet it was one of the secondary tones at 3378 Hz that possessed the strongest coherence along the entire chord. The primary tone and other secondary tones on the suction surface possessed stronger coherence values near the trailing edge ($x/C = 0$ to 0.4), whereas on the pressure side these coherences were strongest near the leading edge ($x/C = 0.9$ to 1). The region on the chord, $x/C = 0$ to 0.4, represents where the separated boundary layer was reattached to the suction surface. For the pressure surface, the secondary tone coherence values were strongest near the leading edge where the boundary layer was attached.

Selected single frequency coherence plots at the investigated Reynolds numbers and angles of attack are displayed to further assist the visualisation and understanding of the coherences between the flow and noise signals at the observed tone frequencies. Note that in these figures x/C increases from 0 to 1 from left

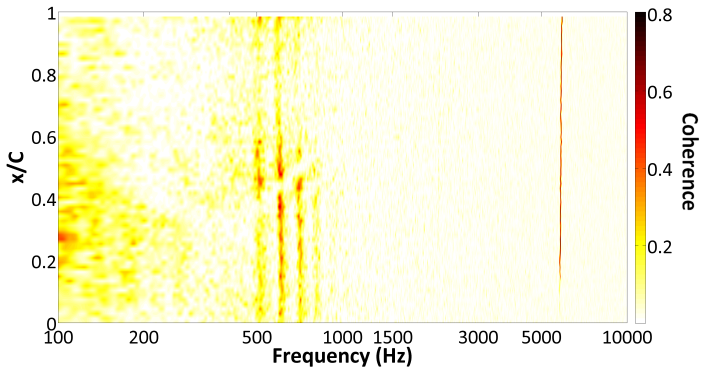

(a)

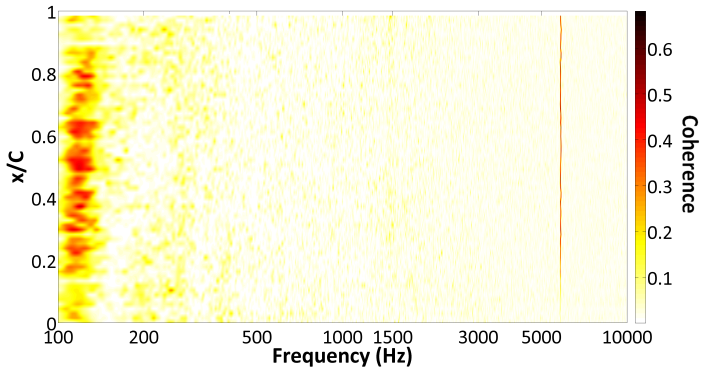

(b)

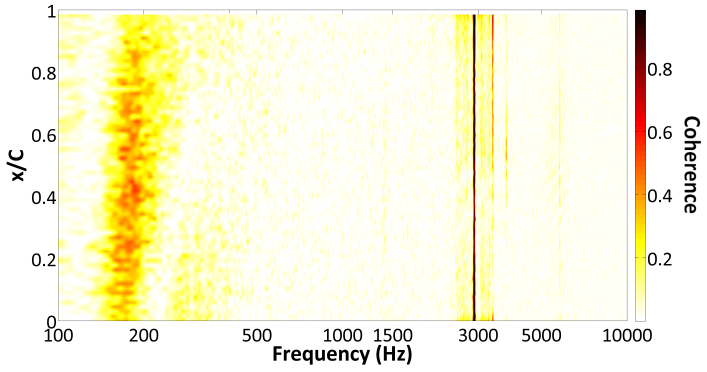

(c)

Figure 5.32: Coherence between flow and noise, measured on the pressure surface at $\alpha = 1.58°$, $z/C = 0.015$, $y/C = 0$ along the airfoil profile from $x/C = 0$ to 1 and at $Re =$ (a) 50,000, (b) 100,000 and (c) 150,000.

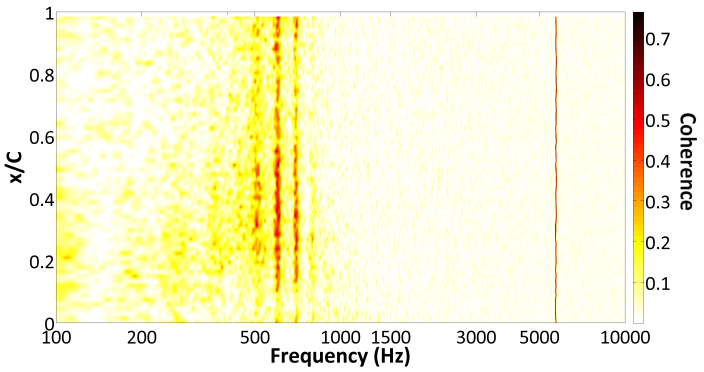

(a)

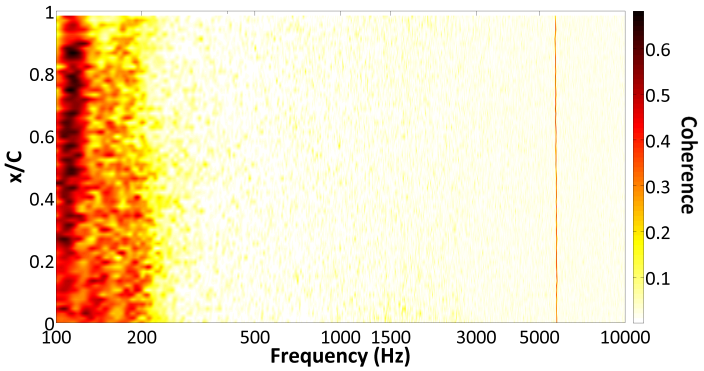

(b)

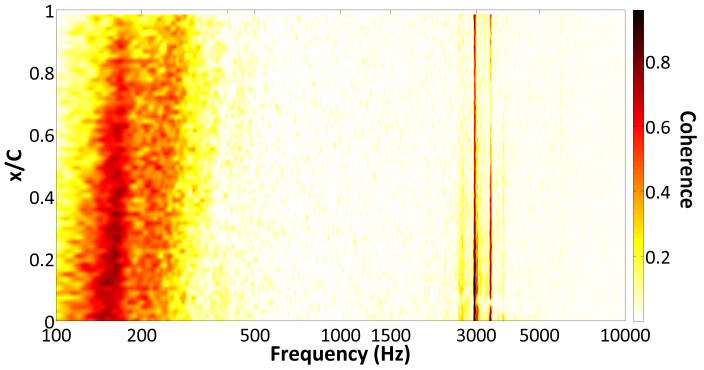

(c)

Figure 5.33: Coherence between flow and noise, measured on the suction surface at $\alpha = 1.58°$, $z/C = 0.015$, $y/C = 0$ along the airfoil profile from $x/C = 0$ to 1 and at $Re =$ (a) 50,000, (b) 100,000 and (c) 150,000.

to right. Figure 5.34 presents the primary and secondary tone frequency coherences at Re = 100,000 and 150,000 for $\alpha = 0°$. This figure helps illustrate the significant differences in the coherence at tonal frequencies between these two Reynolds numbers. At Re = 100,000, the primary tone clearly possessed very strong coherence along the entire airfoil chord, as observed in Figure 5.34a. The coherence at the secondary tone frequency of 1640 Hz was strongest closer to the trailing edge (x/C = 0 to 0.3) whereas the coherence at the secondary tone frequency of 1233 Hz was much weaker along the chord, with its maximum near the leading edge.

Increasing Re from 100,000 to 150,000 resulted in significant changes in the coherences of the flow and noise at the primary and secondary tone frequencies. As observed from Figure 5.34b, the coherence at the primary tone frequency did not exceed 0.4 and the strongest secondary tone coherence at 3108 Hz was near the leading edge. All of the other secondary tone frequencies possessed coherence values less than 0.25.

Figure 5.35 presents the coherence values between flow and noise at the primary and secondary tone frequencies at Re = 150,000 and $\alpha = 1.58°$ on both the airfoil pressure and suction surfaces. This helps observe the differences in coherence values at the tone frequencies between both surfaces.

From Figure 5.35a on the pressure surface, the primary tone at 2898 Hz possessed a strong coherence along the airfoil chord (values of 0.85 to 1), with a slight decrease in coherence value to 0.75 over approximately $x/C = 0.3$ to 0.4. The secondary tone frequency at 3378 Hz possessed strong coherence at the trailing edge and near the leading edge (x/C = 1 to 0.85) and weakened strength mid-chord, between $x/C = 0.1$ to 0.55. Another secondary tone frequency at 3055 Hz possessed negligible coherences near the trailing and leading edges but possessed moderate coherence values (near 0.5) mid-chord, at $x/C = 0.5$ to 0.6. The other secondary tone frequencies showed negligible coherence values along the chord, with coherence values less than 0.35.

Figure 5.35b shows the coherence values at the same tone frequencies, obtained

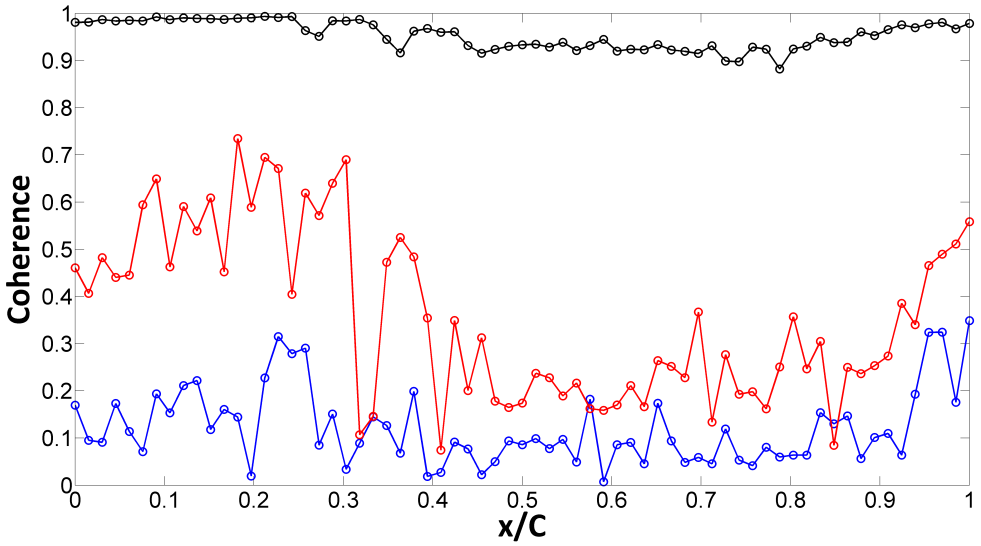

(a)

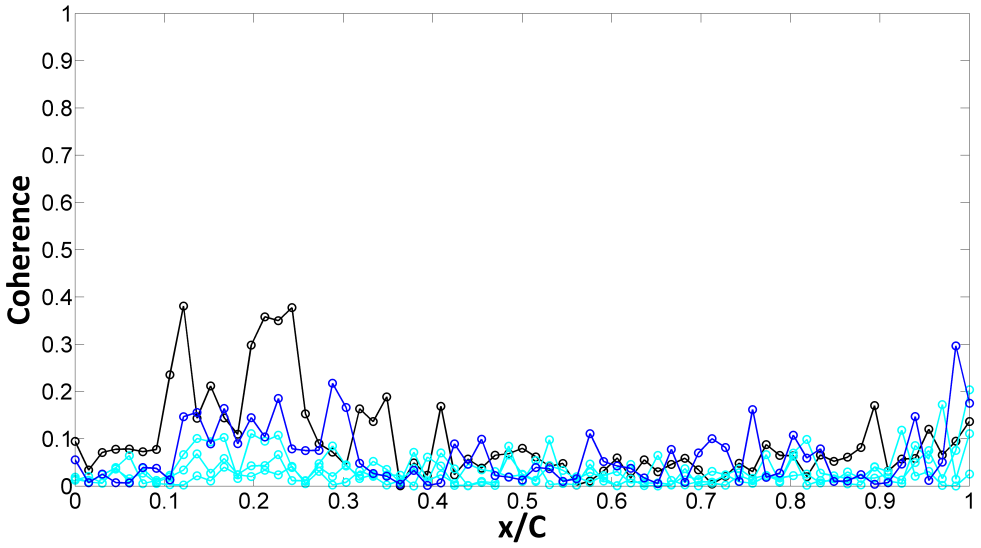

(b)

Figure 5.34: Coherence values between flow and noise, measured at $\alpha = 0°$, $y/C = 0$ and $z/C = 0.015$, from $x/C = 1$ to 0. (a) Re = 100,000 and the black, red and blue lines represent 1426 Hz (primary tone), 1640 Hz (secondary tone) and 1233 Hz (secondary tone) respectively. (b) Re = 150,000 and the black, blue and cyan lines represent 2050 Hz (primary tone), 3108 Hz (secondary tone) and all other secondary tone frequencies (1738 Hz, 2395 Hz and 2780 Hz) respectively.

on the airfoil suction surface. Interestingly, the primary tone frequency at 2898 Hz showed negligible coherence along the airfoil chord and the secondary tone frequency at 3378 Hz possessed strong coherence values from the trailing edge to $x/C \approx 0.4$. By observing the coherence values at 3378 Hz on both the pressure and suction surfaces, it can be seen that on the chordwise locations that showed strong coherence values on one surface, the other surface showed weak coherence values. All other secondary tone frequencies showed weak coherence values, below approximately 0.4.

By observing the coherence between the flow and noise signals, in most cases, there existed strong causality between the velocity fluctuations in the boundary layer and the measured tones. Some cases defied this pattern, such as the flow conditions where the secondary tone possessed stronger coherence values than the primary tone. There were some cases, such as $Re = 100{,}000$ and $\alpha = 1.58°$, that displayed negligible coherence between flow and noise, that may be due to the location of the hot-wire probe relative to the small boundary layer. During investigations of the suction airfoil surface, the hot-wire probe was out of the line-of-sight of the microphone (i.e., the microphone was 600 mm above the airfoil, and the hot-wire probe was 1 mm under the airfoil). This may have impacted the coherence between the flow and noise signals, relative to the $\alpha = 0°$ and 1.58° pressure surface investigations.

5.2.3 Influence of boundary layer trips

This section discusses the influence on boundary layer trips on the measured noise and MASL. The section was divided into three parts discussing: the upper surface trip; applying trips to both airfoil surfaces; and the influence of trips on the MASL.

5.2.3.1 One surface trip

Figure 5.36 presents the PSDs when a trip was applied solely to the upper airfoil surface. The tripped airfoil at $Re = 50{,}000$ and $\alpha = 0°$ produced less self-noise for frequencies less than 800 Hz than the untripped airfoil, as observed in Figure 5.36a.

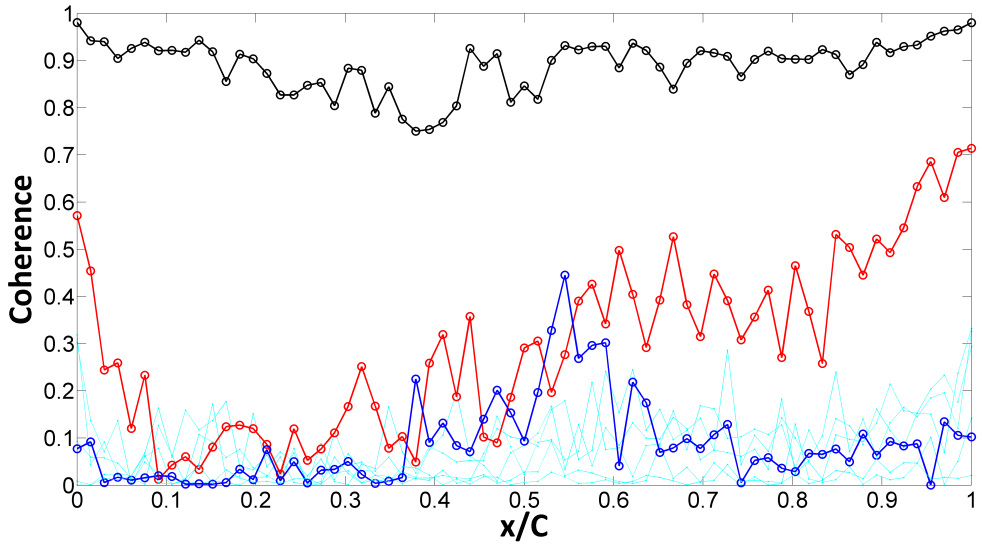

(a)

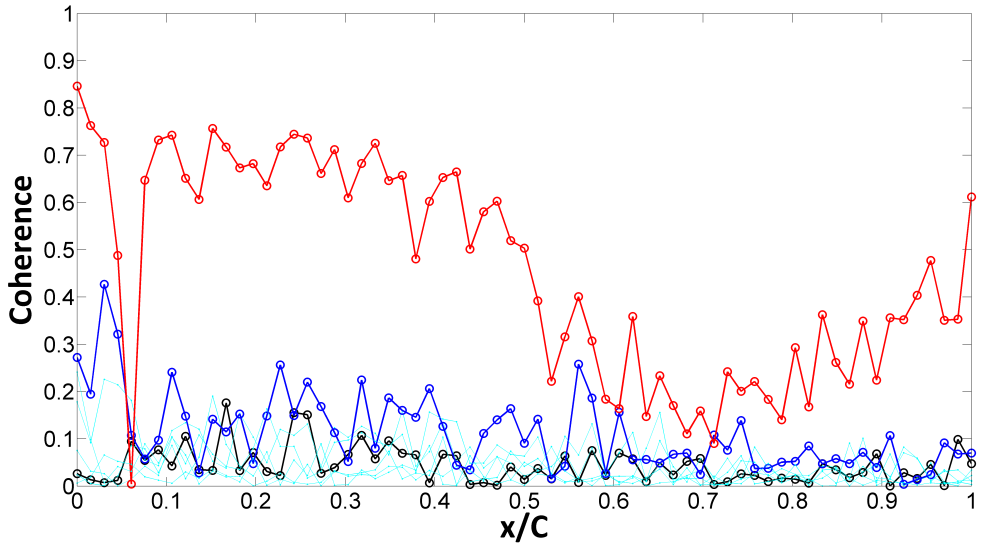

(b)

Figure 5.35: Coherence values between flow and noise, measured at Re = 150,000 and $\alpha = 1.58°$. Measurements were obtained at $y/C = 0$ and $z/C = 0.015$, from x/C = 1 to 0 on the (a) pressure surface and (b) suction surface. The black, red, blue and cyan lines represent 2898 Hz (primary tone), 3378 Hz (secondary tone), 3055 Hz (secondary tone) and all other secondary tone frequencies (2047 Hz, 2523 Hz, 2728 Hz, 3754 Hz and 4050 Hz) respectively.

At frequencies greater than 800 Hz, the tripped and untripped airfoils produced similar broadband noise magnitudes. The observed broadband contribution centred at 600 Hz for the untripped airfoil was 20 dB greater in magnitude than the tripped case. Both the tripped and untripped noise displayed peaks at the same tonal frequencies, with decreased magnitudes for the tripped case. The airfoil self-noise was dependent on an interaction of the flow on both sides of the airfoil and one airfoil surface alone could not produce the untripped noise.

The differences in the untripped and tripped PSDs at Re = 75,000 to 150,000 were far less significant than at Re = 50,000. At Re = 75,000, four tones were identified at 970 Hz, 1110 Hz, 1260 Hz and 1400 Hz, as shown in Figure 5.36b. Applying a trip to the upper surface of the airfoil did not affect frequencies of any of the tones but did affect their magnitude. The primary tone magnitude at 1110 Hz decreased by 2 dB by introducing the trip on the upper surface of the airfoil. It was possible that the trip on the upper surface caused the primary tone magnitude to decrease, but 2 dB was within the error bounds of the microphone sampling method. The effect of the trip on the secondary tones varied for each tone. At 970 Hz, the magnitude of the tone was 2 dB less than the untripped airfoil (within error bounds), whereas at 1260 Hz, the tone was 12 dB less than for the untripped airfoil. At 1400 Hz, the tone observed for the untripped airfoil was not present when the trip was introduced. It can be deduced that disturbing the boundary layer on one airfoil surface using a trip decreased the magnitudes of each tone differently, with a greater difference in amplitudes at higher frequencies.

Applying a trip to the upper airfoil surface at Re = 100,000 caused the primary tone magnitude at 1426 Hz to decrease by 5 dB, relative to the untripped airfoil. The secondary tone at 1233 Hz was unaffected whereas the secondary tone at 1640 Hz decreased in magnitude by 3 dB. These comparisons can be observed in Figure 5.36c. Because the magnitude change of each tone differed by applying the trip line on one surface of the airfoil, it was possible that each tone was reinforced by separate mechanisms, requiring unique interactions with the other airfoil surface.

Similar behaviour was also observed at $Re = 125{,}000$. The primary and secondary tone magnitudes also decreased by varying amounts, as presented in Figure 5.36d.

At $Re = 150{,}000$, both the tripped and untripped PSDs show a distinct primary tone at 2039 Hz and a broadband contribution between 1000 Hz and 4000 Hz, as shown in Figure 5.36e. The secondary tones at 1738 Hz and 2395 Hz appear to have the same frequency and magnitude for both the tripped and untripped cases. Upon closer inspection, both the primary tone and secondary tones were approximately 2 dB greater in magnitude than for the untripped airfoil; this is within the error bounds of the magnitude estimation.

Interrupting the boundary layer on the lower surface of the airfoil produced near-identical results to interrupting the boundary layer on the upper surface. This showed that the tonal noise generation mechanisms at $\alpha = 0°$ did not occur on one airfoil surface only and that the flows over both surfaces were responsible for the measured noise without trips. By observing distinct similarity in the PSDs of the upper trip only and lower trip only experiments also showed that the tonal noise generating mechanisms existed on both sides and that their contribution to the PSD was equal or near-equal. The contribution of the broadband noise from each airfoil surface was harder to deduce. The trip line interfered with the flow causing the rapid formation of a turbulent boundary layer downstream of it. Turbulent boundary layers possess broadband noise generating mechanisms that differ from an untripped airfoil at low-to-moderate Reynolds number. Thus quantifying the differences in broadband noise magnitudes from a tripped to untripped PSD would not result in a true measure of the broadband noise generation of one airfoil surface only.

The effect on tonal noise magnitudes via interrupting the boundary layer on one airfoil surface was more pronounced at lower Reynolds numbers ($Re = 50{,}000$ and 75,000) than at higher Reynolds numbers ($Re = 100{,}000$ to 150,000). The impact of the trip line at $Re = 150{,}000$ did not cause significant noise reduction, yet at $Re = 50{,}000$ the tonal and broadband noise contributions were decreased by

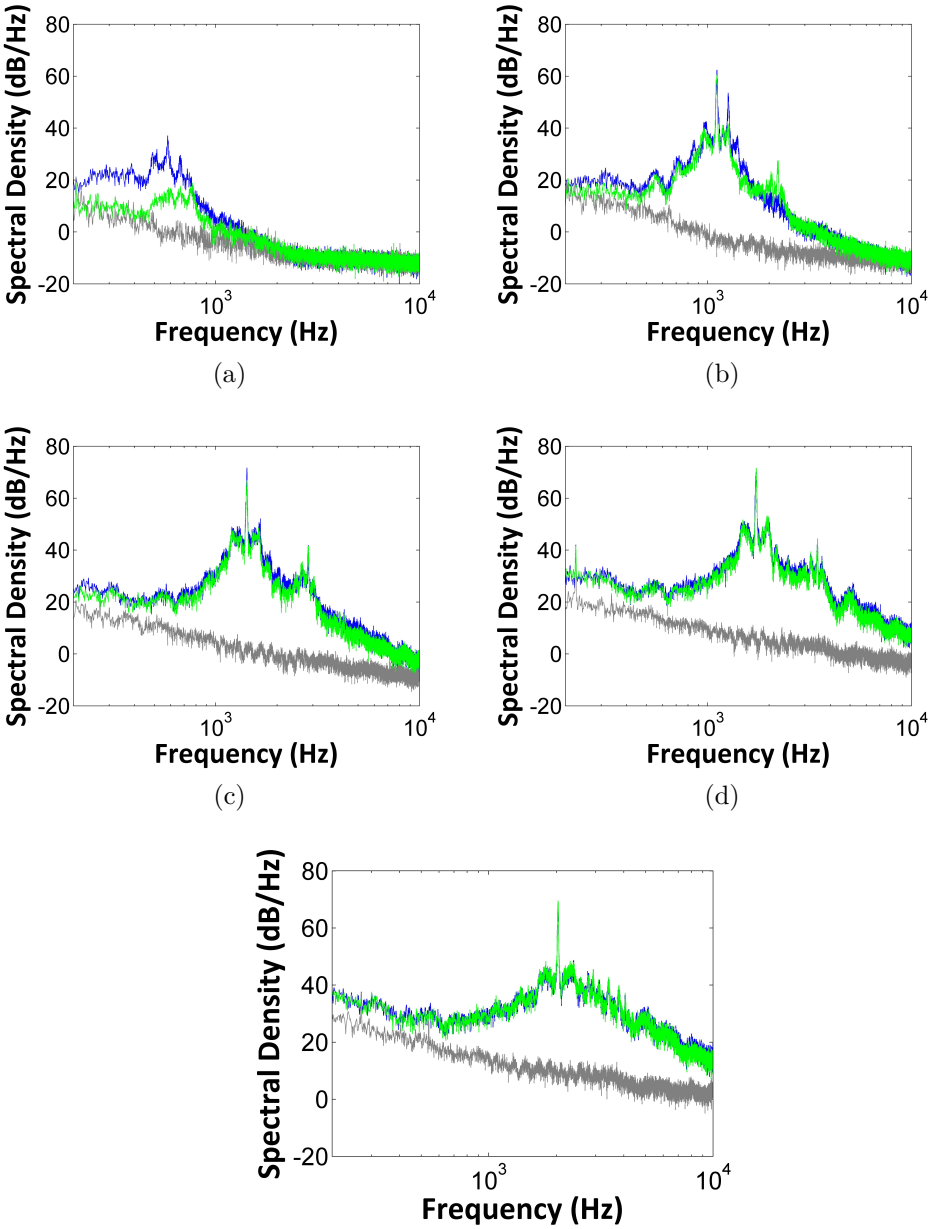

Figure 5.36: PSDs of a NACA 0012 airfoil and with a trip on the upper airfoil surface, at $\alpha = 0°$ and a Reynolds number of (a) 50,000, (b) 75,000, (c) 100,000, (d) 125,000 and (e) 150,000. The blue, green and grey lines represent the untripped NACA 0012 airfoil, the tripped airfoil on the upper surface and the background noise with flow respectively.

Table 5.8: Decrease in noise magnitude when a trip line was applied to the airfoil upper surface, compared to the untripped airfoil at $\alpha = 0°$. Entries that have (0) adjacent to them identify values that are within the dB error estimate.

Re	Decrease in noise magnitude (dB)		
	Primary ($f_{n,max}$)	Secondary ($f_{n,max} > f_n$)	Secondary ($f_{n,max} < f_n$)
50,000	20	15	12
75,000	2 (0)	2 (0)	12
100,000	5	0	3 (0)
125,000	0	0	0
150,000	-2 (0)	-2 (0)	-2 (0)

up to 20 dB. The effects of the trip line on the primary and secondary tones were quantified in Table 5.8 which contains two columns identifying secondary tones. The tones $f_{n,max} > f_n$ and $f_{n,max} < f_n$ are the secondary tones, f_n, with a lower and higher frequency than the primary tone, $f_{n,max}$, respectively. To denote the values within the error estimate, a (0) was placed adjacent to them. The results in Table 5.8 show that increasing the Reynolds number with a disturbed boundary layer on one surface decreased its effect on the noise spectrum. This further suggests that the mechanisms responsible for creating both primary and secondary tones are less susceptible to the disturbance of one boundary layer at higher Reynolds numbers.

The MASL values for the upper surface tripped airfoil are not presented here as they were very similar to the untripped MASL values. The standing wave pattern was observed in the tonal and broadband hump frequency range, and at low signal to noise ratios the MASL was averaged about the trailing edge. There was a small net shift of the MASL values upstream, by an average of $x/C = 0.05$. This can be explained by an interaction of the flow with the trip line, creating an acoustic source radiating broadband noise at the trip line. The beamformer cross-spectral output resulted from a combination of the trailing edge and trip line noise sources. This shifted the MASL upstream, as the beamformer was not able to detect the two distinct sources.

5.2.3.2 Both surface trips

Applying trips to both airfoil surfaces produced broadband noise only, as observed in Figure 5.37. Disturbing the natural development of the boundary layer on both surfaces of the airfoil disrupted all tonal noise generating mechanisms. These results also showed that applying a trip of this nature to any airfoil surface will completely cease the existence of a tonal noise generating mechanism on that surface. It can be further deduced that the tones measured when a trip was applied to one airfoil surface only, were due to the mechanism that existed on the untripped surface only. The interaction of the tripped surface with the untripped surface provided no contribution to the magnitude of those tones but only to the measured broadband noise. The broadband contributions observed in the PSDs were due to the interaction of turbulent boundary layers formed by the airfoil trips on both surfaces with the airfoil trailing edge. Tones were not present when both airfoil surfaces were tripped, causing the MASL to be averaged about the trailing edge, as recorded for broadband-only noise.

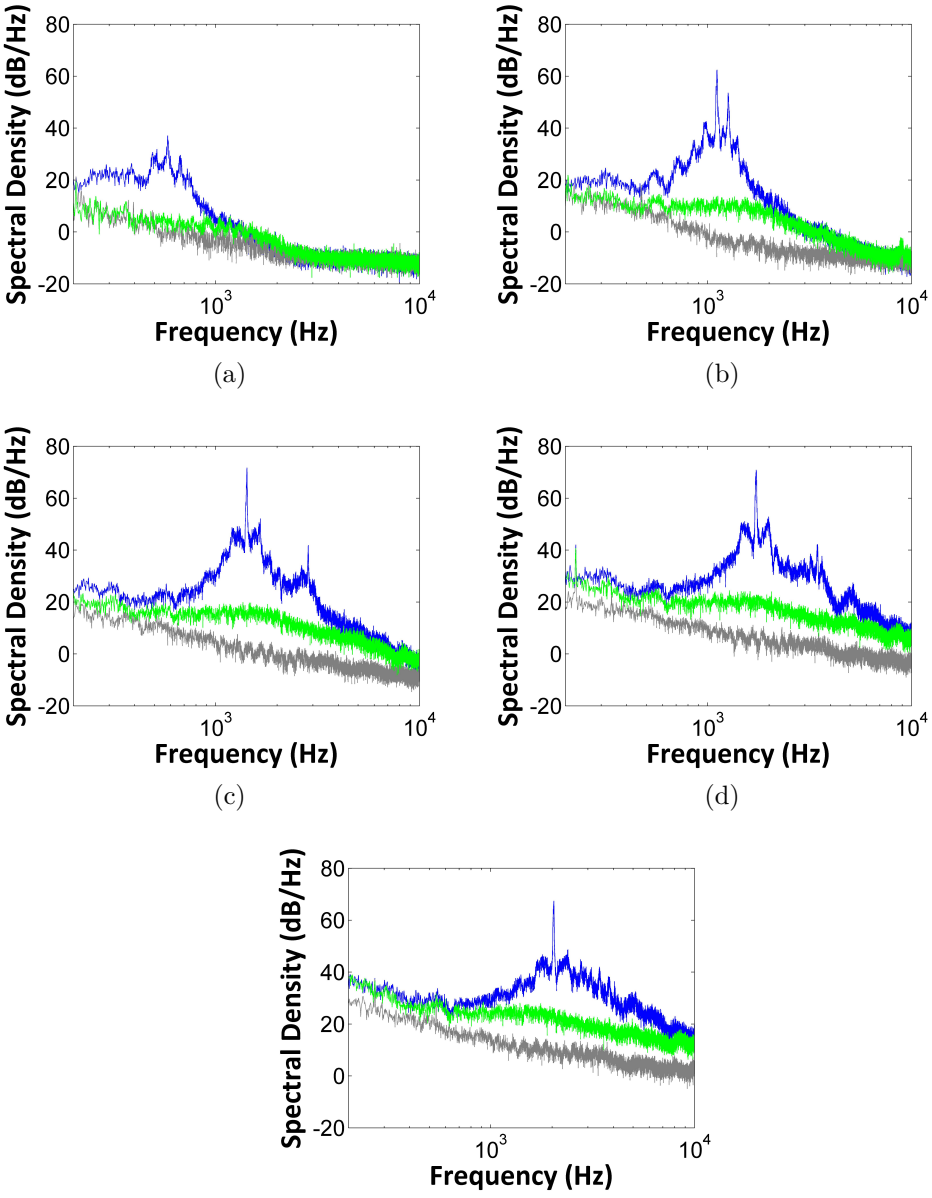

Figure 5.37: PSDs of a NACA 0012 airfoil and with a trip on both airfoil surfaces, at $\alpha = 0°$ and a Reynolds number of (a) 50,000, (b) 75,000, (c) 100,000, (d) 125,000 and (e) 150,000. The blue, green and grey lines represent the untripped NACA 0012 airfoil, the tripped airfoil on both surfaces and the background noise with flow respectively.

5.2.4 Discussion of facility effects

This section provides a discussion of the feasibility of non-feedback related mechanisms. There was no conclusive evidence to suggest that the tone producing mechanisms were or were not due to an acoustic feedback mechanism or a combination of vortex shedding and an acoustic feedback mechanism. Insufficient bandwidth in acoustic spectra prevented Paterson et al. (1973) observing a series of secondary tones, leading to their proposed vortex shedding theory. This alone was not capable of explaining the secondary tones and the entire acoustic spectrum observed for all Reynolds numbers and angles of attack. Their theory upon closer inspection however cannot be totally disregarded, as it did not eliminate the possibility of the primary acoustic tone being totally or partially formed via vortex shedding and the secondary tones being caused by an acoustic feedback mechanism.

Nash et al. (1999) measured primary and secondary tones via experiment in a hard-walled wind tunnel. Despite the observation of secondary tones, they proposed that the primary tone was due solely to a vortex shedding process and that the secondary tones were generated by facility effects. They proposed this theory for tonal noise generation for a series of Reynolds numbers and non-zero angles of attack. Tam and Ju (2011) supported this theory via DNS, showing that at Re = 200,000 to 500,000 and $\alpha = 0°$ there existed only a primary tone.

At Re = 150,000 and $\alpha = 0°$, a primary tone was measured with secondary tones of diminished strength compared to lower Reynolds numbers. The magnitude of the broadband hump grew with increasing Reynolds number as the tone magnitudes diminished. If this behaviour was to continue to Re = 200,000, it could be possible that the secondary tone magnitudes would not be detected, as the broadband hump magnitude would be greater than them, resulting in the measurement of a single primary tone superimposed on a strong broadband hump. Therefore, Tam and Ju's (2011) theory of secondary tones being caused by facility effects may not be valid at $Re > 150,000$, but accurate for their considered Reynolds number range. Unfortunately the AWT fan speed limited the maximum testable Reynolds number

to approximately 150,000 so this could not be experimentally verified.

Results by Nash et al. (1999) were presented for Reynolds numbers greater than 200,000 at non-zero angles of attack. Tam and Ju (2011) did not eliminate the possibility of secondary tone measurements at non-zero angle of attack measurements. Therefore Tam and Ju's (2011) study did not directly support Nash et al.'s (1999) theory. The present study showed that secondary tones were indeed present for a range of Reynolds numbers and angles of attack, similar to other experimental studies, including Arbey and Bataille (1983) and Chong and Joseph (2009). The experimental facilities used in these studies included airfoils of different chord lengths, walls of different reflective properties and anechoic rooms of varying dimensions. Therefore it is highly unlikely that facility effects were solely responsible for secondary tone generation.

Chapter 6

Acoustic Feedback Mechanisms

This chapter presents an analysis of potential acoustic feedback mechanisms, using parameters obtained via experiment and presented in the previous chapter. An acoustic feedback model proposed by Arbey and Bataille (1983) is used to investigate various feedback lengths and predicted acoustic tones were compared with experimentally measured tones. A new acoustic feedback model is proposed, incorporating a dual acoustic feedback mechanism.

6.1 Acoustic feedback models

The analysis of various feedback lengths that were used in Arbey and Bataille's (1983) feedback model are covered in this section. Recall from Section 2.3.6

$$f_n = \frac{C_r}{L}\left(n + 0.5\right)\left(1 + \frac{C_r}{C_0 - U}\right)^{-1} \tag{6.1}$$

where f_n represents the tone frequency (Hz) as a function of n, L is the feedback loop length, C_r is the convection flow velocity, C_0 is the speed of sound (343 m/s), U is the free-stream flow speed (m/s) and n is a positive integer, that is determined by the best fit between f_n and experimentally/numerically obtained tone frequencies using the feedback model. The plausible feedback lengths from the previous chapter

were analysed using this model and comparisons were made between the predicted and measured tones.

Previous work (Tam, 1974; Arbey and Bataille, 1983; Desquesnes et al., 2007) used constant values of C_r and L with respect to Reynolds number and angle of attack, yet experiments from this study revealed this was not necessarily the case. Use of values of L and C_r as functions of Re and α is unique to this research and these were investigated using Arbey and Bataille's (1983) model. Tam (1974), Desquesnes et al. (2007) and Chong and Joseph (2009) concluded that the MASL was slightly downstream of the trailing edge and therefore their feedback lengths are not comparable with the lengths investigated here.

Arbey and Bataille's (1983) model was used to replicate their results using their experimental data at Re = 107,000 and $\alpha = 0°$. This was done to determine the accuracy of their predicted tones using MMVL as a feedback length, where in their case L = 69 mm. They used an 80 mm chord in a freestream flow of 20.2 m/s. It was assumed that C_0 was 343 m/s. The convective speed ratio was not provided in their paper, but by knowing their predicted tone frequencies and corresponding values of n, it was estimated as $C_r/U = 0.588$ via trial and error. The predicted tones here matched those in their paper within less than 1 Hz. The error between their predicted tones and their experimentally obtained tones was 3% or less.

Their theory claimed that the measured tones would be equispaced for all flow conditions. At Re = 107,000 and $\alpha = 0°$, they predicted an equispacing of 166 Hz. Their experimental data, however, revealed that the tones were not equispaced; the differences between the tones had an average of 161 Hz with a standard deviation of 23 Hz. The results of the current experiments in the AWT also showed that the tones were not equispaced. It was difficult to compare the current results with Arbey and Bataille's (1983) data because of the difference in Reynolds numbers and chord lengths, but for the current experiments at Re = 100,000 and $\alpha = 0°$, the tones were separated by an average of 204 Hz with a standard deviation of 18 Hz. Both the current experimental data and Arbey and Bataille's (1983) data showed

that the tones were not equispaced and therefore Arbey and Bataille's (1983) model could only ever at best provide good agreement, but never an exact match, with experimental data.

6.1.1 Leading edge to TE, L_{LE}

For the current study this was simply the chord value of $L_{LE} = 67$ mm for all Reynolds numbers and angles of attack. The results of using L_{LE} in the feedback model (Equation 6.1) for $\alpha = 0°$ and $1.58°$ are provided in Table 6.1.

As observed from Table 6.1 there existed reasonable agreement between the measured and predicted tones using L_{LE}. The largest prediction error was 6% for the primary tone at $Re = 50{,}000$ and $\alpha = 1.58°$ and the lower frequency secondary tone at $Re = 100{,}000$ and $\alpha = 0°$. All of the other tone predictions were within 4%. Furthermore, recall the coherences between flow and noise at the primary tone frequencies were strong along the airfoil chord, at $\alpha = 0°$ and $Re = 50{,}000$, 100,000 as presented in Figures 5.31a and 5.31b respectively. This could provide evidence for disturbances originating at the airfoil leading edge, propagating downstream to the trailing edge where the acoustic source originated, radiating back upstream to the leading edge and closing an acoustic feedback loop.

Table 6.1: Acoustic feedback analysis using L_{LE} at $\alpha = 0°$ and 1.58°. In each cell, the top number is the predicted tone, f_n (Hz), and the bracketed number adjacent to it is the corresponding value of n. The number in the middle of each cell is the experimentally measured tone frequency (Hz) and the relative error (%) of f_n with respect to the experimentally measured tone is provided at the bottom of each cell. The experimentally measured primary tones are presented in bold case.

Re ($\times 10^3$)	Tone frequencies (Hz) using L_{LE}							
	L_{LE}: $\alpha = 0°$							
50	506(9)	612(11)	666(12)	772(14)				
	505	**589**	680	756				
	≤ 1%	4%	2%	2%				
100	1307(10)	1432(11)	1681(13)					
	1233	**1426**	1640					
	6%	≤ 1%	3%					
150	1722(8)	1925(9)	2330(11)	2736(13)				
	1738	**2050**	2395	2780				
	1%	4%	3%	2%				
	L_{LE}: $\alpha = 1.58°$							
50	495(6)	571(7)	724(9)					
	517	**607**	713					
	4%	6%	2%					
100	1274(8)	1424(9)	1724(11)	1874(12)	2024(13)			
	1236	**1463**	1701	1862	2035			
	3%	3%	1%	≤ 1%	≤ 1%			
150	2031(10)	2611(13)	2804(14)	2998(15)	3191(16)	3384(17)	3771(19)	3965(20)
	2047	2523	2728	**2898**	3055	3378	3754	4050
	≤ 1%	4%	3%	3%	4%	≤ 1%	≤ 1%	2%

6.1.2 Point of maximum velocity to TE, L_U

Arbey and Bataille (1983) used the MMVL as their feedback loop length, with the assumption that the acoustic source was at the trailing edge. Their feedback lengths did not assume a Reynolds number dependence, although from experiment it was found that the MMVL was not constant with Reynolds number at non-zero angles of attack. Their experiments were performed at $\alpha = 0°$ only and thus it remains to be seen as to whether this feedback length would accurately predict tones at non-zero angles of attack. The values of L_U obtained via experiment and XFOIL (Drela, 1989) are listed in Table 6.2. For $\alpha = 1.58°$, the feedback lengths on the airfoil pressure and suction surfaces were denoted by L_{Up}/L_{UXp} and L_{Us}/L_{UXs} respectively. Note that these lengths are linear, straight-lines, not the distance corresponding to the curved distance along the airfoil chord.

For all Reynolds numbers, agreement within 1 mm ($x/C = 0.015$) was achieved between the experimentally measured and XFOIL MMVL values, at $\alpha = 0°$ and the pressure surface at $\alpha = 1.58°$. On the airfoil suction surface at $\alpha = 1.58°$ the maximum observed difference was 5 mm ($x/C = 0.075$) with the other measurements being within 3 mm ($x/C = 0.045$). The experimentally measured and XFOIL obtained feedback lengths were each used in the feedback model and the comparison of measured and predicted tones are provided in Tables 6.3 and 6.4 respectively.

Using the experimentally measured values of L_U, the primary and secondary tones were predicted to within 4%, for all Reynolds numbers at $\alpha = 0°$. On the airfoil pressure surface at $\alpha = 1.58°$, all of the primary and secondary tones were predicted within 4% and 5% respectively employing L_{Up} as a feedback length. Using the feedback length on the airfoil suction surface, L_{Us}, at $Re = 50{,}000$ and $\alpha = 1.58°$ showed a poorer agreement with the measured tones, with errors up to 16%. Two of the secondary tones, with frequencies 2728 Hz and 3055 Hz were not able to be predicted with a suitable integer value of n. Much better agreement was achieved at $Re = 100{,}000$ with errors within 4%. Therefore at lower Reynolds numbers there existed no valid acoustic feedback mechanisms at non-zero angle of attack using L_{Us}

Table 6.2: Values of L_U for acoustic feedback loop analysis, as obtained via XFOIL (Drela, 1989) and hot-wire anemometry experiments for $\alpha = 0°$ and 1.58°. A positive angle of attack represents the airfoil pressure side, L_{Up} (experimental) and L_{UXp} (XFOIL); a negative angle represents the airfoil suction side, L_{Us} (experimental) and L_{UXs} (XFOIL).

Re ($\times 10^3$)	L_U, L_{Up} and L_{Us} (mm)		
	0°	1.58°	-1.58°
50	58	63	41
100	58	63	45
150	58	63	43
	L_{UX}, L_{UXp} and L_{UXs} (mm)		
	0°	1.58°	-1.58°
50	58	63	40
100	58	63	40
150	58	63	40

as an acoustic feedback length. The airfoil pressure surface feedback length, L_{Up}, appears to be a reasonable candidate.

The values of L_{Up} and L_{UXp} did not differ for the flow conditions considered. Therefore the comparison between the experimentally measured and XFOIL obtained feedback lengths was for the suction surface, L_{Us} and L_{UXs}. The greatest error measurement at $\alpha = 1.58°$ using L_{Us} was 16% for the lowest frequency secondary tone at Re = 50,000. A similar result was observed using L_{UXs}, being a 14% error for the same tone. The other tones were predicted within 9% using L_{UXs}, whereas L_{Us} predictions lay within 8%. There were no significant differences in the prediction of tones using L_U and L_{UX} feedback lengths at zero and non-zero angles of attack. Overall, reasonable agreement was observed using either experimental or XFOIL measured lengths at $\alpha = 0°$ (errors within 4%) and on the airfoil pressure surface at $\alpha = 1.58°$ (errors within 5%).

Table 6.3: Acoustic feedback analysis using L_U, L_{Up} and L_{Us} at $\alpha = 0°$ and 1.58°. In each cell, the top number is the predicted tone, f_n (Hz), and the bracketed number adjacent to it is the corresponding value of n. The number in the middle of each cell is the experimentally measured tone frequency (Hz) and the relative error (%) of f_n with respect to the experimentally measured tone is provided at the bottom of each cell. The experimentally measured primary tones are presented in bold case.

Re ($\times 10^3$)	Tone frequencies (Hz) using L_U, L_{Up} and L_{Us}							
	L_U: $\alpha = 0°$							
50	527(6)	608(7)	689(8)	770(9)				
	505	**589**	680	756				
	4%	3%	1%	2%				
100	1223(8)	1366(9)	1654(11)					
	1233	**1426**	1640					
	≤ 1%	4%	≤ 1%					
150	1756(7)	1990(8)	2458(10)	2692(11)				
	1738	**2050**	2395	2780				
	1%	3%	3%	3%				
	L_{Up}: $\alpha = 1.58°$							
50	527(6)	608(7)	689(9)					
	517	**607**	713					
	2%	≤ 1%	3%					
100	1196(7)	1514(9)	1674(10)	1833(11)	1993(13)			
	1236	**1463**	1701	1862	2035			
	3%	4%	2%	2%	2%			
150	1954(9)	2571(12)	2777(13)	2982(14)	3188(15)	3394(16)	3805(18)	4011(19)
	2047	2523	2728	**2898**	3055	3378	3754	4050
	5%	2%	2%	3%	4%	≤ 1%	1%	1%
	L_{Us}: $\alpha =$ -1.58°							
50	436(3)	560(4)	685(5)					
	517	**607**	713					
	16%	8%	4%					
100	1228(5)	1451(6)	1674(7)	1897(8)	2120(9)			
	1236	**1463**	1701	1862	2035			
	≤ 1%	≤ 1%	2%	2%	4%			
150	1959(6)	2561(8)	n/a	2863(9)	n/a	3465(11)	3767(16)	4068(19)
	2047	2523	2728	**2898**	3055	3378	3754	4050
	4%	2%	n/a	1%	n/a	3%	≤ 1%	≤ 1%

Table 6.4: Acoustic feedback analysis using L_{UX}, L_{UXp} and L_{UXs} at $\alpha = 0°$ and 1.58°. In each cell, the top number is the predicted tone, f_n (Hz), and the bracketed number adjacent to it is the corresponding value of n. The number in the middle of each cell is the experimentally measured tone frequency (Hz) and the relative error (%) of f_n with respect to the experimentally measured tone is provided at the bottom of each cell. The experimentally measured primary tones are presented in bold case.

Re ($\times 10^3$)	Tone frequencies (Hz) using L_{UX}, L_{UXp} and L_{UXs}							
	L_{UX}: $\alpha = 0°$							
50	523(8)	584(9)	707(11)	769(12)				
	505	**589**	680	756				
	4%	≤ 1%	4%	2%				
100	1223(8)	1366(9)	1654(11)					
	1233	**1426**	1640					
	≤ 1%	4%	≤ 1%					
150	1756(7)	1990(8)	2458(10)	2692(11)				
	1738	**2050**	2395	2780				
	1%	3%	3%	3%				
	L_{UXp}: $\alpha = 1.58°$							
50	527(6)	608(7)	689(9)					
	517	**607**	713					
	2%	≤ 1%	3%					
100	1196(7)	1514(9)	1674(10)	1833(11)	1993(13)			
	1236	**1463**	1701	1862	2035			
	3%	4%	2%	2%	2%			
150	1954(9)	2571(12)	2777(13)	2982(14)	3188(15)	3394(16)	3805(18)	4011(19)
	2047	2523	2728	**2898**	3055	3378	3754	4050
	5%	2%	2%	3%	4%	≤ 1%	1%	1%
	L_{UXs}: α = -1.58°							
50	447(3)	574(4)	702(5)					
	517	**607**	713					
	14%	5%	2%					
100	1130(4)	1381(5)	1632(6)	1883(7)	2134(8)			
	1236	**1463**	1701	1862	2035			
	9%	6%	4%	1%	5%			
150	2106(6)	2429(7)	2753(8)	n/a	3077(9)	3401(10)	3725(11)	4049(12)
	2047	2523	2728	**2898**	3055	3378	3754	4050
	3%	4%	≤ 1%	n/a	≤ 1%	≤ 1%	≤ 1%	≤ 1%

6.1.3 Origin of convective disturbances to TE, L_{CD}

The location where the convective disturbance waves became apparent on the airfoil chord appeared attractive as an acoustic feedback loop point. At some of the flow conditions however (Re = 150,000 and $\alpha = \pm 1.58°$, and Re = 50,000 and α = -1.58°) there were no discernible convective disturbance waves and therefore L_{CDp} and L_{CDs} were undefined in these flow conditions. The applicable feedback lengths were used in the acoustic feedback model and yielded predicted tone estimates with errors on average greater than 10 to 15%. Therefore, based on the poor agreement with measured tones and the number of non-applicable feedback lengths, L_{CD} was not further considered.

6.1.4 Point of separated shear layer reattachment to TE, L_R

The separated shear layer would reattach only at certain Reynolds numbers and angles of attack. This considered feedback length, L_R, was the distance between the point of reattachment to the trailing edge. Due to the separated shear layer reattachment occurring close to the trailing edge for $\alpha = 0°$, the feedback lengths were too small to be considered plausible for use in Arbey and Bataille's (1983) acoustic feedback model. Using the smallest value of n and appropriate value of L_R (n = 1, L_R = 2 mm) the lowest predicted tone frequencies significantly exceeded the experimentally measured tone frequencies. In some of the flow conditions flow reattachment did not occur, making L_R an invalid option for explaining an acoustic feedback mechanism.

It was considered plausible on the airfoil suction surface at $\alpha = 1.58°$ that a feedback loop could exist as the L_R were much longer. The tonal noise generated from it could potentially constructively interfere with another feedback mechanism on the airfoil pressure surface. Upon investigation, large errors (up to 35%) between the predicted and measured tones were observed when L_{Rs} and L_{RXs} were employed

Table 6.5: Values of L_S for $\alpha = 0°$ and values of L_{Sp} and L_{Ss} for $\alpha = \pm 1.58°$ for acoustic feedback loop analysis, as obtained via surface flow visualisation experiments. A positive angle of attack represents the airfoil pressure side, L_{Sp}; a negative angle represents the airfoil suction side, L_{Ss}.

Re ($\times 10^3$)	L_S, L_{Sp} and L_{Ss} (mm)		
	0°	1.58°	-1.58°
50	45	54	62
100	38	37	57
150	26	23	46

as acoustic feedback lengths on the airfoil suction surface at $\alpha = 1.58°$. The only exception was observed at Re = 150,000 when L_{RXs} provided a good agreement to within 4% for both the primary and secondary tones. Due to the overall poor performance of this feedback length, it was not further considered as a valid candidate for an acoustic feedback length.

6.1.5 Origin of boundary layer separation to TE, L_S

The point of boundary layer separation from the airfoil surface to the trailing edge, L_S, seemed a suitable candidate as a feedback length. It was quantifiable at every Reynolds number and angle of attack. The values of L_S obtained via experiment are listed in Table 6.5. For $\alpha = 1.58°$, the feedback lengths on the airfoil pressure and suction surfaces were denoted by L_{Sp} and L_{Ss} respectively. Employing the separation lengths obtained via XFOIL, L_{SX}, many of the predicted tones differed from the experimentally measured values by 10% or greater and therefore were not tabulated here for comparison with other feedback lengths.

The results of using the feedback lengths listed in Table 6.5 are presented in Table 6.6. Employing L_S at Re = 50,000 and 100,000 and $\alpha = 0°$ predicted both primary tones to within 1% or less of the measured tones. The secondary tones at these Reynolds numbers were all predicted to within 2%. At Re = 150,000 and

$\alpha = 0°$ the primary tone was not able to be predicted and the secondary tones were estimated to within 6%. On the airfoil pressure side at $\alpha = 1.58°$ using L_{Sp}, the primary and secondary tones were predicted within 4% for Re = 50,000 and 100,000. One of the secondary tones at 1862 Hz was not able to be predicted. At Re = 150,000 the secondary tones were predicted within 4% which was reasonable; however, the primary tone at 2898 Hz and the secondary tones at 2728 Hz, 3055 Hz and 4050 Hz were not able to be predicted. Alternatively, employing the feedback length on the suction side L_{Ss} at Re = 150,000 and $\alpha = 1.58°$, all of the tones are predicted and the primary tone is within 2% and the secondary tones within 6%. The predictions using L_{Ss} and L_{Sp} at Re = 50,000 and 100,000 were similar, in that the primary and secondary tones were predicted within 7%, with the exception of the lower frequency secondary tone at Re = 50,000 that was predicted within 4%.

6.2 Discussion of feedback models

The best predictions of tones occurred when L_U and variations of L_S were used as feedback lengths. One candidate was not clearly superior over the other due to the small differences in tone prediction accuracy between them. The other feedback lengths were dismissed due to larger errors in tone prediction and/or some of these lengths did not exist at some Reynolds numbers and angles of attack.

The results presented in Table 6.6 made it unclear as to whether the point of boundary layer separation to the airfoil trailing edge length was a suitable feedback length, due to the greater prediction errors at Re = 150,000 using L_S and L_{Sp} compared to other models. Using L_{Ss}, all of the tones were predicted within a 7% error. Consideration was given to a separation length feedback mechanism that could operate on the airfoil suction surface alone at non-zero angles of attack. At zero angle of attack, where it was ambiguous as to whether L_S was a valid candidate, another feedback length such as L_U or L_{LE} could operate. This would suit Arbey and Bataille's (1983) findings, who analysed a NACA 0012 airfoil at $\alpha = 0°$.

Table 6.6: Acoustic feedback analysis using experimentally obtained values of L_S, L_{Sp} and L_{Ss} at $\alpha = 0°$ and 1.58°. In each cell, the top number is the predicted tone, f_n (Hz), and the bracketed number adjacent to it is the corresponding value of n. The number in the middle of each cell is the experimentally measured tone frequency (Hz) and the relative error (%) of f_n with respect to the experimentally measured tone is provided at the bottom of each cell. The experimentally measured primary tones are presented in bold case.

Re ($\times 10^3$)	Tone frequencies (Hz) using L_S, L_{Sp} and L_{Ss}							
	L_S: $\alpha = 0°$							
50	515(6)	595(7)	674(8)	753(9)				
	505	**589**	680	756				
	2%	≤ 1%	≤ 1%	≤ 1%				
100	1207(5)	1427(6)	1646(7)					
	1233	**1426**	1640					
	2%	≤ 1%	≤ 1%					
150	1760(3)	n/a	2263(4)	2766(5)				
	1738	**2050**	2395	2780				
	1%	n/a%	6%	≤ 1%				
	L_{Sp}: $\alpha = 1.58°$							
50	520(5)	614(6)	709(7)					
	517	**607**	713					
	≤ 1%	1%	≤ 1%					
100	1222(4)	1493(5)	1764(6)	n/a	2036(7)			
	1236	**1463**	1701	1862	2035			
	1%	2%	4%	n/a	≤ 1%			
150	1972(3)	2535(4)	n/a	n/a	3098(5)	n/a	3662(6)	n/a
	2047	2523	2728	**2898**	3055	3378	3754	4050
	4%	≤ 1%	n/a	n/a	1%	n/a	2%	n/a
	L_{Ss}: α = -1.58°							
50	535(6)	617(7)	700(8)					
	517	**607**	713					
	4%	2%	2%					
100	1322(7)	1498(8)	1674(9)	1850(10)	2026(11)			
	1236	**1463**	1701	1862	2035			
	7%	2%	2%	≤ 1%	≤ 1%			
150	2113(7)	2394(8)	2676(9)	2958(10)	3239(11)	3521(12)	3803(13)	4084(14S)
	2047	2523	2728	**2898**	3055	3378	3754	4050
	3%	5%	2%	2%	6%	4%	1%	≤ 1%

Via interpretation of Arbey and Bataille's (1983) graphical data, they achieved 3% agreement or better between the predicted and experimentally measured tones at zero angle of attack. As they were not able to compare experimental data at non-zero angle of attack, it is possible that a different acoustic feedback mechanism exists at non-zero angle of attack, involving the airfoil suction surface, and a feedback length such as L_{Ss}.

6.2.1 Dual acoustic feedback mechanisms

It was proposed that feedback mechanisms existed on both the pressure and suction surfaces with feedback lengths L_{Sp} and L_{Ss} respectively, based on the tone predictions at Re = 50,000, 100,000 and $\alpha = 1.58°$. The measured noise would have been a product of the interaction of the noise generating mechanisms on both surfaces. This had the potential to also occur at zero angle of attack as the noise generated one airfoil surface would interfere with the same noise generated on the other surface.

The primary and secondary tones were more accurately predicted when the best case tone predictions using L_{Ss} and L_{Sp} were selected, as compared to using L_{Ss} and L_{Sp} individually. The most accurate tone predictions from the L_{Ss} and L_{Sp} data were gathered and presented in Table 6.7 and this new feedback length was defined as L_{Sp+s}. The values of n followed by a P or S indicated that the pressure or suction surface length was used respectively. Some tones possessed two values of n; this meant that the predicted values on both the pressure and suction surfaces were within 10 Hz of each other or less. In these cases the average of the two predicted tone frequencies was presented. For example, at Re = 50,000 and $\alpha = 1.58°$, using L_{Sp} and L_{Ss} predicted 614 Hz and 617 Hz respectively and thus the presented frequency in Table 6.7 was 616 Hz. Note that the error of 614 Hz and 617 Hz with respect to the measured tone of 607 Hz were 1%, consistent with the average value of 616 Hz that possessed a 1% error.

All of the primary and secondary tones at $\alpha = 1.58°$ were predicted to within

Table 6.7: Acoustic feedback analysis using experimentally obtained values of L_S at $\alpha = 0°$ and values of L_{Sp+s} at $\alpha = 1.58°$. In each cell, the top number is the predicted tone, f_n (Hz), and the bracketed number adjacent to it is the corresponding value of n. The number in the middle of each cell is the experimentally measured tone frequency (Hz) and the relative error (%) of f_n with respect to the experimentally measured tone is provided at the bottom of each cell. The experimentally measured primary tones are presented in bold case.

Re ($\times 10^3$)	Tone frequencies (Hz)							
	$L_S : \alpha = 0°$							
50	515(6)	595(7)	674(8)	753(9)				
	505	**589**	680	756				
	2%	≤ 1%	≤ 1%	≤ 1%				
100	1207(5)	1427(6)	1646(7)					
	1233	**1426**	1640					
	2%	≤ 1%	≤ 1%					
150	1760(3)	n/a	2263(4)	2766(5)				
	1738	**2050**	2395	2780				
	1%	n/a%	6%	≤ 1%				
	Best agreement values of L_{Ss} and L_{Sp}, $L_{Sp+s} : \alpha = \pm 1.58°$							
50	520(5P)	616(6S,7P)	709(7P)					
	517	**607**	713					
	≤ 1%	1%	≤ 1%					
100	1222(4P)	1496(5P,8S)	1674(9S)	1850(10S)	2031(7P,11S)			
	1236	**1463**	1701	1862	2035			
	1%	2%	4%	≤ 1%	≤ 1%			
150	2113(7S)	2535(4P)	2676(9S)	2958(10S)	3098(5P)	3521(12S)	3803(13S)	4084(14)
	2047	2523	2728	**2898**	3055	3378	3754	4050
	4%	≤ 1%	2%	2%	1%	4%	1%	≤ 1%

4% of the measured tones using L_{Sp+s}, with the majority of predictions being 2% or less. Using L_{Sp+s} provided the best fit of all of the feedback lengths considered.

Other feedback lengths including L_U were investigated to see if a matching prediction of tone frequencies occurred on both surfaces (i.e., a dual acoustic feedback mechanism using the MMVL as the feedback length). It was found that the tone predictions using L_{Us} and L_{Up} matched exactly at Re = 100,000 and $\alpha = 1.58°$ (1674 Hz) for one of the secondary tones (measured 1701 Hz), but not for other tones at this flow condition or any of the other Reynolds numbers within a reasonable error estimate. Therefore the single match was most likely a coincidence and the concept of feedback loops on both surfaces was discarded for L_{Us} and L_{Up}.

6.2.2 Magnitudes of tones

To support the theory of dual feedback processes, integer values of n could be selected such that the same (or similar) tones on both airfoil surfaces were predicted. For example, at Re = 100,000 and $\alpha = 1.58°$, L_{Sp} = 37 mm and L_{Ss} = 57 mm. By using n = 5 and 8 for the pressure and suction surfaces respectively, f_n was calculated as 1493 Hz and 1498 Hz that only differ by 5 Hz. This is represented in Figure 6.1. Here n = 5 when f = 1493 Hz on the airfoil pressure surface and the trailing edge; similarly, n = 8 when f = 1498 Hz on the suction surface. This particular angle of attack and Reynolds number flow condition specifically causes this to occur. At other flow speeds, while maintaining the same angle of attack, the boundary layer separation points on both surfaces will be different and thus integer values of n may be nonsensical on both surfaces. At Re = 50,000 and $\alpha = 1.58°$ the primary tone predictions were 614 Hz and 617 Hz (much less than a 1% difference). Note that only the primary tones were matched by both surfaces, with the exception of the secondary tone of 2035 Hz at Re = 100,000 and $\alpha = 1.58°$. This is important in explaining the magnitudes of the primary and secondary tones.

The proposed here is that the noise sources constructively interfere when the

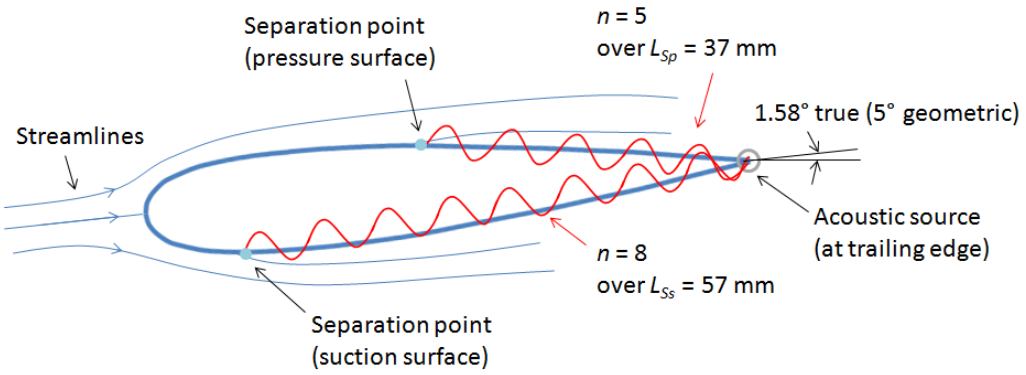

Figure 6.1: Schematic diagram of the dual acoustic feedback loops at $Re = 100{,}000$ and $\alpha = 1.58°$. Values of $n = 5$ and 8 used in the feedback model on both the pressure and suction surfaces predict tone frequencies 1493 Hz and 1498 Hz on the airfoil pressure and suction surfaces respectively.

acoustic feedback mechanisms on both airfoil surfaces have a very close prediction, indicating the potential for strong reinforcement of the feedback loops. If the tone predictions on both surfaces are very close, a narrow band tone is produced. The secondary tones, whose predictions match reasonably well on both surfaces but not as well as the primary tones, may result in the superposition of two acoustic sources with a sufficiently large frequency difference to produce a tone with a broader bandwidth and lesser magnitude, due to the reinforcement between the loops being diminished.

The number of secondary tones increased when α was increased from 0° to 1.58°. There exist more permutations of feedback lengths with the combination of pressure and suction surfaces, generating a greater number of tones. Based on this, it is therefore unlikely that the true feedback length L is a fixed length with respect to Re or α, such as L_{LE} or even L_U. At $\alpha = 0°$, the separation lengths on the upper and lower surfaces are the same and therefore fewer tones are produced; however, assuming that a dual acoustic feedback mechanism occurs, all of the tones generated at $\alpha = 0°$ are reinforced on both the upper and lower surfaces. There will exist specific angles of attack that produce stronger tones than others, as the

Table 6.8: The difference between tone predictions, *df* (Hz), of L_{Sp} and L_{Ss} where applicable and the magnitudes of the tones relative to the broadband noise level (dB). The experimentally measured primary tones are presented in bold case.

	Re = 50,000, $\alpha = \pm 1.58°$				
L_{Ss}	535	**617**	700		
L_{Sp}	520	**614**	709		
df	15	3	9		
dB	8	10	8		
	Re = 100,000, $\alpha = \pm 1.58°$				
L_{Ss}	1322	**1498**	1674	1850	2026
L_{Sp}	1222	**1493**	1764	n/a	2036
df	100	5	90	n/a	10
dB	6	18	8	5	8

separation lengths will vary on both the airfoil pressure and suction surfaces with angle of attack. Thus separation lengths on the pressure and suction surfaces that possess integer permutations of n will generate the strongest tones.

Table 6.8 lists the difference of the tone predictions between L_{Sp} and L_{Ss} where applicable. Also listed are the magnitudes of the corresponding tones relative to the broadband contribution (i.e., if the tone has a magnitude of 60 dB and exceeds the broadband noise by 20 dB, it is listed as 20 dB). This was done to show the connection between the strength of the tones and the difference between the tone predictions. The data are presented for Re = 50,000 and 100,000 because both L_{Sp} and L_{Ss} predict the primary tones. This did not occur for Re = 150,000 and is therefore not presented.

Notice that the primary tones possess the smallest values of *df* and the greatest magnitudes. In other words, the closer the match, the stronger the tone. The tones with $df \leq 15$ Hz also show strong tones but weaker than the primary tone, which are thus by definition secondary tones. Where L_{Ss} predicted a tone at 1850 Hz, L_{Sp} did not predict a tone; this tone possessed the weakest magnitude, as there was no tone of a similar frequency to produce any constructive interference. The prediction

of tones with frequencies 1322 Hz and 1222 Hz at Re = 100,000 and $\alpha = \pm 1.58°$ have df = 100 Hz and only a 6 dB tone. Therefore there exists some evidence to show that the superposition and constructive interference of tonal noise generation mechanisms on both the airfoil and suction surfaces contribute to the characteristics of the measured noise.

6.2.3 Influence of boundary layer trips

The magnitudes of some primary and secondary tones were affected by applying a trip to one surface only. At $\alpha = 0°$ and Re = 50,000 and 100,000, the primary tones were decreased by a greater amount than the secondary tones. This suggests that generation of the primary tone was dependent on the interaction of both airfoil surfaces to a greater degree than the secondary tones. The decrease of primary tone magnitude was shown to diminish with increasing Reynolds number; i.e., at lower Reynolds number the effect of the boundary layer trip on the tone magnitudes is more pronounced. Interestingly at Re = 150,000 all of the tones slightly increased in magnitude or remained the same. The primary tone at $\alpha = 1.58°$ and Re = 150,000 differed from Re = 50,000 and 100,000 in that it appeared not to be a result of the interaction of both the pressure and suction surfaces. Therefore it is possible that the dual acoustic feedback mechanism employing L_{Sp} and L_{Ss} was applicable for $Re \leq$ 100,000 and a different mechanism occurs at $Re \geq$ 150,000, due to the separation lengths at these higher Reynolds numbers.

6.2.4 Accuracy of tone prediction

The model proposed by Arbey and Bataille (1983) was very sensitive to the input parameters. For example, the experimentally measured primary tone at Re = 100,000 and $\alpha = 0°$ was 1426 Hz. Using L_S = 38 mm, $n = 6$, $C_r/U = 0.38$, U = 22.54 m/s and C_0 = 343 m/s, the predicted tone, f_n was 1427 Hz. If there existed a ±1 mm error ($x/C = \pm$ 0.015) in measuring L_S so that it was 37 mm or 39 mm, then f_n = 1466 Hz

and 1390 Hz respectively, while keeping all other variables constant. These errors between the predicted and experimentally measured tones corresponded to 3% and 2% respectively. Therefore a 1 mm ($x/C = 0.015$) measurement error during the interpretation of surface flow visualisation images (to obtain L_S) would increase the relative error of f_n by 3%. A 1 mm error of a 38 mm measurement corresponds to a 3% relative error. Therefore in these experiments the measurement error in L corresponded approximately to the error in f_n. Based on the transitional nature of boundary layer separation locations, there exists some required interpretation and a ±1 mm error in identifying these locations was highly probable.

Consider the following expression contained in Arbey and Bataille's (1983) model

$$\left(1 + \frac{C_r}{C_0 - U}\right)^{-1} \tag{6.2}$$

To maximise the impact of this expression on the full equation, $C_r/(C_0 - U)$ must be maximised. Using parameters from $Re = 150{,}000$ and $\alpha = 0°$, $C_r/(C_0 - U)$ was maximised at 0.046. Therefore the expression contained in Arbey and Bataille's model was calculated as 0.96. If the flow speed U was larger, closer to C_0, then this parameter would be much smaller. Considering that all of the terms in the feedback model are multiplied with each other and $0.96 \approx 1$, the sensitivity of Arbey and Bataille's (1983) model to its input parameters was dependent upon the remainder of the model equation, being

$$\frac{C_r}{L}\,(n + 0.5) \tag{6.3}$$

Here n is a fixed, integer parameter and was thus not considered in the sensitivity of the model as it is an exact number. The remaining parameters were experimentally estimated C_r and L, where $3.6 \leq C_r \leq 14.2$ and $0.023 \text{ m} \leq L \leq 0.067$ m. Every permutation using the maxima and minima of C_r and L were technically possible and therefore $(C_r/L)_{max} = 14.2/0.023 \approx 617$ and $(C_r/L)_{min} = 3.6/0.067 \approx 54$. Thus $(C_r/L)_{max}/(C_r/L)_{min} \approx 12$, showing that the estimation of the tonal noise frequencies, f_n, could vary by approximately a factor of 12 by using incorrect feedback

lengths and convective disturbance speeds. This indicates that the feedback model was very sensitive to the feedback length and convective disturbance speeds and that the successful evaluation of f_n was highly dependent on accurate estimations of these parameters.

Arbey and Bataille (1983) used data from a one-dimensional linear amplification study over a flat plate (Obremski et al., 1969) to evaluate C_r/U for every boundary layer disturbance frequency, f_n. Naturally the development of T-S waves and disturbances in the boundary layer of a flat plate will differ from that of a NACA 0012 airfoil as the curvature of the airfoil impacts the development of the boundary layer and point of separation. The error that could have resulted from using these values of C_r/U is hard to quantify, as Arbey and Bataille performed tests at Reynolds numbers that could not be replicated in the current experiments in the AWT. The points of boundary layer separation on a flat plate and a NACA 0012 airfoil are different and thus it is possible the convective disturbances in the boundary layer would propagate at a different speed for both objects due to the curvature of the airfoil compared to the flat plate.

Arbey and Bataille (1983) employed L_U as a feedback length and assumed that it did not vary with Reynolds number. This assumption may have been valid for the Reynolds number range they investigated, as it was shown by experiment that values for L_U did not change for $Re \geq 100{,}000$ at $\alpha = 0°$. Varying C_0 for the purpose of error analysis from values of 330 m/s to 350 m/s had little impact on the predicted tones. The value of U was not varied for error analysis as there was confidence of the measurement accuracy of the freestream velocity using hot-wire anemometry probes in the AWT contraction to within ±0.1 m/s.

Due to the non-constrictive nature of n (i.e., it can be any integer and does not need to start at one or any particular value), even erroneous feedback lengths would still provide tone predictions on average within approximately 10%. From experiments, the tones were not equispaced and thus Arbey and Bataille's (1983) model, regardless of the feedback length and convective disturbance speeds used, will never

predict all of the tones to within 1% or less. Using their model with data from this current study has predicted some tones to within this accuracy, but not all, as the model predicts equispaced tones that were not observed in experiments. The magnitude of the measured standard deviation of the tone frequency differences prevents perfect predictions with the tone data, even if a falsified (i.e., reverse engineered) feedback length is used to best fit the data.

Consideration was given to the curvature of the NACA 0012 airfoil profile and the effect on accuracy of the tone prediction using the proposed feedback model. The difference between the linear, straight-line feedback lengths (used in this study) and the curved distance along the airfoil chord from the same start-to-finish point was calculated. Small linear line segments along the airfoil profile were calculated using Pythagoras' Theorem and their sum provided an estimate of the curved airfoil distance. Points were selected in the chordwise direction, in 1 mm, 0.5 mm and 0.1 mm increments and the sum of their distances were 68.24 mm, 68.28 mm and 68.31 mm respectively. The increments were not reduced further, as it can be observed that the curved airfoil distance would converge at a value close to 68.3 mm (approximately 1.3 mm longer than the 67 mm airfoil chord), which is sufficient to provide the following reasoning.

The longest feedback length considered in this study (other than $L_{LE} = 67$ mm) is $L_{Ss} = 62$ mm for the flow condition $Re = 50{,}000$ and $\alpha = -1.58°$. Note that this feedback length commences 5 mm downstream of the leading edge and that the majority of the airfoil curvature exists near the leading edge. The curved distance from the leading edge to 5 mm downstream is 6.04 mm and thus the difference between the straight-line feedback length and the curved distance over the airfoil profile in this 5 mm range is 6.04 mm - 5 mm = 1.04 mm. Thus the difference between the straight-line and curved feedback length L_{Ss} for $Re = 50{,}000$ and $\alpha = -1.58°$ is approximately 1.3 mm - 1.04 mm $\approx$ 0.3 mm, to be conservative. The estimated error of the experimentally obtained points MMVL, origin of convective disturbances and origin of boundary layer separation, is approximately ± 1 mm or greater. This

distance is much larger than the expected difference between the straight-line and curved feedback lengths over the airfoil (0.3 mm maximum) and provides justification of the use of simpler straight-line feedback lengths as compared to curved distances along the airfoil chord.

6.3 Proposed feedback model

A dual acoustic feedback mechanism is proposed that incorporates both the airfoil pressure and suction surfaces, with feedback lengths between the points of boundary layer separation on each surface and the trailing edge. The points of boundary layer separation differed on the pressure and suction surfaces, allowing two unique feedback loops for each non-zero angle of attack flow condition. From the analyses of previous results from the literature and the experimental results from this study, it was found that the pressure or suction surface alone was not responsible for the measured noise, rather the interaction of both surfaces and the tones produced by each feedback loop. Where the feedback lengths existed such that n-values corresponded to matching tone frequencies, acoustic reinforcement occurred producing a primary tone. When n-values on each surface did not match tone frequencies, this reinforcement process did not occur (or it was a weaker reinforcement) and a tone weaker than the primary, namely a secondary tone, was produced.

At $\alpha = 0°$, the points of boundary layer separation by definition occurred at the same location on both the upper and lower surfaces and thus reinforcement occurred for all tonal frequencies, with a suitable n-value. This explained why the tone magnitudes at $\alpha = 0°$ were greater than at $\alpha = 1.58°$ for the same Reynolds numbers. The strength of secondary tones, relative to other secondary tones for the same flow condition, were explained by the selected amplified frequencies on the pressure and suction surfaces. When the difference between these frequencies was smaller, then the magnitude of the tone was greater.

The proposed feedback model requires that the feedback length L is a function of

Re and α, differing from other studies. Further to this, each flow condition possesses two values of L, being L_{Sp} and L_{Ss} that exist on the pressure and suction surfaces respectively. This increased complexity allows an explanation for the different tone magnitudes as well as the accurate prediction of tone frequencies. A mathematical representation of the proposed feedback model is given by

$$f_n\left(Re,\alpha\right) = \frac{C_r\left(Re,\alpha\right)}{L_{Sp+s}\left(Re,\alpha\right)}\left(n+0.5\right)\left(1+\frac{C_r\left(Re,\alpha\right)}{C_0-U}\right)^{-1} \tag{6.4}$$

where 50,000 $\leq Re \leq$ 150,000 and $0° \leq \alpha \leq 1.58°$.

A schematic diagram of the proposed feedback model is presented in Figure 6.2. The two stages of the feedback process are shown in Figure 6.2a and 6.2b and is explained as follows. As the flow passes over both airfoil surfaces, the boundary layer separates. The flow passing over at least one airfoil surface reattaches and an acoustic diffraction process occurs, causing broadband noise to propagate in all directions. These acoustic waves radiate upstream with a 180° phase shift to the points of boundary layer separation on both the pressure and suction surfaces. In the cases where an appropriate integer number of n is matched with the feedback length L_S, hydrodynamic disturbances convect downstream to the trailing edge, acoustic waves are diffracted again from the trailing edge and thus an acoustic feedback loop is created. The feedback mechanisms are identical for zero angle of attack flow conditions although the processes on the upper and lower airfoil surfaces are identical.

If the dual acoustic feedback theory is true, the primary tones will be produced on both airfoil surfaces at near-similar frequencies and acoustic beating could be observed (unless the tones produced on both surfaces are exactly the same). The beating frequency will be the difference in the predicted primary tone frequencies, as listed as dF in Table 6.8. The beating frequencies at $\alpha = 1.58°$ and Re = 50,000 and 100,000 are 3 Hz and 5 Hz respectively. Investigations of the amplitude modulation of the acoustic time series were performed and no clear low frequency modulation (between 1 Hz to 10 Hz) was detected. Due to the predicted errors of frequency

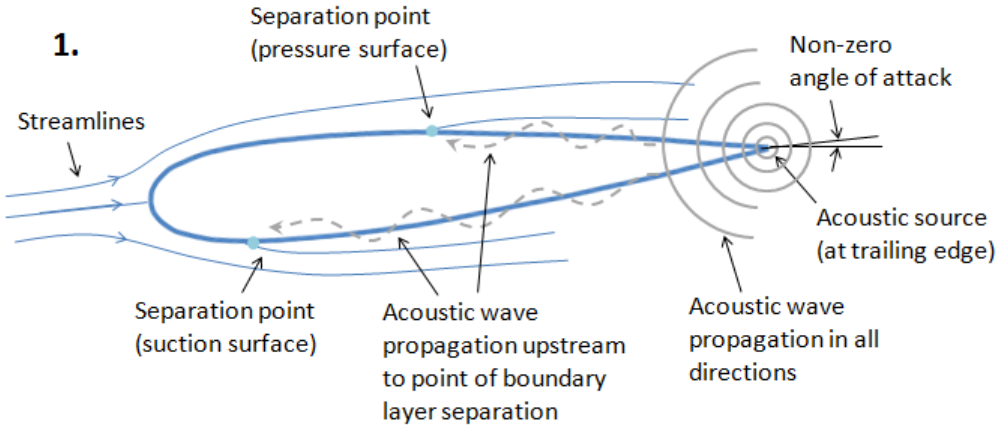

(a)

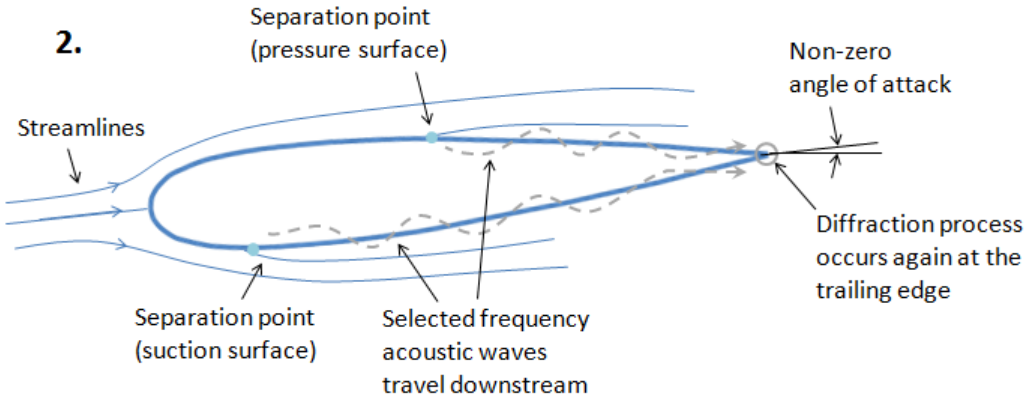

(b)

Figure 6.2: Proposed acoustic feedback model, in two consecutive stages (a) and (b). The acoustic feedback occurs back and forth from (a) to (b).

tone estimation, the true beating frequencies were difficult to calculate and verify. A ± 1 Hz error in tone measurement was expected from a single microphone measurement as discussed in Section 3.2.3.1 that could have changed the dF value at Re = 50,000 and $\alpha = 1.58°$ from 3 Hz to 1 Hz or 5 Hz, without even taking into account the potentially greater errors of surface flow visualisation and convective disturbance speed estimations.

6.4 Summary of analysis

Several feedback length candidates were investigated using Arbey and Bataille's (1983) feedback model. The two feedback lengths that predicted the tones most accurately were the point of maximum flow velocity to the trailing edge, L_U, the length-type used by Arbey and Bataille (1983), and the point of boundary layer separation to the trailing edge, L_S. Both models predicted tones to within 5% accuracy, but neither length was found to be better than the other for accurately predicting the tones.

The concept of a dual acoustic feedback mechanism was proposed, where at non-zero angles of attack, acoustic feedback loops exist on the airfoil suction and pressure sides simultaneously. For each Reynolds number and angle of attack, both surfaces generate tones within a feedback loop and the tones that are closely matched on both surfaces produce an acoustic superposition. The closest matched tone is the primary tone and all other tones, weakly-matched or not, are secondary tones. This principle provided excellent agreement with experimental results when the point of boundary layer separation to the trailing edge, L_S, was employed at $50{,}000 \leq Re \leq 150{,}000$. This theory also provided a qualitative explanation of the relative tonal magnitudes.

The acoustic feedback model derived by Arbey and Bataille (1983), regardless of the feedback length used, was highly sensitive to accuracy of the estimations of C_r and L. Errors in estimating L_S and C_r are likely regardless of the feedback model used, due to the interpretation surface flow visualisation data and phase differences between flow and noise near the airfoil surface, respectively.

Chapter 7

Conclusions

The tonal noise generation mechanisms of airfoils at low-to-moderate Reynolds number have been investigated extensively using both numerical and experimental methods since the 1970's. There is no clear agreement regarding the characteristics of the typical acoustic spectra of airfoils for various Reynolds numbers, angles of attack and airfoil profile. The various studies present differing quantities of tones, varying relative magnitudes and broadband contributions. There is disparity in the analysis of the flow around and near the airfoil surface, the existence of separation bubbles (mid-chord and near the trailing edge), where instabilities originate in the boundary layer and points of boundary layer separation and reattachment.

Many studies suggest that an acoustic feedback mechanism was responsible for the generation of a series of acoustic tones (Tam, 1974; Longhouse, 1977; Arbey and Bataille, 1983; Desquesnes et al., 2007; Jones et al., 2010; Ikeda et al, 2012). There exists discrepancy as to whether acoustic feedback loops exist on one or both airfoil surfaces at non-zero angles of attack (Desquesnes et al., 2007; Probsting et al., 2015). Some studies showed that an acoustic feedback mechanism was not necessary for tone generation and that all recorded secondary tones were due to the interaction of vortex shedding processes producing a primary tone that interacted with the testing facility (Nash et al., 1999; Tam and Ju, 2011).

The primary gap addressed in this thesis was the feasibility of an acoustic feedback mechanism at low-to-moderate Reynolds number. It was hypothesised that an acoustic feedback mechanism is responsible for tonal noise generation for an airfoil, and exists between the noise source location (trailing edge) and the point of boundary layer separation on both the suction and pressure surfaces.

To address this hypothesis, a series of experiments were performed in a small-scale anechoic wind tunnel (AWT), using a 67 mm chord NACA 0012 airfoil at $\alpha = 0°$, 1.58° and 3.16° and at $Re = 50{,}000$ to 150,000. Single microphone measurements were obtained over 4 seconds in the acoustic far-field (600 mm from the airfoil) to estimate the acoustic spectra of the airfoil. A hot-wire anemometry probe was attached to a traverse that obtained velocity data over 4 seconds. This measured the mean velocity and velocity spectral densities around the airfoil profile (1 mm and greater from the surface) and in the near-wake. Four-second sampling times were found to be accurate to within ±1 Hz and ±0.1 m/s for acoustic and velocity data respectively. The acoustic and flow signals were obtained simultaneously to determine the coherence between the signals, at each hot-wire anemometry measurement location. Trips were applied near the airfoil leading edge on each airfoil surface, to quantify the change in acoustic spectra and separation location(s), caused by interruption of the natural development of the boundary layer. Surface flow visualisation, using an in-house developed mixture of talcum powder and flaxseed oil, was used to estimate points of boundary layer separation and separated shear layer reattachment and compared against XFOIL (Drela, 1989) estimations.

An acoustic beamformer was designed, manufactured and installed in the AWT to locate acoustic sources near or on the airfoil surface. Sixty-three microphones were arranged in a unique Arcondoulis spiral pattern, that was designed to improve noise source resolution within the airfoil self-noise frequency range. White noise sources were placed in the AWT 600 mm from the array to determine the array response and determine the errors in location estimation. By comparing the array response in the AWT with similar tests in an anechoic chamber, it was determined

that the AWT possessed some weak standing wave behaviour, affecting the ability of the beamformer to accurately locate an acoustic source. The standing waves caused the beamformer image to shift, and the amount that the image shifted was frequency dependent. The image shift with respect to frequency was observed to be constant for all noise source types; this was taken into account when interpreting the airfoil self-noise source locations.

Single microphone measurements conducted for airfoil angles of attack of $\alpha = 0°$ and 1.58° revealed that a strong primary tone was present with several weaker secondary tones, superimposed on a broadband contribution, yet only broadband noise was recorded at $\alpha = 3.16°$. The number of tones and the ratio of primary to secondary tone magnitudes varied with both Reynolds number and angle of attack. The primary tone followed a ladder-structure with respect to flow velocity, where the transition of a secondary tone, sufficiently increasing in magnitude to surpass the previous primary tone, caused an apparent jump in primary tone frequency.

Hot-wire anemometry revealed the maximum mean velocity location along the airfoil chord, used as a feedback loop closing point by Arbey and Bataille (1983), that showed excellent agreement with XFOIL (Drela, 1989). Simultaneous measurements obtained by single microphones and hot-wire anemometry revealed the coherence between the acoustic and velocity signals. Strong coherence was observed along the airfoil chord for most of the primary tone frequencies, whereas some secondary tone frequencies possessed moderate-weak coherences and showed no clear relationship with respect to location on the airfoil chord. Strong coherences were also observed in the near-wake for the primary tone frequencies.

The phase differences between the acoustic and velocity signals along the airfoil chord were used to measure the points of instability and phase change in the boundary layer. The origin of convective disturbances appeared to move upstream with increasing Reynolds number, yet some locations were not clear and difficult to identify. The convective disturbance wavelength was calculated by measuring the chordwise distance between the points of abrupt phase change. Multiplying this

distance by the tone frequency, the convective disturbance velocity was calculated and shown to vary slightly at each Reynolds number and angle of attack.

Surface flow visualisation revealed locations of boundary layer separation and reattachment. Separation was observed near mid-chord at $\alpha = 0°$ and closer to the trailing edge at non-zero angles of attack. The point of separation moved closer to the leading edge with respect to increasing Reynolds number and reattachment was observed for all Reynolds numbers and angles of attack, with the exception of $\alpha = 0°$ and $Re = 50{,}000$ and 75,000.

Acoustic beamforming identified that the maximum acoustic source location was at the trailing edge. This was deduced by understanding the frequency-dependent standing wave behaviour pattern of the maximum acoustic source location relative to the trailing edge. The net shift of the standing wave behaviour pattern was located directly in-line with the array centre, that corresponded to the trailing edge location.

Applying a trip to one of the airfoil surfaces produced rapid transition to turbulence in the boundary layer, resulting in some of the secondary tones diminishing in magnitude. Applying trips to both surfaces ceased all tone generating mechanisms. This provided evidence that tones could be generated on one airfoil surface only, but the processes on one airfoil surface did not produce the untripped airfoil self-noise acoustic spectra, thus showing that both airfoil surfaces were responsible for the airfoil self-noise spectra.

A dual acoustic feedback model was proposed, where feedback processes acted independently on the airfoil pressure and suction surfaces. A model proposed by Arbey and Bataille (1983) was adapted such that the feedback lengths were between the acoustic source at the trailing edge and the points of boundary layer separation on the pressure and suction surfaces. At non-zero angles of attack, acoustic feedback mechanisms existed on the airfoil suction and pressure sides simultaneously. For each Reynolds number and angle of attack, both surfaces generated tones within a feedback loop. The tones that were closely matched on both surfaces produced an

acoustic superposition. By considering processes on each airfoil surface, tones were generated on both airfoil surfaces independently and the tones with the same or similar frequencies constructively interfered, thus explaining the strong primary tone magnitude. The primary tone possessed near exact frequencies on both surfaces, whereas the secondary tones had weak or large differences in frequencies between both surfaces, causing little or no superposition, and thus explaining their relative diminished magnitude to the primary. Using this model, good agreement was achieved between the experimentally obtained and predicted tone frequencies. This theory also provided a qualitative explanation of the relative tonal magnitudes.

Chapter 8

Future Work

There is a significant amount of analysis, both experimental and numerical, that could be performed to help resolve the noise generating mechanisms of an airfoil at low-to-moderate Reynolds number. This chapter details the recommended experimental procedures that would support the work presented in this thesis, that were not capable within the time-frame of this research and due to the physical limitations of the facilities available.

The proposed theory of a dual acoustic feedback model could be strengthened by performing experiments in a facility that could produce a Reynolds numbers greater than 200,000. This would allow the comparison of the acoustic spectra with Nash et al., (1999) and Tam and Ju (2011) who claim that secondary tones should not be present at $\alpha = 0°$. A larger testing facility would help remove any facility effects that may have impacted the measured noise, such as standing wave behaviour. An anechoic environment without standing wave behaviour (a quiet outdoor environment would be ideal) should be used, as it could put the argument of facility effects, impacting the measured acoustic spectra and the generation of secondary tones, to rest or verify it.

These experiments could be performed using a larger airfoil chord (100 mm +) with a much larger test section, to prevent the airfoil at larger angles of attack

significantly blocking the contraction outlet flow. A larger chord will reduce the percentage-chord error in estimating points of boundary layer separation, produce larger boundary layer profiles and allow the investigation of higher Reynolds numbers for the same flow speed as a smaller airfoil chord. Tests could be performed with smaller Reynolds number increments (such as 10,000) and angles of attack from zero to the smallest angle of attack that does not produce tones. A greater range of Reynolds numbers and angles of attack would provide more feedback analysis cases, with different sets of tones and points of boundary layer separation to use in an acoustic feedback model. In addition, the origin of convective disturbances could be measured more accurately and could indeed be a valid acoustic feedback candidate. A thicker boundary layer would allow a more accurate estimation of this location for all Reynolds numbers and angles of attack.

The transition of tonal noise generating mechanisms from $\alpha = 0°$ to small non-zero angles of attack should be investigated. Some theories discussed in the literature proposed tonal noise generation mechanisms at either zero or non-zero angles of attack, rather than both. Detailed analyses at small angles of attack, such as $\alpha = 0.5°$, $1°$ and $1.5°$ would help reveal any sudden transitional changes in acoustic feedback (or other tone generating mechanisms) from zero to non-zero angles of attack and determine if there exists a smooth transition of feedback processes with increasing angle of attack or whether behaviour suddenly changes at a certain angle of attack.

Analyses should also be performed with different airfoil profiles to determine the influence of airfoil thickness on boundary layer separation, measured tone frequency and magnitudes. A revised acoustic feedback model, including the airfoil thickness as a parameter, could then be proposed. Quantification of the tone magnitudes generated by the acoustic superposition of feedback processes on the airfoil pressure and suction sides would help finalise the proposed model. Then acoustic tone frequencies and magnitudes could be predicted for any flow condition and NACA airfoil profile, at low-to-moderate Reynolds number. This would have significant benefits in the design of small-scale fans, submarine propellers and micro-wind turbines.

References

Amiet, R., 1977, *Refraction of Sound by a Shear Layer*, 15th AIAA Aeroacoustic Conference, AIAA 1977-54.

Arbey, H., and Bataille, J., 1983, *Noise generated by airfoil profiles placed in a uniform laminar flow*, Journal of Fluid Mechanics. Vol. 134, pp. 33-47.

Archibald, F., 1975, *The Laminar Boundary Layer Instability Excitation of an Acoustic Resonance*, Journal of Sound and Vibration. Vol. 38, pp. 387-402.

Balzer, W., and Fasel, H.F., 2010, *Direct numerical simulation of laminar boundary-layer separation and separation control on the suction side of an airfoil at low Reynolds number conditions*, 40th AIAA Fluid Dynamics Conference and Exhibit (American Institute of Aeronautics and Astronautics) Chicago, Illinois, 2010.

Bies, D.A., and Hansen, C.H., 2003, *Engineering Noise Control: Theory and Practice*, Third ed. E & FN Spon, London, New York.

Blake, W.K., 1975, *A Statistical Description of Pressure and Velocity Fields at the Trailing Edges of a Flat Strut*, DTNSRDC Report 4241, David Taylor Naval Ship R & D Center, Bethesda, Maryland.

Boutilier, M.S.H., and Yarusevych, S., 2012, *Separated shear layer transition over an airfoil at a low Reynolds number*, Phys. Fluids Vol. 24, 084105 (2012).

Brendel, M., and Mueller, T.J., 1986, *Boundary-Layer Measurements on an Airfoil at Low Reynolds Numbers*, Journal of Aircraft. Vol. 25(7), pp. 612-617.

Brooks, T., and Humphreys, W., 2006a, *A Deconvolution Approach for the Mapping of Acoustic Sources (DAMAS) determined from Phased Microphone Arrays*, Journal of Sound and Vibration. Vol 294, pp. 856-879.

Brooks, T., and Humphreys, W., 2006b, *Extension of DAMAS Phased Array Processing for Spatial Coherence Determination (DAMAS-C)*, 12th AIAA/CEAS Aeroacoustics Conference, May 8-10 2006, Cambridge, MA.

Brooks, T., Humphreys, W., Hunter, W., and Meadows, K., 1998, *Design and Use of Microphone Directional Arrays for Aeroacoustic Measurements*, AIAA 98-0471, 36th Aerospace Sciences Meeting & Exhibit, January 12-15 1998, Reno, NV.

Brooks, T., and Hutcheson, F., 2002, *Measurement of Trailing Edge Noise using Directional Array and Coherent Output Power Methods*, AIAA 2002-2472, 8th AIAA/CEAS Aeroacoustics Conference, June 17-19 2002, Breckenridge, Colorado.

Brooks, T., and Hutcheson, F., 2004, *Effects of Angle of Attack and Velocity on Trailing Edge Noise*, AIAA 2004-21031, 42nd AIAA Aerospace Sciences Meeting, January 5-8 2004, Reno, NV.

Brooks, T., Pope, D., and Marcolini, M., 1989, *Airfoil Self-Noise and Prediction*, Tech. Rep., NASA Reference Publication 1218.

Brüel & Kjær., 2004, *Technical Review - Beamforming, No. 1 2004*, Copyright 2004, Brüel & Kjær Sound & Vibration Measurement A/S.

Brusniak, L., 2008, *DAMAS2 Validation for Flight Test Airframe Noise Measurements*, Berlin Beamforming Conference (BeBec), February 19-20 2008.

Burdic, W.S., 1984, *Underwater Acoustic System Analysis*, Prentice-Hall Inc., Englewood Cliffs, NJ, 1984.

Chong, T., and Joseph, P., 2009, *An Experimental Study of Tonal Noise Mechanism of Laminar Airfoil*, AIAA Paper 09-3345, 15th AIAA/CEAS Aeroacoustic Conference (30th AIAA Aeroacoustic Conference) 11-13 May 2009, Miami, Florida, U.S.A.

Curle, N., 1955, *The influence of solid boundaries upon aerodynamic sound*, Proceedings of the Royal Society London A231, pp. 505-514.

Desquesnes, G., Terracol, M., and Sagaut, P., 2007, *Numerical investigation of the tone noise mechanism over laminar airfoils*, Journal of Fluid Mechanics. Vol. 591, pp. 155-182.

Dobrzynski, W., Ewert, R., Pott-Pollenske, M., Herr, M., and Delfs, J., 2008, *Research at DLR towards airframe noise prediction and reduction*, Journal of Aerospace Science and Technology. Vol. 12, pp. 80-90.

Dougherty, R., 2005, *Extensions of DAMAS and Benefits and Limitations of Deconvolution in Beamforming*, AIAA 2005-2961, 11th AIAA/CEAS Aeroacoustics Conference (26th AIAA Aeroacoustics Conference), 23-25 May 2005, Monterey, California.

Dovgal, A.V., Kozlov, V.V., and Michalke, A., 1994, *Laminar boundary layer separation: Instability and associated phenomena*, Prog. Aerosp. Sci. Vol. 30(1), pp. 61-94 (1994).

Drela, M., 1989, *XFOIL: An analysis and design system for low Reynolds Number airfoils*, Conference on Low Reynolds Number Airfoil Aerodynamics, University of Notre Dame.

Elliot, R.S., 1966, *The Theory of Antenna Arrays*, Microwave Scanning Antennas, R.C. Hansen, Ed., Academic Press, 1966.

Ffowcs Williams, J.E., and Hall, L.H., 1970, *Aerodynamic Sound Generation by Turbulent Flow in the Vicinity of a Scattering Half Plane*, Journal of Fluid Mechanics. Vol. 40, pp. 657-670.

Fink, M.R., 1975, *Prediction of airfoil tone frequencies*, Journal of Aircraft. Vol. 12, pp. 118-120.

Gaudriot, L., Hellion, A., Bequet, B., and Arbey, H., 1981, *Analyse du bruit de profil par r'eseaux de capteurs proches ou lointains*. Rev. d'Acoust. Vol. 63, pp. 208-210.

Gaster, M., 1963, *On stability of parallel flows and the behaviour of separation bubbles*. PhD Dissertation, University of London.

Gaster, M., 1968, *Growth of disturbances in both space and time*. Phys. Fluids. Vol. 11, pp.723-727.

Geyer, T., Sarradj, E., and Fritzsche, C., 2010, *Measurement of the noise generation at the trailing edge of porous airfoils*, Experiments in Fluids. Vol. 48, pp. 291-308.

Grosche, F.R., Stiewitt, H., and Binder, B., 1977, *Acoustic Wind-Tunnel Measurements with a Highly Directional Microphone*, AIAA Journal. Vol. 15(11), pp. 1590-1596.

Hannemann, K., and Oertel Jr, H., 1989, *Numerical simulation of the absolutely and convectively unstable wake*, Journal of Fluid Mechanics. Vol. 199, pp. 55-88.

Howe, M.S., 1978, *A Review of the Theory of Trailing Edge Noise*, Journal of Sound and Vibration. Vol 61(3), pp. 437-465.

Howe, M.S., 2006, *Hydrodynamics and Sound*, Cam. Uni. Press, New York (2006).

Ikeda, T., Atobe, T., and Takagi, S., 2012, *Direct simulations of trailing-edge noise generation from two-dimensional airfoils at low Reynolds numbers*, Journal of Sound and Vibration. Vol. 331, pp. 556-574.

Jones, L.E., Sandberg, R.D., and Sandham, N.D., 2008, *Direct numerical simulations of forced and unforced separation bubbles on an airfoil at incidence*, Journal of Fluid Mechanics. Vol. 602, pp. 175-207.

Jones, L.E., Sandberg, R.D., and Sandham, N.D., 2010, *Stability and Receptivity Characteristics of a Laminar Separation Bubble on an Aerofoil*, Journal of Fluid Mechanics. Vol. 648, pp. 257-296.

Kendall, J.M. Jr., 1977, *Airframe Noise Measurements by Acoustic Imaging*, AIAA Paper 77-55, AIAA 15$^{\text{th}}$ Aerospace Sciences Meeting, Los Angeles, CA, January, 1977.

Kingan, M., and Pearse, J., 2009, *Laminar boundary layer instability noise produced by an aerofoil*, Journal of Sound and Vibration. Vol. 322, pp. 808-828.

Leclerq, D., Doolan, C.J., and Reichl, J., 2007, *Development and Validation of a Small-Scale Anechoic Wind Tunnel*, 14$^{\text{th}}$ International Congress on Sound and Vibration, 2007, Cairns, Australia.

Lighthill, M.J., 1952, *On Sound Generated Aerodynamically. II. Turbulence as a Source of Sound*, Proc. R. Soc. Lond. A. Vol. 222, pp. 1-32.

Lowson, M.V., Fiddes, S.P., and Nash, E.C., 1994, *Laminar Boundary Layer Aeroacoustic Instabilities*, AIAA 94-0358, 32$^{\text{nd}}$ Aerospace Sciences Meeting and Exhibition, 1994, Reno, NV.

Longhouse, R.E., 1977, *Vortex shedding noise of low tip speed, axial flow fans.* Journal of Sound and Vibration. Vol. 53, pp. 25-46.

McAlpine, A., Nash, E.C., and Lowson, M.V., 1999, *On the generation of discrete frequency tones by the flow around an aerofoil*, Journal of Sound and Vibration. Vol. 222, pp. 753-779.

Moreau, D.J., Brooks, L.A., and Doolan, C.J., 2011, *Broadband noise from sharp-edged struts*, 17$^{\text{th}}$ AIAA/CEAS Aeroacoustics Conference (32$^{\text{nd}}$ AIAA Aeroacoustics Conference), June 6-8 2011, Portland, Oregon, USA.

Moreau, D.J., Brooks, L.A., and Doolan, C.J., 2011, *On the aeroacoustic tonal noise generation mechanism of a sharp-edged plate*, J. Acoust. Soc. Am. Vol 129, Issue 4, pp. 154-160.

Moreau, D.J., Prime, Z., Porteous, R., Doolan, C.J., and Valeau, V., 2014, *Flow-induced noise of a wall-mounted finite airfoil at low-to-moderate Reynolds number*, Journal of Sound and Vibration. Vol. 333, pp. 6924-6941.

Munson, B., Young, D., and Okiishi, T., 2002, *Fundamentals of Fluid Mechanics*, Fourth Edition, Copyright 2002, John Wiley & Sons Inc.

Nakano, T., Fujisawa, N., and Lee, S., 2006, *Measurement of tonal-noise characteristics and periodic flow structure around NACA0018 airfoil*, Experiments in Fluids. Vol. 40, pp. 482-490.

Nakayama, A., 1987, *Curvature and Pressure-Gradient Effects on a Small-Defect Wake*, Journal of Fluid Mechanics. Vol. 175, pp. 215-246.

Nash, E., Lowson, M., and McAlpine, A., 1998, *Boundary-Layer Instability Noise on Aerofoils*, Journal of Fluid Mechanics. Vol. 382, pp. 27-61.

O'Meara, M.M., and Mueller, T.J., 1987, *Laminar separation bubble characteristics on an airfoil at low Reynolds numbers*, AIAA Journal. Vol 25(8), pp. 1033-1041.

Obremski, H.J., Morkovin, M.V., Landahl, M., Wazzan, A.R., Okamura, T.T., and Smith, A.M.O., 1969, *A portfolio of stability characteristics of incompressible boundary layers.* AGARDograph 134.

Oerlemans, S., Fisher, M., Maeder, T., and Kögler, K., 2008, *Reduction of Wind Turbine Noise using Optimized Airfoils and Trailing-Edge Serrations*, 14th AIAA/CEAS Aeroacoustics Conference (29th AIAA Aeroacoustics Conference), May 5-7 2008, Vancouver, BC Canada.

Passchier-Vermeer W., and Passchier W.F., 2000, *Noise exposure and public health*, Environ. Health Perspect. 108 Suppl 1: 123-31.

Paterson, R., Vogt, P., Fink, M., and Munch, C., 1973, *Vortex Noise of Isolated Airfoils*, Journal of Aircraft. Vol. 10(5), pp. 296-302.

Pauley, L.L., Moin, P., and Reynolds, W.C., 1990, *The structure of two-dimensional separation*, Journal of Fluid Mechanics. Vol. 220, pp. 397-411.

Plogmann, B., Herrig, A., and Würz, W., 2013, *Experimental investigations of a noise feedback mechanism on a NACA 0012 airfoil*, Experiments in Fluids. Vol. 54, pp. 1480.

Probsting, S., Serpieri, J., and Scarano, F., 2014, *Experimental investigation of aerofoil tonal noise generation*, Journal of Fluid Mechanics. Vol. 747, pp. 656-687.

Probsting, S., Scarano, F., and Morris, C., 2015, *Regimes of tonal noise on an airfoil at moderate Reynolds number*, Journal of Fluid Mechanics. Vol. 780, pp. 407-438.

Rist, U., Maucher, U., and Wagner, S., 1996, *Direct numerical simulation of some fundamental problems related to transition in laminar separation bubbles in Computational Fluid Dynamics* edited by J.-A. D'esid'eri, C. Hirsch, P. Le Tallec, M. Pandolfi, and J. P'eriaux (Wiley, 1996), pp. 319-325.

Rist, U., and Maucher, U., 2002, *Investigations of time-growing instabilities in laminar separation bubbles*, Eur. J. Mech. B/Fluids Vol. 21(5), pp. 495-509.

Sandberg, R., Jones, L., Sandham, N., and Joseph, P., 2008, *Direct numerical simulations of tonal noise generated by laminar flow past airfoils*, Journal of Sound and Vibration. Vol. 320, pp. 838-858.

Schlinker, R.H., 1977, *Airfoil Trailing Edge Noise Measurements With a Directional Microphone*, AIAA Paper 77-1269, 4$^{\text{th}}$ AIAA Aeroacoustics Conference, Atlanta, GA, October, 1977.

Schumacher, K.L., Doolan, C.J., and Kelso, R.M., 2014, *The effect of a cavity on airfoil tones*, Journal of Sound and Vibration. Vol. 333, pp. 1913-1931.

Tam, C., 1974, *Discrete Tones of isolated airfoils*, The Journal of the Acoustic Society of America. Vol. 55(6), pp. 1173-1177.

Tam, C., and Ju, H., 2011, *Airfoil Tones at Moderate Reynolds Number: A Computational Study*, 17$^{\text{th}}$ AIAA/CEAS Aeroacoustics Conference (32$^{\text{nd}}$ AIAA Aeroacoustics Conference), AIAA-2011-2711, June 6-8 2011, Portland, OR.

Traub, W.L., 2011, *Experimental Investigation of the Effect of Trip Strips at Low Reynolds Number*, Journal of Aircraft. Vol. 48(5), pp. 1776-1784.

Underbrink, J.R., 2002, *Aeroacoustic Phased Array Testing in Low Speed Wind Tunnels: Aeroacoustic Measurements*, edited by Mueller T.J., Springer-Verlag, New York, 2002, pp. 98-140.

Wang, M., 1998, *Computation of Trailing-Edge Noise at Low Mach Number using LES and Acoustic Analogy*, Center for Turbulence Research Annual Research Briefs.

Yarusevych, S., Sullivan, P.E., and Kawall, J.G., 2003, *Control of Airfoil Wake Structure at Low Reynolds Numbers by Acoustic Excitation*, 33rd AIAA Fluid Dynamics Conference and Exhibit, June 23-26 2003, Orlando, Florida.

Yarusevych, S., Sullivan, P.E., and Kawall, J.G., 2004, *Investigation of Airfoil Boundary Layer and Wake Development at Low Reynolds Numbers*, 34th AIAA Fluid Dynamics Conference and Exhibit June 28 - July 1 2004, Portland, Oregon.

Yarusevych, S., Sullivan, P.E., and Kawall, J.G., 2008, *Unsteady Separated Flow Characterization on Airfoils Using Time-Resolved Surface Pressure Measurements*, AIAA Journal. Vol. 46(2), pp. 508-516.

Yarusevych, S., Sullivan, P.E., and Kawall, J.G., 2009, *Smoke-Wire Flow Visualization in Separated Flows at Relatively High Velocities*, AIAA Journal. Vol. 47(6), pp. 1592-1595.

Defending Australia in the Asia Pacific Century: Force 2030, 2016, Defence White Paper, 2016, viewed June 2016, <http://www.defence.gov.au/whitepaper/Docs/2016-Defence-White-Paper.pdf>.

Domestic Roof-Mounted Wind Turbines - The Current State of the Art, August 2005, Mid Wales Energy Agency, viewed June 2010, <http://www.bwea.com/pdf/small/mid-wales-microwind.pdf>.

Appendix A

Arcondoulis spiral array coordinates.

Arcondoulis spiral array coordinates (all z-coordinates are 0 mm)		
Microphone number	x-coordinate (mm)	y-coordinate (mm)
1	0.0	0.0
2	-10.0	-16.0
3	-27.0	-11.0
4	-31.2	7.5
5	-22.8	24.5
6	-5.2	34.3
7	15.7	32.7
8	32.9	19.0
9	39.6	-3.0
10	32.5	-25.9
11	12.8	-41.6
12	-13.4	-43.4
13	-37.2	-29.6
14	-49.5	-3.7
15	-45.0	26.0
16	-23.5	48.9
17	8.4	56.0
18	40.2	43.4
19	60.2	13.7
20	60.0	-23.6
21	37.9	-55.6
22	0.0	-70.2
23	-41.3	-60.6
24	-71.2	-27.9
25	-77.8	17.8
26	-56.6	61.0
27	-12.9	85.8
28	39.3	81.5
29	81.7	47.2
30	98.0	-7.3
31	80.1	-63.9

Arcondoulis spiral array coordinates, continued ...

(all z-coordinates are 0 mm)

Microphone number	x-coordinate (mm)	y-coordinate (mm)
32	31.5	-102.0
33	-32.8	-106.3
34	-90.6	-72.3
35	-120.4	-9.0
36	-108.9	62.9
37	-56.8	118.0
38	20.3	134.9
39	96.6	104.1
40	144.2	32.9
41	143.3	-56.3
42	90.3	-132.4
43	0.0	-166.8
44	-97.8	-143.4
45	-168.2	-66.0
46	-183.3	41.8
47	-133.0	143.4
48	-30.3	201.2
49	91.8	190.7
50	190.6	110.1
51	228.3	-17.1
52	186.1	-148.4
53	73.0	-236.6
54	-75.9	-246.0
55	-209.2	-166.9
56	-277.4	-20.8
57	-250.5	144.6
58	-130.4	270.8
59	46.6	309.0
60	220.9	238.0
61	329.0	75.1
62	326.4	-128.1
63	205.2	-301.0